Ytterbium and Lithium Quantum Gases: Heteronuclear Molecules and Bose-Fermi Superfluid Mixtures

Richard J. Roy

A dissertation
submitted in partial fulfillment of the
requirements for the degree of

Doctor of Philosophy

University of Washington

2017

Reading Committee:

Subhadeep Gupta, Chair

Sanjay Reddy

Alejandro Garcia

Program Authorized to Offer Degree:
Physics

University of Washington

Abstract

Ytterbium and Lithium Quantum Gases:
Heteronuclear Molecules and Bose-Fermi Superfluid Mixtures

Richard J. Roy

Chair of the Supervisory Committee:
Associate Professor Subhadeep Gupta
Department of Physics

This dissertation describes a series of experiments conducted in an ultracold mixture of fermionic ^{6}Li and bosonic ^{174}Yb atoms, with a focus on the creation of heteronuclear YbLi molecules and the realization of a mixture of Bose and Fermi superfluids. Measurements of field-dependent inelastic scattering between metastable ($^3P_2$) Yb and ground state ($^2S_{1/2}$) Li are discussed, revealing the existence of interspecies Feshbach resonances which in principle may be used to create ultracold YbLi molecules in a coherent fashion, but in practice exhibit prohibitively large inelastic loss in the specific scattering channel used. An alternative all-optical two-photon pathway to ground state YbLi molecules is also explored, with the initial results presented here being the exploration of excited state YbLi molecular potentials using photoassociation spectroscopy, and the successful production of YbLi* molecules in a dual-species magneto-optical trap. An upgraded crossed optical dipole trap is implemented on the Yb-Li experimental apparatus, with a novel application of time-averaged potential shaping for very rapid and efficient Yb BEC production. Lastly, we detail the realization of an interacting mixture of Bose and Fermi superfluids, and identify the exchange of angular momentum between the superfluids by the excitation of a rotational mode of oscillation in the bosonic component due to interspecies interactions.

ACKNOWLEDGMENTS

The journey through graduate school is one that I did not navigate alone, and I am greatly indebted to a number of people for their support, teaching, mentorship, and encouragement. These past six years have been wonderfully spent, both inside and out of the lab, and I count myself lucky for being surrounded by the people who made them so.

In the course of growing as an experimental physicist, I believe the greatest skills I have learned are the ability to approach new physical questions or lines of inquiry with confidence, a dash of intuition, and a methodical tool set, and, possibly more importantly, the ability to think critically about which questions are the most essential and constructive to be asked. To accurately acknowledge all the people who fostered this scientific growth, I must begin with two undergraduate professors of mine from the University of Puget Sound: Alan Thorndike and Greg Elliott. In my time at UPS, these two mentors imparted to me invaluable ways of thinking about physics, both at the chalkboard and in the lab. I remember fondly discussing classic physics problems with Alan on his sailboat out on Commencement Bay in Tacoma, and owe much of my desire to uncover the most basic, nonsense-free explanations of physical systems to him. Greg Elliott had the unfortunate task of being my first lab advisor, and thus teaching me the basics of thinking like an experimental physicist. I learned a great deal of technical and analytical skills from Greg, and my confidence in the lab setting is in no small part because of him. I am grateful to have been able to keep in touch with Greg over the years, including visits to his home on Vashon Island to brew beer.

At the end of my first year of graduate school, after a short stint in an experimental condensed matter lab, I joined the group of Deep Gupta. For these past five years, Deep has been a remarkable mentor, both as a physicist and as a person. Deep's ability to distill difficult concepts down to the important ideas, and his clear desire to convey that understanding to others has been inspiring. I feel lucky to have had an advisor with such a persistently positive attitude, and know that this certainly impacted my growth as a physicist and my effectiveness in the lab. We have shared many intellectually stimulating conversations about physics and life over the years, and I will miss having those chats in the future.

Upon entering the group, the graduate students on the lithium-ytterbium mixture experiment were Anders Hansen, Alex Khramov, and Will Dowd. I am grateful to all three of them for answering my many questions about the experiment and related ideas in my early days in the lab. Though my time in the lab with Anders was shorter than the others, I gleaned a great deal of practical expertise from him on how to operate the experiment, and enjoyed our many chats about brewing beer, as well as joining him as a leader on the Blair Outing. Though he was not able to impart any of his vast knowledge of foreign languages to me, Alex similarly taught me a great deal about running the experiment. I enjoyed going on various hikes with Alex, as well as climbing at the UW gym with him often. After both Alex and Anders graduated, Will and I continued the march towards creating LiYb molecules. We shared many a late night wrestling with a stubborn 404 nm laser, and hiding the famous lab gnome in various places around the lab.

Also already in the group when I joined, Alan Jamison and Ben Plotkin-Swing were operating a BEC contrast interferometer experiment. Alan, a transplant from particle theory, has an amazing grasp on physics as a whole, and was instrumental in my coming up to speed quickly in the field of atomic physics. We have shared many a great hike in the Northwest (and Northeast since he moved to MIT), and I am delighted that we've been able to stay in touch and remain good friends since our years together in the lab. Ben Plotkin-Swing and I have also shared good times both in and out of the lab, including discussing and troubleshooting our respective experiments together, talking about our various outdoor adventures, and enjoying campfires in the backyard of his house. Ben has built up an impressive Yb BEC machine in the new lab, and I'm very excited to see the fruit that it bears in the near future.

Later additions to the mixture team include graduate students Alaina Green and Jun Hui See Toh, and postdocs Raj Shrestha and Ryan Bowler. Alaina is now the senior graduate student on the Li-Yb experiment, and has put in a great deal of effort improving the apparatus. Her dedication and hard work in the lab is easily noticeable, and it feels great to leave the lab in such capable hands. Along with the newest addition to the mixture group, Jun, I am sure Alaina will realize exciting new results in the near future. Raj and Ryan were instrumental in upgrading various aspects of the lab, including Raj's development of our 671 nm tapered amplifier system, and Ryan's implementing various digital electronics projects for our future optical lattice. I am appreciative of their time in the lab in helping to realize various experimental goals over the past few years.

These past six years would not have been as enjoyable without my many friends outside of the physics department in Seattle, many of whom are fellow Loggers from UPS. I like to say that I've kept my life as balanced as possible during my time in graduate school, and to this end it was so helpful to have such fun, supportive friends around along the way.

The most important acknowledgement of course goes to my family. My parents, Susan and Richard, fostered in me an open mind that yearns to question and explore, and have always cheered me on to do whatever makes my heart and mind feel fulfilled. My father's deeply inquisitive mind and ability to give so much of himself has shaped much of who I am today, and my mother's example of looking at the world in such a positive, hopeful light, and always pursuing meaningful connection with others is a constant inspiration, helping to keep me grounded. My three older brothers, Kevin, Ryan, and Sean, have been supportive of me from my adolescent years until now, and I'm grateful for all that I've learned from them over the years. Lastly, and most importantly, I could not have accomplished what I did in graduate school without the constant love and support of my fiancée, Vienna. Her patience and understanding of the late nights and overall busy reality of being a graduate student was more than I could have ever asked for, and her encouragement along the way was essential. We've had so many exciting adventures in the Washington outdoors and elsewhere over these past few years, and have grown so much together. This six year journey was exponentially more enjoyable because I had her by my side.

TABLE OF CONTENTS

LIST OF FIGURES

Figure Number Page

Chapter 1

INTRODUCTION

This chapter attempts to place the experiments of this thesis within the broader context of ultracold atomic physics experiments, as well as to outline the chronological progression of my efforts in the lab. Many of the long term goals in our group, and in a majority of the cold atom experiments in operation today, involve utilizing the pristine control over single- and few-body degrees of freedom offered in these systems to realize and probe novel many-body states. Indeed, a hallmark achievement in the early days of neutral atom trapping was the realization of Bose-Einstein condensation [2, 24], resulting in a many-body quantum state exhibiting superfluidity. Soon after, the observation of superfluidity in two-component Fermi gases [114] with arbitrarily tunable interactions further increased the promise of trapped quantum gases to simulate complicated many-body systems, including the potential to study models of high-T_C superconductivity with strongly interacting fermions in optical lattices [45, 86, 20]. In addition to these pioneering studies in systems with isotropic s-wave interactions, there has been a strong push to realize systems with long-range, anisotropic interactions using both polar molecules [108, 85, 103, 78] and highly magnetic atoms [68, 5, 56]. It is within this already successful, yet still burgeoning field of quantum gases that we aim to highlight the novelty and utility of our ytterbium-lithium mixture. In the course of these past 5 years, the prospective trajectory of the experiment has undergone a few transformations, with an eye always towards uncovering the most fundamentally interesting physics. As we'll see, one must be malleable in their experimental pursuits in this field.

1.1 Yb and Li: Mixtures and molecules

The specific choice of atoms for an ultracold quantum gas experiment is one that must be made with considerable forethought. The time it takes to design and construct a working apparatus is often at least few years, and the ability to switch elements down the road can be prohibitively difficult due to the specificity of the equipment necessary for trapping a given atom (e.g. lasers, vacuum and magnetic coil designs). Thus it behooves a lab to have an extensive list of possible experiments to be performed on a given system, as there may be countless, unforeseeable technical and/or fundamental limitations that may render various endeavors impossible.

The choice of a mixture of ytterbium (Yb), which features many bosonic and fermionic isotopes in natural abundance, and fermionic lithium-6 (^{6}Li) in our apparatus indeed affords a variety of physical phenomena to be explored. For the most commonly used isotope of ytterbium in our lab, bosonic ^{174}Yb, the interspecies combination features a very large mass ratio of 29, and is a novel combination of a spin-singlet and spin-doublet atom. In the context of few-body physics, this leads to the potential for realizing ultracold, heteronuclear ground state molecules that possess both a magnetic and electric dipole moment. Furthermore, the magnetic susceptibility(insensitivity) of Li(Yb) allows for individual addressing of Li with magnetic fields, and the ability to control the interspecies cloud overlap. The large mass ratio is predicted to result in 3-body Efimov bound states with small energetic spacing in the vicinity of a Feshbach resonance, allowing for the possible detection of many trimer resonances.

The choice of an alkaline-earth like atom (Yb) over a second alkali for the mixture has additional advantages, owing to the richer internal structure. Yb features two optically accessible metastable excited states, $^3P_2$ and $^3P_0$, which introduce the possibility of studying interspecies or intraspecies anisotropic interactions. Furthermore, the fermionic isotopes of Yb have non-zero nuclear spin that does not couple to the electronic angular momentum for the $^1S_0$ and $^3P_0$ states, giving rise to an SU(N) symmetry of two-body interactions and exciting applications in quantum simulation [19].

In the realm of many-body physics, ^{6}Li is a prototype atom for studies of strongly interacting fermions. The addition of ^{174}Yb presents a bosonic impurity probe of the fermionic gas, and could be used to study fundamental aspects of Fermi superfluidity (e.g. critical velocity, equation of state properties). Additionally, there is the prospect of achieving simultaneous superfluidity in the bosonic and fermionic components, and studying the resulting coupled-superfluid dynamics. Such a system was first prepared in a mixture of ^{6}Li-^{7}Li [31], with the realization in our lab occurring roughly 2 years later [95].

1.2 The search for tunable interactions

Many of the models that we desire to simulate in quantum gas mixture experiments require tunability of interspecies interactions. Furthermore, the most successful method for creating ultracold heteronuclear molecules has been to coherently create loosely bound Feshbach dimers using a Landau-Zener sweep at a Feshbach resonance, and subsequently bridge the large energy scale to the rovibrational ground state using coherent two-photon optical transfer. Thus, an important first step in the Yb-Li mixture is to go in search of such magnetically tunable Feshbach resonances.

In many combinations of alkali species, this tunability is readily achieved because of their specific internal structure. Though not globally true, the bialkali systems often feature broad Feshbach resonances resulting from the strong exchange interaction, which couples the entrance (or open) channel (e.g. triplet) to the closed, or molecular channel (e.g. singlet) over a wide range of magnetic field values.

In the Yb-Li system, the situation is much more grim, due to the presence of only a single scattering channel in the electronic ground state combination Yb($^1S_0$) + Li($^2S_{1/2}$). While theorists have predicted a Feshbach resonance mechanism for this scattering complex [15], the resulting resonances have widths on the order of mG (at best), and reside at fields near 1000 G. Thus, while the potential payoff from realizing an interspecies Feshbach resonance in this system warranted brief searches early on, we eventually abandoned hope for these resonances and turned our attention to a metastable excited state in Yb. In the combination Yb($^3P_2$) + Li($^2S_{1/2}$), there were predicted many broad Feshbach resonances resulting from the considerable anisotropic Van der Waals coupling mechanism [35, 65].

Indeed, after considerable effort to populate and spin purify a sample of $^3P_2$ atoms (Yb*) in our lab, we initiated studies of interspecies collisions as a function of magnetic fields, and identified behavior linked to Feshbach resonances [27]. Unfortunately, the inelastic loss that accompanies elastic tunability for resonances of this type (i.e. atoms in excited electronic states) proved to be too great to continue towards forming Feshbach dimers of Yb* and Li. The investigation of interspecies interactions in this mixture is discussed in chapter 5.

1.3 Photoassociation and prospects for YbLi ground state molecules

Shortly after our experiments in the Yb*-Li mixture, we turned our attention back to the ground state combination, and initiated spectroscopic studies of YbLi* molecular potentials asymptoting to the ^2P state in Li using photoassociation (PA). Inspired by experiments with ^{84}Sr [102], the plan for creating ground state YbLi molecules became to utilize the enhanced overlap of the scattering and molecular wave functions offered in a tightly confining optical lattice to achieve efficient two-photon transfer from free atoms to a ground state, vibrationally excited molecule, thus circumventing the need for a magnetically tunable resonance altogether.

Due to initial complications encountered when attempting these measurements in the optical trap, we opted to perform this spectroscopy in a dual-species magneto-optical trap (MOT). Though this required overcoming various technical hurdles because of the vastly different MOT parameters for Yb and Li, it proved to be a fruitful route towards creating excited state YbLi* molecules via PA, as we identified a few excited-state molecular resonances [96].

These photoassociation studies are being revisited in our group and extended into the optical trap. In addition to successfully locating lines deeper in the excited state potential, we have found the position of the least bound vibrational state in the electronic ground state potential, a key step towards realizing the eventual goal of coherent two-photon transfer. While further PA studies are necessary to be sure that the two-photon route chosen offers the largest possible free atom-to-molecule coupling (i.e. that the chosen vibrational state in the excited state has the largest possible Franck-Condon factor), the steps forward are clear, and the implementation of a three-dimensional optical lattice imminent.

1.4 Improvements to the apparatus and combined Bose-Fermi Superfluidity

The photoassociation studies in the dual-MOT were quickly followed by an accidental loss of ultra-high vacuum (UHV) in our experiment. While the headache of re-achieving UHV lessened the pace of scientific investigation in the lab, the interlude gave us time to implement much needed upgrades to the apparatus, including making the Yb and Li MOT optics setups much more robust with optical fibers and intensity feedback, and completely redesigning the optical trapping setup. Concurrently, in the interim I initiated a series of numerical simulations aimed at optimizing the efficiency and speed of evaporative cooling in our new optical trap setup, utilizing the dynamical trap shaping capabilities offered with time-averaged potentials. The ensuing experimental investigations with ^{174}Yb proved surprisingly successful, and we were able to optimize this technique to achieve the fastest experimental cycle time for the creation of Bose-Einstein condensates in an optical trap to date, as well as the largest ever Yb condensates [94].

In addition to enhanced ^{174}Yb quantum degenerate gas production, the redesigned optical trap and more robust MOT setup resulted in huge gains for our quantum degenerate mixture preparation. With the further upgrade of adding sub-Doppler cooling for Li, the signal-to-noise of the mixture at quantum degeneracy was significantly greater than in previous experiments. This turned out to be a crucial ingredient to allowing us to achieve fermionic superfluidity in our system. These experiments culminated in the achievement of a combined Bose-Fermi superfluid mixture, the first such realization in a mixture of two different elements [95], which is detailed in chapter 8.

Part I

BACKGROUND AND RELEVANT CONCEPTS

Chapter 2

TRAPPED, IDEAL ATOMIC GASES

The field of experimental atomics physics underwent a profound shift with the advent of laser cooling and trapping of neutral atoms, beginning in the 1980s. Soon after, with the implementation of collisional evaporative cooling in conservative potentials, Bose-Einstein condensates (BECs) of dilute atomic gases were realized. Application of the same tools to fermionic species of atoms further boosted the promise of ultracold atomic physics, in large part because of the stability of strongly-interacting two-component Fermi gases. While the history of the now ubiquitously-used tools of ultracold atomic physics is indeed rich, we aim here to present a concise yet sufficient account of relevant physical concepts. Towards this end, we forgo a complete discussion of laser cooling and trapping, and instead only highlight the physical origins of the light scattering force and the dipole force (or AC Stark effect), which are at the heart of ultracold atomic physics experiments. We then move on to discuss the optical dipole trap, as well as the extension to time-averaged potentials using a rapidly moving trapping laser beam focus. Finally, we present an overview of the relevant thermodynamics of ideal, trapped quantum gases.

2.1 Atoms in laser fields

The treatment of an atom in the presence of an external electromagnetic field is of central importance to the field of laser cooling and trapping of neutral atoms. In the beginning of this section we will focus on the dynamic response of an atom in such a field, as well as how the field couples to atomic motion. For more on the specifics of Zeeman slowing, magneto-optical trapping, Doppler cooling, and sub-Doppler cooling, the reader is referred to a couple of the many texts discussing these topics [33, 75]. We will however discuss the optical dipole trap in detail, as this is the ultimate tool we use to achieve quantum degeneracy, and is the setting for most of our experiments.

2.1.1 Basic interaction

To examine the response of a real atom in a monochromatic laser field, we consider a two-level system with a dissipation rate Γ from the excited state, corresponding to the natural linewidth of the atomic transition. Typically, we are concerned with cycling dipole transitions between S and P atomic orbitals. Within the dipole approximation, the atom-laser interaction Hamiltonian is given by $H_{AL} = -\vec{d} \cdot \vec{E}$, which we treat as a perturbation on top of the bare atomic Hamiltonian H_0 with eigenstates $|g\rangle$ (ground, S) and $|e\rangle$ (excited, P) and energy separation $E_e - E_g = \hbar\omega_0$. Here, $\vec{d} = e\vec{r}$ and $\vec{E} = \vec{E}_0 \cos(\omega_L t - k_L x)$, where we assume the light is traveling in the x direction and is linearly polarized in the z direction, i.e. $\vec{E}_0 = E_0\hat{z}$. One can then proceed to solve for the dynamics using time-dependent perturbation theory, where we write the atomic state as $|\psi\rangle(t) = c_g|g\rangle + c_e e^{-i\omega_0 t}|e\rangle$. However, if we work within the rotating-wave approximation, valid for $\omega_L - \omega_0 \ll \omega_L + \omega_0$, the dynamics including dissipation from spontaneous emission can be solved exactly (see for example the treatment by Foot [33], or the more rigorous treatment by Cohen-Tannoudji [22]). The result is the famous optical Bloch equations, which govern the dynamics of the elements of the atomic density matrix, ρ. Furthermore, using the expression for $|\psi\rangle(t)$ above one can show that the expectation value of the dipole operator $d_z = \vec{d} \cdot \hat{z}$ evolves according to (at $x = 0$)

$$\langle d_z \rangle (t) = 2e\langle g|z|e\rangle \left[u \cos(\omega_L t) - v \sin(\omega_L t)\right], \tag{2.1}$$

where u and v are the real and imaginary parts of the off-diagonal density matrix element $\rho_{ge} = \langle g|\rho|e\rangle$, also called the coherence.

Hence, in the presence of a driving AC electric field, the atom acquires an oscillating dipole moment at the laser frequency, ω_L, with both in-phase (u) and quadrature (v) components. These respective components are thus associated with conservative and dissipative interactions with the laser field. The relative strength of each of these is determined by the magnitudes of u and v, which, in the steady state, are given by

$$u = \frac{2\delta}{\Omega}\frac{s}{1+s+(2\delta/\Gamma)^2}, \quad \text{and} \quad v = \frac{2\Omega}{\Gamma}\frac{1}{1+s+(2\delta/\Gamma)^2}. \tag{2.2}$$

Here, $\Omega \equiv e\langle g|\vec{r}\cdot\vec{E}_0|e\rangle/\hbar$ is called the Rabi frequency, Γ is the rate of spontaneous emission from the excited state, $s \equiv 2\Omega^2/\Gamma^2$, and $\delta = \omega_L - \omega_0$ is the detuning. The parameter s is often used to define the saturation intensity, I_{sat}, according to $s \equiv I/I_{\text{sat}}$[1]. From $u/v = 2\delta/\Gamma$, we see that the dissipative process (i.e. spontaneous scattering) dominates for small detuning, and the conservative interaction for large detuning.

Next we compute the time-averaged force on the atom $\langle\vec{F}\rangle = -\overline{\langle d_z\rangle\nabla E_z}$, where the bar indicates a time average over the period $T = 2\pi/\omega_L$, to get an explicit form for the respective forces [22]. Therefore, at $x = 0$ we find

$$\begin{aligned}\langle\vec{F}\rangle &= -\frac{2e}{T}\langle g|z|e\rangle\int_0^T (u\cos(\omega_L t) - v\sin(\omega_L t))\left((\nabla E_0)\cos(\omega_L t) + E_0 k_L\hat{x}\sin(\omega_L t)\right)dt \\ &= -\hbar\left(u\nabla\Omega - v\Omega k_L\hat{x}\right). \end{aligned} \tag{2.3}$$

Writing $\langle\vec{F}\rangle = \vec{F}_{\text{dip}} + \vec{F}_{\text{scat}}$, and using the expressions in equation (2.2) for u and v, we find

$$\vec{F}_{\text{dip}} = -\frac{\hbar\delta}{2}\nabla\ln\left(1+\frac{\Omega^2/2}{\delta^2+(\Gamma/2)^2}\right), \quad \text{and} \quad \vec{F}_{\text{scat}} = \hbar k_L\hat{x}\frac{\Gamma}{2}\frac{s}{1+s+(2\delta/\Gamma)^2}. \tag{2.4}$$

The magnitude of the spontaneous scattering force in equation (2.4) can be expressed as $F_{\text{scat}} = \hbar k_L\Gamma_{\text{scat}}$, where $\hbar k_L$ is the momentum carried by a single laser photon, and $\Gamma_{\text{scat}} = \Gamma\rho_{ee}$ is the rate at which the atom scatters photons. We explicitly see here the conservative nature of the dipole force, as it can be written as the gradient of a potential. Thus, we express the dipole force as $F_{\text{dip}} = -\nabla V_{\text{dip}}$, where $V_{\text{dip}} = \hbar\Omega^2/(4\delta)$ for large detuning, and $\Omega(\vec{r}) \propto \sqrt{I(\vec{r})}$ depends on position through the spatial mode of the laser beam. Since $V_{\text{dip}} < 0$ for $\delta < 0$, we see that a local maximum of intensity can be used as a conservative trap for atoms with a red-detuned laser beam. This type of trap is referred to as an optical dipole trap, or ODT.

---

[1] With this form for s, and using $\Gamma = \omega_0^3 e^2|\langle g|\vec{r}|e\rangle|^2/(3\pi\epsilon_0\hbar c^3)$, one can show that $I_{\text{sat}} = 2\pi^2\hbar c\Gamma/(3\lambda_0^3)$, where $\lambda_0 = 2\pi c/\omega_0$.

While the above discussion highlights the close relationship between the scattering and dipole forces, it is only valid within the rotating-wave approximation (i.e. close to atomic resonance). In most ultracold atom experiments, however, the ODT is produced by a focused laser beam with very large detuning from atomic resonance. In this case, one cannot make the rotating-wave approximation, as $(\omega_L - \omega_0)/(\omega_L + \omega_0)$ is typically greater than 10%. To find the form of the potential, then, one performs a perturbation theory analysis to find the energy shift of the ground electronic state due to the trapping-laser couplings to excited states[2], which will be valid to leading order provided $|c_e|^2 \ll 1$ (or equivalently $\Gamma_{\text{scat}}/\Gamma \ll 1$). The most general form of the AC Stark shift, including an arbitrary number of excited states $\{|e_i\rangle\}$, can be found in this way to be

$$V_{\text{dip}} = -\frac{\hbar}{4}\sum_i \Omega_{ge_i}^2 \left(\frac{1}{\omega_{ge_i} - \omega_L} + \frac{1}{\omega_{ge_i} + \omega_L}\right) = -\frac{\hbar}{2}\sum_i \frac{\omega_{ge_i}\Omega_{ge_i}^2}{\omega_{ge_i}^2 - \omega_L^2}, \tag{2.5}$$

where $\omega_{ge_i} = (E_{e_i} - E_g)/\hbar$ and $\Omega_{ge_i} = e\langle g|\vec{r}\cdot\vec{E}_0|e_i\rangle/\hbar$. As found within the rotating-wave approximation, we again have $V_{\text{dip}} \propto I(\vec{r})$. In general, we can write $V_{\text{dip}}(\vec{r}) = -\alpha(\lambda_L)I(\vec{r})/(2\epsilon_0 c)$ [37], where $\alpha(\lambda_L)$ is the real part of the atomic polarizability at the laser wavelength λ_L.

The spontaneous scattering and dipole forces underlie all of the experimental tools used to produce ultracold atomic gases with temperatures below 1 μK and mean velocities in the range 1-100 mm/s, starting from atomic beams with initial mean velocities of a few 100 to 1000 m/s. The lion's share of this tremendous bridging of energy scales is accomplished with the spontaneous scattering force, as it is responsible for slowing of the atomic beam to near 0 m/s, and subsequently magneto-optical trapping and Doppler cooling to temperatures of tens to a few hundred μK. The remaining cooling (neglecting sub-Doppler cooling techniques) typically occurs in a conservative trap, by utilizing atomic collisions and the finite height of the potential to selectively remove, or evaporate, the most energetic particles. Many experiments utilize low-field seeking magnetic substates of certain atoms in conservative

---

[2] This analysis can be performed with a classical field using time-dependent perturbation theory, or with a quantized electromagnetic field with time-independent perturbation theory [107]. Both methods give the result in equation (2.5) in the limit of large photon number.

magnetic traps to perform evaporative cooling, but as this technique is not employed in our lab, we only discuss the ODT.

2.1.2 Optical dipole traps

As discussed in the previous section, the most basic implementation of an optical dipole trap (ODT) involves focusing a red-detuned laser beam onto the atomic cloud. In practice, the most common source for such a trap is the TEM_{00} Gaussian output mode of a single-mode optical fiber. Accounting for the possible introduction of ellipticity, the general form for the intensity profile is then

$$I(x, y, z) = \frac{2P}{\pi w_x(z) w_y(z)} e^{-\frac{2x^2}{w_x^2(z)} - \frac{2y^2}{w_y^2(z)}}, \tag{2.6}$$

where P is the total laser power, $w_i(z) = w_{0,i}\sqrt{1 + (z/z_{R,i})^2}$ $(i = x, y)$ is the transverse distance from the beam center to the point at which the intensity has decreased by a factor of $1/e^2$, $w_{0,x}$ and $w_{0,y}$ are the beam waists in the x and y directions, and $z_{R,i} = \pi w_{0,i}^2/\lambda_L$ is the Rayleigh range. The peak intensity is given by $I_0 = 2P/(\pi w_{0,x} w_{0,y})$.

In choosing the wavelength λ_L of the trapping laser, one must consider the competition between the spontaneous scattering and dipole forces. From the relation (valid for $|\delta| \gg \Gamma$) $\Gamma_{\mathrm{scat}} = (V_{\mathrm{dip}}/\hbar)(\Gamma/\delta)$ we see that using a high power laser with large negative detuning will mitigate the issue of heating from spontaneous scattering. A standard solution is to utilize commercially available solid state lasers at 1064 nm with output powers of up to hundreds of Watts. For a loading trap depth of order 100 μK, this results in a scattering rate of[3] $\Gamma_{\mathrm{scat}} = 0.5\ \mathrm{s}^{-1}$. Typically, one quickly lowers the trapping laser power after loading the atoms from the MOT to begin forced evaporative cooling, thus lowering the spontaneous scattering rate.

Another important parameter of the ODT is the beam waist size. In general, this becomes a compromise between having a large enough waist to provide a large initial trap volume for capturing atoms from the MOT, and a small, or tight, enough waist to ensure large particle

---

[3] For these estimates we use the values for Li of $\lambda_0 = 671$ nm, $I_{\mathrm{sat}} = 2.54\ \mathrm{mW/cm}^2$, and $\Gamma/2\pi = 6$ MHz.

density and thus sustained evaporative cooling at low trap depths[4]. For most optical trapping experiments, this compromise results in beam waists of 20 to 30 μm. As we will see in the following section, one can actually satisfy both of these conditions, large initial and small final trap volume, by using the time-averaged potential of a rapidly moving beam focus.

Using equation (2.6) and defining $V_0 = |V(0)| = 2|\alpha(\lambda_L)/(2\epsilon_0 c)|P/(\pi w_{0,x} w_{0,y})$, we have for a Gaussian beam shape

$$V(\vec{r}) = -\text{sgn}(\alpha(\lambda_L)) \frac{V_0}{\prod\limits_{i=x,y} \sqrt{1+(z/z_{R,i})^2}} e^{-\frac{2x^2}{w_x^2(z)} - \frac{2y^2}{w_y^2(z)}}, \tag{2.7}$$

where the atomic polarizability $\alpha(\lambda_L) > 0$ (< 0) for red-detuned (blue-detuned) trapping wavelengths. From this point forward we will assume a red-detuned ODT, or $\alpha(\lambda_L) > 0$. Typically, atomic ensembles held in an ODT quickly equilibrate by evaporation to temperatures satisfying $V_0/k_B T \approx 10$. Therefore, we expect that the vast majority of atoms will sample regions of the trap very near the potential minimum. Solving $V(x^*) - V(0) = V_0/10$ for $y = z = 0$, we find $x^* = 0.46 w_{0,x}$. As expected, the classical turning point corresponding to the thermal energy $k_B T$ is close to the trap center, justifying the following expansion[5] for equation (2.7),

$$V(\vec{r}) \approx -V_0 \left[1 - \frac{2x^2}{w_{0,x}^2} - \frac{2y^2}{w_{0,y}^2} - \frac{z^2}{z_R^2} \right], \tag{2.8}$$

where $z_R = \sqrt{2}(z_{R,x}^{-2} + z_{R,y}^{-2})^{-1/2}$. Ignoring the constant energy offset in equation (2.8) and writing it as $V(\vec{r}) = \frac{m}{2}(\omega_x^2 x^2 + \omega_y^2 y^2 + \omega_z^2 z^2)$, we find

$$\omega_x = \sqrt{\frac{4V_0}{m w_{0,x}^2}}, \quad \omega_y = \sqrt{\frac{4V_0}{m w_{0,y}^2}} \quad \text{and} \quad \omega_z = \sqrt{\frac{2V_0}{m z_R^2}}, \tag{2.9}$$

where m is the atomic mass, and the quantities ω_i ($i = x, y$ and z) are referred to as the trap frequencies. The aspect ratio of the circular Gaussian beam trap is then $\omega_x/\omega_z = \sqrt{2} z_R / w_0 = \sqrt{2}\pi w_0/\lambda_L$, which equals 125 for $w_0 = 30$ μm and $\lambda_L = 1064$ nm. This

---

[4] See section 3.2 for more details on forced evaporative cooling.

[5] Indeed, the ratio of the quartic and quadratic terms evaluated at the classical turning point x^* is 20%.

large anisotropy becomes a significant issue when trying to reach quantum degeneracy by performing evaporative cooling at low trap depths. For this reason, additional confinement along the axial (z) dimension is often necessary. A general solution involves intersecting the first Gaussian beam focus with a second beam at some angle, creating a so-called crossed-beam ODT. In the case of magnetic atoms, one can also provide this axial confinement with magnetic field curvature along z.

As hinted at earlier, there are situations in which it is beneficial to be able to dynamically change the trapping beam shape. While this can be accomplished by movement of the optical elements (e.g. lenses) themselves, such a solution suffers from the slow speeds with which such changes can be made. In the next section, we detail a technically simple method for producing arbitrarily-shaped potentials that can be dynamically modified on very short timescales.

2.1.3 Time-averaged optical potentials

The basic method for realizing time-averaged optical potentials involves rapidly modulating the center position of the laser beam focus on a timescale much faster than the radial trap frequency, and has been implemented by many groups in the past [76, 34, 1, 49, 98]. In this case, the atoms do not respond to the instantaneous motion of the beam, and instead see a potential proportional to the time-averaged intensity profile. We will refer to this method as either center position modulation (CPM) or, as it is colloquially referred to, "painting". In this section, we will only concern ourselves with CPM in a single dimension, with the second transverse dimension maintaining its Gaussian shape. To begin, we address the issue of modulation bandwidth.

Trap frequencies at high ODT powers are commonly of order 1-10 kHz, necessitating CPM frequencies of 10-100 kHz. The most straightforward way to accomplish such high bandwidth CPM is to utilize the frequency-dependent deflection angle of an acousto-optic modulator (AOM). In short, an AOM consists of a crystal (e.g. TeO_2) attached to a radio-frequency (RF) transducer, allowing for the creation of high-frequency sound waves in the crystal from

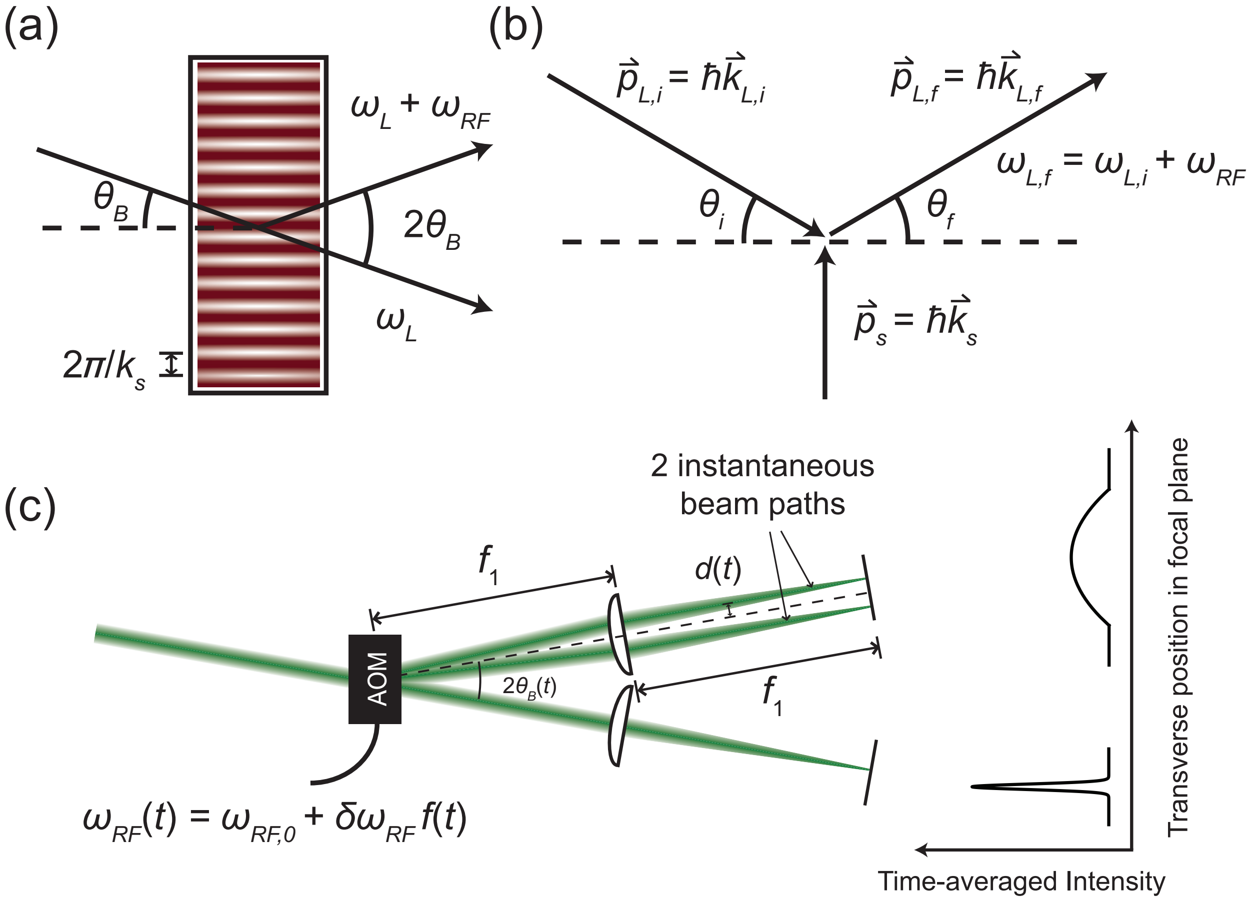

Figure 2.1: (a) Bragg scattering in an AOM. A traveling sound wave in the crystal creates a periodic modulation of the refractive index, off of which a laser beam may diffract if it satisfies the Bragg condition $mk_s = 2k_L \sin\theta_B$ (first order $m = 1$ shown). (b) Photon-phonon picture of first-order Bragg diffraction, in which an initial photon of frequency $\omega_{L,i}$ and momentum $\hbar\vec{k}_{L,i}$ absorbs a phonon of frequency ω_{RF} and momentum $\hbar\vec{k}_s$. The constraints of energy and momentum conservation give $\theta_i = \theta_f$. (c) Painting with an AOM. The time-dependent AOM driving frequency $\omega_{RF}(t)$ results in a time-dependent Bragg diffraction angle $\theta_B(t)$. By choosing a suitable FM waveform $f(t)$, one can realize arbitrary time-averaged intensity profiles. The focal length f_1 of the lens following the AOM determines the conversion of FM amplitude $\delta\omega_{RF} f(t)$ to CPM amplitude $d(t)$.

a high-power RF source. The sound waves create a density modulation in the crystal at the sound wave vector $\vec{k}_s$, as shown in figure 2.1(a). This modulation forms a grating off of which an incident laser beam can undergo Bragg diffraction, with the first-order diffracted beam traveling at an angle $2\theta_B = 2\sin^{-1}(k_s/(2k_L))$ with respect to the incident beam, where θ_B is the well-known Bragg angle. Therefore, for small angles we find that the deflection angle is proportional to the RF frequency $\theta_B \propto \omega_{RF} = c_s k_s$, where c_s is the speed of sound in the crystal.

As depicted in figure 2.1(b), this process can also be analyzed at the level of photon-phonon interactions, whereby an incident photon with wave vector $\vec{k}_{L,i}$ absorbs a phonon with wave vector $\vec{k}_s$, resulting in a scattered photon with wave vector $\vec{k}_{L,f}$. By analyzing the conditions for energy and momentum conservation, one can show[6] that $\theta_i = \theta_f = \theta_B$. In this way we can understand higher-order diffraction as multi-phonon absorption, and negative-order diffraction as emission of phonons into the crystal.

Figure 2.1(c) gives a schematic of the CPM method for creating arbitrarily-shaped time-averaged potentials. In this figure, we assume that the initial Gaussian beam is collimated before the AOM. We depict two instantaneous snapshots of the first-order beam deflection path, which varies in time due to the time-dependent Bragg angle $\theta_B(t) \propto \omega_{RF}(t)$. The diffracted beam then encounters a lens with a distance from the AOM equal to its focal length, f_1, resulting in a first-order beam which now varies in transverse displacement, $d(t)$, not angle. In designing such a setup, the most important consideration is the magnitude of the beam center position displacement in the transverse plane at the ODT focus. Using a Bragg angle of 10 mrad, a frequency modulation (FM) amplitude of $\delta\omega_{RF}/\omega_{RF} = 0.1$, and a collimating lens focal length of $f = 100$ mm, we find that the maximum displacement is $d_{\max} \approx 2\theta_B(\delta\omega_{RF}/\omega_{RF})f = 200$ μm. This order of magnitude is in agreement with our experimental implementation, as with similar parameters we achieve CPM amplitudes of

---

[6] The momentum and energy conservation conditions are $k_{L,i}\cos\theta_i = k_{L,f}\cos\theta_f$, $k_s - k_{L,i}\sin\theta_i = k_{L,f}\sin\theta_f$, and $\omega_{L,f} = \omega_{L,i} + \omega_{RF}$. Since $\omega_{RF}/\omega_{L,i} \approx 10^{-7} - 10^{-8}$, we have $\omega_{L,f} = \omega_{L,i}$, or equivalently $k_{L,i} = k_{L,f}$. From here it is easy to show that $\theta_i = \theta_f = \theta_B$.

about $10w_0$, where $w_0 = 30\ \mu$m. We note here that our implementation of the painted ODT involves two more lenses after the initial focusing lens shown in figure 2.1(c), which slightly complicates the conversion from $\delta\omega_{RF}$ to $d_{\max}$.

With an understanding of the technical details of CPM, we move on to the form of the resulting time-averaged intensity profile. Without loss of generality, we assume that the CPM occurs in the x dimension. Given a driving RF signal for the AOM with carrier $\omega_{RF,0}$ and FM waveform $f(t)$ and amplitude $\delta\omega_{RF}$, we expect a resulting time-dependent transverse position in the focal plane of $x'(t) = x - hf(t)$. The function $f(t)$ is periodic with frequency ω_{mod} and attains maximum and minimum values of $+1$ and -1. We will refer to h as the CPM amplitude. The time-averaged intensity profile is then given by

$$\tilde{I}(x,y,z) = \frac{\omega_{\text{mod}}}{2\pi} \int\limits_{0}^{2\pi/\omega_{\text{mod}}} I(x - hf(t), y, z)\, dt, \tag{2.10}$$

where $I(\vec{r})$ is given by equation (2.6). As we will see, our prescription for choosing the function $f(t)$ ensures that we can equivalently evaluate the time-averaged profile for half an oscillation period, π/ω_{mod}, provided the integration begins at a time t_0 satisfying $f(t_0) = +1$ or -1. Figure 2.2 shows the time-averaged intensity profiles for sinusoidal and triangle-wave modulation[7]. We can see that sinusoidal modulation quickly results in a double-well trap, while triangle-wave creates a one-dimensional box potential for large CPM amplitudes. While these waveforms are simple to implement, we haven't yet realized the goal of creating arbitrarily-shaped potentials. What remains is devising a method to determine the necessary function $f(t)$ to create a desired potential shape $\tilde{I}(x,0,0)$.

---

[7] The triangle-wave example is particularly simple to analyze. Using equation (2.6) for $I(\vec{r})$, we can compute the time-averaged profile over a half-period of the triangle wave analytically, giving

$$\begin{aligned} \tilde{I}(x,0,0) &= \frac{2I_0}{T} \int\limits_{-T/4}^{T/4} \exp\left(-\frac{2}{w_0^2}\left(x - h\frac{4t}{T}\right)^2\right) \\ &= I_0 \sqrt{\frac{\pi}{2}} \frac{w_0}{4h} \left[\operatorname{erf}\left(\frac{\sqrt{2}(x+h)}{w_0}\right) - \operatorname{erf}\left(\frac{\sqrt{2}(x-h)}{w_0}\right)\right]. \end{aligned} \tag{2.11}$$

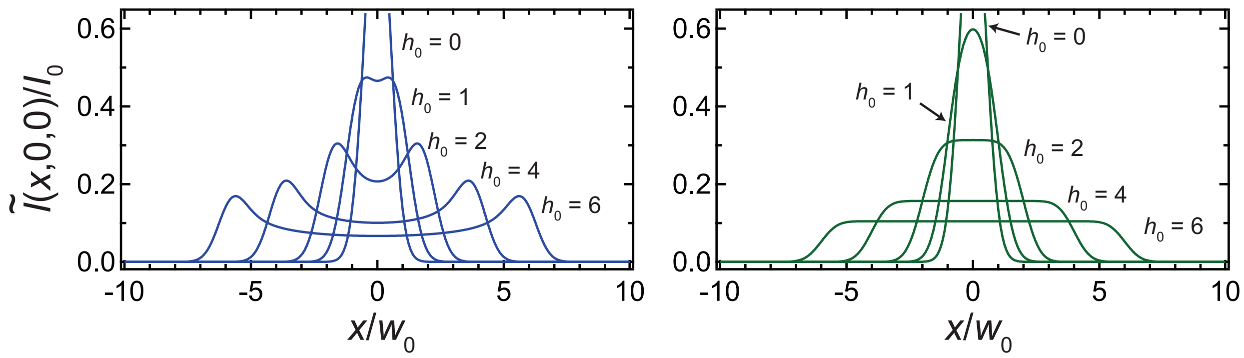

Figure 2.2: Time-averaged potentials for sinusoidal (left) and triangle-wave (right) modulation. The CPM amplitude h for each curve is given in units of the Gaussian beam waist w_0. For large h, the sinusoidal modulation develops a double-well character, while the triangle-wave leads to a box-like potential.

To find a straightforward recipe for determining the painting function $f(t)$ for a given $\tilde{I}(x,0,0)$, we adopt an approximate method where we assume the unpainted beam (the "paintbrush") to be a delta function in the x dimension. In what follows, we work with one-dimensional intensity profile given by $I_{1D}(x) = \int \tilde{I}(x,y,0)\,dy$, which can generally be written as $I_{1D}(x) = I_{1D}(0)g(x/h)$, where $g(y)$ is the desired potential shape satisfying $g(1) = g(-1) = 0$. Since we know the desired function g, we reason that the modulation function $f(t)$ must spend an amount of time at the value f' that satisfies

$$\frac{dt|_{f=f'}}{dt|_{f=0}} = \frac{I_{1D}(hf')}{I_{1D}(0)} = g(f'). \tag{2.12}$$

Then, substituting $df/\dot{f}$ for dt and defining $\dot{f}|_{f=0} \equiv v_0$, we have

$$\frac{df'}{dt} = \frac{v_0}{g(f')}. \tag{2.13}$$

Integrating equation (2.13) we get

$$\int_0^{f(t)} g(f')\,df' = v_0 t. \tag{2.14}$$

Lastly, we must solve equation (2.14) for $f(t)$ and create the suitable periodic continuation since this prescription only gives $f(t)$ over one-half of a period[8]. This can be done analytically for many profiles, including the offset linear potential shown in figure 2.3(a)-(b), where $g(x) = (1+ax)\Theta(1-|x|)$ and $-1 \leq a \leq 1$, giving $f(t) = \frac{1}{a}(\sqrt{1+2at}-1)$ for $\frac{a}{2}-1 \leq t \leq \frac{a}{2}+1$. Notice that in the limit $a \to 0$, the FM waveform becomes a triangle wave as expected. This potential shape is of special interest as the linear slope can be tuned to cancel the effect of gravity within the trapping region.

To determine the analytical form of the time-averaged potential in the case of the delta-function paintbrush, we write the 1-dimensional profile as

$$I_{1\mathrm{D}}(x) = \frac{2P}{T} \int\limits_{-T/4}^{T/4} dt\, \delta(x - hf(t)), \tag{2.15}$$

where we use that the 1-dimensional intensity profile for the paintbrush is given by $P\delta(x)$, and that our procedure for determining $f(t)$ gives us half of a period centered on $t = 0$. We then find

$$I_{1\mathrm{D}}(x) = \frac{2P}{T} \int\limits_{-T/4}^{T/4} dt\, \frac{\delta(t - t_0)}{h|\dot{f}(t_0)|}, \tag{2.16}$$

where t_0 satisfies $x - hf(t_0) = 0$, and from equation (2.13) we have $\dot{f}(t_0) = v_0/g(f(t_0))$ on the domain $-1 \leq f \leq 1$. Clearly the integral in equation (2.16) will evaluate to zero unless $|t_0| \leq T/4$, which is equivalent to our initial requirement that $|f(t_0)| \leq 1$. We can then evaluate the integral and find

$$I_{1\mathrm{D}}(x) = \frac{2P}{hv_0T} g(f(t_0)) = \frac{2P}{hv_0T} g(x/h). \tag{2.17}$$

Thus, we see that our procedure for determining $f(t)$ does indeed result in the correct time-averaged shape, and that the peak intensity for the delta-function-painted potential is given

---

[8] We only get one-half of a period in $f(t)$ because we are looking for its functional form between t_- and t_+, where $f(t_-) = -1$ and $f(t_+) = +1$. Therefore, we can define the full period of the FM waveform according to $T = 2(t_+ - t_-)$. The second half of the period is then defined by $f(t_+ + t) = f(t_+ - t)$ for $t < T/2$.

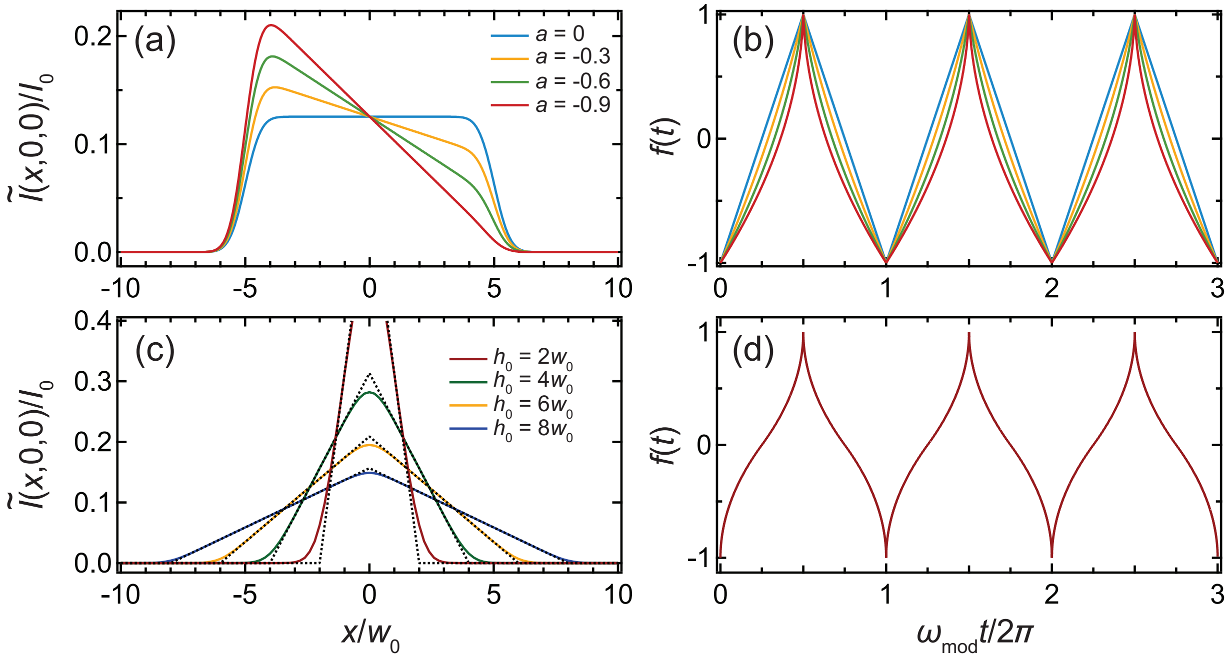

Figure 2.3: Calculated time-averaged intensity profiles for tilted-box and absolute-value potentials. (a)-(b) Time-averaged potentials for a Gaussian paintbrush with $h = 5w_0$ and $g(x) = (1 + ax)\Theta(1 - |x|)$, where $-1 \leq a \leq 1$, and associated CPM waveform $f(t)$ for various slopes a. As $a \to 0$ we recover the flat box potential from figure 2.2. The waveforms $f(t)$ used here are found analytically according to equation (2.14). (c)-(d) Absolute value time-averaged potentials with $g(x) = \mathrm{Max}(1-|x|, 0)$ for various CPM amplitudes using both delta function (dashed lines) and Gaussian (solid colored lines) paintbrushes. The waveform in (d) is found using the numerical scheme described in the end of the section.

by $I_{1\mathrm{D}}(0) = 2P/(hv_0 T)$. In situations where $f(t)$ can be determined analytically, one will find that $T \propto v_0^{-1}$, and thus v_0 drops out of the expression for $I_{1\mathrm{D}}(0)$.

We can also imagine situations where analytical solutions may not exist. Therefore, we desire a generally applicable numerical scheme for determining the correct function $f(t)$. In general, we can write equation (2.14) as $G(f(t)) - v_0 t = 0$, where $G(x)$ is the antiderivative of $g(x)$, and $G(0) = 0$. Then, we simply need to numerically solve the equation $G(f(t_i)) - v_0 t_i = 0$ for a set of times $\{t_0, t_1, ..., t_N\}$, where $t_0 = G(-1)/v_0$ and $t_N = G(1)/v_0$. One can then check this procedure by numerically evaluating equation (2.10) using the values $\{f(t_0), f(t_1), ..., f(t_N)\}$. Figure 2.3(c)-(d) shows the numerical solution for the example of the absolute value potential, $g(x) = \mathrm{Max}(1 - |x|, 0)$, for both Gaussian and delta function initial beam shapes.

We will return to the topic of time-averaged potentials in chapter 7 where we discuss experiments that utilize the dynamic trap shaping made possible by painting to achieve notably efficient quantum degenerate gas production, as well as the fastest all-optical BEC production time to date of 1.6 seconds. For these measurements, as well as the subsequent experiments on combined Bose and Fermi superfluids of Yb and Li, we choose a parabolic time-averaged potential profile. The pristine harmonic nature of the resulting trap allows for a quantitative understanding of the evaporation dynamics, which we then model and optimize to achieve efficient (or fast) cooling.

2.1.4 Optical lattices

A more qualitative change of the trapping geometry involves the implementation of an optical lattice, which creates a periodic potential for the atoms with lattice sites separated by a distance on the order of the lattice laser wavelength. For modest lattice potential depths, the center-of-mass (COM) wave functions of the atoms become most easily understood as delocalized Bloch waves extended throughout the lattice, similar to those of conduction electrons in a metal. In the case of very deep lattice potentials, one adopts the Wannier picture of localized atomic COM wave functions at each lattice site, and nearest-neighbor

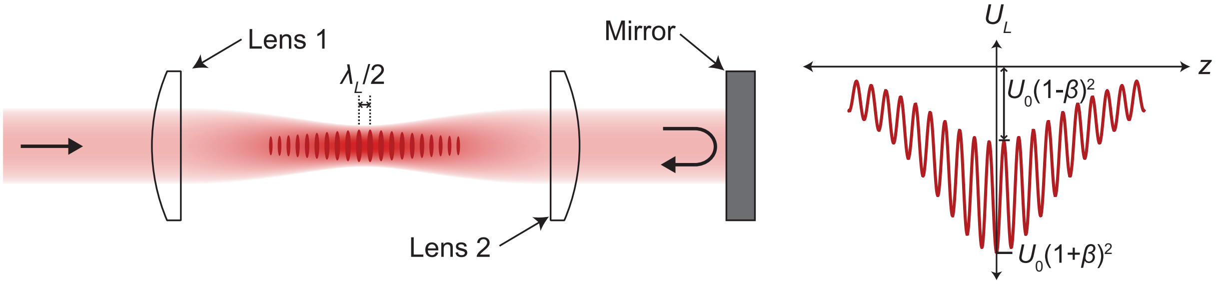

Figure 2.4: Schematic (left) and potential landscape (right) of a typical red-detuned 1D optical lattice formed by retro-reflection. The incident trapping beam is focused by lens 1, collimated by lens 2, retro-reflected by a mirror, and then refocused back onto the atoms by lens 2. While the incident beam is characterized by the electric field $\vec{E}_0 \cos(\omega_L t - k_L z)$ for $x = y = 0$, the reflected beam has an attenuated field strength $\beta \vec{E}_0 \cos(\omega_L t + k_L z)$ due to losses in optical elements, where $0 \leq \beta \leq 1$.

hopping takes the place of the kinetic energy in the Hamiltonian. The utility of the optical lattice in ultracold atomic physics cannot be overstated. Indeed, a large number of the experiments described as "quantum simulation" rest on the direct analogy of neutral atoms in optical lattices to electrons (or quasiparticles) in solid-state systems.

The standard implementation of an optical lattice involves interfering counter-propagating Gaussian laser beams, usually accomplished by retro-reflection. As shown in figure 2.4, the beam is first focused down onto the atom cloud on its first pass, and must therefore encounter another lens before the retro-reflecting mirror. While the retro-reflected beam ideally retains the full initial electric field amplitude, E_0, experimental realities (e.g. losses in viewports, lenses, mirrors, etc.) result in a reflected beam with amplitude βE_0 at the atoms, where $0 \leq \beta \leq 1$. The resulting potential at the position of the atoms is then given by

$$V_{L,\mathrm{1D}}(\vec{r}) = \mathrm{sgn}(\alpha(\lambda_L)) V_0 \left(2\beta \cos(2k_L z) + \beta^2 + 1\right) e^{-\frac{2x^2}{w_{0,x}^2} - \frac{2y^2}{w_{0,y}^2}}, \tag{2.18}$$

where $k_L = 2\pi/\lambda_L$, V_0 is defined as in equation (2.7), and we assume $z \ll z_R$ for simplicity. In the case $\beta = 0$, we recover equation (2.7), and for $\beta = 1$ we find (assuming a red-detuned beam)

$$V_{L,1\mathrm{D}}(\vec{r}) \underset{\beta\to 1}{=} -4V_0\cos^2(k_L z)e^{-\frac{2x^2}{w_{0,x}^2}-\frac{2y^2}{w_{0,y}^2}}. \tag{2.19}$$

Importantly, the depth of the optical lattice potential with $\beta = 1$ is 4 times that of a traveling wave ODT because of the constructive interference of the electric field amplitude. For intermediate values of β, the potential possesses both a standing wave and traveling wave component, as depicted in figure 2.4. To realize periodic potentials in 2D and 3D, one can simply superimpose 2 or 3 retro-reflected 1D lattices with orthogonal vectors $\vec{k}_L$, resulting in a simple cubic lattice for the 3D case[9].

For $\beta = 1$, we can expand about the potential minimum at $z = 0$ to get the lattice harmonic frequency,

$$\omega_{\mathrm{lat},z} = \sqrt{8V_0k_L^2/m} = 2E_{\mathrm{rec}}\sqrt{s_{\mathrm{lat}}}/\hbar, \tag{2.20}$$

where $E_{\mathrm{rec}} = \hbar^2k_L^2/(2m)$ is the photon recoil energy and $s_{\mathrm{lat}} = 4V_0/E_{\mathrm{rec}}$ is the lattice depth in units of recoils. To estimate the trap frequencies involved, we consider ^{6}Li in a $\lambda_L = 1064$ nm optical lattice, for which $E_{\mathrm{rec}}/\hbar = 2\pi \times 29$ kHz. The much higher frequencies realized in optical lattices compared to those in standard dipole traps make stabilization of lattice laser power and frequency very important, as noise in the frequency band of one to a few $\omega_{lat,z}$ can cause heating of the atoms.

2.2 *Ideal quantum gases*

We consider the ideal quantum gas to be a thermodynamic system in which N identical particles are in thermal equilibrium and obey a separable many-body Hamiltonian, $H = \sum_{i=1}^{N} H_i(\vec{r}_i)$, where $H_i(\vec{r}_i) = \vec{p}_i^{\,2}/2m + V(\vec{r}_i)$. This idealization of course necessitates

---

[9] In addition to orthogonal $\vec{k}_L$, it is necessary to have orthogonal polarizations for the three retro-reflected beams to avoid additional interference effects. Since the mutually orthogonal polarization condition is never perfectly met in practice, it is also necessary to provide a frequency offset between each beam. In this case, any residual interference time-averages to zero.

that interparticle interactions be negligible, which can be the case for sufficiently weak interactions in any system, or for arbitrary interactions in a sufficiently dilute system. While the presence of interparticle interactions is essential to the production of quantum degenerate gases using evaporative cooling, the two-body interactions of interest (i.e. s-wave interactions) are usually of such short range that they can be neglected in the treatment of the statistical properties of the gas[10]. Here we restrict our discussion to temperatures satisfying $k_B T \ll E_{\ell=1}$, where $E_{\ell=1} \approx \hbar^2/(\mu_r r_{\text{int}}^2)$ is the p-wave barrier, μ_r is the reduced mass of the two-body scattering system, and r_{int} is the range of the interaction potential. In this case, we quantify the degree to which a gas is weakly interacting with the parameter na^3, where n is the particle density and a is the s-wave scattering length. One can further consider this quantity to be the number of particles contained within the "scattering volume" $|a|^3$. Using typical values of $n \approx 10^{13} - 10^{14}$ cm^{-3} and $a \approx 1 - 10$ nm, we find $na^3 \approx 10^{-8} - 10^{-4}$. Lastly, note that our definition of the ideal gas allows for the inclusion of an external potential, $V(\vec{r})$, since this is required in order to treat our trapped atomic gases.

2.2.1 Thermodynamics and statistical mechanics

To determine the thermodynamic properties of ideal gases in arbitrary external potentials $V(\vec{r})$ subject to either Bose or Fermi statistics, we work within the grand canonical ensemble [32]. In this case, the thermodynamic potential of interest is the grand potential, sometimes called the Landau free energy,

$$\Omega = E - TS - \mu N \Rightarrow d\Omega = -SdT - PdV - Nd\mu. \tag{2.21}$$

Thus, we can calculate the (mean) total entropy S, number N, and pressure P from

$$S = -\left(\frac{\partial \Omega}{\partial T}\right)_{V,\mu}, \quad P = -\left(\frac{\partial \Omega}{\partial V}\right)_{T,\mu}, \quad \text{and} \;\; N = -\left(\frac{\partial \Omega}{\partial \mu}\right)_{T,V}. \tag{2.22}$$

---

[10] A notable exception to this occurs when the weakly-interacting gas undergoes Bose-Einstein condensation (BEC). In this case, the kinetic energy of the particles in the condensate is sufficiently small that interactions become the dominant effect.

In order to connect these thermodynamics quantities to particle statistics, we begin with the grand canonical partition function, $\mathcal{Z} = \exp(-\Omega/k_BT)$, which is defined in the context of the probability for a many-particle system S to be in a given state. Specifically, we define $P_{i,N}$ to be the probability that the system S is in a many-particle state $|i\rangle$ with total energy E_i and total particle number N, both of which we assume may vary (e.g. by exchange with a neighboring thermodynamic system), giving

$$P_{i,N} = \frac{e^{-\beta(E_i-\mu N)}}{\mathcal{Z}}, \tag{2.23}$$

where $\beta = 1/k_BT$. From the constraint $\sum_{i,N} P_{i,N} = 1$, we find that the normalization factor is $\mathcal{Z} = \sum_{i,N} e^{-\beta(E_i-\mu N)}$.

For an ideal gas, we may use that the total energy of the many-particle state i is determined by the distribution n_α of the $N = \sum_\alpha n_\alpha$ particles into single particle quantum states with energy ε_α, giving $E_i = \sum_\alpha \varepsilon_\alpha n_\alpha$. Denoting the set of all possible distributions for a given total number N by $\{n_\alpha\}$, we find that the partition function can be written as

$$\begin{aligned}
\mathcal{Z} &= \sum_{N=0}^{\infty} e^{\beta\mu N} \sum_{\{n_\alpha\}} e^{-\beta\sum_\alpha \varepsilon_\alpha n_\alpha} \times \delta_{N_i,\sum_\alpha n_\alpha} \\
&= \sum_{\{n_\alpha\}} \prod_\alpha \left(e^{-\beta(\varepsilon_\alpha-\mu)}\right)^{n_\alpha} \\
&= \prod_\alpha \sum_n \left(e^{-\beta(\varepsilon_\alpha-\mu)}\right)^{n}.
\end{aligned} \tag{2.24}$$

Note that in going from the first to second lines above, the sum over sets of occupation number sets $\{n_\alpha\}$ becomes unrestricted, or independent of the total sum. Furthermore, in going from the second to third line, the summation over occupation number sets becomes a simple sum over all possible particle numbers for a single state.

For indistinguishable bosons, the occupation number may be any nonnegative integer, $n = 0, 1, ..., \infty$, while for indistinguishable fermions, $n = 0$ or 1 due to the Pauli exclusion principle. Thus, for both types of particles, we can easily perform the summation in equation

(2.24) and find $\mathcal{Z} = \prod_\alpha \mathcal{Z}_\alpha$, where

$$\mathcal{Z}_{\alpha,B} = \frac{1}{1 - e^{-\beta(\varepsilon_\alpha - \mu)}} \ \text{(bosons)}, \quad \mathcal{Z}_{\alpha,F} = 1 + e^{-\beta(\varepsilon_\alpha - \mu)} \ \text{(fermions)}. \tag{2.25}$$

Then, using $\Omega = -k_B T \ln \mathcal{Z}$, we find that $\Omega = \sum_\alpha \Omega_\alpha$, with

$$\Omega_\alpha = \pm \frac{1}{\beta} \ln \left(1 \mp e^{-\beta(\varepsilon_\alpha - \mu)} \right), \tag{2.26}$$

where the upper sign refers to bosons, and the lower to fermions. The thermodynamic quantity of most interest to us at present is the mean occupation of the various quantum states. Using equation (2.22), we can express the mean particle number as

$$N = \sum_\alpha \bar{n}_\alpha, \quad \text{where} \ \ \bar{n}_\alpha = \frac{1}{e^{\beta(\varepsilon_\alpha - \mu)} \mp 1} = f(\varepsilon_\alpha). \tag{2.27}$$

The distributions $f(\varepsilon_\alpha)$ are of course the famous Bose-Einstein (upper sign) and Fermi-Dirac (lower sign) distributions for non-interacting many-particle quantum systems. Note that in the high-temperature limit, we recover the result for a classical Boltzmann gas, $f(\varepsilon) = \exp\left(-\beta(\varepsilon - \mu)\right)$.

It is assumed in the grand canonical ensemble that the particle number may change through exchange with a neighboring system. However, in practice we fix the particle number in equation (2.27) and use the sum over energy levels to determine the chemical potential, μ. The topic of the next section will be performing this sum in a useful way for trapped atomic gas experiments.

2.2.2 Trapped quantum gases

As discussed in section 2.1.2, we are primarily concerned with atomic gases held in harmonic traps, where

$$V(\vec{r}) = \frac{m}{2} \left(\omega_x^2 x^2 + \omega_y^2 y^2 + \omega_z^2 z^2 \right), \tag{2.28}$$

where m is the mass of the particle and ω_i is the trap frequency in the $i = x, y$ or z direction. In general, the distributions of interest to us are the spatial density distribution and the momentum distribution of the ensemble. While one can easily solve for the single particle quantum states for the potential in equation (2.28), $\varepsilon(n_x, n_y, n_z) = \sum_{i=x,y,z} \hbar\omega_i \left(n_i + \frac{1}{2}\right)$, and use these levels to determine the thermodynamic quantities discussed in section 2.2.1, this would only give us global quantities for the entire ensemble (e.g. the total number N and total entropy S), and not local ones like the spatial density profile $n(\vec{r})$. In order to determine local quantities we invoke the Thomas-Fermi approximation, which is a semi-classical approximation allowing us to replace the quantized energy level spectrum ε_α with a continuous one corresponding to the classical energy $\varepsilon(\vec{r}, \vec{p}) = \vec{p}^2/2m + V(\vec{r})$, while retaining the quantum statistics of the particle through the distribution function (equation (2.27)). This approximation is valid for $k_B T \gg \hbar\omega_i$, and amounts to replacing the idea of occupation of eigenstates of the Hamiltonian with occupation of a cell in $\{\vec{r}, \vec{p}\}$ phase-space of volume $(2\pi\hbar)^3$. Accordingly, we replace the summation over discrete energy levels ε_α with an integral over the continuous variables $\vec{r}$ and $\vec{p}$, $\sum_\alpha \to (2\pi\hbar)^{-3} \int d^3r\, d^3p$.

Thus, the particle distribution function from equation (2.27) becomes

$$f(\vec{r}, \vec{p}) = \frac{1}{e^{\beta\left(\frac{\vec{p}^2}{2m} + V(\vec{r}) - \mu\right)} \mp 1}. \tag{2.29}$$

from which we calculate the spatial density [58]

$$n(\vec{r}) = \frac{1}{(2\pi\hbar)^3} \int d^3p \; f(\vec{r}, \vec{p}) = \pm \frac{1}{\lambda_{\mathrm{dB}}^3} \mathrm{Li}_{3/2}\left(\pm e^{\beta(\mu - V(\vec{r}))}\right), \tag{2.30}$$

where the upper and lower signs refer to bosons and fermions, respectively, $\lambda_{\mathrm{dB}} = \sqrt{2\pi\hbar^2/mk_BT}$ is the de-Broglie wavelength, and $\mathrm{Li}_m(z)$ is the m^{th} order polylogarithm[11] of z. Then, we can determine the total atom number (or, pragmatically speaking, fix the total atom number

---

[11] The polylogarithm is defined as $\mathrm{Li}_m(z) = \sum_{k=1}^{\infty} \frac{z^k}{k^m}$, but can also be expressed as

$$\mathrm{Li}_m(z) = \frac{1}{\pi^m} \int d^{2m}x \; \frac{1}{e^{\vec{x}^2}/z - 1},$$

where $\vec{x}$ is a $2m$ dimensional vector. The important limiting values for us are

$$\lim_{z\to 0} \mathrm{Li}_m(z) = z \quad \text{and} \quad \lim_{z\to\infty} -\mathrm{Li}_m(-z) = \frac{1}{\Gamma(m+1)} \ln^m(z).$$

and determine the chemical potential) from

$$N = \int d^3r\ n(\vec{r}) = \pm\left(\frac{k_BT}{\hbar\bar{\omega}}\right)^3 \mathrm{Li}_3\left(\pm e^{\beta\mu}\right), \tag{2.31}$$

where $\bar{\omega} = (\omega_x\omega_y\omega_z)^{1/3}$ is the geometric mean trap frequency.

The first limit we consider for the trapped quantum gas is that of high temperature, where we expect both the boson and fermion cases to reduce to the classical Boltzmann gas. Indeed, for $T \to \infty$, $\exp(\beta(\mu - V(\vec{r})) \to 0$, and we find the classical result

$$n_{\mathrm{cl}}(\vec{r}) = \lambda_{\mathrm{dB}}^{-3} e^{\beta\mu} e^{-\frac{\beta m}{2}\left(\omega_x^2x^2+\omega_y^2y^2+\omega_z^2z^2\right)} = \frac{N}{\pi^{3/2}R_xR_yR_z} e^{-\sum_i x_i^2/R_i^2}, \tag{2.32}$$

where $R_i = \sqrt{2k_BT/m\omega_i^2}$. We can extend equation (2.32) to apply to ideal gases after they have been suddenly released from the trap and allowed to undergo ballistic expansion for a time t. In this case, the radii R_i become rescaled in a time-dependent fashion, $R_i(t) = R_i(0)\sqrt{1+\omega_i^2t^2} = \sqrt{R_i(0)^2 + 2k_BTt^2/m}$. Thus, ballistic expansion provides a simple yet very precise way to measure the temperature of a classical trapped gas. Note that in the limit $t \gg \omega_i^{-1}$, the temperature T is the only fit parameter on a curve of $R_i(t)$, and the initial size becomes irrelevant.

Next we consider the properties of quantum degenerate gases, where the onset of quantum degeneracy occurs when $n\lambda_{\mathrm{dB}}^3 = 1$. Here, the quantity $n\lambda_{\mathrm{dB}}^3$ is referred to as the phase space density, and can be roughly thought of as the number of particles occupying a cell in phase space of volume $\hbar^3$.

Lastly, one can also show that

$$\int_{-\infty}^{\infty} dx\ \mathrm{Li}_m\left(ze^{-x^2}\right) = \sqrt{\pi}\mathrm{Li}_{m+1/2}(z)$$

2.2.3 Quantum degeneracy

For fermions in the limit $T \to 0$, we determine the chemical potential $\mu(T=0)$ from equation (2.31),

$$N = -\left(\frac{k_B T}{\hbar\bar{\omega}}\right)^3 \frac{1}{\Gamma(4)}(\beta\mu)^3 \quad \Rightarrow \quad E_F \equiv \mu(T=0) = \hbar\bar{\omega}(6N)^{1/3}, \tag{2.33}$$

where we have defined the Fermi energy E_F. To see what this quantity represents, observe that in the limit $T \to 0$, the Fermi-Dirac distribution function equation (2.27) becomes a step function, $\lim_{\beta\to\infty} f(\varepsilon_\alpha) = \Theta(\mu - \varepsilon_\alpha) = \Theta(E_F - \varepsilon_\alpha)$. Thus, the Fermi energy equals the energy of the highest occupied energy level at zero temperature. Two convenient quantities to define at this point are the Fermi temperature, $T_F = E_F/k_B$, and the Fermi wave vector, $k_F = \sqrt{2mE_F}/\hbar$. Using equation (2.31), we find a simple formula for the ratio of the temperature T to the Fermi temperature T_F,

$$\frac{T}{T_F} = \left[-6\,\mathrm{Li}_3(e^{\beta\mu})\right]^{1/3}. \tag{2.34}$$

For Fermi gases with $0 < T/T_F \ll 1$, the spatial distribution is given by equation (2.30), while for the $T = 0$ Fermi gas, we find

$$\begin{aligned} n(\vec{r}) &= \frac{1}{\lambda_{\mathrm{dB}}^3}\frac{1}{\Gamma(5/2)}\beta^{3/2}\left[\max\left(E_F - V(\vec{r}), 0\right)\right]^{3/2} \\ &= \frac{(2m)^{3/2}}{6\pi^2\hbar^3}\left[\max\left(E_F - V(\vec{r}), 0\right)\right]^{3/2} \\ &= \frac{8N}{\pi^2 R_{F,x}R_{F,y}R_{F,z}}\left[\max\left(1 - \sum_i \frac{x_i^2}{R_{F,i}^2}, 0\right)\right]^{3/2}, \end{aligned} \tag{2.35}$$

where $R_{F,i} = \sqrt{2E_F/m\omega_i^2}$ is the Fermi radius in the x_i direction. In practice, the difference between the density distribution in equation (2.35) and that in equation (2.30) is remarkably small for $T/T_F \ll 1$, making accurate thermometry difficult for deeply degenerate Fermi clouds. This problem is compounded with the fact that measurements of quantum degenerate clouds using absorption imaging correspond to integrating along the line of sight of the imaging beam, resulting in the density distribution $n_{\mathrm{2D}}(x,y) \propto \int dz\, n(x,y,z)$. Figure 2.5

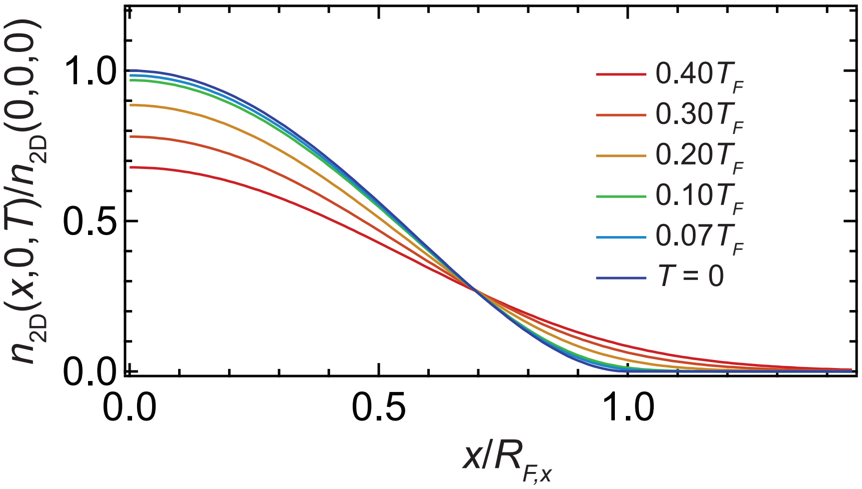

Figure 2.5: 2D profiles (integrated along the line of sight direction z of an absorption imaging beam) of a non-interacting Fermi gas for various temperatures T/T_F. The particle number N and Fermi energy $E_F = k_B T_F = \hbar\bar{\omega}(6N)^{1/3}$ are equal for all curves. The vertical axis is normalized to the peak 2D density for a zero temperature Fermi gas.

shows the 2D density profiles [12] for zero-temperature and finite-temperature Fermi clouds, where we set $y = 0$ and display the shape along the x direction, in units of the Fermi radius $R_{F,x}$. It is clear that for $T/T_F < 0.1$, the difference between the finite-temperature and zero-temperature cloud shapes becomes quite small. Indeed, when one considers the noise inherent in absorption imaging measurements, it becomes infeasible to extract temperatures

---

[12] After performing the integration along the imaging beam direction, the Fermi gas profiles for the zero and finite temperature clouds become

$$n_{2\mathrm{D}}(x, y, T = 0) = n_0 \left[\max\left(1 - \frac{x^2}{R_{F,x}^2} - \frac{y^2}{R_{F,y}^2}, 0\right)\right]^2$$

and

$$n_{2\mathrm{D}}(x, y, T \neq 0) = -2n_0 \left(\frac{T}{T_F}\right)^2 \mathrm{Li}_2\left(-\exp\left[\beta\mu - \frac{T_F}{T}\left(\frac{x^2}{R_{F,x}^2} + \frac{y^2}{R_{F,y}^2}\right)\right]\right)$$

Here n_0 is the peak 2D density of the zero-temperature Fermi gas, and the additional factors in front of the polylogarithm ensure that the total number in either case is the same (for the same Fermi energy E_F).

below $0.05 - 0.07T_F$ with a fit.

Note that the shapes in figure 2.5 would be identical if we transformed to cylindrical coordinates where $\rho^2/R_{F,\rho}^2 = x^2/R_{F,x}^2 + y^2/R_{F,y}^2$ and plotted the density as a function of $\rho/R_{F,\rho}$. This turns out to be of considerable use in fitting absorption images of deeply degenerate Fermi clouds, since one-dimensional slices of the imaged 2D profile (like that shown in figure 2.5) have low signal-to-noise, especially in the tails of the distribution. Instead, one can perform an elliptical average of the whole 2D image, and thus obtain an identically shaped distribution to the one in figure 2.5, but with large signal-to-noise in the tails.

For bosons, the behavior of the ensemble as T approaches zero, or more specifically in the regime of quantum degeneracy $n\lambda_{\mathrm{dB}}^3 \approx 1$, is remarkably different. To see this, let us first remark on the behavior of the chemical potential for the fermionic case. In the limit of high temperature, we can rewrite equation (2.30) to find the phase space density at the center of the trap

$$n(0)\lambda_{\mathrm{dB}}^3 = e^{\beta\mu} \quad \Rightarrow \quad \mu = k_B T \ln\left(n(0)\lambda_{\mathrm{dB}}^3\right). \tag{2.36}$$

Since we know the phase space density is much smaller than unity at high temperature, we find that the chemical potential is large and negative in the Boltzmann regime. Thus, in going from high to low ($T/T_F \ll 1$) temperature, where the chemical potential approaches the Fermi energy, μ must cross smoothly through zero. For the Bose gas, inspection of equation (2.27) reveals that this clearly cannot happen. Setting the ground state energy ε_0 to zero, we find that the ground state population diverges if $\mu \to 0$, which is the phenomenon of Bose-Einstein condensation. Turned on its head, this argument instead gives us the chemical potential in terms of the ground state, or condensed population N_0. For $N_0 \gg 1$, we find $\mu \approx -k_B T/N_0$. Thus, while the ground state population need not formally diverge (i.e. μ need not be exactly zero), we may take μ to be zero at and below a critical temperature T_c in computing the statistical properties of all other energy levels, or semiclassically, for all momenta $\vec{p} \neq 0$. Setting $\mu = 0$ in equations (2.30) and (2.31), we find for the non-condensed component[13] the density distribution

$$n_{\text{th}}(\vec{r}) = \frac{1}{\lambda_{\text{dB}}^3}\text{Li}_{3/2}\left(e^{-\beta V(\vec{r})}\right), \tag{2.37}$$

and at the phase transition $T = T_c$ the total number

$$N = \left(\frac{k_B T_c}{\hbar\bar{\omega}}\right)^3 \text{Li}_3(1) \quad \Rightarrow \quad T_c = \hbar\bar{\omega}\left(\frac{N}{\zeta(3)}\right)^{1/3} = 0.94\hbar\bar{\omega}N^{1/3}. \tag{2.38}$$

At the transition, the phase space density at the center of the cloud fulfills the condition for Bose-Einstein condensation of a homogeneous Bose gas $n(0)\lambda_{\text{dB}}^3 = \text{Li}_{3/2}(1) = \zeta(3/2) = 2.612$, and remains saturated at this value for lower temperatures. Below the transition temperature, the number of non-condensed atoms is found to be $N_{\text{th}} = N(T/T_c)^3$, while the rest pile up in the ground state. Thus, we find the number of atoms in the Bose-Einstein condensate (BEC) to be $N_0 = N - N_{\text{th}}$, or in terms of the condensed fraction

$$\frac{N_0}{N} = 1 - \left(\frac{T}{T_c}\right)^3. \tag{2.39}$$

The combination of condensed and non-condensed components of the ensemble below the critical temperature result in a bimodal density distribution,

$$n(\vec{r}) = n_0(\vec{r}) + n_{\text{th}}(\vec{r}). \tag{2.40}$$

For the non-interacting Bose gas, the condensate distribution $n_0(\vec{r})$ is the square of the harmonic oscillator ground state wave function multiplied by N_0. However, due to the large density and small kinetic energy $\approx \hbar\bar{\omega}$ characteristic of BECs, the interaction energy term dominates the kinetic energy term even though $n_0 a^3 \ll 1$. Consequently, interactions cannot be neglected in solving for $n_0(\vec{r})$ for most realistic systems, but the BEC may still be considered weakly interacting. In the next chapter, we will explore the effects of interparticle interactions in a variety of settings, including the solution of the Schrödinger equation for a weakly interacting BEC.

---

[13] Equations (2.30) and (2.31) explicitly neglect the contribution from the ground state. In the semiclassical formalism, we see this because the measure in the integral $d^3p = 4\pi p^2 dp$, and therefore the zero momentum state is given zero weight. If formulated in terms of an energy levels, the sum over quantum state occupations (equation 2.27) becomes the integral $N = \int_0^\infty d\varepsilon\, g(\varepsilon) f(\varepsilon)$, where $g(\varepsilon) \propto \sqrt{\varepsilon}$ for the homogeneous Bose gas and $g(\varepsilon) \propto \varepsilon^2$ for the harmonically trapped Bose gas. In both cases, the state $\varepsilon = 0$ is again explicitly not included in the integral.

Chapter 3

INTERACTING ATOMIC GASES

Due to the extremely dilute nature of trapped atomic gases, interactions tend not to strongly affect the statistical and thermodynamic properties of the system for a wide range of conditions. That being said, interparticle interactions are required in order to perform the collisional evaporative cooling necessary to reach quantum degeneracy. The diluteness of these atomic systems implies that only two-body interactions feature and we can neglect three or higher-body interactions, greatly simplifying the theoretical treatment. In the case of weakly-interacting BECs, the large decrease in kinetic energy with respect to that of the thermal gas ensures that interactions, which enter at the mean-field level, play a dominant role in the dynamics. Importantly, interactions in a BEC give rise to the phenomenon of superfluidity. In special circumstances, the few-body and many-body physics of an atomic system can be strongly altered with the use of tunable two-body scattering resonances, referred to as Feshbach resonances. As we'll see, molecular physics plays a central role in determining the scattering behavior of a two-body atomic system. In fact, one can exploit these scattering resonances to form ultracold diatomic molecules (in either a coherent or incoherent fashion). The utilization of Feshbach resonances for studies of many-body physics in ultracold atomic systems reached profound heights with the realization of superfluidity in two-component Fermi gases across the so-called Bose-Einstein condensate to Bardeen-Cooper-Schreiffer (BEC-BCS) crossover [58], including studies of the unitary Fermi gas [79, 80, 67]. In this chapter we review concepts of interacting atomic gases in both the few and many-body context, focusing on examples relevant to the work presented in part II of this thesis.

3.1 Elastic scattering

Elastic scattering refers to an interaction event between free particles that does not change the internal quantum state or quantum numbers of the participating particles. A simple example of such a system is two spin-half particles (e.g. two hyperfine states of ^{6}Li in its ground electronic state $^2S_{1/2}$). In this case, the spin angular momentum of the two scattering partners can add to be $S = 0$ or 1 (i.e. singlet or triplet), which constitute the two possible scattering channels, each with an associated molecular potential. Our statement of elasticity implies that upon scattering, the two-particle system remains in the same scattering channel as it was in prior to the interaction. The case of multi-channel scattering, i.e. when the various collision channels are coupled by the scattering interaction, is an important one which we will consider in our discussion of Feshbach resonances later in this chapter.

3.1.1 Basic formalism

The scattering problem of two free atoms at low collision energy features elegant simplicity as it can be parametrized by a single quantity, the s-wave scattering length a. To see why this is, we begin with the characterization of the interacting two-body system in the center-of-mass coordinate frame. For two particles (labeled 1 and 2) with phase space coordinates $(\vec{r}_1, \vec{p}_1)$ and $(\vec{r}_2, \vec{p}_2)$ in the reference frame where the center-of-mass is motionless, we are left with only the relative coordinate $\vec{r} = \vec{r}_2 - \vec{r}_1$ and relative momentum $\vec{p} = \vec{p}_2 - \vec{p}_1$. For the systems we'll consider here, the interatomic potential $V(r)$ is assumed to be spherically symmetric, as is the case for the Van der Waals interaction ($V(r) = -C_6/r^6$) between two S orbital atoms[1]. The kinetic energy is then given by $E = \vec{p}^2/(2\mu_r) = \hbar^2 k^2/(2\mu_r)$, where $\mu_r = m_1 m_2/(m_1 + m_2)$ is the reduced mass and we've defined the scattering wave vector $\vec{k} = \vec{p}/\hbar$. At large interatomic distance and for $\vec{k} = k\hat{z}$, the scattering wave function has the

---

[1] The case where one or both of the atoms have finite orbital angular momentum or spin angular momentum will be of interest for results presented later in this thesis. In this case, the Van der Waals interaction has some angular dependence and the collision need not conserve ℓ or m_ℓ. In the context of multi-channel scattering, this allows for the coupling of incoming s-wave scattering states with outgoing states in molecular potentials (i.e. channels) of higher orbital angular momentum $\ell = 2, 4, 6...$

form [100]

$$\psi(\vec{r}) \propto e^{ikz} + f(k,\theta)\frac{e^{ikr}}{r}, \tag{3.1}$$

where we clearly see that the scattering state is a linear combination of an incident plane wave and a scattered spherical wave. The coefficient $f(k,\theta)$ is typically referred to as the scattering amplitude, and quantifies the amplitude of the scattered spherical wave into the angle θ given the collision momentum $\hbar k$. By considering the incoming and outgoing probability flux due to the scattering event, we find that the differential cross section is $\frac{d\sigma}{d\Omega} = |f(k,\theta)|^2$. One can show that the scattering amplitude for a spherically symmetric potential can be written as

$$f(k,\theta) = \sum_{\ell=0}^{\infty}(2\ell+1)f_\ell(k)P_\ell(\cos\theta), \tag{3.2}$$

where P_ℓ is the Legendre polynomial of degree ℓ, and $f_\ell(k)$, called the partial-wave amplitude, quantifies the strength of the effect of the scattering potential on the ℓ^{th} partial wave. Then, similarly expanding the plane wave e^{ikz} in terms of spherical waves, we find

$$\psi(\vec{r}) \propto \frac{1}{2ikr}\sum_{\ell=0}^{\infty}(2\ell+1)P_\ell(\cos\theta)\left[(-1)^{\ell+1}e^{-ikr} + (1+2ikf_\ell(k))e^{ikr}\right]. \tag{3.3}$$

Thus the scattering wave function is shown to be the combination of incoming and outgoing spherical waves with unequal coefficients. By combining the fact that the central potential cannot couple partial waves of different angular momentum with the fact that the incoming and outgoing fluxes of probability must be equal, we find that the coefficients of the spherical waves in equation (3.3) must be of equal magnitude for each ℓ [100]. Defining the S-matrix element $S_\ell \equiv 1 + 2ikf_\ell(k)$, this implies that $|S_\ell| = 1$. Thus, the action of the scattering potential is to provide a phase shift to the outgoing scattering wave, while leaving the incoming wave unchanged. By convention, we write this phase shift as $S_\ell = e^{2i\delta_\ell}$, which results in the following expression for the partial-wave amplitude [100]:

$$f_\ell(k) = \frac{e^{i\delta_\ell}\sin\delta_\ell}{k} = \frac{1}{k\cot\delta_\ell - ik}. \tag{3.4}$$

Either by direct integration of the differential cross section or by utilizing the optical theorem, we now find the total cross section in terms of the phase shift of each partial wave

$$\sigma_{\text{tot}} = \frac{4\pi}{k}\text{Im}\left[f(k,\theta=0)\right] = \frac{4\pi}{k^2}\sum_{\ell=0}^{\infty}(2\ell+1)\sin^2\delta_\ell. \tag{3.5}$$

We remark here that since the central potential cannot mix states of different orbital angular momentum, ℓ, the scattering problem may be solved individually for each partial wave. This is also the reason that the S-matrix has only one index, i.e. it is diagonal in the quantum number ℓ. Thus, we can write the scattering wave function as

$$\psi(\vec{r}) \propto \sum_{\ell=0}^{\infty}(2\ell+1)P_\ell(\cos\theta)\frac{\phi_\ell(r)}{r}, \tag{3.6}$$

where the radial wave functions obey the one-dimensional Schrödinger equation

$$-\frac{\hbar^2}{2\mu_r}\frac{d^2\phi_\ell}{dr^2} + \left(V(r) + \frac{\hbar^2\ell(\ell+1)}{2\mu_r r^2}\right)\phi_\ell = E\phi_\ell. \tag{3.7}$$

For large interatomic separation r, the centrifugal term presents a long-range barrier that dominates the effective potential (so long as $V(r)$ falls off faster than $1/r^2$) for all $\ell \neq 0$. This allows us to argue qualitatively that, for low collision energies $E = \hbar^2k^2/(2\mu_r)$ and $\ell > 0$, the incoming plane wave is almost entirely reflected by the centrifugal barrier, and thus does not contribute to the scattered wave (i.e. $f_l \to 0$ for $\ell > 0$). More quantitatively, one can show that for scattering off a short range potential near the collision threshold $k \to 0$, the phase shift obeys the relation $\tan\delta_\ell \propto k^{2\ell+1}$ [99]. Therefore, in the limit $k \to 0$, the s-wave contribution to the scattering phase shift dominates. As was introduced in the early days of nuclear physics [8], we can perform an effective range expansion of the s-wave phase shift in the $k \to 0$ limit as follows:

$$k\cot\delta_0 = -\frac{1}{a} + \frac{1}{2}r_{\text{eff}}k^2 + \mathcal{O}(k^4), \tag{3.8}$$

where $a = -\lim_{k\to 0}\tan\delta_0/k$ is called the s-wave scattering length, and r_{eff} is the effective range of the potential, which is typically of order the Van der Waals length $r_{\text{VdW}} = (2\mu_r C_6/\hbar^2)^{1/4}/2$. It is usually sufficient to drop the effective range term, resulting in the

s-wave scattering amplitude $f_0 = (-a^{-1} + r_{\text{eff}}k^2/2 - ik)^{-1} \to -a$, and the total scattering cross section

$$\sigma_{\text{tot}}(k \to 0) = 4\pi a^2, \tag{3.9}$$

which is identical to the scattering cross section for a hard sphere of radius a [100].

3.1.2 Identical particles

There is an important subtlety in the case of identical particles which modifies the result in equation (3.9). Recall that the scattering wave function is a function of the relative coordinate $\vec{r} = \vec{r}_2 - \vec{r}_1$ only. Therefore, the (anti)symmetrization requirement for identical particles implies that $\psi(\vec{r}) = \pm\psi(-\vec{r})$, where the (lower)upper sign applies to (fermions)bosons. Writing this condition as $\psi(r,\theta) = \pm\psi(r,\pi-\theta)$, we see the proper wave functions are $\psi_B = (\psi(r,\theta) + \psi(r,\pi-\theta))/\sqrt{2}$ and $\psi_F = (\psi(r,\theta) - \psi(r,\pi-\theta))/\sqrt{2}$, from which we see that the differential cross section becomes

$$\frac{d\sigma}{d\Omega} = |f(k,\theta) \pm f(k,\pi-\theta)|^2, \quad \text{where } 0 \leq \theta \leq \pi/2. \tag{3.10}$$

Recalling that $f(k,\theta)$ is a sum over Legendre polynomials $P_\ell(\cos\theta)$ times the ℓ^{th} partial-wave amplitude, and that $P_\ell(-x) = (-1)^\ell P_\ell(x)$, we see that the (anti)symmetrization requirement results in a cancellation of the (even)odd partial-wave amplitudes for (fermions)bosons. Since the integral over Ω now includes half the range of θ as it did before, the net effect of the (anti)symmetrization is to double the (odd)even partial-wave amplitudes for identical (fermions)bosons relative to equation (3.5), giving

$$\sigma_{\text{tot}} = \frac{8\pi}{k^2}\begin{cases} \sum\limits_{\ell\ \text{even}} (2\ell+1)\sin^2\delta_\ell & \text{(bosons)} \\ \sum\limits_{\ell\ \text{odd}} (2\ell+1)\sin^2\delta_\ell & \text{(fermions)} \end{cases}. \tag{3.11}$$

Specifically, in the s-wave limit we find that the cross section for fermions vanishes, and that for bosons becomes $\sigma_{\text{tot}} = 8\pi a^2$. This fact that identical fermions cannot interact in the s-wave limit makes ultracold atomic gases of fermions arguably the most ideal quantum gas system.

3.1.3 Pseudo-potentials and mean-field interaction energy

When the de-Broglie wavelength of the constituent particles is much larger than the range of the interparticle interactions $\lambda_{\mathrm{dB}} \gg r_{\mathrm{VdW}}$, as is typically the case in ultracold atomic systems, the fine details of the potential $V(r)$ are irrelevant. In this case, it may be replaced with any model potential that produces the same phase shift upon scattering as would $V(r)$. This is easily achieved using the zero-range, or contact pseudo-potential $V(\vec{r}) = g\delta(\vec{r})$. Using the first-order Born approximation, one can show $f_0 = \mu_r g/(2\pi\hbar^2)$. Thus, to match the partial-wave amplitude $f_0 = -a$ from section 3.1.1, we find that g must equal $2\pi\hbar^2 a/\mu_r$.

The delta-function pseudo-potential is especially useful for evaluating the energetic consequences of s-wave scattering for a single particle with a large number of other particles, be they identical or distinguishable. For purposes of this derivation, we consider a $T = 0$ Bose-Einstein condensate (BEC) in which all atoms occupy the same single particle state, $\phi(\vec{r}_i)$, normalized such that $\int d^3r\, |\phi(\vec{r})|^2 = 1$. This single particle wave function is at this point unknown, but will be found shortly using a variational calculation. The ansatz for the many-body wave function is simply

$$\Psi(\vec{r}_1, \vec{r}_2, ..., \vec{r}_N) = \prod_{i=1}^{N} \phi(\vec{r}_i). \tag{3.12}$$

Then, using the contact potential above, the Hamiltonian for the condensate is

$$H = \sum_{i=1}^{N} \left(\frac{\vec{p}_i^{\,2}}{2m} + V_T(\vec{r}_i) \right) + \frac{g}{2} \sum_{i=1}^{N} \sum_{i \neq j} \delta(\vec{r}_i - \vec{r}_j), \tag{3.13}$$

where $V_T(\vec{r})$ is the external trapping potential, and the factor of 1/2 in the interaction energy term accounts for the double counting of the summations. The total energy of the many-body wave function $E = \langle \Psi | H | \Psi \rangle$ is then be found to be [89]

$$E = \int d^3r \left(-N \frac{\hbar^2}{2m} |\nabla\phi(\vec{r})|^2 + N V_T(\vec{r}) |\phi(\vec{r})|^2 + \frac{N(N-1)}{2} g |\phi(\vec{r})|^4 \right). \tag{3.14}$$

To proceed, we introduce a Lagrange multiplier $-\mu N$ to this functional and minimize the quantity $E - \mu N$ with respect to ϕ^*, which ensures that we maintain the normalization of

$\phi(\vec{r})$. Here we anticipate the connection to the BEC chemical potential in our definition of μ. Defining the wave function for the condensate as $\psi(\vec{r}) = \sqrt{N}\phi(\vec{r})$ with associated particle density $n(\vec{r}) = |\psi(\vec{r})|^2$, this minimization results in the Gross-Pitaevskii equation

$$\left(-\frac{\hbar^2}{2m}\nabla^2 + V_T(\vec{r}) + g|\psi(\vec{r})|^2\right)\psi(\vec{r}) = \mu\psi(\vec{r}). \tag{3.15}$$

Thus, in this mean field picture, the effect of s-wave scattering of a single particle with the rest of the ensemble is to produce an effective potential given by

$$V_{MF}(\vec{r}) = gn(\vec{r}) = \frac{2\pi\hbar^2 n(\vec{r})}{\mu_r}. \tag{3.16}$$

While this derivation utilized the specific example of a BEC, the mean-field interaction potential in equation (3.16) applies to both distinguishable and indistinguishable particles, and to fermionic systems as well as non-condensed bosonic systems. In this work, we will utilize equation (3.16) for modeling elastic interactions in a mixture of Bose and Fermi superfluids of ^{174}Yb and ^{6}Li in chapter 8.

3.2 Evaporative Cooling

Evaporative cooling is a ubiquitous process in nature (e.g. the atmosphere, cups of coffee), but holds a special place in the field of atomic physics. Indeed, the implementation of evaporative cooling in the context of trapped atomic gases was essential to the realization of Bose-Einstein condensation, and is still the primary method for producing quantum degenerate gases. As discussed in chapter 2, Doppler cooling involves the continuous absorption and spontaneous emission of photons, and typically produces atomic gases with temperatures in the range $10 - 100$ μK. For experiments on quantum degenerate gases, we desire a trapping potential that is conservative and does not have a fundamental lower limit on the ensemble temperature. To this end, the Doppler-cooled gas is subsequently transferred into a conservative magnetic or optical potential, where evaporative cooling can then occur. While the kinetics of evaporation are identical for magnetic and optical traps, there are particular aspects of evaporative cooling in magnetic traps that distinguish the method from that in optical traps (e.g. RF evaporation). However, since this thesis deals only with experiments in optical traps, we will not touch on these details.

We begin with an overview of the kinetic model for evaporative cooling of a classical Boltzmann gas, then move on to discuss evaporation dynamics when the height of the conservative trap is forcibly reduced, and finally present the full equations for modeling evaporative cooling in the presence of inelastic loss mechanisms.

3.2.1 Kinetics of evaporative cooling

To model the dynamics of an evaporating atomic gas, we restrict ourselves to considering a Boltzmann ensemble (i.e. $n\lambda_{\mathrm{dB}}^3 \ll 1$) held in a conservative trap of the form[2]

$$V_T(\vec{r}) = \min\left(\frac{m}{2}\left(\omega_x^2 x^2 + \omega_y^2 y^2 + \omega_z^2 z^2\right), V_0\right), \tag{3.17}$$

where we refer to V_0 as the trap depth, where the atoms interact with a scattering cross-section σ. We follow the treatment from [72], where we assume that the gas is sufficiently ergodic and that the Boltzmann distribution function is modified by truncating it at the energy corresponding to the trap depth, V_0:

$$f(\varepsilon) = n_0 \lambda_{\mathrm{dB}}^3 e^{-\beta\varepsilon}\Theta(V_0 - \varepsilon), \tag{3.18}$$

where $n_0 = N(m\bar{\omega}^2/2\pi k_B T)^{3/2}$ is the peak density of a classical gas in a harmonic trap.

As done in chapter 2, we can similarly define the distribution function in $\{\vec{r}, \vec{p}\}$ phase space. The assumption of ergodicity implies that the phase-space distribution is a function of the single particle energy only, $f(\vec{r}, \vec{p}) = \int d\varepsilon\, \delta(\vec{p}^2/2m + V_T(\vec{r}) - \varepsilon) f(\varepsilon)$, giving

$$f(\vec{r}, \vec{p}) = n_0 \lambda_{\mathrm{dB}}^3 e^{-\beta\left(\vec{p}^2/2m + V_T(\vec{r})\right)}\Theta(V_0 - \vec{p}^2/2m - V_T(\vec{r})). \tag{3.19}$$

The dynamics of the distribution $f(\vec{r}, \vec{p})$ of the gas are then described by the Boltzmann kinetic equation (for a detailed derivation of the following results, see [72]). Since we are

---

[2] The Gaussian optical potentials used in most evaporative cooling experiments have significant anharmonicities associated with their shape. However, as we'll see, for atoms with large enough scattering cross sections σ, the resulting fast evaporation rate ensures that the vast majority of atoms are cold enough to be sampling only the parts of the potential near $\vec{r} = 0$, where it is well approximated as harmonic.

interested in the number of atoms with energy greater than the trap depth, we would like to transform the Boltzmann kinetic equation into an equation governing the dynamics of the distribution function in energy. This is accomplished by multiplying each side of the kinetic equation by the density of states $\rho(\varepsilon) = (2\pi\hbar)^3 \int d^3r\, d^3p\, \delta(\vec{p}^2/2m + V_T(\vec{r}) - \varepsilon)$, resulting in the equation

$$\rho(\varepsilon)\dot{f}(\varepsilon) = \frac{1}{(2\pi\hbar)^3} \int d^3r d^3p\ \delta(\vec{p}^2/2m + V_T(\vec{r}) - \varepsilon)\mathcal{I}(\vec{r},\vec{p}), \tag{3.20}$$

where $\mathcal{I}(\vec{r},\vec{p})$ is the usual collision integral. Note that the number of atoms in the trap with an energy between ε and $\varepsilon + d\varepsilon$ is given by $\rho(\varepsilon)f(\varepsilon)d\varepsilon$. Thus, this protocol gives us a way to determine the rate at which the high-energy tail of the distribution is repopulated by collisions.

We now assume that the atoms in the tail of the distribution with energy greater than the trap depth are immediately lost to evaporation, resulting in the number loss rate

$$\begin{aligned} \dot{N}_{\text{evap}} &= -\int\limits_{V_0}^{\infty} d\varepsilon\ \rho(\varepsilon)\dot{f}(\varepsilon) \\ &= -\frac{m\sigma}{\pi^2\hbar^3} \int\limits_{\varepsilon_4 > V_0} d\varepsilon_1 d\varepsilon_2 d\varepsilon_3\, \rho(\varepsilon_3) f(\varepsilon_1) f(\varepsilon_2), \end{aligned} \tag{3.21}$$

where ε_1 and ε_2 are the energies of the two colliding atoms before the collision, ε_3 and ε_3 are those after, and σ is the two-body scattering cross section. It is assumed here that σ is energy independent, as is usually the case for s-wave scattering[3]. The integral is evaluated on the domain that satisfies the following conditions: the energies of the incoming particles are each less than the trap depth, or $\varepsilon_1 < V_0$ and $\varepsilon_2 < V_0$, and the energy of one of the outgoing particles is *greater than* the trap depth, $\varepsilon_4 = \varepsilon_1 + \varepsilon_2 - \varepsilon_3 > V_0$. Then, equation (3.21) becomes

$$\dot{N}_{\text{evap}} = -n_0\sigma\bar{v}\frac{\mathcal{V}_{\text{evap}}}{\mathcal{V}_{\text{eff}}}N, \tag{3.22}$$

---

[3] For the unitary Fermi gas, the scattering length diverges and one is left with the maximum two-body collision cross section $\sigma = 4\pi/k^2$ allowed by the optical theorem.

where $\bar{v} = \sqrt{8k_BT/\pi m}$ is the mean particle speed, $\mathcal{V}_{\text{eff}} = N/n_0 = (2\pi k_BT/m\bar{\omega}^2)^{3/2}$ is the effective volume of the harmonically trapped gas, and the evaporation volume is given by

$$\mathcal{V}_{\text{evap}} = \lambda_{\text{dB}}^3 e^{-\eta} \int_0^{V_0} d\varepsilon\, \rho(\varepsilon) \left[(\eta - \varepsilon/k_BT - 1)e^{-\varepsilon/k_BT} + e^{-\eta}\right], \tag{3.23}$$

where $\eta = V_0/k_BT$. Note that the prefactor $n_0\sigma\bar{v}$ in equation (3.22) is the peak elastic scattering rate Γ_{el} in the trapped gas. Using the density of states for the harmonic potential $V_T(\vec{r})$, $\rho(\varepsilon) = \varepsilon^2/2(\hbar\bar{\omega})^3$, the evaporation volume becomes

$$\mathcal{V}_{\text{evap}} = \frac{\lambda_{\text{dB}}^3(k_BT)^3}{6(\hbar\bar{\omega})^3}\left[24e^{-\eta} + 6(\eta-4) + \eta e^{-\eta}(18 + \eta(6+\eta))\right]. \tag{3.24}$$

Then, in the limit $k_BT \ll V_0$, or $\eta \gg 1$, this simplifies to

$$\mathcal{V}_{\text{evap}} = \mathcal{V}_{\text{eff}}(\eta - 4)e^{-\eta}. \tag{3.25}$$

Our final expression for the evaporative loss rate then becomes

$$\dot{N}_{\text{evap}} = -n_0\sigma\bar{v}(\eta - 4)e^{-\eta}N. \tag{3.26}$$

What remains is to determine the effect of the evaporative loss on the temperature dynamics. Similarly to the number loss rate, we find the rate of change of internal energy of the gas from

$$\dot{E}_{\text{evap}} = -\int_{V_0}^{\infty} d\varepsilon\, \varepsilon\rho(\varepsilon)\dot{f}(\varepsilon). \tag{3.27}$$

One can show that in the limit $\eta \gg 1$, this reduces to [72]

$$\dot{E}_{\text{evap}} = \left(V_0 + \frac{\eta-5}{\eta-4}k_BT\right)\dot{N}_{\text{evap}}. \tag{3.28}$$

Thus we see that the effect of evaporation on the total energy of the trapped gas is that, for each particle removed by evaporation, the ensemble loses an average energy of $\approx V_0 + k_BT$.

To connect the internal energy dynamics to temperature, we turn to the equation of state for an ideal gas in a harmonic trap, $E = 3Nk_BT$. Taking the time derivative, we find

$$\begin{aligned}\dot{T}_{\text{evap}} &= \frac{\dot{E}_{\text{evap}}}{3k_BN} - T\frac{\dot{N}_{\text{evap}}}{N} \\ &= \left(\eta + \frac{\eta - 5}{\eta - 4} - 3\right)\frac{\dot{N}_{\text{evap}}}{N}\frac{T}{3}. \qquad (3.29)\end{aligned}$$

3.2.2 *Forced evaporative cooling*

Due to the exponential factor $e^{-\eta}$ in equation (3.26), the rate of evaporative loss slows greatly as the gas is cooled at fixed trap depth V_0. Typically, on timescales relevant for quantum gas experiments ($10-20$ seconds) the temperature of the gas asymptotes to a value $T \approx V_0/(10k_B)$. Since the trap depth upon loading of the atomic gas from the Doppler cooling stage is typically in the range 100 μK - 1 mK, this saturation of the evaporative cooling power would not feasibly permit temperatures below 1 μK. To overcome this in optical traps, the solution is to dynamically reduce the trap depth by decreasing the trapping laser intensity over time. This process is referred to as forced evaporative cooling. For a Gaussian-shaped optical trapping beam of fixed waist, there is a reduction of the trap frequencies associated with the changing trap depth V_0. From equation (2.9), we find

$$\frac{\dot{\bar{\omega}}}{\bar{\omega}} = \frac{1}{2}\frac{\dot{V}_0}{V_0}. \qquad (3.30)$$

Since the harmonic confinement decreases while performing forced evaporative cooling, the potential energy of the gas changes, provided the change is adiabatic. Writing the potential energy as $E_{\text{pot}} = E_x + E_y + E_z$, where $E_i = m\omega_i^2\langle x_i^2\rangle/2 = E_{\text{pot}}/3$, we find that

$$\dot{E}_{\text{pot}} = \frac{E_{\text{pot}}}{3}(\dot{\omega}_x + \dot{\omega}_y + \dot{\omega}_z) = E_{\text{pot}}\frac{\dot{\bar{\omega}}}{\bar{\omega}}. \qquad (3.31)$$

Then, recalling that $E = E_{\text{pot}}/2$ for the harmonic oscillator, we find the adiabatic contribution to the temperature change

$$\dot{T}_{\text{ad}} = \frac{\dot{\bar{\omega}}}{\bar{\omega}}T. \qquad (3.32)$$

It is important to note here that although the adiabatic reduction of temperature associated with reducing the trap depth can be used to achieve impressively low temperatures, there is no associated gain in phase-space density since the change is adiabatic.

A well-known problem with performing forced evaporative cooling in optical traps is that the continued reduction of laser power and thus trap frequencies results in very small collision rates at the lowest depths, and thus long evaporative cooling timescales. In chapter 7 of this thesis we will discuss a method which overcomes this issue using time-averaged potentials (see section 2.1.3). In short, one can dynamically change the size of the optical trapping beam at its focus to achieve independent control over the trap depth V_0 and frequency $\bar{\omega}$.

3.2.3 Effects of background and inelastic loss

Up to this point we have only considered the consequences of elastic interactions. However, in many situations there are inelastic scattering processes that can greatly limit the efficiency of evaporative cooling. In general, inelastic scattering refers to a scattering event where the particles exit in a different scattering channel, which covers a broad range of possible scenarios. In this section, we will evaluate the consequences of two-body and three-body inelastic loss for the rate equations governing the number N and temperature T evolution in the trap. Additionally, we will look at the effects of atom loss due to collisions with background gas particles in the vacuum chamber, i.e. one-body loss.

Three-body loss is a scattering event in which three free particles come together, two of them associate to form a molecule, and the third carries away the necessary energy and momentum to satisfy conservation laws. This is often referred to as three-body recombination. The other important type of inelastic scattering in the cold atom context, two-body inelastic scattering, involves the release of internal electronic energy from one or both of the atoms in a two-body scattering event. For three-body loss, the energy released is typically far larger than the trap depth, resulting in loss of all atoms involved from the trap, while for two-body loss, the amount of energy released depends on the loss channel in question.

The relative importance of two-body and three-body loss depends sensitively on the choice of atomic species. For bosons, three-body inelastic collisions are always an issue, and dominate the number loss at high densities, while the strength of two-body loss processes depend on the structure of the atom in question. Alternatively, for experiments on two-component fermionic gases away from a Feshbach resonance, three-body recombination is greatly inhibited due to the Pauli exclusion principle, as it would require two identical fermions to encounter each other at short range.

For a trapped gas with local density $n(\vec{r})$, the effects of background one-body loss and two-body and three-body inelastic loss are described by the rate equation

$$\dot{n}_{\text{inelastic}}(\vec{r}) = -\left(\Gamma_{\text{bg}} + K_2 n(\vec{r}) + K_3 n^2(\vec{r})\right) n(\vec{r}), \tag{3.33}$$

where Γ_{bg} is the density- and temperature-independent rate of collisions with background gas particles and K_2 (K_3) is the two-body (three-body) inelastic loss rate coefficient. To find the net effect on the atom number $N = \int d^3r\, n(\vec{r})$, we integrate equation (3.33) over space using $n(\vec{r}) = n_0 \exp[-\frac{m}{2k_BT}(\omega_x^2 x^2 + \omega_y^2 y^2 + \omega_z^2 z^2)]$, giving

$$\dot{N}_{\text{inelastic}} = -\left(\Gamma_{\text{bg}} + \Gamma_{\text{2b}}(N,T) + \Gamma_{\text{3b}}(N,T)\right) N, \tag{3.34}$$

where

$$\Gamma_{\text{2b}}(N,T) = K_2 N \left(\frac{m\bar{\omega}^2}{4\pi k_B T}\right)^{3/2} \propto \frac{N}{T^{3/2}} \tag{3.35}$$

is the two-body per-particle loss rate and

$$\Gamma_{\text{3b}}(N,T) = \frac{K_3 N^2}{\sqrt{27}} \left(\frac{m\bar{\omega}^2}{2\pi k_B T}\right)^{3} \propto \frac{N^2}{T^3} \tag{3.36}$$

is the three-body per-particle loss rate. Note that the per-particle loss rate due to evaporation in equation (3.26) also scales as $N/T^{3/2}$ since this is also a two-body collisional effect.

To evaluate the effects of these loss processes on the temperature of the gas, we first determine the dynamics of the total energy of the ensemble, and then relate this to temperature using the equation of state. The local energy density of the gas is given by

$\mathcal{E}(\vec{r},\vec{p}) = (\vec{p}^2/2m + V_T(\vec{r}))n(\vec{r})$. Thus, we find the rate of change of the total ensemble energy from [109]

$$\dot{E}_{\text{inelastic}} = \int d^3r d^3p\, \dot{\mathcal{E}}(\vec{r},\vec{p}) = \int d^3r \left(\langle \vec{p}^2/2m \rangle_{\vec{p}} + V_T(\vec{r}) \right) \dot{n}_{\text{inelastic}}(\vec{r}). \tag{3.37}$$

Using the classical gas result $\langle \vec{p}^2/2m \rangle_{\vec{p}} = 3k_BT/2$ and defining the density-weighted integrals

$$X_l = \frac{1}{n_0^l} \int d^3r\, (n(\vec{r}))^l \quad \text{and} \quad Z_l = \frac{1}{n_0^l} \int d^3r\, V_T(\vec{r})(n(\vec{r}))^l, \tag{3.38}$$

equation (3.37) becomes

$$\dot{E}_{\text{inelastic}} = \frac{3k_BT}{2} \dot{N}_{\text{inelastic}} - \left(\Gamma_{\text{bg}} \frac{Z_1}{X_1} + K_2 \frac{Z_2}{X_1^2} N + K_3 \frac{Z_3}{X_1^3} N^2 \right) N. \tag{3.39}$$

For these spatial integrals, we assume the untruncated form of the trapping potential $V_T(\vec{r}) = \frac{m}{2} \sum \omega_i^2 x_i^2$ and integrate over all space.

Next, we connect these energy dynamics with temperature using the equation of state $E = 3k_BT$, as done in section 3.2.1. Using the relation $\dot{T}_{\text{inelastic}} = \dot{E}_{\text{inelastic}}/(3k_BN) - T\dot{N}_{\text{inelastic}}/N$ and equations (3.34) and (3.39), one finds the following equation for the temperature dynamics in terms of the two- and three-body per-particle loss rates [106]:

$$\dot{T}_{\text{inelastic}} = \left(\frac{\Gamma_{2\text{b}}(N,T)}{4} + \frac{\Gamma_{3\text{b}}(N,T)}{3} \right) T. \tag{3.40}$$

Note that there is no contribution from the one-body loss term to the temperature dynamics because this process occurs uniformly throughout the gas and thus does not affect the average energy. On the other hand, two- and three-body inelastic processes are favored near the center of the trap where the density is highest. Since these atoms have a local average energy smaller than that of the trap-averaged ensemble, we can think of causing a sort of "anti-evaporation," whereby atoms are removed from the low-energy portion of the distribution $n(E)$ and the remaining ensemble equilibrates to a *larger* average energy.

3.2.4 Heating from spontaneous scattering

Even though the atoms are held in a far off-resonant optical dipole trap, they still undergo some amount of spontaneous scattering. This results in a small, but non-zero heating term

$\dot{E}_{\text{scat}} = \Gamma_{\text{scat}} E_{\text{rec}} N$, where $\Gamma_{\text{scat}} = (V_0/\hbar)(\Gamma/\delta)$ is the rate of spontaneous scattering from the ODT beam, $E_{\text{rec}} = \hbar^2 k_L^2/2m$ is the recoil energy for a photon with wave vector k_L, Γ is the natural linewidth of the atomic transition in question, and $\delta = \omega_L - \omega_0$ is the detuning of the ODT laser from the atomic transition frequency (usually very large). Here we approximate the heating rate to be constant across the whole cloud and given by the peak scattering rate in the trap, which is reasonable for clouds with a large value of η. Again using the equation of state to relate the temperature dynamics to those of the total energy, we find that

$$\dot{T}_{\text{scat}} = \frac{\Gamma_{\text{scat}} E_{\text{rec}}}{3k_B}. \tag{3.41}$$

3.2.5 The full dynamical equations

At this point we are in a position to quantitatively describe all of the dynamics involved during forced evaporative cooling experiments. First, let us define the per-particle rate of evaporative cooling in the high-η limit (see equation (3.26)), $\Gamma_{\text{evap}} \equiv \dot{N}_{\text{evap}}/N = \Gamma_{\text{el}}(\eta-4)e^{-\eta}$. Then, the complete equation for the number evolution is

$$\begin{aligned}\dot{N} &= \dot{N}_{\text{evap}} + \dot{N}_{\text{inelastics}} \\ &= -(\Gamma_{\text{evap}}(N,T) + \Gamma_{\text{bg}} + \Gamma_{\text{2b}}(N,T) + \Gamma_{\text{3b}}(N,T))N,\end{aligned} \tag{3.42}$$

and for temperature

$$\begin{aligned}\dot{T} &= \dot{T}_{\text{evap}} + \dot{T}_{\text{inelastics}} + \dot{T}_{\text{ad}} + \dot{T}_{\text{scat}} \\ &= -\left(\frac{\Gamma_{\text{evap}}}{3}\left(\eta + \frac{\eta-5}{\eta-4} - 3\right) - \frac{\Gamma_{\text{2b}}}{4} - \frac{\Gamma_{\text{3b}}}{3} - \frac{\dot{\bar{\omega}}}{\bar{\omega}}\right) T + \frac{\Gamma_{\text{scat}} E_{\text{rec}}}{3k_B}.\end{aligned} \tag{3.43}$$

We will return to this system of equations in chapter 7 when we simulate the evaporation dynamics for Yb in a dynamically shaped time-averaged potential.

3.3 Feshbach resonances

Until this point, we have been considering two-body elastic collisions that occur in a single scattering channel in the s-wave limit, and can therefore be characterized by a fixed scattering length a. As discussed in section 3.1, the specific value of a for a given two-body collision system is determined by the S-matrix element $S_0 = e^{2i\delta_0}$ (i.e. by the scattering phase shift δ_0), which in turn is determined by the interatomic potential, $V(\vec{r})$. In many realistic situations, however, the two colliding particles have internal structure that results in more than one possible scattering channel, and therefore multiple potentials $V_\alpha(\vec{r})$. Furthermore, there often exists an interaction mechanism that couples states from the different channels. In this case, the S-matrix acquires new indices corresponding to the labels for the scattering channels[4], $S_{\alpha\beta}$, and is no longer diagonal. Typically, this coupling is very weak and the scattering can be taken to be intra-channel only (i.e. $S_{\alpha\beta}$ diagonal). However, in the case where a bound state of one channel becomes degenerate in energy with the scattering state in another channel, the channels become mixed and the scattering character strongly modified. This resonance phenomenon is an example of what are referred to as Feshbach resonances, which is a more general class of scattering resonances involving the coupling of bound states to a continuum. For a complete treatment of Feshbach resonances in ultracold gases, the reader is referred to some of the many great reviews on the topic [64, 21, 58].

3.3.1 An illustrative example: Two hyperfine states in ^{6}Li

While it is possible to have many scattering channels for a given two-atom collision system, it is illustrative and often sufficient to consider just two channels in the vicinity of a Feshbach resonance. As an example system, we consider two distinguishable spin one-half particles, namely the two lowest energy hyperfine states in the ^{6}Li $^2S_{1/2}$ electronic ground state, with nuclear spin $I = 1$. At zero magnetic field, these states, labeled $|1\rangle$ and $|2\rangle$, are specified by the quantum numbers $F = 1/2$, $m_F = 1/2$ and $F = 1/2$, $m_F = -1/2$, respectively. At finite field, however, only $m_F = m_I + m_J$ is a good quantum number and is conserved by the scattering interaction [21]. Thus, only channels with the same value of m_F may be coupled by the interaction.

---

[4] In this expression for the S-matrix we drop the angular momentum label ℓ, since we are considering only $\ell = 0$ scattering.

It is useful to consider the scattering problem in the total spin basis, where $\vec{S} = \vec{S}_1 + \vec{S}_2$ for atoms $i = 1$ and 2 with electronic spin $\vec{S}_i$. In this case, the two channels of interest correspond to the singlet and triplet combinations with $S = 0$ and 1, respectively, and associated interatomic potentials $V_s(r)$ and $V_t(r)$. The two-channel interaction operator can then be written as [10]

$$\begin{aligned}\hat{V}(r) &= \tfrac{1}{4}\left(3V_t(r) + V_s(r)\right) + \vec{S}_1 \cdot \vec{S}_2 \left(V_t(r) - V_s(r)\right) \\ &= \tfrac{1}{4}\left(3V_t(r) + V_s(r)\right) + 2\vec{S}_1 \cdot \vec{S}_2 V_{\text{ex}}(r),\end{aligned} \tag{3.44}$$

where $V_{\text{ex}}(r)$ is the exchange potential. Clearly, the tensor term proportional to $\vec{S}_1 \cdot \vec{S}_2$ will be responsible for any inter-channel coupling. However, if the scattering states are eigenstates[5] $|S, m_S\rangle$ of the total spin $\vec{S}$, no such coupling will occur since the off-diagonal terms $\langle 1, m_S|\vec{S}_1 \cdot \vec{S}_2|0, 0\rangle$ and $\langle 0, 0|\vec{S}_1 \cdot \vec{S}_2|1, m_S\rangle$ vanish. Of course, the states $|1\rangle$ and $|2\rangle$ under consideration are not true eigenstates of the spin operator $\vec{S}_i$, and therefore don't form pure spin singlets or triplets.

At high magnetic field, the two lowest hyperfine states can be written in the $|m_{S_i}, m_{I_i}\rangle$ basis as

$$\begin{aligned}|1\rangle &= \sqrt{1-\eta_1}\,|-\tfrac{1}{2}, 1\rangle + \sqrt{\eta_1}\,|\tfrac{1}{2}, 0\rangle \\ |2\rangle &= \sqrt{1-\eta_2}\,|-\tfrac{1}{2}, 0\rangle + \sqrt{\eta_2}\,|\tfrac{1}{2}, -1\rangle,\end{aligned} \tag{3.45}$$

where $\eta_1 \ll 1$ and $\eta_2 \ll 1$ are the residual effects of the hyperfine interaction. Thus, away from a scattering resonance, the collision is entirely of triplet character, as $m_{S_1} = m_{S_2} = -1/2$. However, near a resonance, the admixing of different m_{S_i} states in equation (3.45) due to the hyperfine interaction allows for non-zero off-diagonal terms in the two-channel interaction operator above. It is important to note that although the hyperfine admixing is weak, Feshbach resonances of this type are quite strong because the exchange interaction term in equation (3.44) is typically quite large.

---

[5] Note that for ^{6}Li in the $^2S_{1/2}$ ground state, there is no orbital angular momentum and $\vec{J} = \vec{S}$. Therefore, we use m_J and m_S interchangeably in this context.

3.3.2 Two-channel resonance scattering

In general, we refer to the channel in which the atoms predominately scatter in the absence of resonances as the *entrance* channel or *open* channel, and the channel to which it is coupled as the *closed* channel. A necessary ingredient for realizing a scattering resonance is the tunability of the energy of a bound state in the closed potential relative to the energy of the free scattering state in the entrance channel. In this section, we focus on magnetically tunable Feshbach resonances, where the two channels involved have different magnetic moments[6].

Figure 3.1(a) depicts the typical two-channel situation where the scattering state in the entrance channel has a detuning δE relative to some bound state in the closed channel. For our earlier example of states $|1\rangle$ and $|2\rangle$ in ^{6}Li, these channels correspond to the triplet (entrance) and singlet (closed) potentials, and the detuning from resonance is given by $\delta E = \delta\mu(B - B_0) = 2\mu_B(B - B_0)$, where B_0 is the field at which the uncoupled free and bound states have equal energy. As the free and bound states approach each other in energy, the inter-channel coupling replaces the bare free scattering state with a superposition state consisting of both entrance- and closed-channel character.

In terms of elastic scattering in the open channel, the effect of the coupling is to cause the scattering phase shift δ_0 to go through the value $(n+1/2)\pi$, at which point the scattering length has a pole. This is described by the following Breit-Wigner form for the phase in the s-wave limit ($k \to 0$) [21]

$$\delta_0(k) = \delta_{\mathrm{bg}}(k) - \tan^{-1}\left(\frac{\Gamma_0/2}{E(k) - (\delta E - \delta E_0)}\right), \tag{3.46}$$

where $E(k) = \hbar^2 k^2/(2\mu_r)$, $a_{\mathrm{bg}} = -\lim_{k\to 0} \tan\delta_{\mathrm{bg}}/k$ is the background scattering length in the entrance channel, and the inter-channel coupling is responsible for the finite width Γ_0 and energy offset δE_0 of the resonance position[7]. As $k \to 0$, the background phase δ_{bg} vanishes,

---

[6] We'll see later how such tunability can also be achieved in the context of optical Feshbach resonances using the frequency of a laser beam which couples the scattering state in a ground electronic state potential to a bound state in an electronically excited potential.

[7] In general, the width Γ_0 and energy offset δE_0 depend on k, but we take them to be their threshold values here since we will soon take the limit $k \to 0$.

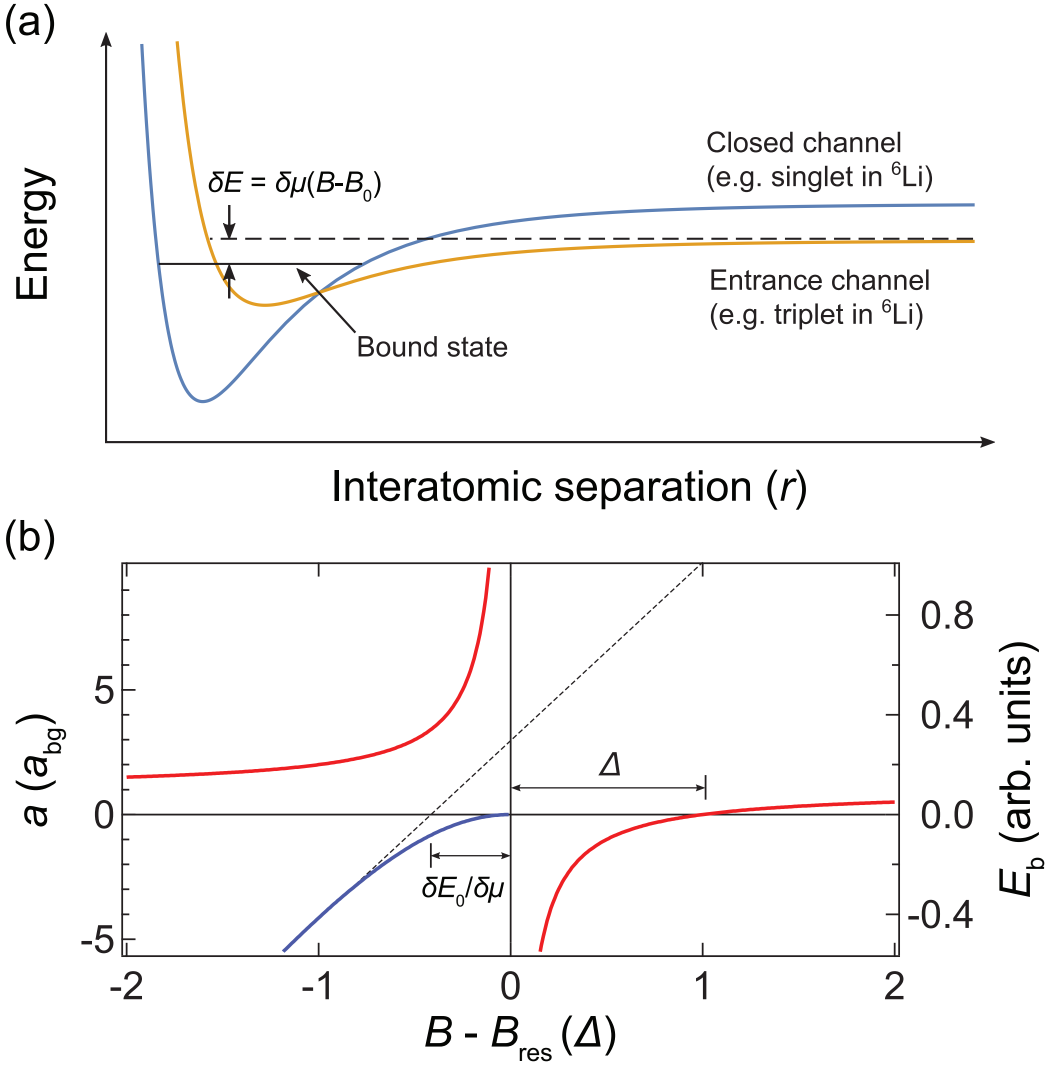

Figure 3.1: Two-channel model of a magnetic Feshbach resonance. (a) The potentials corresponding to each channel are tuned relative to each other using an external magnetic field. In the situation where the bound state energy is below(above) that of the scattering state, $a > 0 (a < 0)$. (b) Behavior of the s-wave scattering length $a(B)$ (red curve) and the dressed molecular state binding energy E_b (blue curve) in the vicinity of a Feshbach resonance. The dashed black line corresponds to the energy tuning of the bare, uncoupled molecular state, which crosses the magnetic field axis a distance $\delta E_0/\delta\mu$ from the true resonance position. For $B > B_{\text{res}}$, the molecular state disappears into the open channel continuum, but the effects on the scattering length remain.

but the resonant component remains. Defining the resonance field $B_{\mathrm{res}} = B_0 + \delta E_0/\delta\mu$ and width $\Delta = \Gamma_0/(2ka_{\mathrm{bg}}\delta\mu)$, we arrive at the following magnetic field dependence for the s-wave scattering length [21]:

$$a(B) = a_{\mathrm{bg}}\left(1 - \frac{\Delta}{B - B_{\mathrm{res}}}\right). \tag{3.47}$$

Figure 3.1(b) shows the scattering length (red curve) in the vicinity of a Feshbach resonance. The energy of the bare, uncoupled bound state is depicted by the dashed line, which crosses the magnetic field axis at the unshifted position $B_{\mathrm{res}} - \delta E_0/\delta\mu$.

For large positive scattering lengths, the two atoms are in a dressed molecular state with binding energy E_{b}, shown by the blue curve in figure 3.1(b), while for $a < 0$, the molecular state "dissolves" into the open channel continuum. Close to resonance where the inter-channel mixing is strong, the binding energy follows the universal formula $E_b = -\hbar^2/(2\mu_r a^2)$. Far away from resonance with $a > 0$, however, the dressed molecular state resides almost entirely in the closed channel, and therefore has binding energy $E_b = \delta\mu(B - B_0)$. In fact, one can utilize the avoided crossing depicted in figure 3.1(b) to coherently create closed channel molecules by adiabatically sweeping the magnetic field from the $a < 0$ to $a > 0$ side of the resonance.

3.3.3 Feshbach resonances with inelastic decay

In our treatment of Feshbach resonances so far, we have assumed that the two-atom system occupies a state in the two-channel subspace. In many cases, however, there are external channels with which the entrance or closed channel may couple that result in a net outgoing flux of probability from the two-channel subspace. The non-unitary character of this scattering process is captured in the open-channel S-matrix element S_{00} by adding a positive imaginary part to the phase shift [52]. We then modify the Breit-Wigner formula (equation (3.46)) to account for the finite lifetime of the state

$$\delta_0(k) = \delta_{\mathrm{bg}}(k) - \tan^{-1}\left(\frac{\Gamma_0/2}{E(k) - (\delta E - \delta E_0) + i(\hbar\gamma/2)}\right), \tag{3.48}$$

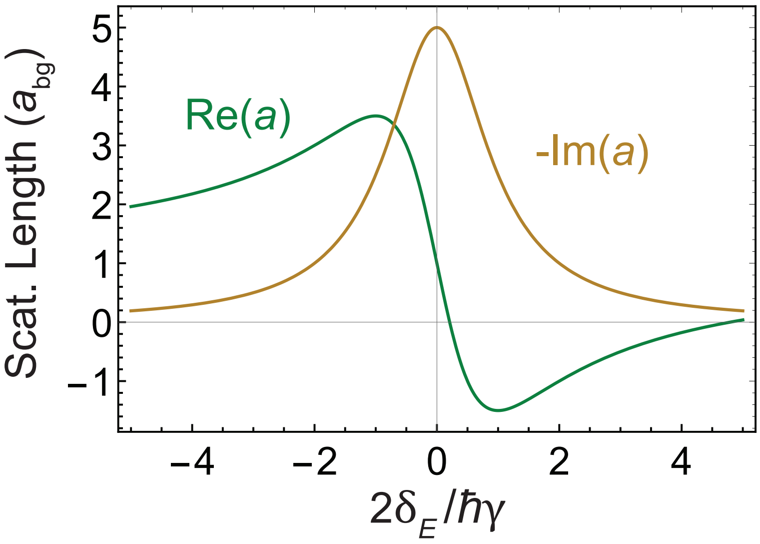

Figure 3.2: Real and imaginary parts of the complex scattering length $\tilde{a}$ in units of the background scattering length a_{bg} in the vicinity of a Feshbach resonance with decay rate γ. For these particular curves, we set $2\Gamma_0/(\hbar\gamma) = 10ka_{\mathrm{bg}}$.

where γ is the decay rate. Writing the resulting complex scattering length as $\tilde{a} = a - ib$ and defining $\delta_E = \delta E - \delta E_0$, we find as $k \to 0$ [21]

$$a = a_{\mathrm{bg}} - \frac{1}{2k} \frac{\Gamma_0 \delta_E}{\delta_E^2 + (\hbar\gamma/2)^2} \quad \text{and} \quad b = \frac{1}{2k} \frac{\Gamma_0 (\hbar\gamma/2)}{\delta_E^2 + (\hbar\gamma/2)^2}. \tag{3.49}$$

Because of the threshold behavior of the resonance coupling $\Gamma_0 \propto k$, a and b remain finite in the limit $k \to 0$. In contrast to equation (3.47), the real part of the scattering length no longer diverges, and the imaginary part is peaked at the resonance location (see figure 3.2). The two-body inelastic collision rate coefficient (units of (length)^3/time) associated with the decay channel is then found from

$$K_2 = \frac{4\pi\hbar g}{\mu_r} b, \tag{3.50}$$

where $g = 1$ for distinguishable scatterers and $g = 2$ for identical scatterers. When the kinetic energy gain associated with the decay is much larger than the trap depth, both atoms will be immediately lost from the trap. In this case the inelastic collision rate is equivalent to a loss rate coefficient, or $\dot{n} = -K_2 n^2$.

In the context of magnetic Feshbach resonances, the inelastic decay channels are states of lower energy than the scattering state that preserve the projection of total angular momentum onto the magnetic field axis. In chapter 5, we will discuss measurements of Feshbach resonances in an ultracold mixture of Li ($^2S_{1/2}$) and metastable Yb ($^3P_2$) where the ability of Yb to decay to lower lying electronic states results in very large inelastic decay rates.

3.3.4 Optical Feshbach resonances and photoassociation

In addition to accessing collisional resonances between free and bound two-body states with external magnetic fields, one can couple a pair of free scattering atoms to an electronically excited molecular state using laser fields. Figure 3.3 shows the general energy diagram for such an optical Feshbach resonance (OFR), where the laser photon energy $\hbar\omega_L$, usually in the optical domain, bridges the large energy scale between electronic states. In this case, the coupling between free and bound states is provided by the dipole coupling of the laser electric field to the induced dipole moment of the molecule [55],

$$\begin{aligned}\hbar\Gamma_{\text{stim}}(I) &= 2\pi \times \left(\frac{2\pi I}{c}\right) |\langle\psi_{\text{mol}}|\, \vec{d}\cdot\vec{e}\, |\psi_{\text{scat}}\rangle|^2 \\ &= 2\pi \times \left(\frac{2\pi I}{c}\right) d_M^2 f_{FC},\end{aligned} \tag{3.51}$$

where $|\psi_{\text{scat}}\rangle$ and $|\psi_{\text{mol}}\rangle$ are the interatomic scattering and molecular bound states (including both electronic and nuclear parts), I and $\vec{e}$ are the intensity and unit polarization vector for the coupling laser, Γ_{stim} is the stimulated scattering rate, $\vec{d}$ is the dipole moment operator, d_M is the molecular dipole moment, and f_{FC}, the Franck-Condon factor, is the square of the overlap between the nuclear wave functions for the scattering and bound states, with units of inverse energy. In contrast to magnetic Feshbach resonances, we see that one can tune the strength of the coupling in an OFR by varying the intensity of the laser beam used to couple free and bound states.

For near-threshold transitions, the molecular dipole moment can be written as $d_M = f_{\text{rot}} d_A$, where f_{rot} is the Hönl-London factor accounting for the change in nuclear orbital angular momentum [82], and $d_A = \hbar\Omega_a/|E_0|$ is the atomic dipole matrix element with associated Rabi frequency Ω_a. Using equation (3.51) and $\Omega_a^2 = I\gamma^2/(2I_{\text{sat}})$, where γ is the molecular rate of spontaneous emission and $I_{\text{sat}} = 2\pi^2\hbar c\gamma/(3\lambda^3)$ is the saturation intensity for the atomic transition, we find[8] [82]

$$\Gamma_{\text{stim}} = \frac{3I\gamma\lambda^3 f_{\text{rot}} f_{FC}}{8\pi c}. \tag{3.52}$$

For near-threshold transitions in heteronuclear diatomic molecules, the spontaneous emission rate is well approximated by the atomic value, $\gamma = \gamma_a$. If instead the two atoms are identical, proper symmetrization of the molecular wave function in the excited electronic state gives rise to super- and sub-radiant states, for which $\gamma = 2\gamma_a$ and $\gamma = 0$, respectively.

In the dressed state picture, we remove the large energy offset between the free and bound states by considering the combined states $|\psi_{\text{scat}}, N+1\rangle$ and $|\psi_{\text{mol}}, N\rangle$, where the

---

[8] In this expression we use Gaussian units and write the laser electric field as $E_0^2 = 8\pi I/c$. In SI units, where $E_0^2 = 2I/(c\epsilon_0)$, the stimulation rate becomes $\Gamma_{\text{stim}} = 3I\epsilon_0\gamma\lambda^3 f_{\text{rot}} f_{\text{FC}}/(2c)$.

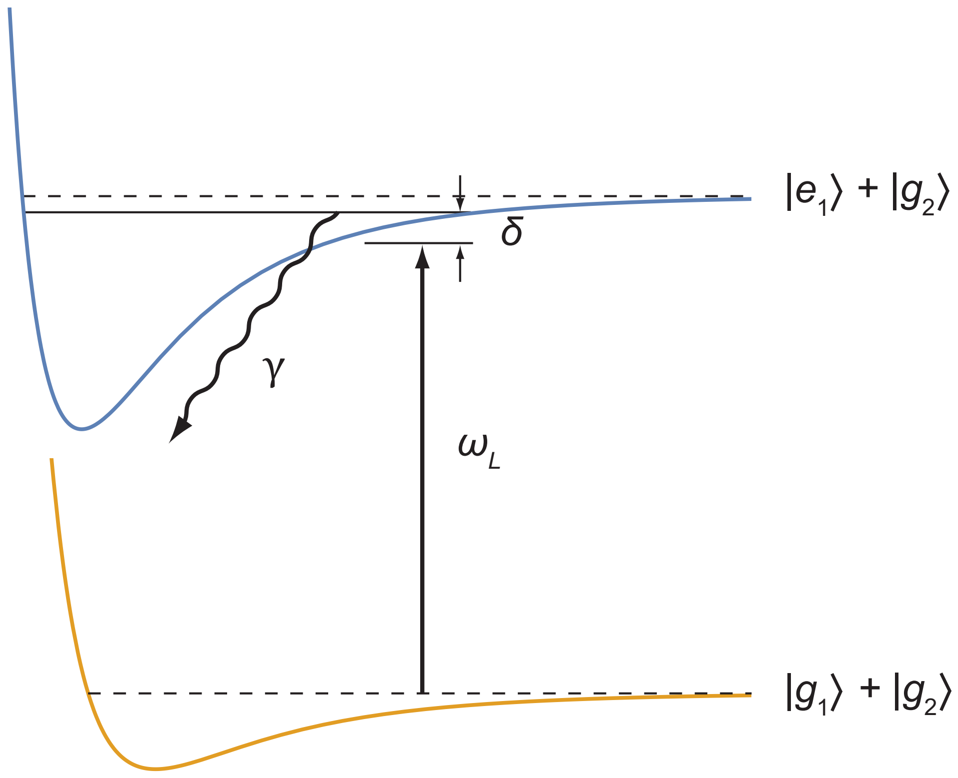

Figure 3.3: Schematic of an optical Feshbach resonance (OFR). In an OFR, one couples free scattering atoms to an electronically excited molecular state using the dipole coupling from a laser beam. The molecular state has an associated decay rate γ, resulting in a strong inelastic component to the resulting collisional resonance. The inelastic scattering events correspond to the creation, or photoassociation (PA) and subsequent decay of electronically excited molecules, resulting in loss of atoms from the trap. The inelastic character of OFRs thus offers a sensitive method for performing laser spectroscopy of molecular potentials.

interatomic scattering and molecular bound states are dressed with $N+1$ and N photons, respectively. Then, the energy difference between the free and bound dressed states is given by $\hbar\delta$, which is easily controllable via the laser frequency. The resulting modification of the background scattering properties near the molecular resonance $\delta = 0$ is quite similar to that of the inelastic magnetic Feshbach resonance discussed in the previous section, with the main difference being that the dipole coupling from the laser field can stimulate population transfer from the excited to ground state, and thus adds to the decay rate of the resonance. For more details, the reader is referred to a particularly nice semianalytical treatment of the OFR problem by Bohn and Julienne [11, 12]. Here, we quote the result for the complex s-wave scattering length $\tilde{a} = a - ib$:

$$a = a_{\text{bg}} + \frac{1}{2k}\frac{\Gamma_{\text{stim}}\delta}{\delta^2 + (\gamma/2)^2 - (\Gamma_{\text{stim}}/2)^2}, \qquad b = \frac{1}{2k}\frac{\Gamma_{\text{stim}}\gamma/2}{\delta^2 + \frac{1}{4}(\gamma + \Gamma_{\text{stim}})^2}. \tag{3.53}$$

The imaginary part of the scattering length, b, represents actual molecule formation in the excited electronic state. This process of molecule formation using a coupling laser field is referred to as *photoassociation* (PA), and has the associated inelastic rate coefficient

$$K_{2,\text{PA}} = \frac{g\pi\hbar}{\mu_r k}\frac{\Gamma_{\text{stim}}\gamma}{\delta^2 + \frac{1}{4}(\gamma + \Gamma_{\text{stim}})^2}. \tag{3.54}$$

The wave vector associated with the collision is given by $k = \sqrt{2E\mu_r}/\hbar$. For a thermal cloud, we take the energy $E = \frac{1}{2}\mu_r \vec{v}_{\text{rel}}^{\,2}$ of the collision to be given by the mean value,

$$\begin{aligned}\langle E\rangle &= \frac{\mu_r}{2}\langle(\vec{v}_1 - \vec{v}_2)^2\rangle \\ &= \frac{\mu_r}{2}\left(\langle\vec{v}_1^{\,2}\rangle + \langle\vec{v}_2^{\,2}\rangle - 2\langle\vec{v}_1\cdot\vec{v}_2\rangle\right) \\ &= \frac{\mu_r}{2}\left(\frac{3k_BT_1}{m_1} + \frac{3k_BT_2}{m_2},\right)\end{aligned} \tag{3.55}$$

where $\vec{v}_i$ and m_i are the velocity and mass of particle $i = 1$ or 2, and T_i is the temperature associated with each ensemble.

We can then find the maximum PA rate coefficient at a given temperature by maximizing the function in equation (3.54) with respect to Γ_{stim} for $\delta = 0$ (i.e. on resonance PA), giving

$$K_{2,\text{PA}}^{\text{max}} = \frac{g\pi\hbar^2}{\sqrt{3k_BT_{\text{eff}}\mu_r^3}}, \tag{3.56}$$

where the effective temperature T_{eff} is defined as

$$T_{\text{eff}} = \frac{m_2 T_1 + m_1 T_2}{m_1 + m_2}. \tag{3.57}$$

For the Yb-Li system, we have $g = 1$ and $\mu_r = 5.8$ amu, giving $K_{2,\text{PA}}^{\max} = \sqrt{100\,\mu\text{K}/T_{\text{eff}}} \times 5.7 \times 10^{-10}\ \text{cm}^3\text{s}^{-1}$. It is often the case that the intensities necessary to achieve this maximum rate coefficient are unreachable in experiments because of the large reduction of the stimulation rate Γ_{stim} due to the free-to-bound Franck-Condon factor f_{FC}.

Photoassociation resonances provide a simple experimental method to perform spectroscopy of molecular potentials, because immediately following formation of excited state molecules, the two-body system decays and both atoms are lost from the trap. This spectroscopy may be performed in a MOT, or in conservative optical or magnetic potentials. In practice, these experiments typically involve starting with the coupling laser frequency tuned just below the bare atomic resonance (i.e. asymptote of the molecular potential), and scanning downwards in frequency until a PA loss feature is discovered. While there were early hopes that the elastic part $\text{Re}(\tilde{a})$ of the OFR would offer a general method to tune interactions in any two-body system [11], it has proved to be very difficult to overcome the loss associated with PA.

3.4 Interacting quantum gases

While it is often reasonable to neglect the effects of interactions for trapped gases with low phase space density (i.e. classical gases), even modest two-body scattering lengths a result in drastic modifications of the properties of trapped gases in the quantum degenerate regime for typical densities. In the case of bosons, an important consequence of interactions is that the BEC ground state wave function in a harmonic trap is not that of the quantum harmonic oscillator, but one in which kinetic energy can largely be ignored (as we'll see). Furthermore, it is because of interactions that BECs acquire the property of superfluidity. For trapped fermions, we will concern ourselves primarily with the case of two-component systems in which the scattering length is arbitrarily tunable using a Feshbach resonance. In this case, one can access the so-called Bose-Einstein condensate to Bardeen-Cooper-Schreiffer (BEC-BCS) crossover, a spectrum of fermionic superfluidity which smoothly connects the regimes of Bose-Einstein condensation of diatomic molecules ($a \rightarrow 0_+$) and condensation of Cooper-paired fermions ($a \rightarrow 0_-$) [113]. At the position of the Feshbach resonance, the scattering length diverges and the resulting scattering cross section is limited by the constraints of unitarity. This so-called unitary Fermi gas, in which the Fermi wave vector provides the only relevant length scale k_F^{-1}, is of immense theoretical interest [6, 50, 46, 47, 104] and is an example of a many-body quantum system that can be experimentally simulated in trapped atomic gases [79, 80, 67] to inform and benchmark many-body theoretical techniques.

3.4.1 Weakly interacting BECs

The ground state, many-body wave function for a trapped BEC is determined by the time-independent Gross-Pitaevskii equation,

$$\left(-\frac{\hbar^2}{2m}\nabla^2 + V_T(\vec{r}) + g|\psi(\vec{r})|^2\right)\psi(\vec{r}) = \mu\psi(\vec{r}). \tag{3.58}$$

which we derived in section 3.1.3. Here, $g = 4\pi\hbar^2/m$, the BEC density distribution is given by $n(\vec{r}) = |\psi(\vec{r})|^2$, $V_T(\vec{r}) = \frac{m}{2}(\omega_x^2 x^2 + \omega_y^2 y^2 + \omega_z^2 z^2)$ is the external trapping potential, and μ is the BEC chemical potential. Equation (3.58) may be solved numerically in general. However, it turns out that in most experimentally relevant situations, the contribution of the kinetic energy term is negligible compared to the interaction energy term [89]. Writing the chemical potential in the local density approximation (valid for $\mu \gg \hbar\bar{\omega}$) as $\mu(\vec{r}) = \mu - V_T(\vec{r})$ and dropping the kinetic energy term, we find the following form for the BEC density distribution:

$$\begin{aligned} n(\vec{r}) &= \frac{1}{g}\max\left(\mu - V_T(\vec{r}), 0\right) \\ &= n_0 \max\left(1 - \sum_i \frac{x_i^2}{R_i^2}, 0\right), \end{aligned} \tag{3.59}$$

where $n_0 = \mu/g$ and $R_i = \sqrt{2\mu/(m\omega_i^2)}$. The approximation leading to equation (3.59) is called the Thomas-Fermi approximation, and the quantities R_i the Thomas-Fermi radii.

From the normalization condition $N = \int d^3r\, n(\vec{r})$, we find that $n_0 = 15N/(8\pi R_x R_y R_z)$. The chemical potential is then found to be

$$\mu = \frac{\hbar\bar{\omega}}{2}\left(\frac{15Na}{a_{\text{ho}}}\right)^{2/5}, \tag{3.60}$$

where $a_{\text{ho}} = \sqrt{\hbar/(m\bar{\omega})}$ is the (geometric mean) harmonic oscillator length. In typical experiments, the BEC chemical potential is $k_B \times 100$'s of nanoKelvin, while the harmonic oscillator energy for trap frequencies of $\bar{\omega} = 2\pi \times 10 - 100$ Hz is $\hbar\bar{\omega}/k_B = 0.5 - 5$ nK. Thus, trapped atomic BECs are well within the limits of the local-density approximation.

Though not discussed here, there is a time-dependent version of the Gross-Pitaevskii equation (equation (3.58) with $\mu \to i\hbar\frac{\partial}{\partial t}$), from which one can derive the spectrum of elemenatary excitations within the BEC. The resulting dispersion relation, describing the so-called Bogoliubov modes, is given by [23]

$$\epsilon(q) = \sqrt{c^2q^2 + \left(\frac{\hbar^2q^2}{2m}\right)^2}, \tag{3.61}$$

where q is the wave vector of the excitation and $c = gn/m$ is the speed of sound in the BEC. For small q, the dispersion is linear and corresponds to phonon modes, while for large q the dispersion smoothly approaches that of a free particle.

3.4.2 Strongly interacting fermions: Overview

With the use of a Feshbach resonance, the s-wave scattering length for a two-component Fermi gas can be tuned with a magnetic field as shown in figure 3.1(b). A crucial part to the utility of Feshbach resonances for studying strongly interacting fermions is the remarkable stability of two-component Fermi gases at and around unitarity where $|a| \to \infty$. In bosonic gases in the vicinity of a Feshbach resonance, three-body inelastic collisions in which a Feshbach molecule and a spectator atom collide to form a deeply bound molecule and release a large amount of kinetic energy are dramatically enhanced. This loss severely limits the ability to observe elastic effects on reasonable timescales in unitary Bose gases. In contrast, in large part because of the Pauli exclusion principle, collisions involving a Feshbach molecule and free atom in two-component Fermi gases are greatly inhibited around unitarity [28, 92, 26], allowing for not only robust studies of strongly interacting Fermi gases in equilibrium, but also very efficient evaporative cooling at the Feshbach resonance.

With well established weakly interacting theories in both the far BEC ($1/k_F a_F \to \infty$) and far BCS ($1/k_F a_F \to -\infty$) limits, trapped quantum gases of fermions with tunable interactions constitute an analog quantum simulator for determining various properties (e.g. thermodynamic quantities and excitation spectra) of interacting many-body systems with arbitrary values of $1/k_F a_F$. This allows for the testing of novel theoretical techniques in regimes where weakly interacting theories break down [9].

With such a pristine testbed for quantum simulation of many-body physics with strong correlations, there are many properties of strongly interacting fermions that one may desire to investigate. Of these, some of the most successful results (and those most relevant to this work) are the measurement of the zero-temperature equation of state (EoS) $n(\mu, a_F)$ of the strongly interacting Fermi gas [80], which determines the thermodynamic properties of the strongly correlated many-body ground state, and that of the finite temperature EoS $n(\mu, T)$ of the unitary Fermi gas (UFG) with $1/k_F a_F = 0$, which includes measuring the critical temperature for the superfluid phase transition [67]. We will discuss the UFG EoS in detail in chapter 8 in the context of performing thermometry of a superfluid Fermi gas of ^{6}Li in our system. In the following section, we will look at the zero-temperature EoS across the BEC-BCS crossover.

3.4.3 Strongly interacting fermions: The zero-temperature equation of state

In this section, we will recount the zero-temperature EoS of a strongly interacting Fermi gas as measured in Navon *et al.* (2010), and follow their notation in doing so. For details regarding the measurement method and analysis, the reader is referred to the original publication [80]. To begin discussing the strongly interacting Fermi gas EoS at zero-temperature, we first focus on the special case of unitarity where $1/k_F a_F = 0$. At unitarity, the only length scale in the problem is given by the interparticle spacing, and usually represented by the inverse Fermi wave vector k_F^{-1}. Thus, like the ideal Fermi gas, the zero-temperature UFG is a scale invariant fluid, and one can show (see for example [113]) that the thermodynamic properties of the UFG are identical to those of the ideal Fermi gas times a universal constant. This universality is typically presented by writing the UFG chemical potential at zero temperature as

$$\mu = \xi E_F, \tag{3.62}$$

where ξ is called the Bertsch parameter, and the quantities μ and E_F are understood to be local quantities (i.e. not defined for a trapped ensemble). From measurements of the finite-temperature UFG EoS, the Bertsch parameter has been measured to be $\xi = 0.37(1)$ [67, 112]. Recalling that $E_F = \hbar^2 k_F^2/(2m)$ and $k_F = (3\pi^2 n)^{1/3}$, we can write the density as

$$n(\mu) = \frac{1}{3\pi^2}\left(\frac{2m\mu}{\xi\hbar^2}\right)^{3/2}. \tag{3.63}$$

By integrating the Gibbs-Duhem relation, $n = (\partial P/\partial\mu)_T$, we find the local pressure of the gas to be

$$P(\mu) = \frac{2}{15\pi^2}\left(\frac{2m}{\hbar^2}\right)^{3/2}\xi^{-3/2}\mu^{5/2} \equiv 2P_0(\mu)\xi^{-3/2}, \tag{3.64}$$

where $P_0(\mu)$ is the pressure of a single-component Fermi gas.

To parametrize the zero-temperature EoS for nonzero values of $1/k_F a_F$, we write the pressure of the interacting gas as [80]

$$P(\mu, a_F) = 2P_0(\tilde{\mu})h(\delta), \tag{3.65}$$

where

$$\tilde{\mu} = \mu + \frac{\hbar^2}{2ma_F^2} \tag{3.66}$$

is the chemical potential without the contribution from the Feshbach molecule binding energy, and

$$\delta = \frac{\hbar}{a_F\sqrt{2m\tilde{\mu}}} \tag{3.67}$$

is a generalization of the parameter $1/k_F a_F$. Subject to the proper constraints in the limits $\delta \to -\infty$ (ideal, non-interacting gas with BCS mean-field correction) and $\delta \to \infty$ (weakly interacting BEC of molecules), as well as $h(0) = \xi^{-3/2}$, the function $h(\delta)$ was measured in [80] using the following parametrization[9]:

$$h(\delta) = \begin{cases} \frac{\delta^2+\alpha_1\delta+\alpha_2}{\delta^2+\alpha_3\delta+\alpha_4} & \delta > 0 \text{ (BEC)} \\ \frac{\beta_1+\beta_2\delta+\beta_3\delta\log(1+\delta)+\beta_4\delta^2+\beta_5\delta^3}{1+\beta_6\delta^6} & \delta < 0 \text{ (BCS)} \end{cases} . \tag{3.68}$$

The function $h(\delta)$ is plotted in figure 3.4(a).

Until this point, we have been discussing the zero-temperature EoS in terms of local variables (i.e. those for a homogeneous gas). However, since we endeavor to apply this EoS to trapped Fermi gases, we need to transform these quantities to those useful for describing experiments in a harmonic trap. Toward this end, we begin by examining the doubly integrated density distribution in the local density approximation where $\mu(\vec{r}) = \mu(0) - \frac{m}{2}(\omega_x^2 x^2 + \omega_y^2 y^2 + \omega_z^2 z^2)$ [80]:

$$\begin{aligned} \bar{n}(z) &= \int dxdy\ n(x,y,z) \\ &= \frac{2}{m\omega_x\omega_y}\int d\tilde{x}d\tilde{y}\ n(\tilde{x},\tilde{y},z) && \left(\tilde{x}_i^2 = \tfrac{m}{2}\omega_i^2 x_i^2\right) \\ &= \frac{4\pi}{m\omega_x\omega_y}\int \tilde{r}d\tilde{r}\ n(\tilde{r},z) && \left(\tilde{r}^2 = \tilde{x}^2+\tilde{y}^2\right) \\ &= \frac{2\pi}{m\omega_x\omega_y}\int_{-\infty}^{\mu(z)} d\mu\ n(\mu) && (d\mu = -2\tilde{r}d\tilde{r}) \\ &= \frac{2\pi}{m\omega_x\omega_y}P(\mu(z)) && \left(n(\mu) = \frac{\partial P}{\partial \mu}\right), \end{aligned} \tag{3.69}$$

where $\mu(z) = \mu(0) - \frac{m}{2}\omega_z^2 z^2$. Now we can enforce the total atom number constraint in the

---

[9] The measured parameter values from [80] are $\alpha_1 = -1.137$, $\alpha_2 = 0.533$, $\alpha_3 = -0.606$, $\alpha_4 = 0.141$, $\beta_1 = 3.78$, $\beta_2 = 8.22$, $\beta_3 = 8.22$, $\beta_4 = -4.21$, $\beta_5 = 3.65$, and $\beta_6 = 0.186$

harmonic trap to determine the chemical potential at the center of the trap $\mu(0)$,

$$\begin{aligned} N &= \int_{-z_0}^{z_0} dz\ \bar{n}(z) \qquad\qquad \left(z_0 = \sqrt{2\mu(0)/(m\omega_z^2)}\right) \\ &= \frac{4\pi}{m\omega_x\omega_y} \int_0^{z_0} dz\ P(\mu(z)) \\ &= \pi\left(\frac{2}{m\bar{\omega}^2}\right)^{3/2} \int_0^{\mu(0)} d\mu\ \frac{P(\mu)}{\sqrt{\mu(0)-\mu}} \\ &= \frac{16}{15\pi}\frac{1}{(\hbar\bar{\omega})^3} \int_0^{\mu(0)} d\mu\ \frac{\mu^2}{\sqrt{\mu(0)/\mu - 1}} h(\delta(\mu)). \end{aligned} \tag{3.70}$$

Then, changing variables from μ to $\delta = \hbar/(a_F\sqrt{2m\mu})$, one can arrive at the following expression for $k_F a_F$ in the trap (i.e. where $k_F = \sqrt{2m\bar{\omega}(3N)^{1/3}/\hbar}$) as a function of the central value $\delta_0 \equiv \hbar/(a_F\sqrt{2m\mu(0)})$:

$$(k_F a_F)^6 = \frac{32}{5\pi}\int_{\delta_0}^{\infty} d\delta\ \frac{h(\delta)}{\delta^7\sqrt{(\delta/\delta_0)^2 - 1}} \qquad \text{for } \delta > 0 \text{ (BEC)} \tag{3.71}$$

and

$$(k_F a_F)^6 = -\frac{32}{5\pi}\int_{-\infty}^{\delta_0} d\delta\ \frac{h(\delta)}{\delta^7\sqrt{(\delta/\delta_0)^2 - 1}} \qquad \text{for } \delta < 0 \text{ (BCS).} \tag{3.72}$$

One can now solve for δ_0 numerically as a function of $1/k_F a_F$, as is shown in figure 3.4(b). Because $\delta_0(1/k_F a_F = 0) = 0$, we can write the function as

$$\delta_0\left(\frac{1}{k_F a_F}\right) = b_1\left(\frac{1}{k_F a_F}\right) + b_2\left(\frac{1}{k_F a_F}\right)^2 + ... \tag{3.73}$$

As an application of this equation, let us solve for the Fermi wave vector $k_F^0 = (3\pi^2 n(0))^{1/3}$ at the center of the trapped cloud as a function of a_F and the trapped Fermi wave vector k_F defined above. Using the Gibbs-Duhem relation, one can show

$$k_F^0 = k_F g\left(\frac{1}{k_F a_F}\right), \tag{3.74}$$

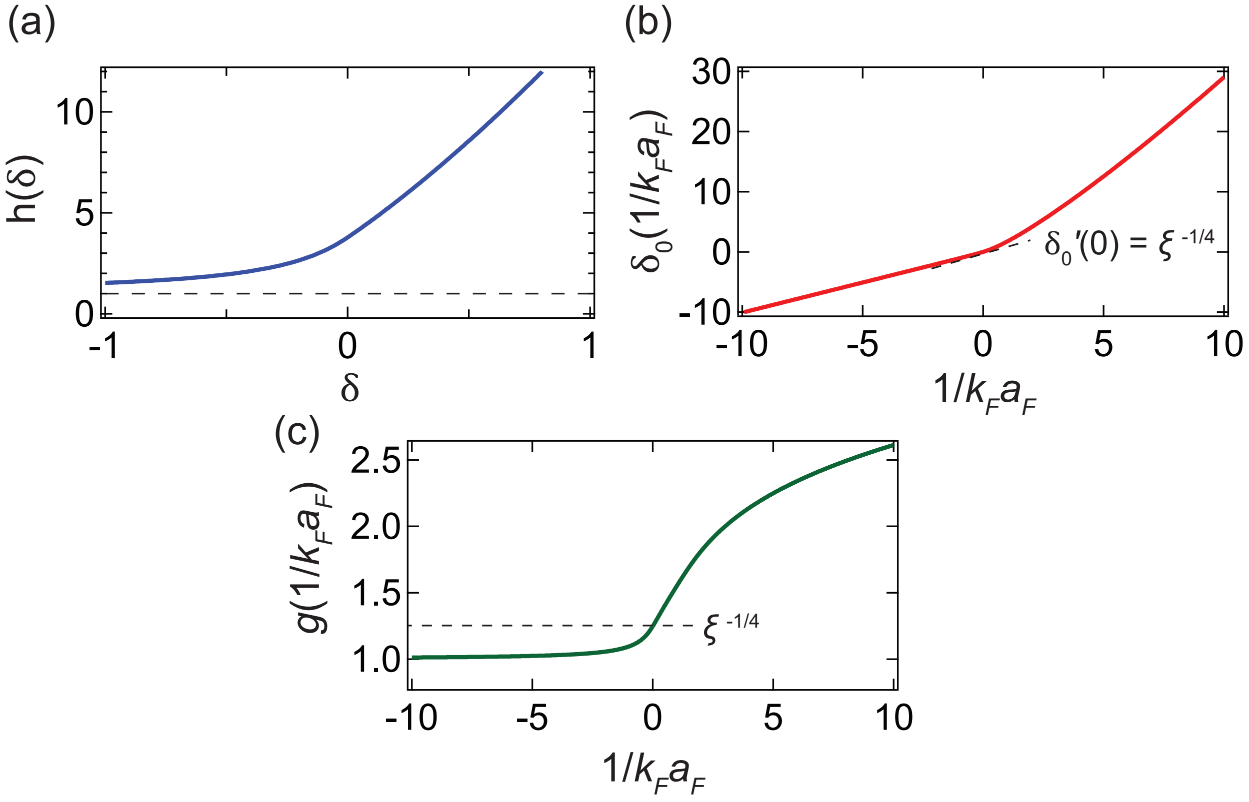

Figure 3.4: Zero-temperature equation of state for the strongly interacting two-component Fermi gas. (a) Pressure normalized to that of the non-interacting Fermi gas. $\delta > 0$ corresponds to the BCS side and $\delta < 0$ to the BEC side of unitarity ($\delta = 0$). (b) Value of $\delta(\mu) = \hbar/(a_F\sqrt{2m\mu})$ at the center of the harmonic trap, with associated chemical potential $\mu(0)$. (c) Ratio of the interacting to non-interacting Fermi wave vector $g(1/k_F a_F) = k_F^0/k_F$ across the crossover. At resonance, $g(0) = \xi^{-1/4}$.

where

$$g\left(\frac{1}{k_F a_F}\right) = (\delta_0 k_F a_F)^{-1} \left(h(\delta_0) - \frac{\delta_0}{5}\frac{\partial h}{\partial \delta}\bigg|_{\delta_0}\right)^{1/3}. \tag{3.75}$$

Thus, the function $\delta_0(1/k_F a_F)$ gives us a way to convert between the Fermi wave vector for the non-interacting gas (k_F) and that for the strongly interacting gas (k_F^0) for any value of $1/k_F a_F$, as shown in figure 3.4(c).

For the UFG, using the local density approximation $\mu(\vec{r}) = \mu(0) - \frac{m}{2}\sum_i \omega_i^2 x_i^2$ and integrating $n(\mu(\vec{r}))$ from equation (3.63) over all space, one can show that $\mu(0) = \sqrt{\xi} E_F$, where $E_F = \hbar\bar{\omega}(3N)^{1/3}$. Therefore, we find that the ratio of the peak density of the unitary Fermi gas to that of the non-interacting gas is $n(\sqrt{\xi}E_F)/n(E_F) = \xi^{-3/4}$, and the ratio of Fermi wave vectors $g(0) = k_F^0/k_F = (n(\sqrt{\xi}E_F)/n(E_F))^{1/3} = \xi^{-1/4}$. Thus, since we know $h(0) = \xi^{-3/2}$, it follows that

$$\lim_{1/k_F a_F \to 0} (\delta_0 k_F a_F)^{-1} = \xi^{1/4} \quad \Rightarrow \quad b_1 = \xi^{-1/4}. \tag{3.76}$$

Indeed, computing $\delta_0'(0)$ with the numerical solution to equation (3.73) agrees with the result $b_1 = \xi^{-1/4}$.

Chapter 4

LITHIUM AND YTTERBIUM

The choice of combining ytterbium and lithium for an ultracold quantum gas mixture experiment was made for a variety of reasons, including exciting potential applications in mass-mismatched fundamental few-body physics, paramagnetic dipolar ultracold molecules, and impurity studies using a bosonic probe (^{174}Yb) inside of a large Fermi superfluid (^{6}Li). In this chapter, we outline some of the basic properties of these two elements, as well as some of the experimental techniques used in our lab to leverage the specific internal structure of Yb and Li for various purposes, focusing on new additions to our experimental toolkit. For a complete discussion of laser cooling, trapping, and absorption imaging of lithium and ytterbium in our apparatus, the reader is referred to the theses of Anders Hansen [42] and Alex Khramov [61]. While an important feature of ytterbium is the availability of many different bosonic and fermionic isotopes in natural abundance, which are also easily trapped with the same laser systems, the work presented in this thesis deals almost entirely with the bosonic ^{174}Yb isotope, with the exception of brief photoassociation studies of ^{172}Yb and ^{176}Yb in combination with ^{6}Li to detect the shift of excited state molecular resonances due to a changing reduced mass. Therefore, we only focus in this chapter on the properties of the 174 isotope.

4.1 Atomic properties

Some of the most important degrees of freedom in ultracold atomic gas systems are the internal states described by the atomic energy level structure, which can be precisely manipulated with external fields. To begin our background discussion of the internal states of ^{174}Yb and ^{6}Li, we look at their low-lying electronic energy level structures, and then discuss the Zeeman spectrum of the ^{6}Li $F = 1/2$ and $F = 3/2$ hyperfine states in the electronic ground state.

4.1.1 Energy level structure

The electronic energy level structures for ^{6}Li and ^{174}Yb are shown in figure 4.1, where we only include those states relevant to our experiment. In Li, all laser cooling and absorption imaging utilize the $^2S_{1/2} \rightarrow {}^2P_{3/2}$ and $^2S_{1/2} \rightarrow {}^2P_{1/2}$ transitions, often referred to as the D_2 and D_1 lines, respectively. The nuclear spin of $I = 1$ in ^{6}Li splits each fine structure level into a set of hyperfine states. Because of the modest hyperfine splitting in the ground state of 228 MHz, laser cooling on the $F = 3/2$ D_2 line and repumping on the $F = 1/2$ D_2 line can be performed with a single laser source shifted by an AOM to access both hyperfine states. Furthermore, because the hyperfine structure in the $^2P_{3/2}$ state is unresolved on the scale of the natural linewidth $\Gamma/2\pi = 5.9$ MHz, the pumping of atoms into the lower $F = 1/2$ hyperfine state is considerable, requiring 6 repumping beams with appreciable intensity. Additionally, the unresolved hyperfine structure in the excited state renders standard sub-Doppler cooling techniques infeasible. Later in this section, however, we will discuss the implementation of so-called “gray molasses”, or “D_1 cooling” of Li below the Doppler temperature of $\hbar\Gamma/(2k_B) = 140$ μK.

The energy level structure of Yb is in many ways more rich, as is shown in figure 4.1(b). Due to the large atomic number $Z = 70$, the exchange interaction in the $6s6p$ configuration is quite large, resulting in a large difference between the two most commonly used Yb wavelengths of $\lambda = 399$ nm ($^1S_0 \rightarrow {}^1P_1$) and $\lambda = 556$ nm ($^1S_0 \rightarrow {}^3P_1$). Because the bosonic isotopes of Yb have zero nuclear spin, $I = 0$, there is no hyperfine substructure. In principle, the transition to $^3P_1$ is forbidden due to the necessity of changing the electron spin from $S = 0$ to $S = 1$. However, due to the strong fine structure interaction in the excited state, there is an admixture of the $^1P_1$ state, resulting in a dipole allowed transition to $^3P_1$ with a narrow linewidth of $\Gamma/2\pi = 180$ kHz. This type of transition is referred to as an intercombination line. Due to the low Doppler temperature associated with the $^3P_1$ transition of 4.5

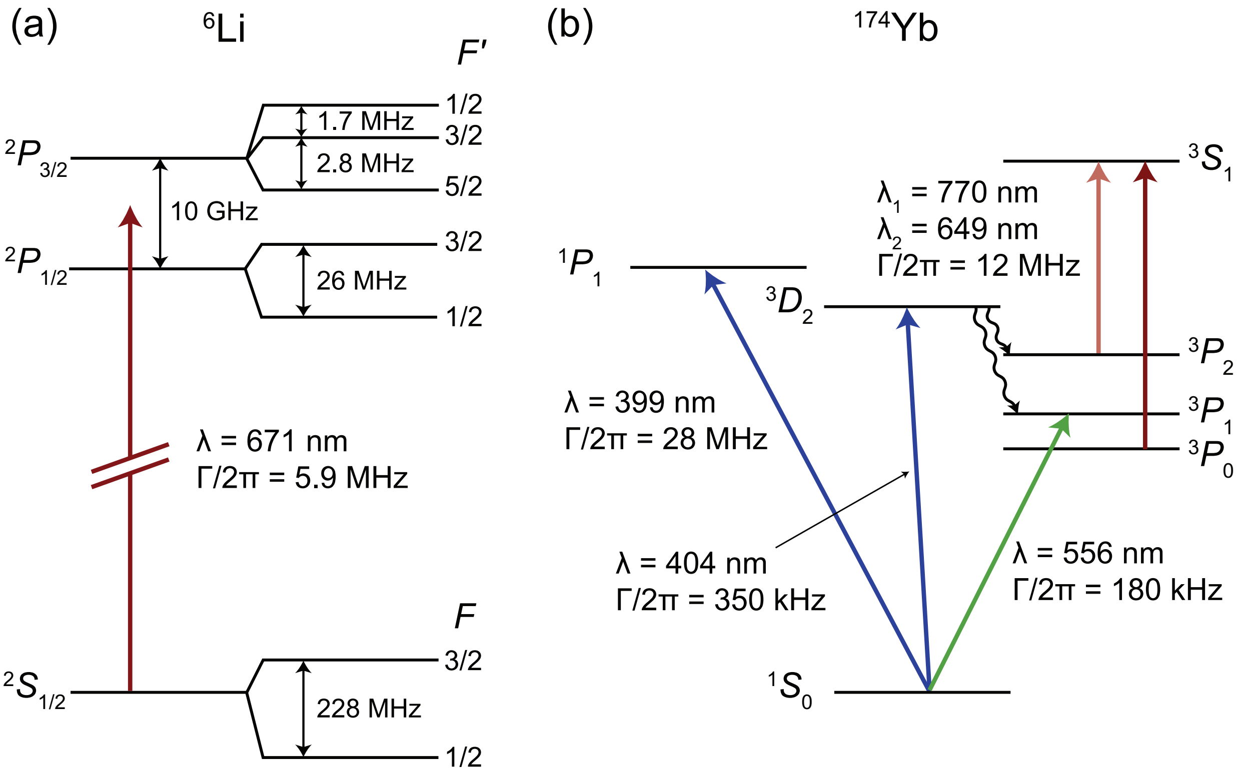

Figure 4.1: Energy level structure for (a) Li and (b) Yb including experimentally relevant states. The nuclear spin of $I = 1$ in ^{6}Li leads to depicted hyperfine substructure of each fine structure level. In Yb, the primary transitions used in the experiment are the broad dipole transition at $\lambda = 399$ nm for Zeeman slowing and absorption imaging, and the narrow intercombination line at $\lambda = 556$ nm for magneto-optical trapping. Additionally, we utilize the electric quadrupole transition from $^1S_0 \rightarrow {}^3D_2$ at $\lambda = 404$ nm in order to populate the metastable $^3P_2$ state via spontaneous emission from $^3D_2$. The metastable state is subsequently detected by pumping back to the ground state using the $^3P_2 \rightarrow {}^3S_1$ transition at $\lambda = 770$ nm, and repumping the atoms lost to $^3P_0$ after spontaneous decay using the $^3P_0 \rightarrow {}^3S_1$ transition at $\lambda = 649$ nm. The configurations of the two valence electrons in Yb for the levels $(^1S_0, ^1P_1, ^3P_J, ^3D_2, ^3S_1)$ are $(6s^2, 6s6p, 6s6p, 5d6s, 6s7s)$.

μK, this line is particularly useful for magneto-optical trapping. The broad transition from $^1S_0$ to $^1P_1$ at $\lambda = 399$ nm with $\Gamma/\pi = 28$ MHz allows for efficient Zeeman slowing, and is also used for absorption imaging.

In addition to the dipole allowed transitions from the $^1S_0$ ground state, Yb features additional optical transitions with very narrow linewidths. Indeed, the $^1S_0 \rightarrow {}^3P_0$ transition in the fermionic isotope ^{171}Yb with a natural linewidth of $\Gamma/2\pi = 10$ mHz is now commonly used in some of the world's most precise atomic clocks [69]. Another state of interest for ultracold atom experiments is the relatively long-lived $^3P_2$ metastable state, which features large angular momentum and the potential for anisotropic, tunable interactions. In our system, we have studied inelastic collisional behavior between this metastable state of ytterbium with itself as well as with ground state ^{6}Li over a range of magnetic fields (see chapter 5). Later in this chapter, we will detail our method for populating and detecting $^3P_2$ ytterbium, which involves utilizing both the $^3D_2$ and $^3S_1$ states.

4.1.2 ^{6}Li hyperfine structure in the $^2S_{1/2}$ ground state

The spectrum of magnetic sublevels in the ground $^2S_{1/2}$ state of ^{6}Li at finite magnetic field is shown in figure 4.2. The states $\{|1\rangle,|2\rangle,|3\rangle,|4\rangle,|5\rangle,|6\rangle\}$ connect at zero field to the $|F, m_F\rangle$ hyperfine eigenstates $\{|\frac{1}{2},\frac{1}{2}\rangle, |\frac{1}{2},-\frac{1}{2}\rangle, |\frac{3}{2},-\frac{3}{2}\rangle, |\frac{3}{2},-\frac{1}{2}\rangle, |\frac{3}{2},\frac{1}{2}\rangle, |\frac{3}{2},\frac{3}{2}\rangle\}$, and at high field asymptotically to the $|m_S, m_I\rangle$ eigenstates $\{|-\frac{1}{2},1\rangle, |-\frac{1}{2},0\rangle, |-\frac{1}{2},-1\rangle, |\frac{1}{2},-1\rangle, |\frac{1}{2},0\rangle, |\frac{1}{2},1\rangle\}$. In our system, we primarily work with the two lowest hyperfine states $|1\rangle$ and $|2\rangle$, as there is no inelastic decay due to spin relaxation in this mixture, and because there exists a broad Feshbach resonance centered at 832 G with which one can study strongly interacting fermions and Fermi superfluidity, as discussed in chapter 3.4.

Figure 4.2(b) shows the s-wave scattering length between states $|1\rangle$ and $|2\rangle$ as a function of magnetic field. The scattering length between these states at zero field is nearly zero. Thus, to perform evaporative cooling in a mixture of $|1\rangle$ and $|2\rangle$, we often ramp the magnetic field to ≈ 300 G, where the scattering length is large and negative ($\approx -290\ a_0$). For higher magnetic fields but below the Feshbach resonance position, there is enhanced inelastic loss

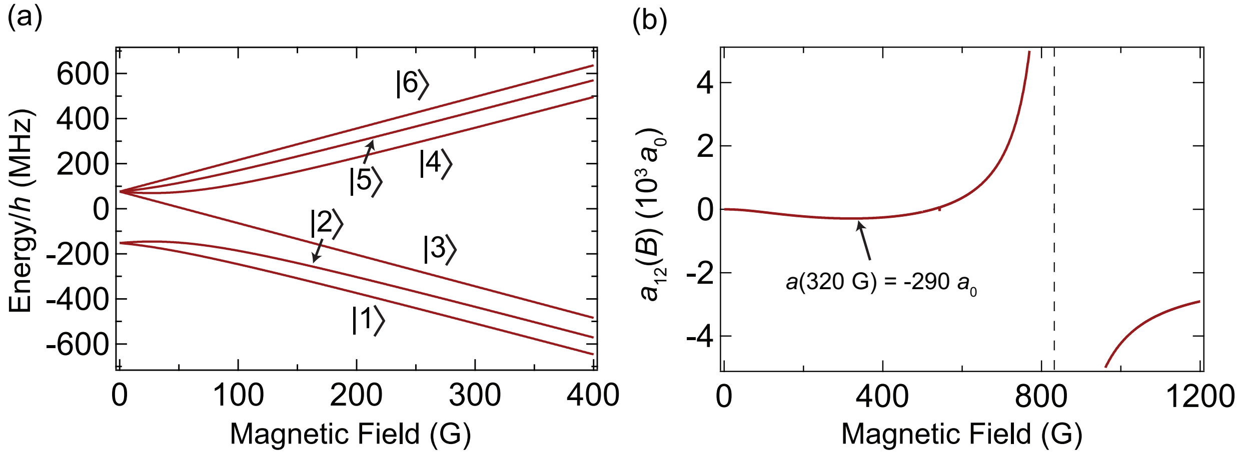

Figure 4.2: (a) Energy spectrum versus magnetic field of the magnetic sublevels of the $^2S_{1/2}$ $F = 1/2$ and $F = 3/2$ hyperfine manifold. At high fields, where F is no longer a valid quantum number, the states approach pure $|m_S, m_I\rangle$ eigenstates, where $m_S = -1/2(+1/2)$ for the lower(upper) three states, and the shift between states of the same slope is the remaining perturbation from the hyperfine interaction. (b) s-wave scattering length $a_{12}(B)$ between states $|1\rangle$ and $|2\rangle$ as a function of magnetic field (units of 10^3 a_0). The broad Feshbach resonance centered at 832 G makes this an ideal system to study strongly interacting fermions.

due to atom-molecule collisions, which causes severe heating of the cloud. Thus, to achieve large atom number clouds at unitarity (832 G), we perform a magnetic field sweep from low field to the resonance position with only a single spin state of Li present, and subsequently prepare a spin mixture using an RF pulse.

4.1.3 RF spectroscopy of Li

Upon loading Li from the compressed MOT into the ODT, we optically pump all atoms out of the $F = 3/2$ state and into the $F = 1/2$ state to avoid the fast inelastic decay from spin relaxation that would otherwise result. Thus, we always begin an experimental cycle with a

50:50 spin mixture of states $|1\rangle$ and $|2\rangle$. In many circumstances, it is desirable to work with just a single spin state of Li. These situations include experiments that necessitate magnetic field sweeps across the lossy region of the magnetic Feshbach resonance in figure 4.2(b), and for our experiments with a single spin state of metastable $^3P_2$ Yb. Furthermore, once we have a spin pure ensemble of Li atoms, we can perform coherent manipulation of the internal state using RF pulses.

To remove either state $|1\rangle$ or $|2\rangle$, we simply apply light resonant with the D_2 ($^2S_{1/2}$, $m_J = -1/2 \rightarrow {}^2P_{3/2}$, $m_J = -3/2$) transition at a high field, ensuring both frequency selectivity between the two states, as well as decoupling of the nuclear spin degree of freedom from the electronic degrees of freedom resulting in a perfect cycling transition. This is the same technique we use to achieve state-selective absorption imaging. With a gas of Li atoms in a single spin state, we can then apply an RF magnetic field to couple states with $\Delta m_F = 0, \pm 1$[1].

Figure 4.3(a) shows a typical RF resonance spectrum between states $|1\rangle$ and $|2\rangle$ at the position of the Feshbach resonance $B = 832$ G. For this particular spectrum, the RF power was 1 Watt, and the exposure time 1 ms. The resonance frequency at this field is $f_0 = 76.276$ MHz. The fitted full width at half maximum (FWHM) is 900 Hz (from a Gaussian fit returning a $1/e^{1/2}$ radius of 380 Hz), which is consistent with the Fourier-transform-limited width for a 1 ms exposure.

Additionally, we can perform Rabi oscillations between states $|1\rangle$ and $|2\rangle$, as shown in figure 4.3(b), performed again at 832 G. For this particular measurement, we use 2 Watts of RF power at the resonance frequency f_0 found in 4.3(a). The $1/e$ decay time for these Rabi oscillations is $\tau = 15$ ms, and the Rabi frequency $\Omega_{12}/h = 430$ Hz. If we perform the same measurement with 1 Watt of RF power, the observed Rabi frequency is 300 Hz, consistent with the expected reduction by a factor of $\sqrt{2}$. It is important to note that

---

[1] Note that although these RF manipulations occur at a large field where F is no longer a valid quantum number, the projection of the total angular momentum $m_F = m_S + m_L + m_J$ onto the magnetic field axis is a valid quantum number, and obeys the selection rule for magnetic dipole transitions $\Delta m_F = 0, \pm 1$.

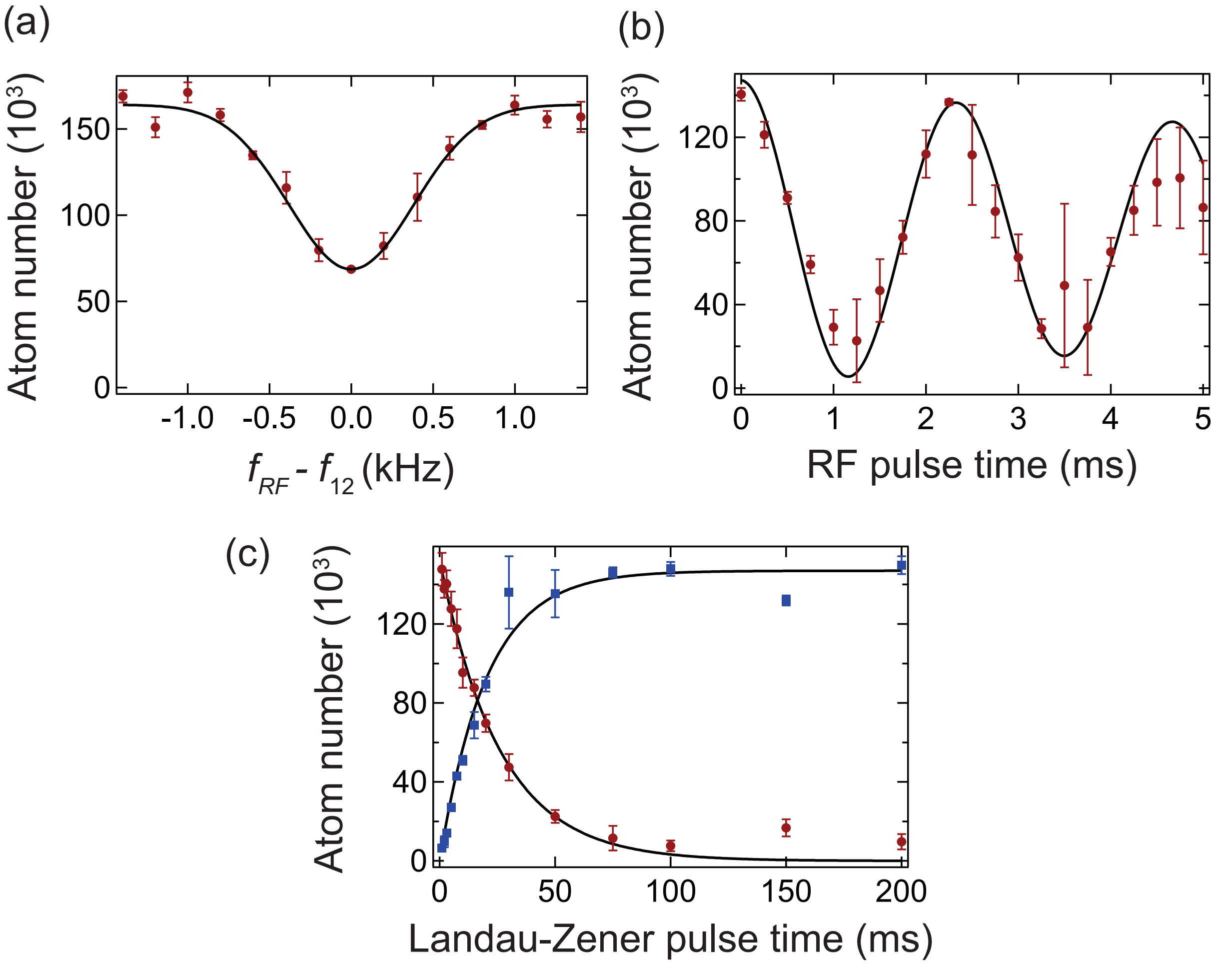

Figure 4.3: RF manipulation of Li states $|1\rangle$ and $|2\rangle$. (a) RF resonance spectrum at $B = 832$ G. We show the atom number remaining in state $|1\rangle$ after the application of a 1 ms, 1 Watt RF pulse. The extracted FWHM of 900 Hz is consistent with that expected from the Fourier-transform-limit. (b) Rabi oscillations between $|1\rangle$ and $|2\rangle$ (state $|1\rangle$ atom number shown). The fit returns a Rabi frequency of 430 Hz, and $1/e$ decay time of 15 ms. (c) Landau-Zener transfer from state $|1\rangle$ (red circles) to $|2\rangle$ (blue squares). Fits return a $1/e$ timescale of 20 ms for a 1 Watt RF pulse with a 50 kHz wide sweep.

the ability to resolve multiple Rabi oscillations in our system is restricted to being in the high-field regime of the Li Breit-Rabi spectrum (figure 4.2(a)). At lower fields, there is a large variation of the resonance frequency f_{12} with magnetic field, with the result that magnetic field inhomogeneities quickly lead to decoherence. In fact, assuming variations in the magnetic field are proportional to B (which is usually the case), the decoherence rate scales as $\frac{\partial f_{12}}{\partial B} \times B$, which has its maximum around 60 G [40].

While it is straightforward to use a $\pi/2$ pulse with fixed RF frequency to prepare the superposition state $(|1\rangle + |2\rangle)/\sqrt{2}$, we find the preparation of this state to be much more reliable using a Landau-Zener sweep, like that shown in figure 4.3(c). This is because slight variations of the magnetic field at the position of the atoms are inevitable on the timescale of days to weeks, and would require us to relocate the center position of the $|1\rangle - |2\rangle$ resonance often. With the Landau-Zener transfer, we can choose a large sweep window approximately centered on the resonance position that is insensitive to these small changes in magnetic field. Typical Landau-Zener pulse times for creating the superposition state $(|1\rangle + |2\rangle)/\sqrt{2}$ are 5-20 ms, using 1-2 Watts and frequency sweep ranges of 10-50 kHz.

4.2 Optical Trapping of Yb and Li

Because of the vastly different mass and electronic structure of Yb and Li, their optical confinement properties are quite different, and the range of wavelengths usable to trap both species restricted. Indeed, many groups working with Yb only choose to operate their ODT at 532 nm, as the polarizability of Yb is large and high powers are readily available in commercial laser systems. However, since Li is untrapped at 532 nm, the logical choice for simultaneous optical trapping of both species is to operate the ODT at 1064 nm, where it is again easy to find high power commercial laser systems.

4.2.1 Optical trapping at 1064 nm

Using equation (2.5) for the dipole potential $V_{\text{dip}}(\vec{r}) = -\alpha(\lambda_L)I(\vec{r})/(2\epsilon_0 c)$, one can find the polarizabilities for Li and Yb with a trapping laser wavelength of $\lambda_L = 1064$ nm to be:

$$\frac{\alpha(\lambda_L = 1064 \text{ nm})}{2\epsilon_0 c} = \begin{cases} 8.4 \times 10^{-37} \text{ m}^2\text{s} & \text{Li} \\ 3.7 \times 10^{-37} \text{ m}^2\text{s} & \text{Yb} \end{cases} . \tag{4.1}$$

Thus, we see that the ratio of the trap depth for Li to that of Yb is $\alpha_{\text{Li}}/\alpha_{\text{Yb}} \approx 2.3$. This has the consequence that, when performing evaporative cooling of Yb with both species in the trap, Li is sympathetically cooled and maintains a very large value of $\eta_{\text{Li}} = (V_0/k_B T)_{\text{Li}} \approx (\alpha_{\text{Li}}/\alpha_{\text{Yb}})(V_0/k_B T)_{\text{Yb}} \approx 2.3 \times 10$. Indeed, whether Li is prepared as a collisionless ideal gas or as a $|1\rangle$-$|2\rangle$ spin mixture with a large scattering length (e.g. at 300 G), we do not observe much loss of Li over the course of sympathetic evaporative cooling to quantum degeneracy.

From the values in equation (4.1), we find the following ratio of trap frequencies for Li and Yb:

$$\frac{\omega_{\text{Li}}}{\omega_{\text{Yb}}} = \sqrt{\frac{\alpha_{\text{Li}}}{\alpha_{\text{Yb}}}\frac{m_{\text{Yb}}}{m_{\text{Li}}}} \approx 8. \tag{4.2}$$

This has the fortunate consequence that the degeneracy temperatures for the two species have the scaling

$$\frac{T_F}{T_{C,\text{Yb}}} = \frac{\hbar\bar{\omega}_{\text{Li}}(3N_{\text{Li}})^{1/3}}{0.94\hbar\bar{\omega}_{\text{Yb}}N_{\text{Yb}}^{1/3}} \approx 12\left(\frac{N_{\text{Li}}}{N_{\text{Yb}}}\right)^{1/3} . \tag{4.3}$$

Therefore, in our typical situation of a large bath of Yb cooling a smaller cloud of Li, Yb remains a thermal cloud and can cool Li far below the Fermi temperature before crossing the BEC transition (and thus becoming a weaker cooling bath). Another consequence of the scalings in equations (4.2) and (4.3) is that there is an interesting possibility to use Yb as an impurity thermometer of a deeply degenerate, strongly interacting Li Fermi gas, which is a notoriously difficult regime in which to perform thermometry.

4.2.2 Controlling interspecies overlap with a magnetic field gradient

While the large mass mismatch between Yb and Li offers exciting possibilities to study novel few-body physics, it presents a technical challenge due to the large resulting differential gravitational sag. In the linear regime, the gravitational sag from the minimum of the optical potential is $\Delta y = g/\omega_y^2$, with the end result that at low optical depths, the two clouds completely separate, making sympathetic cooling and interaction studies difficult in this regime. Fortunately, we can utilize the different internal structures of Yb and Li to mitigate this effect by imposing a linear potential on Li only using a magnetic field gradient $B' = \partial B/\partial y$ in the vertical bias field direction. The resulting potential is

$$\begin{aligned} V_{\mathrm{Li}}(\vec{r}) &= \frac{\alpha_{\mathrm{Li}} I(\vec{r})}{2\epsilon_0 c} + m_{\mathrm{Li}} g y + \mu B' y \\ &= \frac{\alpha_{\mathrm{Li}}}{\alpha_{\mathrm{Yb}}} \left[\frac{\alpha_{\mathrm{Yb}} I(\vec{r})}{2\epsilon_0 c} + \frac{\alpha_{\mathrm{Yb}}}{\alpha_{\mathrm{Li}}} \left(m_{\mathrm{Li}} g y + \mu B' y \right) \right]. \end{aligned} \tag{4.4}$$

Therefore, if we choose a gradient such that $(\alpha_{\mathrm{Yb}}/\alpha_{\mathrm{Li}})(m_{\mathrm{Li}} g + \mu B'_{\mathrm{overlap}}) = m_{\mathrm{Yb}} g$, the Li potential takes the form

$$V_{\mathrm{Li}}(\vec{r}) = \frac{\alpha_{\mathrm{Li}}}{\alpha_{\mathrm{Yb}}} V_{\mathrm{Yb}}(\vec{r}), \tag{4.5}$$

and the two cloud centers will be perfectly overlapped. The corresponding optimal magnetic field gradient is

$$B'_{\mathrm{overlap}} = \frac{\alpha_{\mathrm{Li}}}{\alpha_{\mathrm{Yb}}} \frac{m_{\mathrm{Yb}} g}{\mu_B} \left(1 - \frac{\alpha_{\mathrm{Yb}} m_{\mathrm{Li}}}{\alpha_{\mathrm{Li}} m_{\mathrm{Yb}}} \right) = 68 \text{ G/cm}, \tag{4.6}$$

where we've used $\mu/h = \mu_B/h = 1.4$ MHz/G for states $|1\rangle$ and $|2\rangle$ of Li at high field.

As we'll see in chapter 8, there is an important technical limitation to using the magnetic field gradient to tune interspecies spatial overlap. Especially in situations with tight vertical confinement, but weak confinement in the horizontal plane, any relative misalignments of the directions of the forces of gravity and the magnetic field gradient can lead to large differential displacements of the clouds in the horizontal plane.

4.2.3 One-dimensional optical lattice implementation

An optical lattice at 1064 nm is a necessary tool for many future experiments with Li-Yb mixtures and molecules. During my time in the lab, we demonstrated one dimension of what will eventually become a three-dimensional optical lattice for quantum simulation studies.

The lattice light is derived from the combination of a home built external cavity diode laser (ECDL) setup and a commercial 50 W single frequency fiber amplifier (Nufern NUA-1064-PD-0050-D0). After the ECDL seed light is sent through a polarizing beam splitting cube and coupled into a polarization maintaining optical fiber, there is typically about 70 mW of 1062-1067 nm light entering the fiber amplifier, which can be easily amplified up to 50 W. The ECDL master laser spectrum is continuously monitored on a scanning Fabry-Perot cavity to ensure that its operation is single mode. Following the fiber amplifier is a high power isolator (Thorlabs IO-5-1064-HP) and various half-wave plates (CVI QWPM-1064-10-2), polarizing beam splitters (CVI TFPN-1064-PW-1025-UV) and AOMs (Intraaction ATM-2004DA6) for controlling the frequencies and powers of the individual axes of the lattice. The prepared lattice beams are then coupled into polarization maintaining fibers[2] and ported over to the main experiment where an intensity feedback scheme is implemented using a photodiode and the respective AOM.

In order to demonstrate the first dimension of what will be a three-dimensional optical lattice, we began by implementing the vertical axis of the lattice. Each lattice beam must be combined with an existing MOT beam path using two dichroic mirrors on either side of the main chamber, focused onto the position of the atoms, and then retro-reflected to form the standing wave. For the first dimension, we chose a beam waist of 100 μm and performed experiments with Yb. We initially aligned the lattice beam using a CCD camera

---

[2] For the lattice fibers, we began by using a standard 980 nm 6/125 PM fiber patchcord from Oz Optics (PMJ-A3HPC,A3HPC-1064-6/125-3AS-8-1) terminated with a high power air gap connector to allow for higher output powers. Unfortunately, we burned the high power connector on one of these fibers when attempting to couple in more than 5 W for a standard traveling-wave optical trapping application. For replacements, our plan is to keep the power somewhat lower and use a cheaper PM fiber from Thorlabs (PM980-XP).

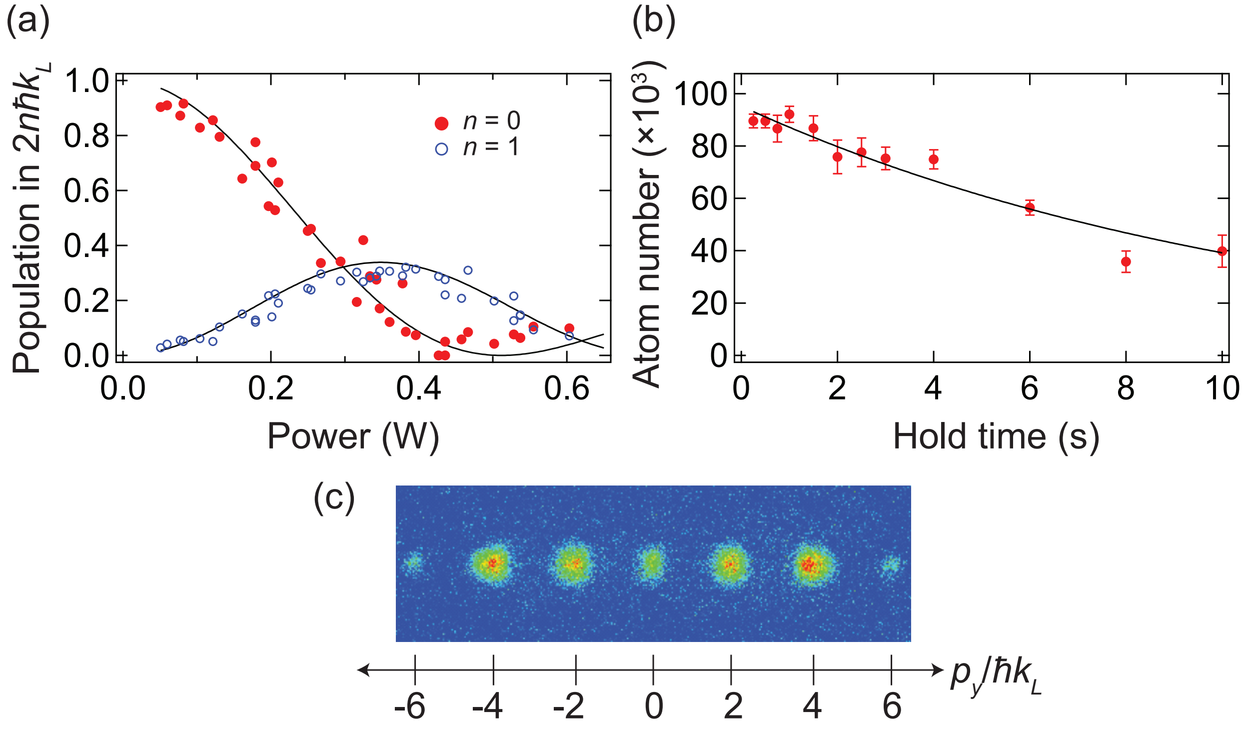

Figure 4.4: Implementing a one-dimensional optical lattice at 1064 nm. (a) Kaptiza-Dirac diffraction (as shown in part (c)) to calibrate the lattice beam alignments. We vary the power per beam P with a fixed square pulse time $\tau = 8.6$ μs, and detect the transfer of population from the $p = 0$ to $p = 2n\hbar k_L$ momentum state in the limit of small transfer, where $k_L = 2\pi/\lambda_L$, and $\lambda_L = 1064$ nm. This data is then fit (black lines) to the functions $[J_n(\beta P)]^2$ to extract $\beta = 2V_0\tau/(\hbar P)$, where V_0 is the Stark shift from a single beam. (b) Lifetime of Yb in a 1D optical lattice with depth parameter $s = 4V_0/E_R = 37$ and power per beam $P = 0.2$ W, where E_R is the recoil energy for a single lattice photon. From an exponential fit to the data with no vertical offset, we find a $1/e$ decay time of 11.3 ± 0.8 s. (c) Absorption image taken after a Kapitza-Dirac diffraction pulse populating many momentum states.

imaging setup focused on the atom cloud. The lattice beam focus was then positioned onto the Yb cloud location on the camera, and subsequently varied to maximize the effect of the Stark shift and then center the beam on the Yb cloud. The initial alignment of the retro-reflected beam was accomplished by coupling the light back into the optical fiber, and was then optimized by performing Kapitza-Dirac diffraction of an Yb BEC (see figure 4.4(a)). For a Kapitza-Dirac square-shaped pulse of duration τ, the relative population transferred to the $2n\hbar k_L$ momentum state is given by $[J_n(\theta)]^2$, where J_n is the n^{th} Bessel function of the first kind, and $\theta = 2V_0\tau/\hbar$, where V_0 is the Stark shift from a single pass of the optical lattice beam (i.e. the full lattice depth is $4V_0$). For a pure BEC the initial state is entirely $n = 0$. For the measurements in figure 4.4(a), where we fix the duration $\tau = 8.6$ μs and vary the power per beam P, we fit to the functions $[J_n(\beta P)]^2$ for $n = 0$ and $n = 1$ in the limit of small population transfer. From this we find $\beta = 5.0 \pm 0.1$ W^{-1}.

After calibrating the beam alignments, we measured the lifetime of the Yb BEC in the lattice with very little confinement from the ODT[3]. The result is shown in figure 4.4(b) for a lattice power of 200 mW per beam. From the calibration in figure 4.4(a), we find that this power corresponds to a lattice depth parameter of $s = 4V_0/E_R = 2\beta P\hbar/(E_R\tau) = 37$, where $E_R = \hbar^2k_L^2/2m$ is the single photon lattice recoil. The fitted $1/e$ decay time of 11.3 ± 0.8 s at this large lattice depth is encouraging for future quantum simulation experiments in a full three-dimensional optical lattice.

4.3 Metastable $^3P_2$ Yb

As discussed in section 1.2, it became clear early on in my time in the group that realizing magnetically tunable interactions between Li and Yb would require searching in a combination of ground state Li and metastable $^3P_2$ Yb (Yb*). To this end, we opted to prepare this state in Yb by an indirect pumping scheme, which is depicted in figure 4.1(b). First, $^1S_0$ Yb atoms are excited by a laser at 404 nm to the $^3D_2$ state, from which they decay

---

[3] The ODT power was set to about 100 mW, which would in the absence of the lattice would be too little power to suspend the Yb atoms against gravity.

to $^3P_2$ (branching ratio of 12%) and $^3P_1$ (branching ratio of 88%). We decided on this indirect excitation scheme as opposed to the direct $^1S_0 \to {}^3P_2$ excitation because the latter is a magnetic dipole transition requiring clock-level stability of the excitation laser, while the $^3D_2$ transition is electric quadrupole, and thus considerably easier to drive. For more information about the 404 nm laser stabilization and details of the excitation scheme, the reader is referred to the thesis of Alex Khramov [61].

Since the eventual goal was to locate Feshbach resonances by performing inelastic loss spectroscopy of Yb* in the presence of Li as a function of magnetic field, we desired to prepare a spin pure ensemble of Yb*. In order to do so, we began by selectively exciting Yb to the $m_J = -2$ state of $^3D_2$, from which it decays to both $m_J = -1$ and $m_J = -2$ in $^3P_2$. Then, we exploited the different polarizabilities and magnetic moments of these two states to selectively spill the $m_J = -2$ state from the trap with a strong magnetic field gradient. As shown in figure 4.5(b), for crossed orientations of the bias magnetic field and ODT electric field, the $m_J = -2$ state is weakly trapped at $\lambda_L = 1064$ nm, making it simple to spill these atoms without affecting the $m_J = -1$ atoms.

With a spin pure sample of $m_J = -1$ Yb* atoms, we could then proceed to prepare other spin states using RF Landau-Zener transfer (figure 4.6(a)). Figure 4.5(a) shows measurements of the polarizability of the $m_J = 0, -1$, and -2 states of Yb* by diabatic trap squeezing. After suddenly changing the trapping laser power, the atoms begin executing a quadrupolar breathing mode. Furthermore, since we already know the polarizability of the $^1S_0$ state at 1064 nm, simply measuring the breathing frequencies of the Yb* states relative to $^1S_0$ gives us their absolute polarizabilities.

Measurements of the stability of a mixture of Li $|1\rangle$ and $m_J = -1$ Yb* at low magnetic field ($B = 12$ G) are shown in figure 4.6(b). The lifetime measurements are consistent with no loss of Li, and reveal a two-body inelastic rate coefficient for Yb*-Yb* collisions of $K_2 = 2.5 \times 10^{-11}$ cm^{3}s^{-1}. In chapter 5, we will discuss experiments in which we extend these measurements of interspecies inelastic behavior over a wide range of magnetic field values.

While the purification scheme used here in principle allows us to perform experiments

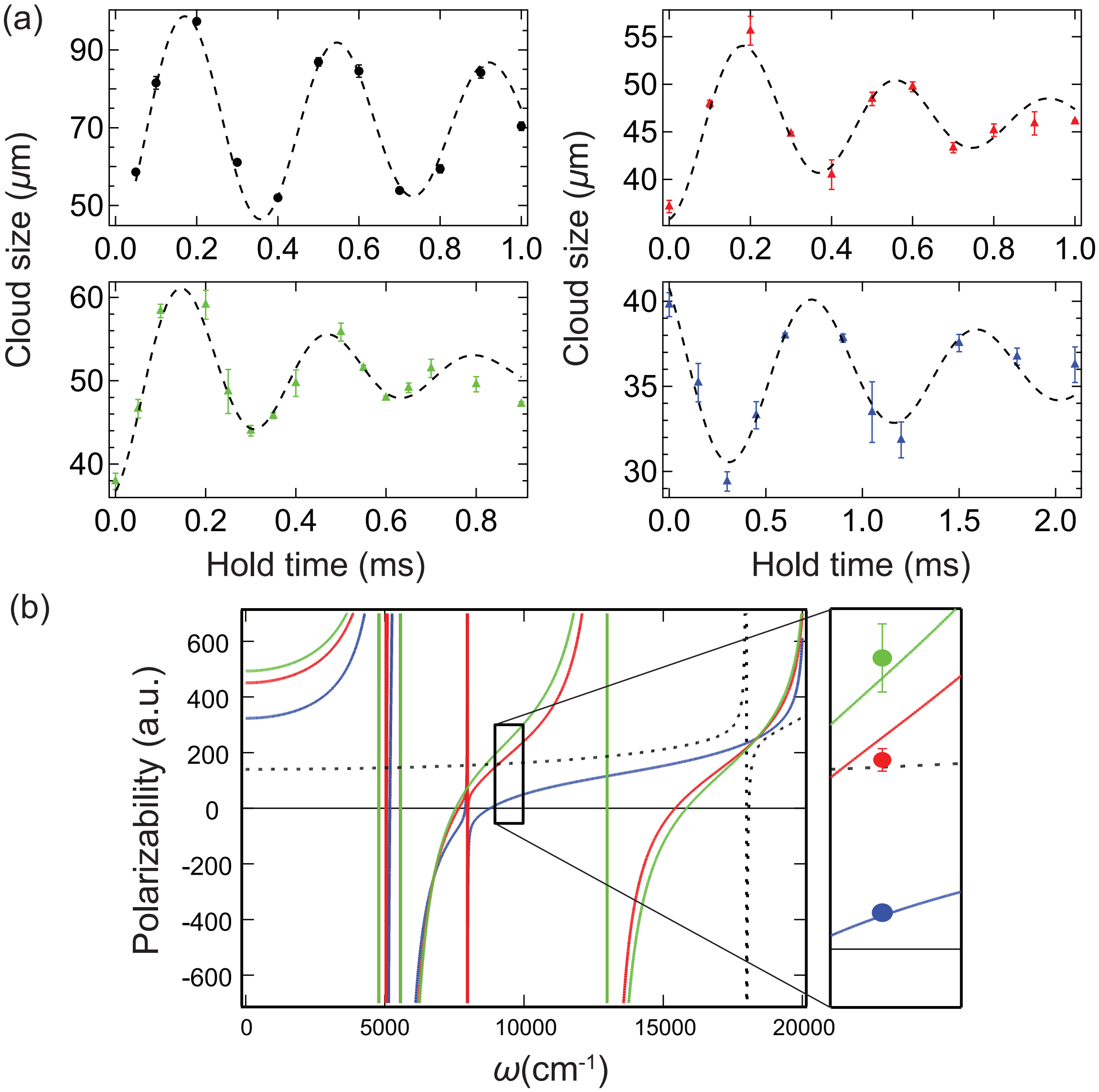

Figure 4.5: Measurements of the polarizability of the Yb $^3P_2$ magnetic substates for perpendicular orientations of the bias magnetic field and optical trap electric field. (a) Trap frequency measurements by diabatic excitation of a quadrupole breathing mode for $^1S_0$ and $|m_J| = 0$ (green), 1 (red), and 2 (blue) of $^3P_2$ for the same trapping laser power. The measurement of the $^3P_2$ state frequencies relative to the $^1S_0$ state gives the absolute polarizability. (b) Polarizability calculation from the group of S. Kotochigova for $|m_J| = 0, 1$, and 2 (same colors as (a)). The polarizability of $^1S_0$ is shown by the dashed black line. (Inset) Polarizability measurements (solid circles) at 1064 nm. Adapted from [59].

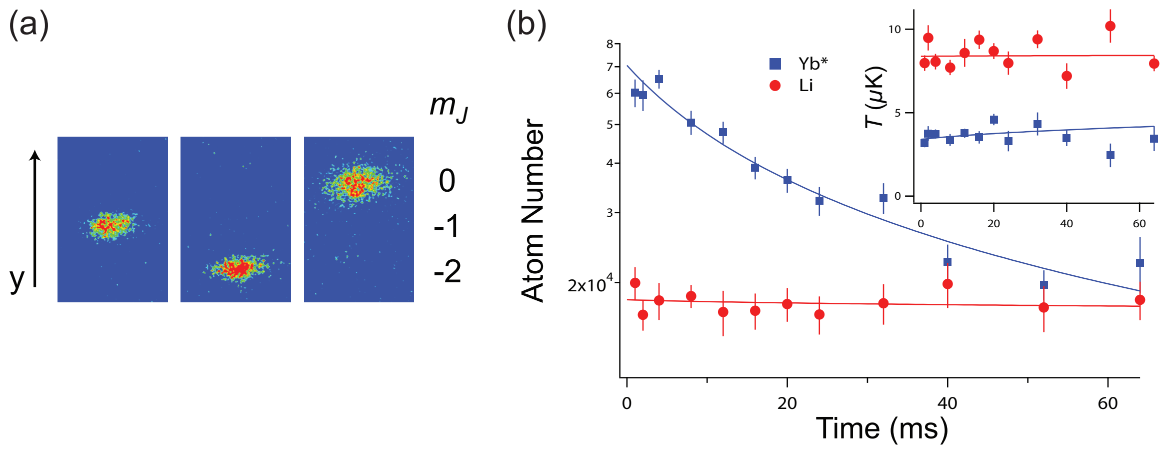

Figure 4.6: (a) Preparation of spin pure gases of Yb*. Following the purification and RF transfer scheme describe in the text, we detect the spin composition by applying a strong magnetic field gradient after releasing the atoms from the optical trap, resulting in a Stern-Gerlach separation in the vertical y direction of the magnetic substates. (b) Measurement of Yb*-Yb* and Yb*-Li (state $|1\rangle$) inelastic scattering in the $m_J = -1$ substate at $B = 12$ G. Solid lines are fits to rate equations for number and temperature coupled dynamics. The Li number evolution is consistent with zero inelastic loss, while the Yb* decay returns an inelastic rate coefficient $K_2 = 2.5 \times 10^{-11}$ cm^{3}s^{-1}. Adapted from [59].

with ground state Li and any single magnetic substate of $^3P_2$, additional challenges prevented us from doing so. Due to the large, sudden change in polarizability upon transferring the Yb* population from the $m_J = -1$ to either adjacent spin state, the cloud would begin executing breathing oscillations and heat up, thus making measurements of interactions with Li very difficult. A more straightforward way to realize mixtures of Li with arbitrary pure spin states of Yb* is to perform the direct $^1S_0 \rightarrow {}^3P_2$ transfer at 507 nm, where a particular m_J substate may be selectively populated at finite field. However, this transition requires optical-clock-level stability and ultra low expansion cavity technology, and therefore was neither easily nor quickly adaptable to our system.

4.4 Sub-Doppler cooling of Li

In the later stages of my time in the group, we set off to realize a mixture of a superfluid Fermi gas of ^{6}Li and a BEC of Yb. In earlier attempts in the lab, the atom number losses and heating incurred while trying to ramp the magnetic field from low values (≈ 300 G) to the center of the $|1\rangle$-$|2\rangle$ Feshbach resonance at 832 G proved too great, and resulted in low signal-to-noise absorption images. However, with a completely redesigned crossed optical trap optimized for efficient CMOT loading and evaporative cooling (described in chapter 7), we were capturing many more Li atoms from the CMOT than previously. To enhance our Li quantum degenerate gas production even more, we decided to implement a sub-Doppler cooling scheme often referred to as "gray molasses" or "D_1 cooling."

First demonstrated on D_2 transitions in alkalis (Rb and Cs) in the mid-1990s [14, 13, 29], gray molasses involves dressing the ground state with counter-propagating laser beams of equal frequency that are blue detuned from an $F \to F' = F$ ($F \to F' = F - 1$) transition, creating one (two) dark states that uncoupled by the light [30]. The coupled state experiences a spatially dependent Stark shift upwards in energy relative to the dark state, and preferentially gets excited to F' near the top of an energetic "hill," and falls into the dark state, thus losing kinetic energy (i.e. Sisyphus mechanism).

Nearly two decades later, the group of Christophe Salomon at ENS adapted this technique to cool fermionic ^{40}K [30] and bosonic ^{7}Li [36] on the D_1 transition, two species where the small hyperfine splitting in the $^2P_{3/2}$ excited state makes traditional sub-Doppler cooling techniques (e.g. polarization gradient Sisyphus cooling) very difficult (K) or impossible (Li). In this situation, a complete description of the cooling mechanism is quite involved, since the role of the lower $F = 1/2$ hyperfine state cannot be neglected. For more details, the reader is referred to the great papers from the ENS group on the topic [30, 36, 101]. Another particularly useful reference involves the first implementation of D_1 cooling in ^{6}Li by the Florence group [16], where an impressive minimum temperature of 40 μK was reached with 10^9 atoms in the molasses. This was quickly followed up by simultaneous D_1 cooling of ^{40}K and ^{6}Li by the ENS group [101].

For the source of the molasses beams in our experiment, we use the output of a home-made tapered amplifier (TA) system seeded by a Toptica DL100 external cavity diode laser, resulting in ≈ 350 mW after the isolator following the TA[4]. This light is then split into two paths by a half-wave plate and polarizing beam splitter (PBS) cube, each of which is sent through a double-pass AOM setup (negative first order) to prepare the necessary frequencies to address the $F = 3/2 \rightarrow F' = 3/2$ (cooling) and $F = 1/2 \rightarrow F' = 3/2$ (repump) transitions. In practice, we establish the various detunings by fixing the frequency of the cooling light AOM to be $f_{\text{AOM,},C} = 208.0$ MHz, resulting in the cooling laser frequency $\omega_C = \omega_L - 2\pi \times 2 f_{\text{AOM,},C} = \omega_L - 2\pi \times 416$ MHz. Therefore, for $\delta_C = 0$ the diode laser itself has a frequency of $\omega_L = \omega_{D_1,F=1/2} + 2\pi \times (416 - 228.2)$ MHz $= \omega_{D_1,F=1/2} + 2\pi \times 187.8$ MHz, where $\omega_{D_1,F=1/2}$ is the resonance frequency for the $^2S_{1/2}, F = 1/2 \rightarrow {}^2P_{1/2}, F' = 3/2$ transition. Then, we can vary the 1-photon cooling detuning δ_C by varying the lock point of the laser ω_L, and the two-photon Raman detuning $\delta = \delta_R - \delta_C$ by varying the frequency of the repump AOM $f_{\text{AOM},R}$. The Raman resonance condition is fulfilled for $f_{\text{AOM},R} = 93.9$ MHz, and $\delta < 0 (\delta > 0)$ for $f_{\text{AOM},R} > 93.9$ MHz($f_{\text{AOM},R} < 93.9$ MHz).

Following the double-pass AOMs, the cooling and repump beams are combined in a PBS cube, resulting in orthogonal polarizations, and then coupled into a polarization maintaining fiber. After the fiber, the cooling and repump beam powers are $P_C = 40$ mW and $P_R = 10$ mW, and we install an expanding telescope to make the beam waist $\approx 4-5$ mm at the atoms. These beams are then combined with the existing MOT beams using PBS cubes before the quarter-wave plates. Therefore, the D_1 molasses beams and the MOT beams have opposite polarization (i.e. $\sigma_+ \rightarrow \sigma_-$). However, this is not an issue for the molasses since it must be performed at zero magnetic field.

The frequency ω_L of the diode laser is stabilized to a commercial wave meter (High Finesse WS7/1275) using a Labview program to provide proportional and integral feedback with a

---

[4] This laser system is the same one used for the dual-MOT photoassociation measurements described in chapter 6.

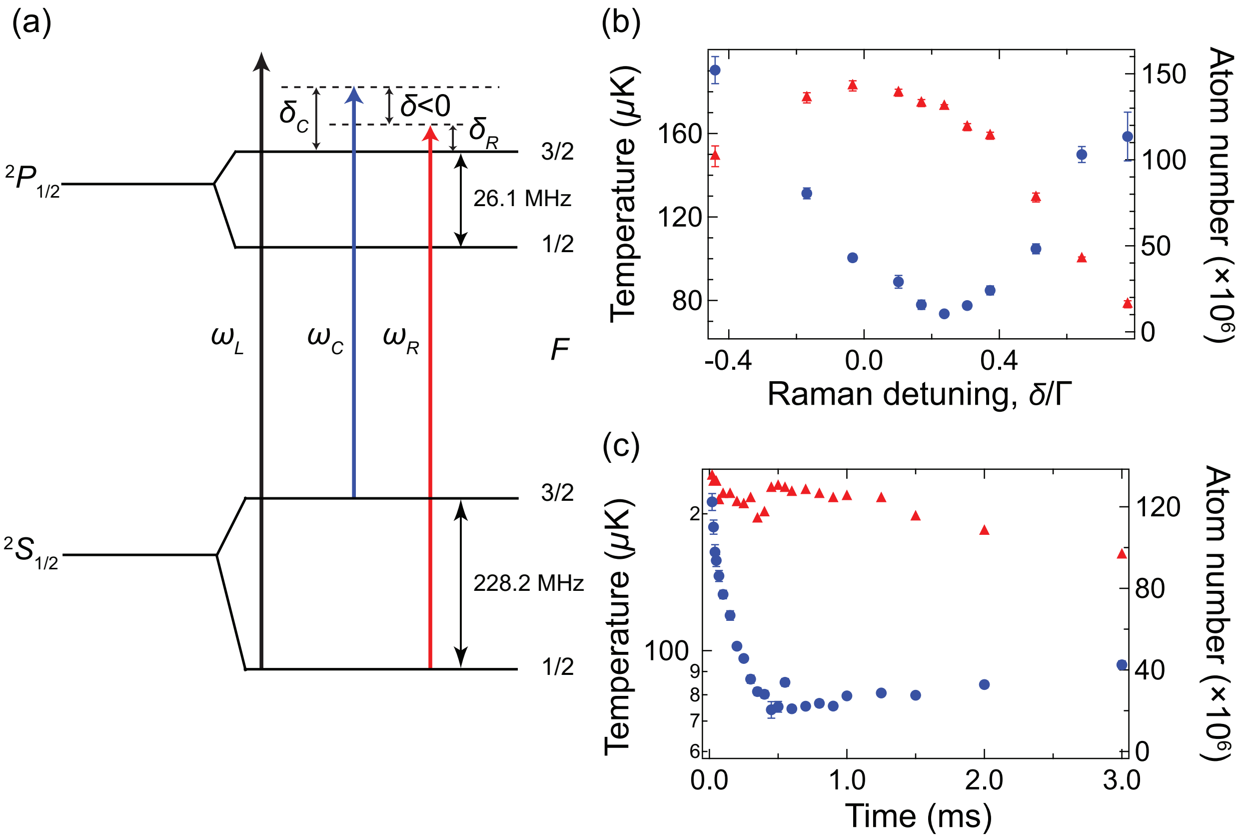

Figure 4.7: D_1 gray molasses cooling of ^{6}Li. (a) Relevant energy levels for the blue-detuned molasses beams. The relative, or Raman detuning is defined as $\delta = \delta_R - \delta_C$. (b) Dependence of temperature (blue circles) and number (red triangles) on Raman detuning (in units of the natural linewidth) for a 1 ms molasses duration. (c) Dependence of temperature (blue circles) and number (red triangles) on the molasses exposure time for $\delta/\Gamma \approx 0.2$.

maximum bandwidth of $\approx$ 100 Hz. Importantly, the D_1 cooling mechanism is relatively insensitive to the absolute detunings of the cooling and repump beams (δ_C and δ_R in figure 4.7(a)), and therefore our slow frequency lock is not an issue. However, the cooling is much more sensitive to the relative stability of the two molasses beams, given by the Raman detuning $\delta = \delta_C - \delta_R$. This Raman detuning is set by the relative stability of the VCO RF sources for the AOMs, which is plenty stable to achieve sufficient coherence between the beams.

In practice, we don't bother locking the diode laser frequency ω_L to an absolute reference, and instead vary the lock point in the Labview program to maximum the observed cooling. Figure 4.7(b) shows the measured dependence of D_1 cooling in our system on the Raman detuning δ in units of the natural linewidth $\Gamma = 2\pi \times 5.9$ MHz, for the experimentally optimized 1-photon detuning δ_C. Then in figure 4.7(c), we see the dependence of ^{6}Li temperature on the duration of the molasses, with a minimum around 0.5 ms, for the optimal Raman detuning of $\delta \approx 0.2\Gamma$. After further optimization of our system, we were able to achieve ^{6}Li clouds consisting of 3×10^8 atoms at a temperature of $70 - 80$ μK. One of the most important technical issues we encountered when trying to get the molasses working was the residual magnetic fields that persist after compressing the MOT and shutting the coils off. To mitigate this issue, we carefully set pretriggers on each of the coils, each with its own particular decay time, in order to have as close to zero magnetic field as possible upon applying the gray molasses. When optimizing D_1 cooling for loading into the optical trap, the parameters had to be tweaked a little bit due to the Stark shift introduced by the ODT.

Part II

EXPERIMENTAL RESULTS

Chapter 5

MAGNETIC FIELD-DEPENDENT INTERACTIONS IN $^{6}\mathbf{Li}(^{2}S_{1/2}) + {}^{174}\mathbf{Yb}(^{3}P_{2})$

In section 4.3 we detailed our procedure for creating spin-polarized gases of metastable $^{3}P_{2}$ Yb (Yb*). After establishing the stability of the Li $^{2}S_{1/2}$ + Yb* mixture at zero magnetic field (see figure 4.6), we set out to detect interspecies magnetic Feshbach resonances by performing inelastic loss spectroscopy. What follows in this chapter is a summary of the measurements and analysis that constitute our 2015 publication on the detection of Feshbach resonances in the lithium - metastable ytterbium mixture [27].

In “traditional” inelastic loss Feshbach spectroscopy, the atoms reside in the electronic ground state and the dominant loss mechanism is three-body collisions close to the resonance position, resulting in a deeply bound molecule and free atom, both of which have enough energy to leave the trap. Furthermore, it is typically the case that there is little to no inelastic loss away from the Feshbach resonance, and thus no background with which to compete. In this situation, it is common to perform the loss spectroscopy by measuring the atom number at a given magnetic field for one short and one long hold time, and taking the ratio to look for resonant, field-dependent loss features.

The situation when using an electronically excited metastable state is quite different. First of all, the dominant loss mechanism is two-body loss, as the energy released corresponds to internal electronic decay and not the formation of a diatomic molecular bond, meaning there is no need for a third scattering particle to carry away the necessary energy and momentum. Furthermore, there is a strong background of Yb*-Yb* inelastics for all magnetic fields, and, as we quickly found after investigating interspecies inelastics at fields around 100 G, strong Li-Yb* inelastics that grow steadily with magnetic field. Thus, there are various backgrounds that could obscure the detection of Feshbach resonances, and that cannot be easily overcome by going to lower and lower density (as would be the case for three body loss).

Therefore, to make our loss spectroscopy as sensitive as possible, we performed well resolved lifetime measurements of Li and Yb* atom number versus hold time together in the trap at a given magnetic field. Then, by fitting to the observed dynamics we extracted the inter- and intraspecies inelastic loss rate coefficients, $K_2'(B)$ and $K_2(B)$, which would reveal a Feshbach resonance as a peak versus magnetic field.

5.1 *Measurement of field-dependent inelastics*

In order to search for resonant features in the inelastic loss spectrum $K_2'(B)$ of Li + Yb*, it is important to have spin-polarized gases of both Li and Yb, as it would otherwise be difficult to know from which channel the resonance originated. The procedures for preparing pure spin states of both Li and Yb* are detailed in chapter 4, as well as in our first publication on the interspecies mixture [59]. For these measurements, the atoms are primarily trapped in a horizontally oriented single beam optical trap at 1064 nm, with a second, much weaker beam at 1070 nm oriented vertically (parallel to the direction of the force of gravity) to provide additional axial confinement and thus increase the value of the Li-Yb* density-density overlap integral.

After 4 seconds of evaporative cooling of Yb ($^1S_0$) and simultaneous sympathetic cooling of Li, we are left with a mixture 500×10^3 Yb ground state atoms and 25×10^3 Li state $|1\rangle$ atoms at a temperature of $T = 1.1$ μK. The trap frequencies for Yb $^1S_0$ in the horizontal beam only at this point are given by $(\omega_x, \omega_y, \omega_z)_{\mathrm{Yb},{}^1S_0} = 2\pi \times (500, 500, 4.9)$ Hz, and the vertical beam has a power of 500 mW and waist $w_0 = 80$ μm. After performing the 404 nm excitation from $^1S_0$ to $^3D_2$ and purifying the resulting $^3P_2$ atoms to realize a spin-polarized $m_J = -1$ gas, we then have 20×10^3 Yb* and 10×10^3 Li atoms at temperatures of 1.7 and 1.5 μK, respectively.

For the magnetic field dependent inelastics measurements, we always perform the $^3P_2$

state preparation at 100 G, and quickly ramp the magnetic field to the desired value immediately (< 5 ms) following the excitation to monitor loss dynamics. To make the magnetic field ramp as fast as possible, we utilized our smaller set of coils, usually used for providing MOT gradient, because of the small inductance. Furthermore, in order to eliminate the effect of gravitational sag on Yb* and ensure the maximum possible overlap between the two species, we perform the lifetime measurements with a magnetic field of 20 G/cm applied against gravity. This gradient was supplied with our largest set of coils, usually called the "Feshbach" coils.

5.1.1 Analysis of Li-Yb* lifetimes

Typical lifetime curves are shown in figure 5.1 for magnetic fields of 100 G and 450 G. In order to extract the interspecies, density-independent inelastic rate coefficient $K_2'(B)$, we must integrate the following equations and fit the solution to our data:

$$\begin{aligned} \dot{n}_{\rm Yb} &= -K_2'(B) n_{\rm Li} n_{\rm Yb} - 2K_2(B) n_{\rm Yb}^2 \\ \dot{n}_{\rm Li} &= -K_2'(B) n_{\rm Li} n_{\rm Yb}. \end{aligned} \tag{5.1}$$

In order to do so, we have to account for the highly anharmonic nature of the potential in the axial z dimension. To begin, we write the overall potential for Yb $^3P_2$, $m_J = -1$ as $V_{m_J=-1}(\vec{r}) = \frac{m_{\rm Yb}\beta_V}{2}(\omega_x^2 x^2 + \omega_y^2 y^2) + f(z)$, where $\beta_V = 1.04$ is the ratio of the polarizability of Yb* $m_J = -1$ to that of $^1S_0$ for a vertically polarized ODT (i.e. $\vec{E}_{\rm ODT} \parallel \vec{B}$), and the trap frequencies are those for the ground state. Including the vertical "dimple" ODT beam and treating the axial confinement from the horizontal ODT beam as a harmonic potential, the overall axial potential is written as

$$f(z) = \frac{m_{\rm Yb}\beta_V}{2}\omega_z^2 z^2 + \beta_H V_{0,\rm vert}\left(1 - e^{-2z^2/w_0^2}\right), \tag{5.2}$$

where $V_{0,\rm vert}$ is the $^1S_0$ depth corresponding to the vertical beam and $\beta_H = 0.65$ is the ratio of polarizability of $m_J = -1$ to that of $^1S_0$ for a horizontally polarized ODT (i.e. $\vec{E}_{\rm ODT} \perp \vec{B}$) [43]. This full analysis is necessary because $k_B T > \beta_H V_{0,\rm vert}$, and therefore the harmonic

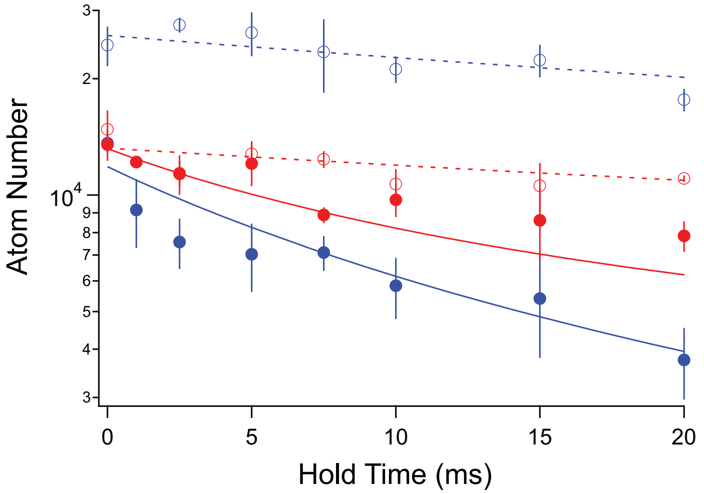

Figure 5.1: Example lifetime curves for Li state $|1\rangle$ (red circles) in the presence of $m_J = -1$ $^3P_2$ Yb (blue circles) at 100 G (open markers) and 450 G (solid markers). The dashed and solid lines are fits from a rate equations analysis including interspecies (Li-Yb*) and intraspecies (Yb*-Yb*) two-body inelastic decay. From [27].

approximation for the vertical ODT beam is not valid. We can write the Li potential in a similar fashion, with $V_{\mathrm{Li}}(\vec{r}) = \frac{m_{\mathrm{Li}}}{2}\frac{\alpha_{\mathrm{Li}}}{\alpha_{\mathrm{Yb}}}(\omega_x^2 x^2 + \omega_y^2 y^2) + g(z)$, where $\alpha_{\mathrm{Li}}/\alpha_{\mathrm{Yb}} = 2.3$ is the ratio of Li to Yb polarizabilities, and

$$g(z) = \frac{\alpha_{\mathrm{Li}}}{\alpha_{\mathrm{Yb}}}\left(\frac{m_{\mathrm{Li}}}{2}\omega_z^2 z^2 + V_{0,\mathrm{vert}}\left(1 - e^{-2z^2/w_0^2}\right)\right). \tag{5.3}$$

Writing the Yb* density profile as $n_{\mathrm{Yb}}(\vec{r}) = n_{0,\mathrm{Yb}}\exp(-V_{m_J=-1}(\vec{r})/k_B T)$, we find

$$n_{0,\mathrm{Yb}} = \frac{N_{\mathrm{Yb}}}{\pi R_x R_y}\left[\int dz\ e^{-f(z)/k_B T}\right]^{-1}, \tag{5.4}$$

and similarly for the Li density profile $n_{\mathrm{Li}}(\vec{r})$. Thus, we can integrate the rate equations in (5.1) over space, performing the necessary integrals in the z dimension numerically, and end up with rate equations for the total atom numbers N_{Yb} and N_{Li}. The dashed and solid lines in figure 5.1 are fits to these spatially integrated rate equations at 100 G and 450 G, respectively.

Since we observe little to no change in temperature over the course of these lifetime measurements, we do not include temperature dynamics into this model [27]. Furthermore, because of diabatic effects associated with the Yb^* state preparation, we limit our analysis of interspecies lifetime measurements to the first 20 ms, where the two clouds have not lost more than 10% of the initial overlap. These diabatic effects include both the impulse from the 404 nm light exposure and magnetic field gradients along the weak axis of the trap, which affect the two species differently.

5.1.2 Inelastic loss spectrum

In order to improve the determination of the interspecies inelastic rate coefficient, $K_2'(B)$, we take a separate lifetime measurement at each magnetic field with Yb^* present only, where we blast Li away immediately before ramping the magnetic field to the desired value. We then fit the solution to $\dot{n}_{\mathrm{Yb}} = -2K_2(B)n_{\mathrm{Yb}}^2$ to the observed Yb^* lifetime measurements, thus fixing $K_2(B)$ in the analysis of the measurements with Li. This results in markedly better fits and uncertainties for $K_2'(B)$.

The resulting inelastic loss spectrum as a function of magnetic field from 100 to 520 G is shown in figure 5.2. While the inter- and intraspecies inelastic rate coefficients are comparable around 100 G, the interspecies inelastics clearly dominate for higher magnetic fields, with several peak-like features pronounced above the overall rise in $K_2'(B)$. Furthermore, after the peak value of the broadest feature around 450 G, the rate coefficient appears to decrease noticeably. The Yb^*-Yb^* intraspecies inelastic coefficient $K_2(B)$ appears to be constant as a function of magnetic field.

For s-wave scattering between two distinguishable particles with an isotropic Van der Waals interatomic potential, $V(r) = -C_6/r^6$, one can show that, when the probability of "reaction" (in our case meaning decay to an inelastic scattering channel) is high at small interatomic separation, the two-body inelastic rate coefficient approaches a universal value

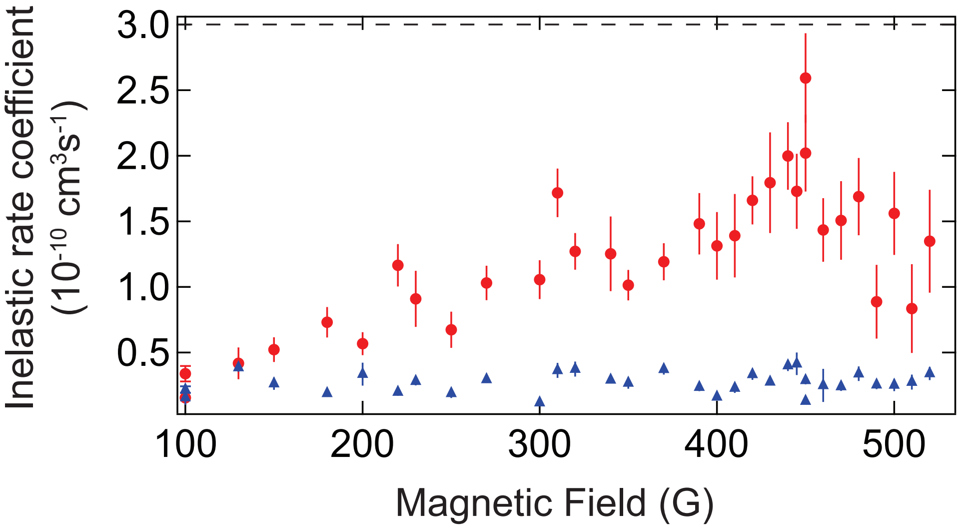

Figure 5.2: Measured inelastic loss rate coefficients for Yb*-Yb* ($K_2(B)$, blue triangles) and Yb*-Li ($K_2'(B)$, red circles) as a function of magnetic field. The dashed line corresponds to the universal rate of $K'_{2,\text{univ}} = 3.0 \times 10^{-10}$ cm^{3}s^{-1}.

[53],

$$K'_{2,\text{univ}} = \frac{4\pi\hbar}{\mu_r}\bar{a}, \tag{5.5}$$

where μ_r is the reduced mass,

$$\bar{a} = \frac{4\pi}{\Gamma\left(\frac{1}{4}\right)^2} r_{\text{VdW}}, \tag{5.6}$$

and

$$r_{\text{VdW}} = \frac{1}{2}\left(\frac{2\mu_r C_6}{\hbar^2}\right)^{1/4} \tag{5.7}$$

is the Van der Waals length, which quantifies the range of the interaction. In our 2014 publication [59], our theory collaborators (the group of S. Kotochigova) calculated the C_6 coefficients for the Born-Oppenheimer Li($^2S_{1/2}$) + Yb($^3P_2$) potentials $\{^2\Sigma, ^4\Sigma, ^2\Pi, ^4\Pi\}$ to be $C_{6\Sigma} = 3279.87\, E_h a_0^6$ and $C_{6\Pi} = 2402.98\, E_h a_0^6$. One can then find the isotropic C_6 coefficient from the relation $C_6 = \frac{1}{3}(C_{6\Sigma} + C_{6\Pi}) = 2695.3\, E_h a_0^6$. Therefore, we find a universal loss rate for this collision complex of $K'_{2,\mathrm{univ}} = 3.0 \times 10^{-10}$ cm^{3}s-1, depicted by the dashed line in figure 5.2.

5.2 Theoretical model for Yb*-Li Feshbach resonances

Given our experimentally determined inelastic spectrum (figure 5.2), the theory group of S. Kotochigova developed a theoretical model to calculate the various interaction potentials and the consequences of Yb*-Li scattering versus magnetic field. For a full description of the theoretical model, the reader is referred to their paper [91], published in parallel with our experimental results [27]. In this section, we will simply recount the anisotropic Van der Waals coupling mechanism [90] that gives rise to the observed Feshbach resonances.

Figure 5.3 shows a schematic of the important channels involved in anisotropy-induced interactions in the Yb*-Li system. Unlike "standard" alkali Feshbach resonances (see section 3.3.1), which couple different channels corresponding to different electronic spin configurations (e.g. triplet and singlet), anisotropy-induced Feshbach resonances result in the coupling of channels with different internuclear orbital angular momentum $\vec{\ell}$. As depicted by the green potential in figure 5.3, the entrance channel for our measurements is always the s-wave ($\ell = 0$) scattering state with $(J, m_J)_{\mathrm{Yb}} = (2, -1)$ and $(m_J, m_I)_{\mathrm{Li}} = (-1/2, 1)$. The anistropic Van der Waals interactions conserve $M_{\mathrm{tot}} = m_{\mathrm{Yb}} + m_{\mathrm{Li}} + m_\ell$, where m_{Yb} and m_{Li} are the total angular momentum projections for the two species and m_ℓ the projection of the relative nuclear orbital angular momentum $\vec{\ell}$ onto the magnetic field axis. Furthermore, these interactions only couple even ℓ.

The molecular, or closed channels that will give rise to magnetic Feshbach resonances are those with dissociation energies above the entrance channel (e.g. the red curve in figure 5.3 asymptoting to the state $m_J = -1$ but with $\ell = 4$). The potentials below the entrance channel give rise to inelastic decay. For our Yb* state of $m_J = -1$, this decay includes both Zeeman sublevel changing collisions and fine structure level changing collisions (i.e. ${}^3P_2 \to {}^3P_1$).

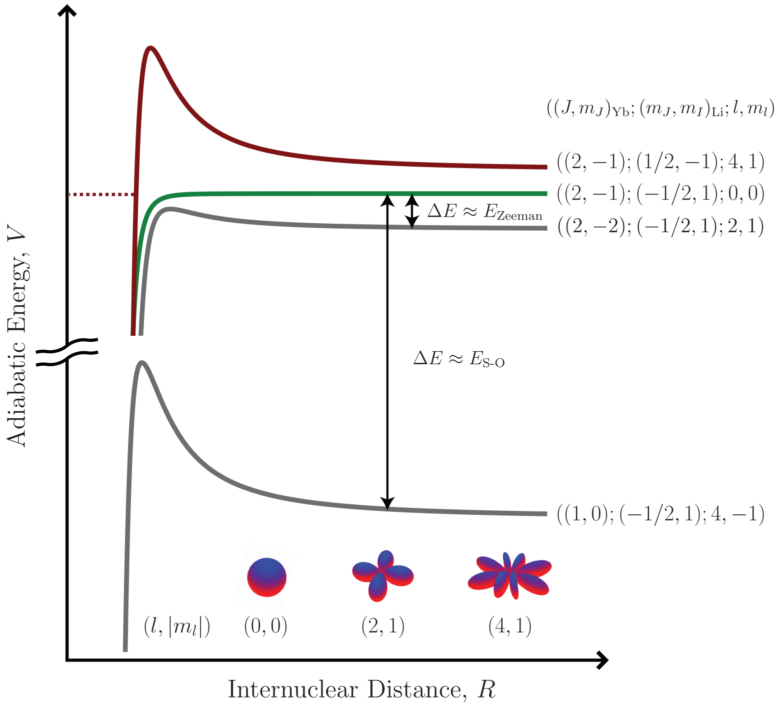

Figure 5.3: Depiction of the relevant channels involved in anisotropic Van der Waals scattering. The entrance channel (green curve) is set by the atomic labels $(J, m_J)_{\rm Yb}$ and $(m_J, m_I)_{\rm Li}$ and the relative nuclear orbital angular momentum $\ell = 0$ for the s-wave scattering state. This channel may be coupled by the Van der Waals, or dispersion potential in equation (5.8) to other channels with $\Delta\ell$ even. For Feshbach resonances, the entrance channel couples to bound states of potentials (e.g. red curve) with dissociation energy greater than the entrance channel. Inelastic decay may occur to lower lying potentials (gray curves) by changing the Zeeman sublevel or fine structure quantum numbers.

The full Van der Waals, or dispersion interaction operator can be written in the form [90]

$$V_{\rm disp}(\vec{r}) = \frac{1}{r^6}\sum_{kq}\sum_{i} c_k^{(i)}(-1)^q\sqrt{\frac{4\pi}{2k+1}}Y_{kq}(\theta,\phi)T_{kq}^{(i)}, \tag{5.8}$$

where $c_k^{(i)}$ are the dispersion coefficients, which can be determined from the Born-Oppenheimer potentials (e.g. $c_0^{(1)} = -C_6 = \frac{1}{3}(C_{6\Sigma}+C_{6\Pi})$), $Y_{kq}(\theta,\phi)$ are the spherical harmonics, the coordinates (θ,ϕ) give the angle of the internuclear axis relative to the magnetic field, and $T_{kq}^{(i)}$ is a tensor of rank k involving tensor products of the individual atomic electronic orbital angular momenta $\vec{\ell}_{\rm Yb}$ and $\vec{\ell}_{\rm Li}$. In order to elucidate the explicit coupling mechanism, let us assume that the main contribution to the anisotropic part of the potential comes from the $k=2$, $q=0$, and $i=1$ term (as was found to be the case in [90]), and write the full dispersion potential as

$$V_{\rm disp}(\vec{r}) = -\frac{C_6}{r^6} + \frac{\Delta C_6}{r^6}\frac{3\cos^2\theta - 1}{2}T_{20}^{(1)}, \tag{5.9}$$

where ΔC_6 is referred to as the anisotropic Van der Waals coefficient. Thus, if the scattering state begins as a single partial wave ℓ (i.e. as a spherical harmonic), this state will evolve under the interaction term given by equation (5.9) because $[V_{\rm disp}, \vec{\ell}^2] \neq 0$, and may be coupled to bound states of other molecular potentials with $\Delta\ell \neq 0$ and even.

The result of the full close-coupling scattering calculation [91, 27] fitted to our experimental data is shown in figure 5.4. In order to perform the fit, the short range shapes of the potentials $\{^2\Sigma, ^4\Sigma, ^2\Pi, ^4\Pi\}$ were varied, thus changing the inelastic rate coefficient spectrum $K_2'(B)$. For this reason, one cannot rule out the possibility of other potentials that are consistent with the experimental data. The fit reveals one clear Feshbach resonance at 450 G, with some weaker modulations at lower fields. The quantum numbers for this resonance, in the separated atomic basis, are $(J, m_J)_{\rm Yb} = (2,-1)$ and $(m_J, m_I)_{\rm Li} = (1/2,-1)$, with relative nuclear orbital angular momentum of both g-wave (60%) and d-wave (40%) character, and $m_\ell = 1$. This particular molecular channel is depicted by the red curve in figure 5.3.

The very high inelastic rate coefficient at the resonance position makes the prospect of tuning elastic interactions or creating heteronuclear molecules rather grim in this combination

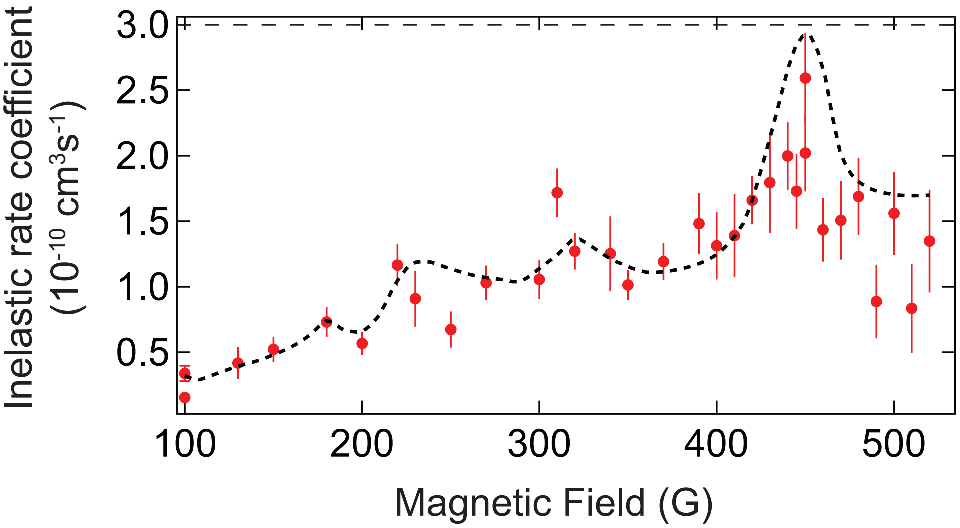

Figure 5.4: Interspecies inelastic rate coefficient $K_2'(B)$ spectrum with fitted theory curve, from [27] and [91]. The fit reveals a clear, broad resonance at 450 G, with a peak inelastic rate coefficient nearly equal to the universal rate of 3.0×10^{-10} cm^{3}s^{-1}.

Yb($^3P_2, m_J = -1$)+Li($|1\rangle$). However, calculations by the Kotochigova group show that the dominant loss mechanism in this combination is decay to the $m_J = -2$ state. This Zeeman sublevel changing inelastic channel is eliminated if one uses the $m_J = -2$ state, and the predicted loss rates at high magnetic field are an order of magnitude smaller than those for $m_J = -1$ [91]. Unfortunately, our state preparation scheme for Yb* is not easily amenable to preparing the $m_J = -2$ state, and thus performing experiments in that mixture would require implementing the direct $^1S_0$ to $^3P_2$ excitation.

Chapter 6

PHOTOASSOCIATIVE PRODUCTION OF YbLi*

After our experiments with lithium and metastable ($^3P_2$) ytterbium revealed dwindling prospects for producing heteronuclear Feshbach molecules, we turned our attention to an all-optical route to ground-state YbLi molecules. The idea is inspired by experiments from the group of Rudi Grimm, in which they achieved a conversion efficiency of 30% in the transfer of free atoms to ground state, vibrationally excited Sr_2 molecules in an optical lattice using stimulated Raman adiabatic passage (STIRAP) [102]. For reference, the production scheme used to create ultracold KRb [81], RbCs [78, 103], NaK [85], and NaRb [39] molecules involves first coherently creating Feshbach molecules using either an adiabatic field sweep or radio frequency pulse on the molecular side of the resonance, and subsequently coherently transferring the loosely bound Feshbach molecules to the absolute ground state using STIRAP through an intermediate electronically excited molecular state. While the two-photon STIRAP transfer in the Feshbach molecule case has near unit efficiency, the formation of the Feshbach molecules themselves limits the final molecule number and phase-space density, with typical efficiencies of 30-40%. Therefore, the overall efficiency achieved in the Sr_2 case in an optical lattice is quite impressive, and shows that the tight confinement in a single lattice well can act to mimic the enhanced wave function overlap that is realized with Feshbach molecules (i.e. increase the free-to-bound Franck-Condon factor).

Thus, our first goal became to identify a feasible two-photon pathway from free Yb and Li atoms to a vibrationally excited molecular state in the YbLi ground state potential by performing photoassociation (PA) spectroscopy. It is important to note here the qualitative differences in the Yb-Li combination that contrast with the Sr_2 situation. First, the homonuclear $Sr(^1S_0) + Sr(^3P_1)$ potential features a long range potential of the form $-C_3/r^3$.

This results in molecular states with Condon points at much longer internuclear separations, which allows for greater wave function overlap between the free scattering and bound states (i.e. greater Franck-Condon factor). Second, the light mass of ^{6}Li makes tight confinement in an optical lattice very difficult, while heavy atoms like Yb and Sr are easily pinned down to single lattice sites. Nevertheless, the all-optical route to ground state YbLi molecules holds good promise, and would be an important demonstration of a general method for creating heteronuclear ground state molecules irrespective of the existence (or usability) of magnetic Feshbach resonances.

6.1 Preparing the system for interspecies photoassociation

There were various important considerations in deciding how to perform the interspecies PA spectroscopy. First, we needed to decide from which atomic transition to begin the search, which determines the molecular potential for the intermediate STIRAP state. From the LeRoy-Bernstein formula for the energy of vibrational states near dissocation in a $1/r^6$ potential,

$$\Delta(\nu) = -\left(\frac{\Gamma(7/6)}{\Gamma(2/3)}\right)^3 \left(\frac{8\pi\hbar^2}{\mu_r}\right)^{3/2} \frac{1}{\sqrt{C_6}}(\nu_F - \nu)^3, \tag{6.1}$$

we see that the spacing between adjacent levels scales as ${\mu_r}^{-3/2}$, where μ_r is the reduced mass, $\nu = -1, -2, -3, ...$ is the vibration quantum number, $\nu = -1$ is the least bound state, and ν_F is a parameter with a value between 0 and 1 that accounts for the short range part of the potential. Therefore, for the YbLi system with $\mu_r \approx m_{\mathrm{Li}}$, the spacing between adjacent levels becomes large very quickly. This has the practical consequence that searching "in the dark" for PA resonances becomes difficult after the first few bound states, and it is necessary to extrapolate down in vibrational quanta ν using equation (6.1). For this reason, as well as because of the readily available high laser powers at 671 nm, we chose to perform PA spectroscopy below the ^2P asymptote in Li. This transition features a much larger linewidth $\Gamma/2\pi = 5.9$ MHz than the 556 nm transition in Yb with $\Gamma/2\pi = 180$ kHz, and thus makes the prospect of searching in the dark for PA resonances much more reasonable.

A second consideration for interspecies PA studies is whether to perform the spectroscopy in a magneto-optical trap or an optical dipole trap. Previous photoassociation studies have been successfully executed in both settings, with some of the relevant advantages for each being the high spatial densities realized in the ODT, and the ability to sweep large frequency ranges in the MOT because of the steady-state nature of the measurement. After brief attempts at PA spectroscopy of weakly bound vibrational states in the ODT, we realized that overcoming the deleterious effects of spontaneous scattering in Li would prove quite difficult in the ODT, but could be mitigated in the MOT because of the continuous reloading of atoms. While the PA studies presented in this chapter take place entirely in a dual-species Yb-Li MOT, we have recently extended these studies into the ODT after significant upgrades to the system preparation and using knowledge of the YbLi* molecular potentials acquired from these MOT studies.

6.1.1 The dual-species MOT

Because neither Li nor Yb feature the ability to implement a dark-spot MOT, we cannot increase the spatial densities beyond the limits imposed by light-assisted collisions in the MOT. Therefore, we enhance our sensitivity to interspecies PA by choosing parameters for the combined MOT that create a probe and bath situation for Yb and Li, respectively.

To this end, we operate with an axial magnetic field gradient $B'_{\mathrm{axial}} = 20$ G/cm that maximizes Li atom number and density. Because of the large mismatch in linewidth for the transitions used for MOTs of both species, $\Gamma_{\mathrm{Li}}/\Gamma_{\mathrm{Yb}} = 33$, this results in a considerably smaller Yb cloud size than Li. Furthermore, because the gradient is far larger than the optimal Yb loading gradient of 3 G/cm, the Yb MOT loading rate and thus equilibrium number is much reduced compared to normal operation, and $N_{\mathrm{Yb}}/N_{\mathrm{Li}} \ll 1$.

The parameters used for the Li cooling (repumping) light addressing the $F = 3/2 \rightarrow F' = 5/2$ ($F = 3/2 \rightarrow F' = 5/2$) transition are $\delta_{\mathrm{cool}} = 5\Gamma_{\mathrm{Li}}$ ($\delta_{\mathrm{rep}} = 3\Gamma_{\mathrm{Li}}$) and $I_{\mathrm{cool}}/I_{\mathrm{sat,Li}} = 8$ ($I_{\mathrm{rep}}/I_{\mathrm{sat,Li}} = 0.9$) per beam, where $I_{\mathrm{sat,Li}} = 2.54$ mW/cm^2. For the Yb $^1S_0 \rightarrow {}^3P_1$ MOT transition, we use a detuning of $\delta_{\mathrm{Yb}} = 20\Gamma_{\mathrm{Yb}}$ and intensity of $I_{\mathrm{Yb}}/I_{\mathrm{sat,Yb}} = 160$, where

$I_{\mathrm{sat,Yb}} = 0.14$ mW/cm^2. The absorption images of the resulting MOT clouds are well fit by Gaussian profiles for both Yb and Li. The atom number, cloud sizes, and peak density of each species in the absence of the other are determined by these Gaussian fits to be $N_{\mathrm{Li}} = 7 \times 10^7$ ($N_{\mathrm{Yb}} = 5 \times 10^6$), $w_{a,\mathrm{Li}} = 700$ μm ($w_{a,\mathrm{Yb}} = 200$ μm), $w_{r,\mathrm{Li}} = 900$ μm ($w_{r,\mathrm{Yb}} = 300$ μm), and $n_{\mathrm{Li}}(0) = 2 \times 10^{10}$ cm^{-3} ($n_{\mathrm{Yb}}(0) = 5 \times 10^{10}$ cm^{-3}), where w_a and w_r are the $1/e$ cloud radii in the axial and radial dimensions, respectively. By observing the cloud expansion in time-of-flight absorption images, we find the MOT temperatures to be $T_{\mathrm{Li}} = 1$ mK and $T_{\mathrm{Yb}} = 130$ μK.

When operating the two MOTs simultaneously, the two-body interspecies inelastics (i.e. light-assisted collisions) result in a reduction of the steady-state Yb number of a factor of 3, and have no effect on the Li number due to the probe-bath nature of the system. To measure the inelastic dynamics, and for the eventual PA spectroscopy measurements, we monitor the fluorescence of the Yb (Li) MOT on a photomultiplier tube (photodiode). By assuming a constant Gaussian density profile in the trap over time (validated by absorption imaging measurements), we can then calibrate the PMT and PD voltage to atomic density in the trap. The fluorescence monitors also give us a method for optimizing the interspecies cloud overlap, by adjusting the Li MOT beam pointing to minimize the fluorescence of the Yb MOT.

With optimized interspecies cloud overlap, we perform measurements of inter- and intraspecies inelastic dynamics by closing the Yb atomic beam shutter and recording the ensuing fluorescence over time. Figure 6.1 shows Yb MOT lifetime measurements both without (a) and with (b) the Li bath present. We quantify the MOT lifetime dynamics using the rate equations

$$\dot{n}_\alpha = \ell_\alpha - \gamma_\alpha n_\alpha - 2K_{2,\alpha}^2 n_\alpha^2 - K_2' n_\beta n_\alpha, \tag{6.2}$$

where $\alpha = \mathrm{Yb(Li)}$ and $\beta = \mathrm{Li(Yb)}$ for the Yb(Li) dynamics, $K_{2,\alpha}$ and K_2' are the homonuclear and heteronuclear two-body inelastic rate coefficients, γ_α is the one-body background lifetime, and ℓ_α is the spatially dependent loading rate. Because of the large mismatch in MOT

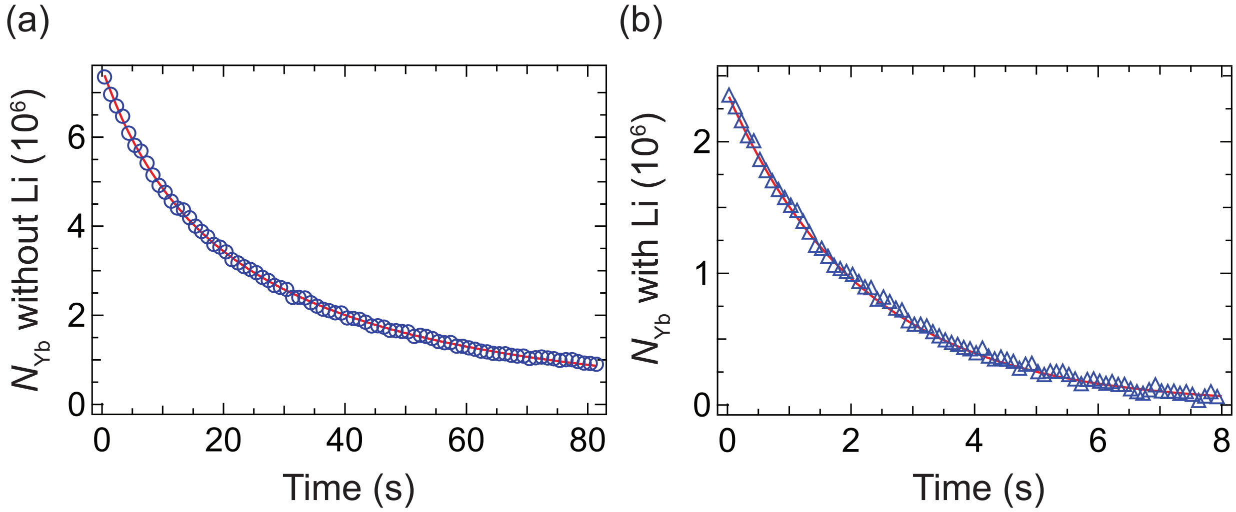

Figure 6.1: Measurement of interspecies inelastics in the Yb-Li double MOT. (a) Without Li, the Yb atom number decay is due to background γ_{Yb} and intraspecies two-body inelastic $K_{2,\mathrm{Yb}}$ loss. (b) In the presence of Li, the interspecies inelastic process K_2' dominates all other loss. Adapted from [96].

number and cloud size for the two species, we can treat Li as unperturbed by the Yb cloud, and replace $n_{\mathrm{Li}}(\vec{r})$ in equation (6.2) with the constant peak value $n_{\mathrm{Li}}(0)$. Then, we can integrate equation (6.2) over space, and solve for the resulting atom number evolution $N_{\mathrm{Yb}}(t)$, and fit to the data in figure 6.1. Due to the vastly different timescales of the inelastics with and without Li present, it is necessary to perform an independent lifetime measurement without Li in order to extract $K_{2,\mathrm{Yb}}$. From the fits to the data in figure 6.1(a), we determine the values $K_{2,\mathrm{Yb}} = 9.8(3) \times 10^{-13}$ cm^{3}s^{-1} and $\gamma_{\mathrm{Yb}} = 13.5(3) \times 10^{-3}$ s^{-1}. Then, fixing these quantities and using the measured peak Li density $n_{\mathrm{Li}}(0) = 1.9 \times 10^{10}$ cm^{-3} for the fit to the data with Li, we extract the interspecies loss rate coefficient $K_2' = 2.3(2) \times 10^{-11}$ cm^{3}s^{-1}. Because of the large disparity between the inter- and intraspecies inelastic coefficients, we find the same value of K_2' if we fit the data in figure 6.1(b) to a one-body loss curve with time constant $[K_2' n_{\mathrm{Li}}(0)]^{-1}$.

6.1.2 PA beam considerations

With the dual-species MOT optimized for interspecies cloud overlap, we move on to considerations for the photoassociation beam. The PA beam is derived from a home built tapered amplifier (TA) system seeded by a Toptica DL100 external cavity diode laser at 671 nm. Because of the broad tails in the output frequency spectrum of the TA, which is due to amplified spontaneous emission (ASE), we place two bandpass filters, centered at 670 nm with a transmission full width at half maximum of 10 nm. This removes frequency components at the $6s6p\ {}^3P_1 \rightarrow 6s7s\ {}^3S_1$ transition in Yb at 680 nm, which otherwise leads to much reduced Yb atom number in the MOT. This light is then coupled into a polarization maintaining fiber, resulting in a total power in the PA beam at the experiment of 100 mW.

The most important consideration for the PA beam is the waist. In order to determine the optimal size of the beam, we examine the loss term of interest for interspecies PA,

$$\dot{n}_{\mathrm{Yb},IPA} = -K_2'(I,\omega_L)n_{\mathrm{Li}}(0)n_{\mathrm{Yb}}, \tag{6.3}$$

where $K_2'(I) = K_{2,\mathrm{bg}}' + K_{2,PA}'(I,\omega_L)$ is the frequency and intensity dependent inelastic loss rate coefficient, accounting for the effects of photoassociation. In general, the PA loss term on the molecular resonance $\omega_L = \omega_0$ takes the form (see section 3.3.4)

$$K_{2,PA}' = K_{2,\max}' \frac{4\Gamma_{\mathrm{stim}}/\gamma_m}{(1+\Gamma_{\mathrm{stim}}/\gamma_m)^2}, \tag{6.4}$$

where $\Gamma_{\mathrm{stim}} \propto I$ is the stimulated scattering rate, γ_m is the spontaneous emission rate of the excited molecular state, and $K_{2,\max}'$ is the maximum achievable loss rate. Since it is usually the case that $\Gamma_{\mathrm{stim}} \ll \gamma_m$ for typical PA powers and Franck-Condon factors, we assume here that $K_{2,PA}' \propto I$. Therefore, in order to maximize the total loss rate of Yb, we want to maximize the right hand side of equation (6.3) integrated over all space, which amounts to maximizing

$$J(w_0) = \int d^3r\ I(\vec{r})n_{\mathrm{Yb}}(\vec{r}), \tag{6.5}$$

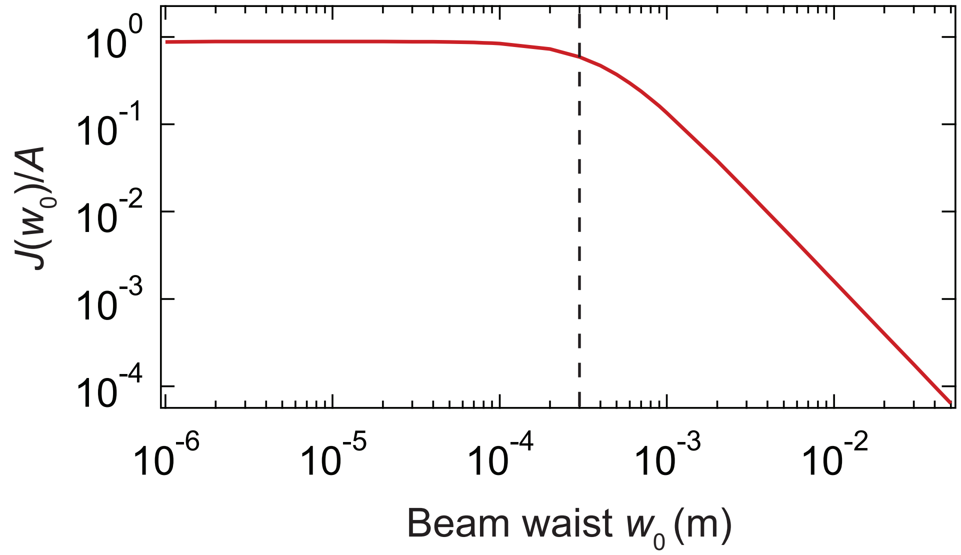

Figure 6.2: Value of the overlap integral of PA Beam intensity and Yb density profiles, for a spherical Yb cloud with $1/e$ radius $w_{\mathrm{Yb}} = 300$ μm (vertical dashed line). Clearly, once the beam is smaller than the radius of the cloud, the gains in intensity for smaller waist are offset by the loss in overlap between the two profiles.

where $I(\vec{r}) = (2P/\pi w^2(z))\exp[-2(x^2+y^2)/w^2(z)]$, $w(z) = w_0\sqrt{1+(z/z_R)^2}$ is the z-dependent beam waist, and $z_R = \pi w_0^2/\lambda$ is the Rayleigh range. For simplicity here, we assume a spherical Yb cloud $n_{\mathrm{Yb}}(r) = n_0 \exp(-r^2/w_{\mathrm{Yb}}^2)$ with a $1/e$ radius of $w_{\mathrm{Yb}} = 300$ μm. Assuming the centers of the PA beam and Yb cloud are the same, equation (6.5) becomes

$$J(w_0) = A\int dz\, \frac{w_{\mathrm{Yb}} e^{-z^2/w_{\mathrm{Yb}}^2}}{w^2(z) + 2w_{\mathrm{Yb}}^2}, \tag{6.6}$$

where $A = 2n_0 P w_{\mathrm{Yb}}$. The value of $J(w_0)/A$ is plotted in figure 6.2.

In fact, this analysis explained some of our early confusion, as we did not observe an increase in the loss due to ${}^3P_1 \to {}^3S_1$ scattering in Yb upon decreasing the waist below the size of the Yb cloud. Eventually we settled on a PA beam waist of about 80 μm. After an initial unsuccessful round of interspecies PA spectroscopy, we decided to increase the effective intensity by recycling the PA beam 4 times and then retro-reflecting the beam, resulting in

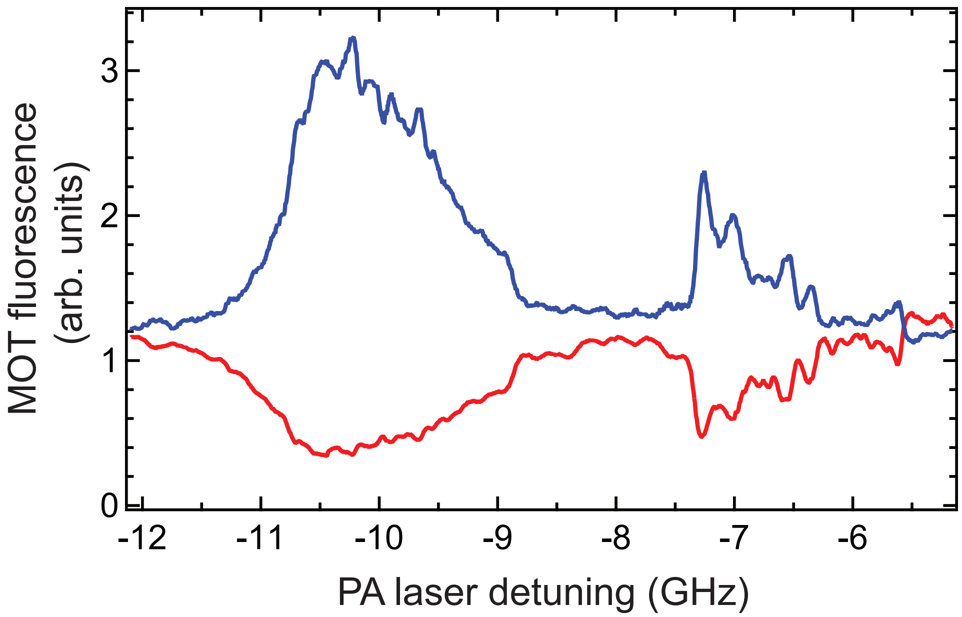

Figure 6.3: Li_2 photoassociation in the Yb-Li dual MOT. The two broad resonances correspond to the $\nu = -82$ and -83 vibrational states of the $1^3\Sigma_g^+$ potential. Because a reduction of Li (red curve) leads to a decrease in interspecies inelastic loss of Yb (blue curve), there is strong enhancement of Yb fluorescence at the Li_2 resonances. From [96].

a total of 8 passes at the atoms. This resulted in a peak intensity of about 6 kW/cm^2.

6.1.3 Li_2 photoassociation in the dual-species MOT

To perform photoassociation spectroscopy in the dual-species MOT, we frequency stabilize the diode laser to a a High Finesse WS7/1275 wave meter using Labview, and sweep the stabilization point in a triangle-wave fashion over a range of 500 MHz with a sweep frequency of 3 mHz. Concurrently, we record the fluorescence from each MOT in Labview and average over 2 periods of the triangle-wave sweep.

Figure 6.3 shows a compiled spectrum from a number of 500 MHz sweeps in the vicinity two Li_2 PA resonances, corresponding to the $\nu = -82$ and -83 vibrational states of the $1^3\Sigma_g^+$

excited-state potential. In order to understand the striking response of the Yb fluorescence on the Li_2 PA resonances, we examine the spatially integrated rate equation

$$\dot{N}_{\mathrm{Yb}} = L_{\mathrm{Yb}} - \gamma'_{\mathrm{Yb}} N_{\mathrm{Yb}} - \frac{K'_2}{V_{\mathrm{Li}}} N_{\mathrm{Li}}(\delta_{\mathrm{PA}}) N_{\mathrm{Yb}}, \tag{6.7}$$

where L_{Yb} is the loading rate in atoms/s, γ'_{Yb} is a one-body loss term that now includes loss due to ${}^3P_1 \rightarrow {}^3S_1$ scattering, $V_{\mathrm{Li}} = N_{\mathrm{Li}}/n_{\mathrm{Li}}(0)$, and we write the Li number as a function of the PA laser beam detuning from the atomic resonance (D_1 line) δ_{PA}. Note that we have ignored the Yb-Yb two-body inelastic term because the relatively large Yb-Li inelastic term ensures a low density of Yb. Furthermore, because of the increased one-body loss γ'_{Yb} due to ${}^3P_1 \rightarrow {}^3S_1$ scattering, Yb intraspecies inelastics are irrelevant even in the absence of Li.

Solving equation (6.7) for N_{Yb} in the steady state, we have

$$N_{\mathrm{Yb}} = \frac{L_{\mathrm{Yb}}}{\gamma'_{\mathrm{Yb}} + K'_2 N_{\mathrm{Li}}(\delta_{\mathrm{PA}})/V_{\mathrm{Li}}}, \tag{6.8}$$

where we find that $K'_2 N_{\mathrm{Li}}(\delta_{\mathrm{PA}})/(V_{\mathrm{Li}}\gamma'_{\mathrm{Yb}}) \approx 10$ from Yb lifetime measurements away from PA resonances. Thus, to first order the Yb atom number is inversely proportional to the Li atom number, and only saturates to its one-body limited value $N_{\mathrm{Yb}} = L_{\mathrm{Yb}}/\gamma'_{\mathrm{Yb}}$ for very large Li loss. From figure 6.3, we see that this inverse relationship of atom number leads to a marked enhancement of the signal-to-noise at Li_2 PA resonances in the Yb atom number detection channel.

6.2 YbLi photoassociation*

Because of the relatively dense background of Li_2 PA resonances in the search for YbLi* resonances, it is necessary to use the combined information of Yb and Li MOT fluorescence to normalize away the dependence of the Yb atom number on that of Li. In other words, we want only the variation of the interspecies inelastic rate coefficient, K'_2, with PA laser frequency, and not any residual signal from Li PA. From equation (6.8) we find that

$$K'_2 = \frac{V_{\mathrm{Li}} L_{\mathrm{Yb}}}{N_{\mathrm{Li}} N_{\mathrm{Yb}}} \left(1 - \frac{\gamma'_{\mathrm{Yb}}}{L_{\mathrm{Yb}}} N_{\mathrm{Yb}}\right), \tag{6.9}$$

where $N_{\mathrm{Yb}}/(L_{\mathrm{Yb}}/\gamma'_{\mathrm{Yb}})$ can be determined from the ratio of the Yb MOT fluorescence with and without Li present. Writing $K'_2 = K'_{2,\mathrm{bg}} + K'_{2,\mathrm{PA}}(\delta_{\mathrm{PA}})$ and noting that we already know the value $K'_{2,\mathrm{bg}}$ from section 6.1.1, we see that we can therefore extract the spectrum of $K'_{2,\mathrm{PA}}(\delta_{\mathrm{PA}})$ in absolute units. Note that we do not need to know the value in absolute units of the prefactor in equation (6.9), since we can simply scale the spectrum to match the known background value.

6.2.1 Observed spectrum

Figure 6.4 shows both the raw fluorescence measurements and extracted $K'_{2,\mathrm{PA}}(\delta_{\mathrm{PA}})$ spectrum in the vicinity of the 4 YbLi* PA resonances found in our dual-MOT experiment. Each of the peaks in figure 6.4(b) has a double-peak substructure consistent with the ground state hyperfine splitting of 228 MHz in Li. For the strongest detected PA resonance at $\delta_{\mathrm{PA}}/2\pi = -15.70$ GHz, the molecule production rate is 5×10^5 s^{-1}.

Our PA search in the dual-species MOT covered the frequency range δ_{PA} = 0 to -250 GHz, where δ_{PA} is the PA laser frequency detuning from the ${}^2S_{1/2} \rightarrow {}^2P_{1/2}$ atomic transition frequency. As we'll see in the next section, these PA resonances correspond to the second most weakly bound vibrational states, $\nu = -2$, for various excited state potentials. Thus, there is another set of lines closer to the atomic resonance. However, due to the drastic increase in spontaneous scattering, we cannot perform PA spectroscopy here. For lines more deeply bound than those shown in figure 6.4(b) (down to $\delta_{PA}/2\pi = -250$ GHz), we can conclude that the Franck-Condon factors are below our detection sensitivity.

While the 228 MHz substructure of each peak ensures that the resonances are due to the presence of ${}^2S_{1/2}$ Li, we must further confirm that the molecules created are not Yb*Li*. To check this, we perform separate tests for the two strongest PA lines at 15.70 and 22.39 GHz, in which we remove excited-state Yb atoms during the PA light exposure by pulsing the Yb MOT light and PA light 180° out of phase with a 10 kHz square wave. The ${}^3P_1$ spontaneous emission rate of $\Gamma = 2\pi \times 180$ kHz ensures that the excited state population is gone for the vast majority of the half period in which the MOT light is off. The detection of the same

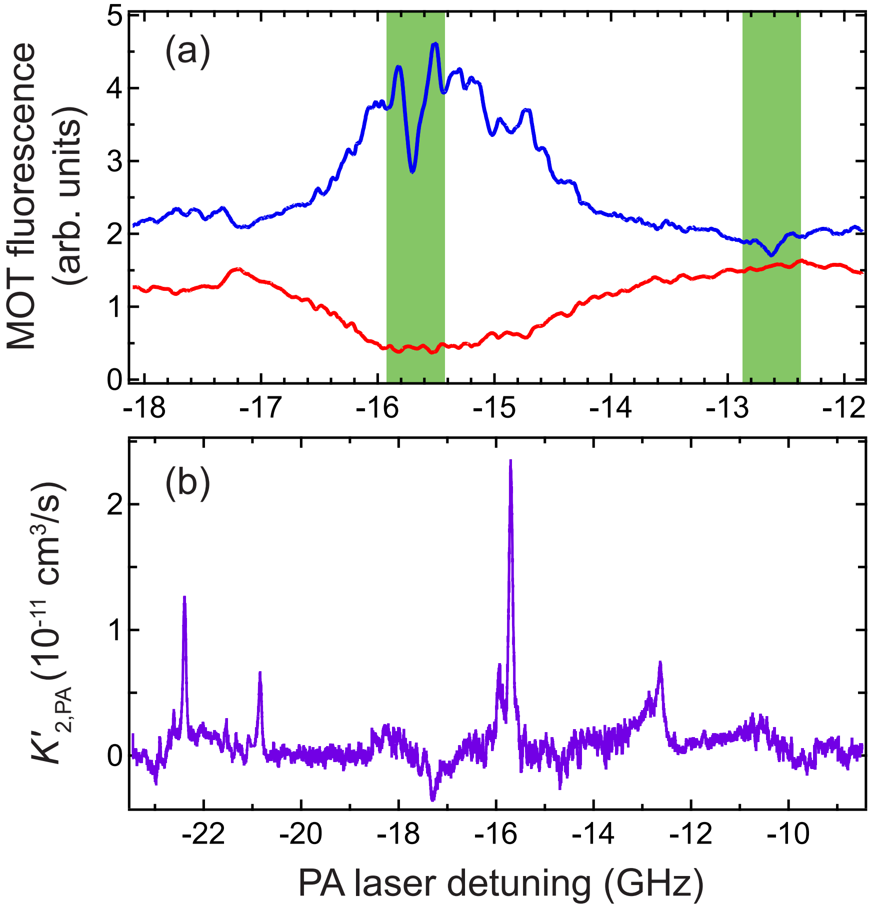

Figure 6.4: Observation of YbLi* photoassociation. (a) Raw fluorescence spectra for Yb (blue curve) and Li (red curve) revealing two interspecies PA resonances (highlighted in green) on top of a broad Li_2 PA feature. (b) Extracted two-body inelastic rate coefficient for YbLi* PA $K'_{2,\mathrm{PA}}(\delta_{\mathrm{PA}})$, where PA resonances now appear as peaks. For each of the 4 clear interspecies PA resonances, there is a double-peak structure with a separation of 228 MHz, corresponding to the ground state hyperfine splitting in Li. From [96].

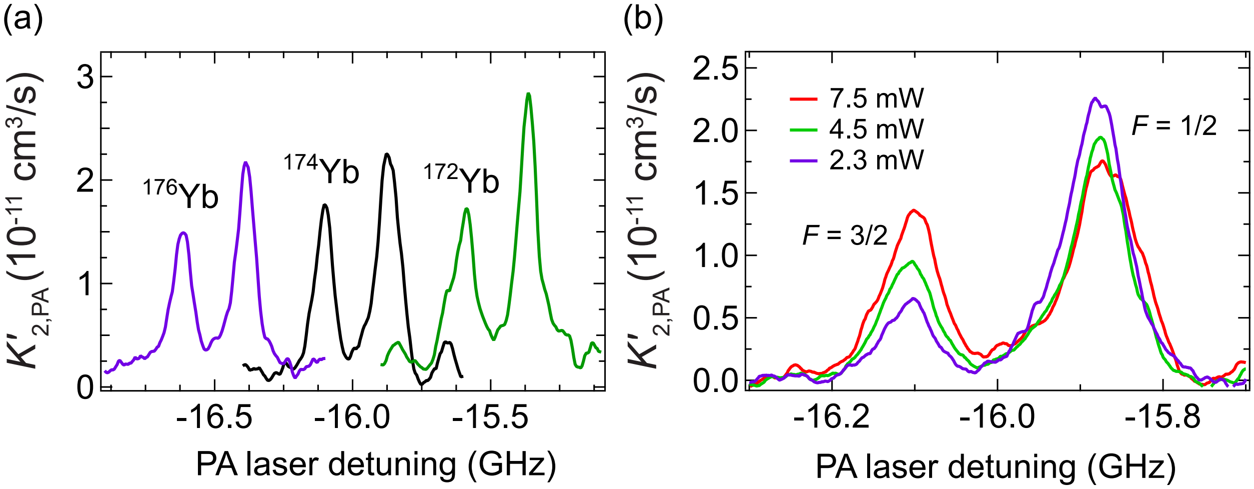

Figure 6.5: (a) Dependence of interspecies PA line position on Yb isotope. The changing reduced mass of YbLi* results in slight shifts of the bound state position. For ^{172}Yb(^{176}Yb) the isotope shift is +510(-510) MHz relative to the ^{174}Yb position. (b) Dependence of Li hyperfine peak substructure on the Li MOT repumping beam power. As the repump power is reduced, the population of the $F = 3/2 (F = 1/2)$ state decreases(increases), leading to the observed changing imbalance between the peaks in $K'_{2,\mathrm{PA}}$.

PA resonances under these conditions verifies that the molecules are indeed YbLi*.

To gain more information about the observed ^{174}Yb^{6}Li* PA resonances, we repeat the PA spectroscopy with two other ytterbium isotopes, ^{172}Yb and ^{176}Yb. The results are shown in figure 6.5(a). The changed reduced mass of YbLi* upon changing the Yb mass results in small shifts of the vibrational state position, with opposite direction for greater/smaller Yb masses. For the measurements at the 15.70 GHz resonance, we find a symmetric shift for ^{172}Yb and ^{176}Yb of positive and negative 510 MHz, respectively. Similarly, at the positions of the 22.39 and 20.89 GHz resonances, we find shifts of 405 and 390 MHZ, respectively. The sign of the isotope shifts are consistent with an accumulated bound state energy shift starting form the bottom of the molecular potential.

Additionally, we investigate the dependence of the PA resonance substructure on the power in the MOT repumping beams. In figure 6.5(b), we plot the extracted value of $K'_{2,\mathrm{PA}}$ in the vicinity of the strongest PA resonance for three different repump powers. As the repump power is decreased, the equilibrium population in the lower energy hyperfine state $F = 1/2$ increases, and that in $F = 3/2$ decreases. Since our rate equations analysis assumes that all Li atoms participate in PA at a single resonance position, the redistribution of ground state Li atoms manifests as a changing imbalance between the two peaks in $K'_{2,\mathrm{PA}}$.

6.2.2 Molecular potential identification and Franck-Condon factors

Armed with the measured spectrum for $K'_{2,\mathrm{PA}}$, the theory group of S. Kotochigova calculated the relativistic molecular potentials asymptoting to the $^2P_{1/2}$ and $^2P_{3/2}$ states [96]. Even though the fine structure splitting of the ^2P state $E_{fs}/h = 10.05$ GHz in Li is small, relativistic (i.e. spin-orbit) effects cannot be ignored for vibrational levels near dissociation. In the relativistic Hund's case (c), the quantum numbers of interest are the total electronic angular momentum $\vec{j} = \vec{l}_1 + \vec{s}_1 + \vec{j}_2$, its projection onto the internuclear axis Ω, and the total angular momentum $\vec{J} = \vec{j} + \vec{\ell}$. Here, $\vec{l}_1$ and $\vec{s}_1$ are the electronic orbital and spin angular momentum for Li, $j_2 = 0$ is the total electronic angular momentum of Yb, and $\vec{\ell}$ is the relative nuclear orbital angular momentum. Thus, there are 3 relativistic potentials with $\ell = 0$ for Yb($^1S_0$) + Li($^2P_{1/2,3/2}$), $j = 1/2$, $\Omega = 1/2$, and $j = 3/2$, $\Omega = 3/2$ and $1/2$, which are labeled $A(\Omega = 1/2)$, $B(\Omega = 3/2)$, and $C(\Omega = 1/2)$, respectively.

The *ab initio* relativistic potentials are used for the short range part of the potential, and are then smoothly connected to long range dispersion interaction potentials calculated using second-order degenerate perturbation theory. Then, the depth of the short range potentials and a heuristically added $-C_8/r^8$ long range term are varied to fit the observed PA resonance locations and isotope shifts. Because the MOT temperatures are well below the p-wave threshold, we begin with $\vec{\ell} = 0$ in the ground scattering state, and therefore have $J = 1/2$ before PA. Due to the additional unit of angular momentum introduced by the photon, the scattering state then couples to potentials with $J = 1/2$ and $3/2$. The resulting line position and potential identification for the 4 PA resonances are shown in Table 6.1. Figure 6.6 shows

	$\Delta_{174}/2\pi$ (GHz)	$\delta_{176-174}/2\pi$ (MHz)	Potl. (MHz)	J	v
E	-12.63	–			
T	-12.63	-512	B	3/2	-2
E	-15.70	-510			
T	-15.71	-513	A	1/2	-2
E	-20.84	-390			
T	-20.94	-398	C	3/2	-2
E	-22.39	-405			
T	-22.26	-405	C	1/2	-2

Table 6.1: PA resonance line positions and potential identifications for the YbLi* resonances in figure 6.4. The experimental (E) and theoretical (T) values for the ^{174}Yb^{6}Li* position $\Delta_{174}/2\pi$ and ^{176}Yb-^{174}Yb isotope shift $\delta_{176-174}/2\pi$ are compared in the second and third columns.

the square of the vibrationally averaged dipole moments (VADM^2) between the ground state scattering wave function and the 4 relevant excited states. The VADM is proportional to the Franck-Condon factor, and thus this plot suggests that the Franck-Condon factors for nearby, more deeply bound vibrational states are indeed much lower, as found experimentally. For more details on the calculations involved, the reader is referred to the original publication [96].

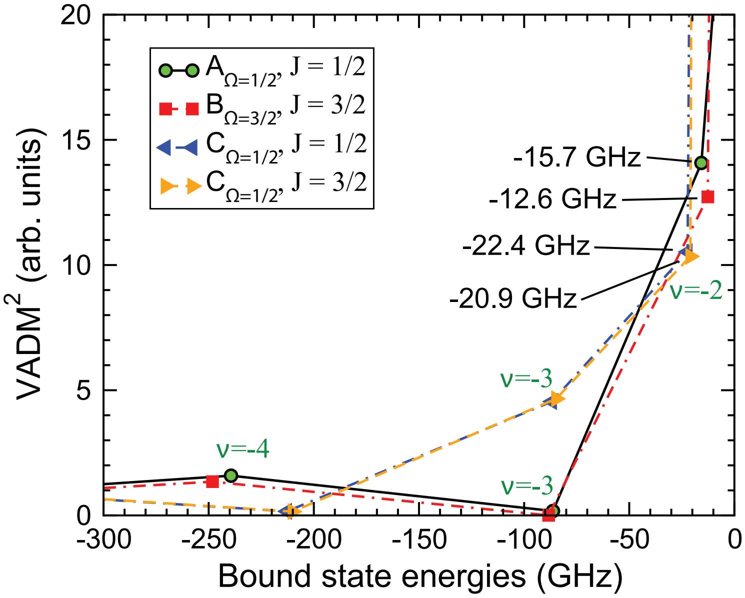

Figure 6.6: Vibrationally averaged dipole moment (squared) between the ground scattering and first few YbLi* vibrational states. The VADM^2 is proportional to the Franck-Condon factor. The sharp decrease after the first 2 vibrational states agrees with our experimental observation that states lower than $\nu = -2$ have Franck-Condon factors below our detection limit. Calculated by the group of S. Kotochigova. From [96].

Chapter 7

EVAPORATIVE COOLING IN DYNAMICALLY SHAPED OPTICAL TRAPS

Optical dipole traps (ODTs) are an extremely valuable tool in ultracold atomic physics[1], as they do not restrict they type of spin state in a magnetic atomic species that may be trapped, as is the case with magnetic traps. Furthermore, ODTs allow for the trapping of atoms with magnetically insensitive electronic ground states, which includes many of the exciting elements used in cold atom experiments today (e.g. Yb and Sr). Because the size scale of the trapping potential in an ODT is set by the Gaussian waist of a tightly focused laser beam, there result large confinement forces and small trap volumes (and thus high atomic densities). However, a shortfall of the ODT is that, in performing forced evaporative cooling by reducing the trapping laser power, the harmonic confinement near the trap minimum decreases as well. This has the end result that the rate of elastic scattering, and thus evaporative cooling, slows appreciably at low trap depths. While one could consider choosing a very small beam waist to ensure sufficiently high confinement at low depths for fast evaporation rates, this introduces the problem of excessively high densities at high depths leading to strong three-body inelastic loss and heating. Thus, we see that achieving efficient cooling is a problem of competing timescales which can change in hierarchy throughout forced evaporative cooling.

A useful way to analyze the competition of timescales in evaporative cooling dynamics is to define the ratio $R = \Gamma_{\mathrm{el}}/\Gamma_{\mathrm{loss}}$, where $\Gamma_{\mathrm{el}} = n_0\sigma\bar{v}$ is the elastic collision rate and Γ_{loss} is the per-particle loss rate for the loss process of interest (e.g. background single-body loss and two-body or three-body inelastic decay). In this chapter, we will concern ourselves only with the

---

[1] See section 2.1.2 for a full discussion of optical dipole traps.

case of a gas of identical bosons in their electronic ground state. In this case, we can neglect two-body decay mechanism and only consider background loss and three-body inelastic decay. Using the values $n_0 = N(m\bar{\omega}^2/2\pi k_B T)^{3/2}$, $\sigma = 8\pi a^2$, and $\bar{v} = \sqrt{8k_B T/\pi m}$ for a harmonically trapped gas of identical bosons in the s-wave limit, we find that $\Gamma_{\mathrm{el}} \propto N\bar{\omega}^3 T^{-1}$. From the analysis in section 3.2, we have that $\Gamma_{\mathrm{bg}} = \text{constant}$ and $\Gamma_{3\mathrm{b}} \propto N^2\bar{\omega}^6 T^{-3}$, resulting in scalings of $R \propto N\bar{\omega}^3 T^{-1}$ and $N^{-1}\bar{\omega}^{-3}T^2$, respectively.

To quantify the idea of "efficient evaporative cooling," we introduce a logarithmic measure of the gain in (peak) phase space density $\rho = n_0\lambda_{\mathrm{dB}}^3$ achieved for a given loss of atom number, defining the evaporation efficiency parameter $\gamma = -\ln(\rho_f/\rho_i)/\ln(N_f/N_i)$, where the subscripts i and f refer the initial and final quantities. We see that large values of the ratio R will result in efficient cooling, as in this case fewer atoms are lost to background or inelastic decay (i.e. N_f/N_i is not too small for a given ρ_f/ρ_i). From the scaling of the phase space density, $\rho \propto N\bar{\omega}^3 T^{-3}$, we see that, in the background-loss-dominated regime, maintaining large atom number N and high trap frequency $\bar{\omega}$ throughout evaporation leads to a large value of R and evaporation efficiency γ [57]. However, when three-body inelastic loss dominates, high values of N and $\bar{\omega}$ lead to a diminished evaporation efficiency. Thus, we desire a method to ensure that, even in the presence of three-body loss channels, the gas is maintained in the regime $R > 1$ throughout evaporation. While some groups have implemented numerical optimization of the power trajectory $P(t)$ during evaporative cooling in Gaussian-shaped traps [109, 84], the lack of independent control over the trap depth V_0 and frequency $\bar{\omega}$ significantly hinders the ability to create large atom number condensates, or condensates with fast cycle times.

The solution we present here is general to all cold atom experimental setups, as it only involves the implementation of time-averaged potentials created by center position modulation (CPM), or "painting" of the trapping laser focus by an acousto-optic modulator (AOM). For these experiments, we focus and evaporative cooling of ^{174}Yb only. The basic idea is to utilize the additional degree of freedom offered by changing the effective size of the trapping beam at the laser focus to achieve independent control over the trap depth

V_0 and frequency $\bar{\omega}$. This allows for dynamic shaping of the trapping potential. With this capability, the trajectory of laser power and painting amplitude may be numerically and/or experimentally optimized to achieve fast or efficient evaporation. We note that although a similar approach of dynamically changing the trap shape has been implemented with good success using a moving lens [63], the scheme presented here offers a much simpler method with faster dynamical shaping bandwidth.

As we'll see, in our experiments this approach turned out to be very successful, and allowed us to create the largest pure Yb BECs to date, as well as to achieve the fastest experimental cycle time for BEC production in optical traps to date [94]. We begin with a discussion of the specific time-averaged potential profile used in our experiments.

7.1 *Parabolic time-averaged potentials*

While one can realize virtually any time-averaged potential shape[2] using the technique of CPM, the potential chosen for these experiments is the parabolic potential. The main impetus for this choice lies in the simplicity of modeling the evaporative cooling dynamics in harmonic traps, as presented in section 3.2. In this section, we begin with a derivation of the FM waveform necessary to achieve a parabolic time-averaged potential. Then, we discuss the resulting trap depth and frequency dependence on the CPM amplitude h, as well as the application of this model for the potential to the actual potential used in our experiment.

7.1.1 FM waveform derivation

To implement this potential experimentally, we need to know the FM waveform that must be sent to the AOM. Using the formalism from section 2.1.3, we can solve for the necessary

---

[2] It is important to recall here that the protocol for creating time-averaged shapes presented in section 2.1.3 assumes a delta-function focus. Thus, when the CPM amplitude is not much larger than the beam waist, the Gaussian features of the true focus shape feature strongly in the resulting time-averaged potential.

painting function $f(t)$ using

$$\int_0^{f(t)} df'\, g(f') = v_0 t, \tag{7.1}$$

where $v_0 = \dot{f}|_{t=0}$ is a constant fixed by the modulation frequency and $g(x) = (1-x^2)\Theta(1-|x|)$ is the desired potential shape. Performing the integration we arrive at the cubic equation

$$f(t) - f(t)^3/3 - v_0 t = 0, \tag{7.2}$$

with solutions plotted in figure 7.1(a). Clearly, the solution of interest for us is the one which spans the range $-1 \leq f \leq 1$. We then create the periodic FM waveform $I_{1\text{D}}(x,h)$ using the prescription described in section 2.1.3, resulting in the time-averaged potential plotted in figure 7.1(b). For these Gaussian-beam-painted profiles, we use the 1-dimensional initial profile $I_{\text{Gauss,1D}}(x) = P(w_0\sqrt{\pi/2})^{-1}\exp(-2x^2/w_0^2)$.

To calculate the analytical form for the delta-function parabolic potential, we again refer to the formalism developed in section 2.1.3. From equation (2.17), we have

$$I_{1\text{D}}(x,h) = \frac{2P}{hv_0T} g(x/h), \tag{7.3}$$

where T is the full period of the FM function f(t). Using equation (7.2) and noting by inspecting figure 7.1(a) that $f(-T/4) = -1$ and $f(T/4) = 1$, we find $T = 8/(3v_0)$, giving

$$I_{1\text{D}}(x,h) = \frac{3P}{4h^3}(h^2 - x^2)\Theta(h - |x|). \tag{7.4}$$

The delta-function-painted potential for various values of h are shown in figure 7.1(b). For CPM amplitudes h larger than a few beam waists, w_0, the painted potential for the Gaussian beam becomes nearly identical to that for a delta-function beam.

7.1.2 Trap frequencies and depth

For the purposes of modeling the evaporation dynamics, we would like to know the dependence of the trap frequencies ω_i and trap depth V_0 on the painting amplitude for the realistic

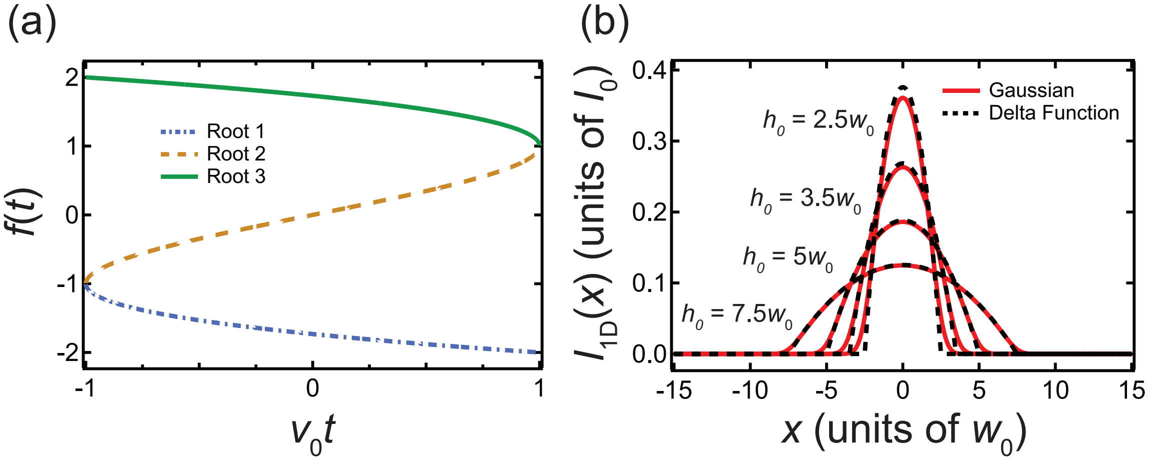

Figure 7.1: Creating a parabolic time-averaged potential. (a) Solutions to the cubic equation (7.2). The dashed yellow curve (root 2) is the one with which we create the periodic FM waveform. (b) 1-dimensional time-averaged profiles for Gaussian (red solid lines) and delta-function (black dashed lines) initial beam profiles for various values of the CPM amplitude h in units of the Gaussian beam waist w_0. From [94].

Gaussian beam paintbrush, where we again assume that painting occurs in the x dimension. In this analysis we will neglect the effects of gravity, but will consider the full realistic trapping potential for our experiment in the following section. Since producing the time-averaged intensity profiles for the Gaussian beam in figure 7.1(b) is a numerical procedure, we do not have an analytical expression with which to calculate these directly. Instead, we can extract these quantities from the numerically calculated profiles themselves by using the peak calculated value for the intensity to determine V_0, and by performing a parabolic fit in the vicinity of $x = 0$ to determine ω_i. To connect these values with the familiar ones for a standard Gaussian beam optical trap, we define the CPM trap frequencies and depth as follows:

$$\begin{aligned} \omega_x^2 &= \frac{8\alpha P}{\pi m w_0^4}(f_\omega(h/w_0))^2, \qquad & \omega_y^2 &= \frac{8\alpha P}{\pi m w_0^4} f_V(h/w_0) \\ \omega_z^2 &= \frac{4\alpha P}{\pi m w_0^2 z_R^2} f_V(h/w_0), \qquad & V_0 &= \frac{2\alpha P}{\pi w_0^2} f_V(h/w_0). \end{aligned} \tag{7.5}$$

Here, α is the atomic polarizability for the particular ODT wavelength. Note that the trap frequencies in the y and z dimensions are only affected by the painting through the reduction of peak intensity, which is quantified with the reduction factor $f_V(h/w_0)$, which clearly must satisfy $f_V(0) = 1$. The x trap frequency reduction factor $f_\omega(h/w_0)$ is determined by comparing a quadratic fit to the numerically calculated potential with the curvature of the Gaussian potential at $h = 0$, ensuring $f_\omega(0) = 1$. The two reduction factors are plotted in figure 7.2.

We expect that for CPM amplitudes much larger than the beam waist, $h \ll w_0$, the trap depth and frequency in the painting dimension should approach those of the delta-function-painted potential in equation (7.4). By comparing the peak values and harmonic expansion near $x = 0$ of $I_{\rm 1D}(x, h)$ in equation (7.4) and $I_{\rm Gauss,1D}(x)$, one can show

$$\frac{\omega_\delta^2(h)}{\omega_x^2(h=0)} = \sqrt{\frac{\pi}{2}}\frac{3w_0^3}{8h^3} \quad \text{and} \quad \frac{V_\delta(h)}{V_0(h=0)} = \sqrt{\frac{\pi}{2}}\frac{3w_0}{4h}, \tag{7.6}$$

where $\omega_\delta(h)$ is the trap frequency and $V_\delta(h)$ the trap depth for an atom in the delta-function-painted potential with CPM amplitude h. Figure 7.2 shows the comparison between the

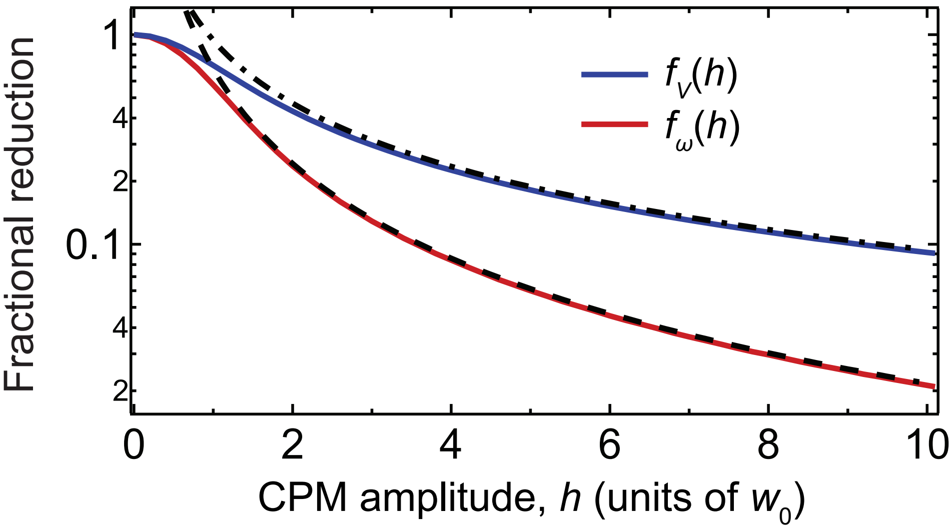

Figure 7.2: Reduction due to painting of trap depth $V_0(h)$ (solid blue line) and frequency $\omega_x(h)$ (solid red line) in the painting dimension relative to the values for a Gaussian trap for fixed laser power as a function of CPM amplitude h, expressed in units of the beam waist w_0. The black dot-dashed (dashed) line is the trap depth (frequency) of the delta-function-painted potential relative to the unpainted Gaussian trap. For large values of h, we see that the difference between the Gaussian and delta-function paintbrushes is negligible. Adapted from [94].

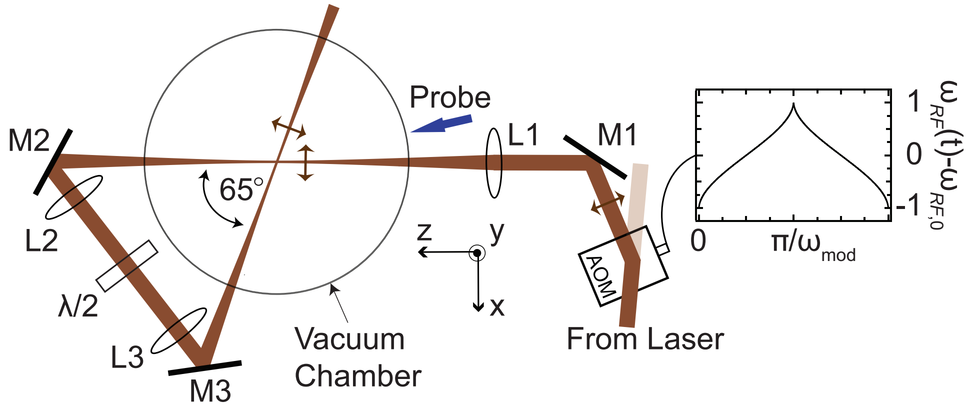

Figure 7.3: Experimental setup for the crossed, painted ODT. The force of gravity points in the y direction. The horizontally oriented AOM is driven by the FM waveform that creates a parabolic time-averaged intensity profile.

delta-function and Gaussian paintbrushes.

7.2 *Experimental realization of the parabolic time-averaged potential*

In this section we describe the specific implementation of the parabolic CPM trap with ^{174}Yb in our crossed optical dipole trap, as well as describe the full treatment of the trap depth and frequencies of the crossed trap in the presence of a linear gravitational potential. This theoretical model for the crossed, painted ODT is then compared with good agreement to measurements of the trap frequency and depth for various combinations of power and CPM amplitude.

7.2.1 Full potential in the presence of gravity

Figure 7.3 shows a schematic of our trapping scheme, where we recycle a single beam to form the crossed trap in order to double the maximum power achievable at the atoms. In this diagram, the y direction is the direction of the force of gravity (i.e. the vertical), and all of the CPM occurs in the horizontal plane.

The output of a 1064 nm fiber laser (IPG YLR-100-LP) is sent through an AOM (80MHz, Intraaction ATM-804DA6B) that receives a frequency-modulated RF signal $\omega_{RF}(t) = \omega_{RF,0} + \delta\omega_{RF} f(t)$, where $f(t)$ is the FM function derived in section 7.1.1, and diffracts a maximum of about 70 W into the first-order beam. This light is then focused onto the atoms and subsequently recycled and imaged back onto the atoms at an angle of 65° with a magnification of 5/6 and with orthogonal polarization. Due to losses in viewports and lenses, the power in the second recycled beam at the atoms is about 90% of that in the first pass. For the largest FM amplitudes used of 7 MHz (14 MHz peak-to-peak), we achieve CPM amplitudes at the atoms of 260 μm (520 μm peak-to-peak).

Introducing a rotated coordinate system (x', y', z') for the second pass of the beam, which is related to (x, y, z) by a 65° rotation in the $z-x$ plane, we can express the complete potential felt by the atoms as

$$V_T(x, y, z, P, h) = V_1(x, y, z, P, h) + V_2(x', y', z', P, h) + mgy, \tag{7.7}$$

where

$$V_i(x, y, z, P, h) = V_{i,0}(z, P, h) \frac{I_{1\mathrm{D}}(x, h)}{I_{1\mathrm{D}}(0, h)} e^{-2y^2/w_{i,y}(z,P)} \tag{7.8}$$

is the potential for the $i = 1, 2$ pass of the beam, and

$$V_{i,0}(z, P, h) = \frac{2\alpha P f_V(h/w_{i,x}(0, P))}{\pi m w_{i,x}(z, P) w_{i,y}(z, P)}. \tag{7.9}$$

Note that since $\alpha < 0$, we have $V_{i,0} < 0$. The potential shape in the painting dimension (x) is given by the function $I_{1\mathrm{D}}(x, h)/I_{1\mathrm{D}}(0, h)$ from section 7.1.1 (see the red curves in figure 7.1(b)). In equation (7.8) we include the effects of beam ellipticity and thermal lensing by using two independent, power-dependent waists $w_{i,x}(z, P)$ and $w_{i,y}(z, P)$. The power dependence of the x and y beam waists is calibrated by monitoring the trapping beam focus on a CCD over the full range of powers used in the experiment.

In order to compute the trap depth and frequencies of the crossed, painted ODT in the presence of gravity, we begin by analyzing the total potential in the vertical direction at the horizontal trap center, $V_T(0, y, 0, P, h)$. The action of gravity is to tilt the crossed beam potential, displace the total potential minimum, and reduce the effective depth of the trap, V_0. Thus, in order to calculate $\bar{\omega}$ and V_0 for arbitrary values of P and h, we must first numerically solve for the two roots $y_1^*(P, h)$ and $y_2^*(P, h)$ of the equation $\partial V_T(0, y, 0, P, h)/\partial y|_{y=y_i^*} = 0$. Because these numerical solutions are rather time consuming, and because we will need these roots for many points $(P(t), h(t))$ while performing numerical simulations of the forced evaporative dynamics, we solve for the two roots numerically for a dense grid of points (P, h) spanning the domain of experimentally used values. We then convert these values into a 2D interpolating function in Mathematica, which can be easily and quickly referenced at each step of a numerical integration of the dynamics.

Assuming $y_1^*(P, h) < y_2^*(P, h)$ (i.e. y_2^* corresponds to the trap minimum), the effective depth of the trap can then be found from

$$\begin{aligned} V_0(P, h) &= V_T(0, y_1^*(P, h), 0, P, h) - V_T(0, y_2^*(P, h), 0, P, h) \\ &= V_{1,0}(0, P, h) \left[e^{-2(y_1^*)^2/w_{1,y}^2} - e^{-2(y_2^*)^2/w_{1,y}^2} \right] \\ &\quad + V_{2,0}(0, P, h) \left[e^{-2(y_1^*)^2/w_{2,y}^2} - e^{-2(y_2^*)^2/w_{2,y}^2} \right] + mg(y_1^* - y_2^*), \end{aligned} \tag{7.10}$$

where we've removed the arguments (P, h) from y_1^*, y_2^*, $w_{1,y}$, and $w_{2,y}$ for simplicity. Then, by expanding the single-beam potentials $V_i(\epsilon, y_2^*, 0, P, h)$, $V_i(0, y_2^* + \epsilon, 0, P, h)$,and $V_i(0, y_2^*, \epsilon, P, h)$ for small displacements ϵ about the trap minimum position $(0, y_2^*, 0)$, we find the trap frequencies for each beam to be

$$\begin{aligned} \omega_{i,x}(P, h) &= \left[\frac{8|\alpha|P}{\pi m w_{i,y} w_{i,x}^3} e^{-2(y_2^*/w_{i,y})^2} \right]^{1/2} f_\omega\left(\frac{h}{w_{i,x}}\right), \\ \omega_{i,y}(P, h) &= \left[\frac{8|\alpha|P}{\pi m w_{i,x} w_{i,y}^3} f_V\left(\frac{h}{w_{i,x}}\right) e^{-2(y_2^*/w_{i,y})^2} \left(1 - \left(\frac{2y_2^*}{w_{i,y}}\right)^2\right) \right]^{1/2}, \\ \omega_{i,z}(P, h) &= \left[\frac{4|\alpha|P\lambda^2}{\pi^3 m w_{i,x}^3 w_{i,y}^3} f_V\left(\frac{h}{w_{i,x}}\right) e^{-2(y_2^*/w_{i,y})^2} \right]^{1/2}, \end{aligned} \tag{7.11}$$

where λ is the trapping laser wavelength. We are now in a position to write the total potential in the harmonic approximation as (dropping the P and h arguments)

$$V_T(x, y_2^* + y, z) \approx \frac{m}{2}\left(\omega_{1,x}^2 x^2 + \omega_{1,y}^2 y^2 + \omega_{1,z}^2 z^2 + \omega_{2,x}^2 (x')^2 + \omega_{2,y}^2 (y')^2 + \omega_{2,z}^2 (z')^2\right), \tag{7.12}$$

where the two coordinate systems are related as follows:

$$\begin{pmatrix} x' \\ y' \\ z' \end{pmatrix} = \begin{pmatrix} \cos\theta & 0 & \sin\theta \\ 0 & 1 & 0 \\ -\sin\theta & 0 & \cos\theta \end{pmatrix} \begin{pmatrix} x \\ y \\ z \end{pmatrix}, \tag{7.13}$$

and θ is the angle between the two crossed beams (65° in our case). Thus, the total trap frequency in the y direction is simply given by $\omega_y = \sqrt{\omega_{1,y}^2 + \omega_{2,y}^2}$. Furthermore, performing the coordinate transformation in equation (7.13), we can write the potential in the $x - z$ plane as the following quadratic form:

$$V_T(x, z) = \frac{m}{2} \begin{pmatrix} x \\ z \end{pmatrix}^\top \begin{pmatrix} a & b/2 \\ b/2 & c \end{pmatrix} \begin{pmatrix} x \\ z \end{pmatrix}, \tag{7.14}$$

where

$$\begin{aligned} a &= \omega_{1,x}^2 + \omega_{2,x}^2 \cos^2\theta + \omega_{2,z}^2 \sin^2\theta, \\ b &= 2\cos\theta\sin\theta(\omega_{2,x}^2 - \omega_{2,z}^2), \\ c &= \omega_{1,z}^2 + \omega_{2,x}^2 \sin^2\theta + \omega_{2,z}^2 \cos^2\theta. \end{aligned} \tag{7.15}$$

We now want to diagonalize the 2×2 matrix in equation (7.14), since the eigenvectors are the principal axes of the trap in the $x - z$ plane, and the eigenvalues the trap frequencies ω_x and ω_z. In fact, we only care about the eigenvalues, since the directions of the principal axes do not feature in the evaporation dynamics. Thus, we arrive at the final trap frequencies:

$$\begin{aligned} \omega_x^2 &= \frac{1}{2}\left(a + c + \sqrt{b^2 + (a-c)^2}\right) \\ \omega_y^2 &= \omega_{1,y}^2 + \omega_{2,y}^2 \\ \omega_z^2 &= \frac{1}{2}\left(a + c - \sqrt{b^2 + (a-c)^2}\right). \end{aligned} \tag{7.16}$$

For the purpose of simulating forced evaporation dynamics, we evaluate the trap depth $V_0(P,h)$ and geometric mean trap frequency $\bar{\omega}(P,h)$ for a dense grid of points (P,h) as done for the two roots y_1^* and y_2^*, and create interpolating functions in Mathematica. These may then be evaluated very quickly for arbitrary values of P and h in each iteration of the numerical integration.

7.2.2 Comparison of trap model with experiment

With a theoretical model for the trap depth $V_0(P,h)$ and frequency $\bar{\omega}(P,h)$ of our crossed, painted ODT, we now compare our predicted trap parameters with those observed in the experiment with ^{174}Yb. To measure the trap depth, we load the Yb cloud from the compressed MOT, quickly change the power and CPM amplitude to desired values, and monitor the evaporation dynamics (i.e. number and temperature as a function of time) at fixed trap depth. Furthermore, at the given setting (P,h), we measure the Yb trap frequencies (to be compared with the model later) using the parametric heating method. We then perform a least squares fit to the data $N(t)$ and $T(t)$ using the number and temperature evolution described by the evaporation dynamics equations in section 3.2.5. We assume that only s-wave scattering occurs as the d-wave threshold for ^{174}Yb is 75 μK, resulting in the collision cross section $\sigma = 8\pi a^2$, where $a = 5.6$ nm. Since there are no two-body loss channels for ground state Yb, $\Gamma_{\mathrm{2b}} \propto K_2 = 0$, and thus the free parameters in this fit are the initial number $N(0)$, the initial temperature $T(0)$, the three-body inelastic rate coefficient K_3, the background lifetime Γ_{bg}, and the trap depth $V_0(P,h)$. Figure 7.4 shows the measured number and temperature dynamics for 3 different fixed trap settings (P,h), along with fits to the evaporative dynamics equations. The extracted trap depths are in good agreement with those predicted by the model over a large dynamic range (from ≈ 10 μK to ≈ 1 mK).

In addition to comparing predicted and measured trap depths, we also want to know how well our model reproduces the trap frequencies, or for evaporation dynamics modeling purposes, the geometric mean $\bar{\omega}$. For this comparison, we measure using the parametric heating method the 3 trap frequencies for 6 different settings of (P,h), including the 3 used

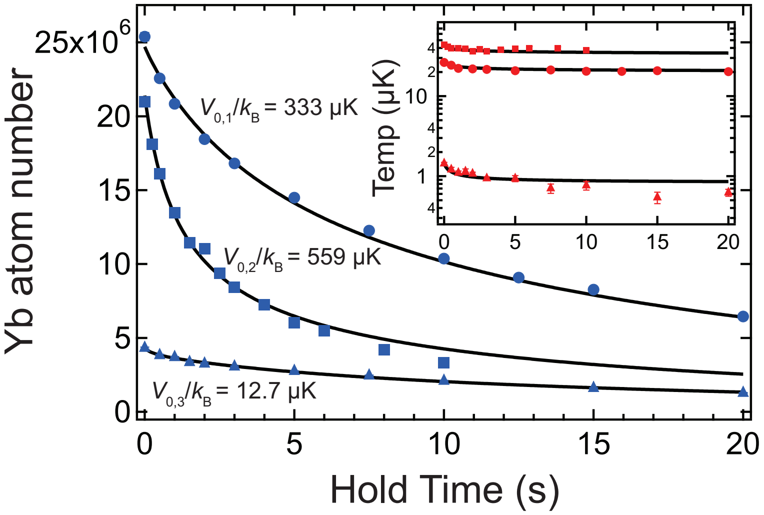

Figure 7.4: Comparison of trap depth model with experiment. For 3 different settings of (P, h), we measure the number $N(t)$ (blue points) and temperature $T(t)$ (red points) evolution at fixed depth. The black solid lines are least squares fits to the data using the equations for evaporation dynamics $\dot{N}$ and $\dot{T}$ from section 3.2.5. The three trap configurations used are: (1, solid circles) $P = 58$ W, $h = 259$ μm; (2, solid squares) $P = 58$ W, $h = 130$ μm; (3, solid triangles) $P = 2.2$ W, $h = 113$ μm. The fitted depths $V_{0,i}$ for each situation are given on the graph above. Our trap model predicts the values $V_{0,1}/k_B = 300$ μK, $V_{0,2}/k_B = 575$ μK, and $V_{0,3}/k_B = 13.3$ μK. From [94].

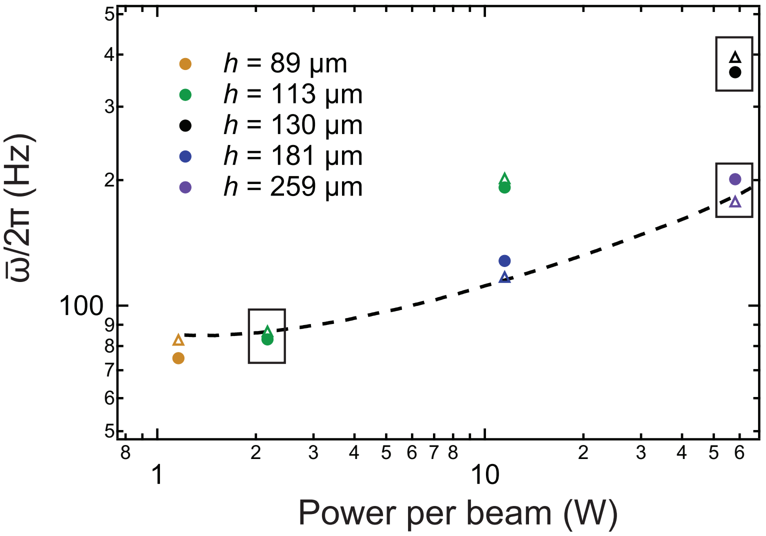

Figure 7.5: Comparison of measured (solid circles) and predicted (open triangles) values for the geometric mean trap frequency. Different CPM amplitudes h are depicted by different colors (see legend). The 3 boxed points correspond to the same trapping conditions used in the measurements in figure 7.4. The black dashed line follows the trap frequency $\bar{\omega}(t)$ for the optimized trajectory presented in figure 7.7. From [94].

for the depth measurements in figure 7.4. The results are shown in figure 7.5, where we plot the geometric mean trap frequency $\bar{\omega}$ as a function of power, and present different values of the CPM amplitude using different colors. As with the trap depth, there is good agreement between the measured values and those predicted by the model in section 7.2.1.

The ability of our trap model to quantitatively reproduce the depth and frequency of the crossed, painted ODT potential over such a large range of P and h values instills confidence that we can use this model to perform simulations of the forced evaporative cooling dynamics for arbitrary trajectories of power $P(t)$ and CPM amplitude $h(t)$. These simulations can then for instance be used to optimize the evaporation efficiency and guide the parameters used in the experiment. This optimization procedure will be the topic of the next section.

7.2.3 Numerical optimization of the forced evaporative cooling trajectory

In the absence of inelastic and background loss and heating due to spontaneous scattering, it is possible to construct analytical solutions to the equations of forced evaporation dynamics that maintain a given value of the parameter $\eta(t) = V_0(t)/(k_B T(t))$, assuming the fixed relationship $\bar{\omega} \propto P^{1/2}$ [83]. These analytical solutions can then be analyzed to maximize the evaporation efficiency γ given the constraint $\dot{\eta} = 0$. With independent control over both the depth V_0 and frequency $\bar{\omega}$ using the laser power and CPM amplitude, however, it becomes essential to implement a numerical optimization procedure in order to predict the most efficient trajectories (i.e. time-dependent profiles) $P(t)$ and $h(t)$. Similarly, in order to include the realistic effects of inelastic loss and heating, one must also turn to numerical methods. Thus, we aim to utilize our trap model for the depth and frequency as a function of the power and CPM amplitude to maximize the efficiency of forced evaporative cooling by numerically integrating the dynamical equations $\dot{N}$ and $\dot{T}$ from section 3.2.5.

To this end, we implement a gradient ascent optimization method with the evaporation efficiency $\tilde{\gamma} = -\ln(\rho(t_f)/\rho(0))/\ln(N(t_f)/N(0))$ as the parameter to be maximized. Here, we require that the final time t_f satisfy $\rho(t_f) = 1$, i.e. we optimize the evaporation trajectory to the point of quantum degeneracy. For these simulations, we use values for the background lifetime $\Gamma_{\mathrm{bg}}^{-1}$ and three-body inelastic rate coefficient K_3 that are consistent with the experimentally optimized trajectory presented later in this section. Furthermore, we fix the initial number $N(0)$ and temperature $T(0)$ (and thus initial phase space density $\rho(0)$) to be equal to the measured initial conditions[3]. Thus, the only parameters to be varied in performing these simulations are those determining the trajectories of power and CPM amplitude. Labeling these parameters $\{p_i\}$, the evaporation efficiency can be written as a function of these only, $\tilde{\gamma}(\{p_i\})$, and the gradient ascent optimization may be executed by running an evaporation simulation to point of quantum degeneracy for some initial set $\{p_{i,0}\}$, calculating $\tilde{\gamma}$ for that trajectory, taking the gradient (numerically) with respect these parameters $\nabla_{\vec{p}}\tilde{\gamma}$, and

---

[3] For these optimization experiments, we always begin forced evaporative cooling with the same trapping conditions, with P and h equal to the values corresponding to the purple points in figure 7.5

iterating until a maximum efficiency $\tilde{\gamma}_{\mathrm{opt}}$ is found for the optimized parameter set $\{p_{i,\mathrm{opt}}\}$.

For this optimization, we attempt both exponential $P(t) = P_0 e^{-t/\tau_P}$ and bi-exponential $P(t) = P_0 \left(c e^{-t/\tau_{P_1}} + (1-c) e^{-t/\tau_{P_2}} \right)$ power profiles, while for the CPM amplitude, we try profiles of the form $h(t) = h_1 e^{-t/\tau_h} + (h_0 - h_1)$, $h(t) = \max(h_0 - \beta t, 0)$, $h(t) = \max(h_0 - h_1(1 - e^{-t/\tau_h}), 0)$, and $h(t) = \max(h_0 - (t/\tau_h)^2, 0)$. As noted above, the initial power $P_0 = 58$ W and CPM amplitude $h_0 = 259$ μm for each of these are fixed while running the optimization algorithm.

From optimizing the evaporation trajectory using a variety of CPM amplitude profiles $h(t)$ with the bi-exponential power profile, we find that the algorithm pushes the bi-exponential towards a single exponential, with $\tau_{P_1} \to \tau_{P_2}$. Furthermore, the optimized evaporation efficiency is very robust to the form of the CPM amplitude profile, with only 1% differences in the optimized efficiency values $\tilde{\gamma}_{\mathrm{opt}}$ for all of the profiles $h(t)$ above in conjunction with the exponential power profile with $\tau_P = 1$ s. Because of this lack of dependence on the specific details of the profile $h(t)$, we choose to utilize the linear profile for subsequent optimization, as it is the simplest option.

In addition to the robustness of the optimized efficiency to the shape of the CPM amplitude profile, $\tilde{\gamma}_{\mathrm{opt}}$ depends very weakly on the timescale of evaporation. To investigate this, we run the optimization algorithm for fixed values of the power trajectory decay constant τ_P, varying only the slope of the linear CPM amplitude ramp, β. The results for the range $0.8 \text{ s} \leq \tau_P \leq 3$ s are shown in figure 7.6, where we plot both $\tilde{\gamma}_{\mathrm{opt}}$ and the optimized value of the slope β_{opt}. Clearly, the maximum achievable efficiency varies little over this range of τ_P, with the slope β_{opt} simply changing to recreate the same final CPM amplitude for each power decay timescale. The slight downward slope of $\tilde{\gamma}_{\mathrm{opt}}$ versus τ_P is likely due to the presence of the fixed background loss timescale, $\Gamma_{\mathrm{bg}}^{-1}$, which cannot be mitigated using dynamical trap shaping. The relatively large value of $\tilde{\gamma}_{\mathrm{opt}} \approx 4$ and its lack of dependence on the evaporation timescale suggests that our parabolic CPM trap successfully mitigates three-body inelastic loss and ensures a large value of η throughout evaporation.

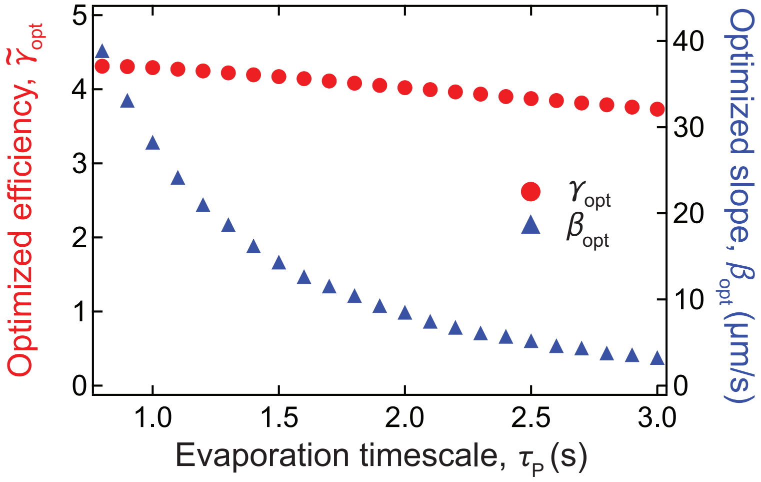

Figure 7.6: Evaporation efficiency optimization for fixed power decay timescale τ_P, revealing the robustness of $\tilde{\gamma}_{\mathrm{opt}}$ to the total evaporation time in this range. The optimized slope β_{opt} of the linear CPM amplitude profile $h(t)$ adjusts with τ_P in order to achieve a similar final trap configuration. From [94].

7.2.4 Experimental optimization of the forced evaporative cooling trajectory

In order to investigate the evaporation efficiency for different power and CPM amplitude trajectories in the experiment, we perform forced evaporative cooling all the way to BEC, and optimize the total number in the condensate. In agreement with the numerical simulation results presented in the previous section, we find through experimental optimization that the maximum efficiency achievable is quite robust to the exponential timescale τ_P, and that the system favors a single exponential decay of power as opposed to the bi-exponential. Furthermore, the largest experimental value of γ is realized for the linear CPM amplitude profile.

Figure 7.7 shows a typical experimentally optimized evaporative cooling trajectory, with an efficiency $\gamma = 3.8$ close to the largest values predicted by our numerical model (see figure 7.6). Before beginning the reduction of power and painting for these measurements, we wait

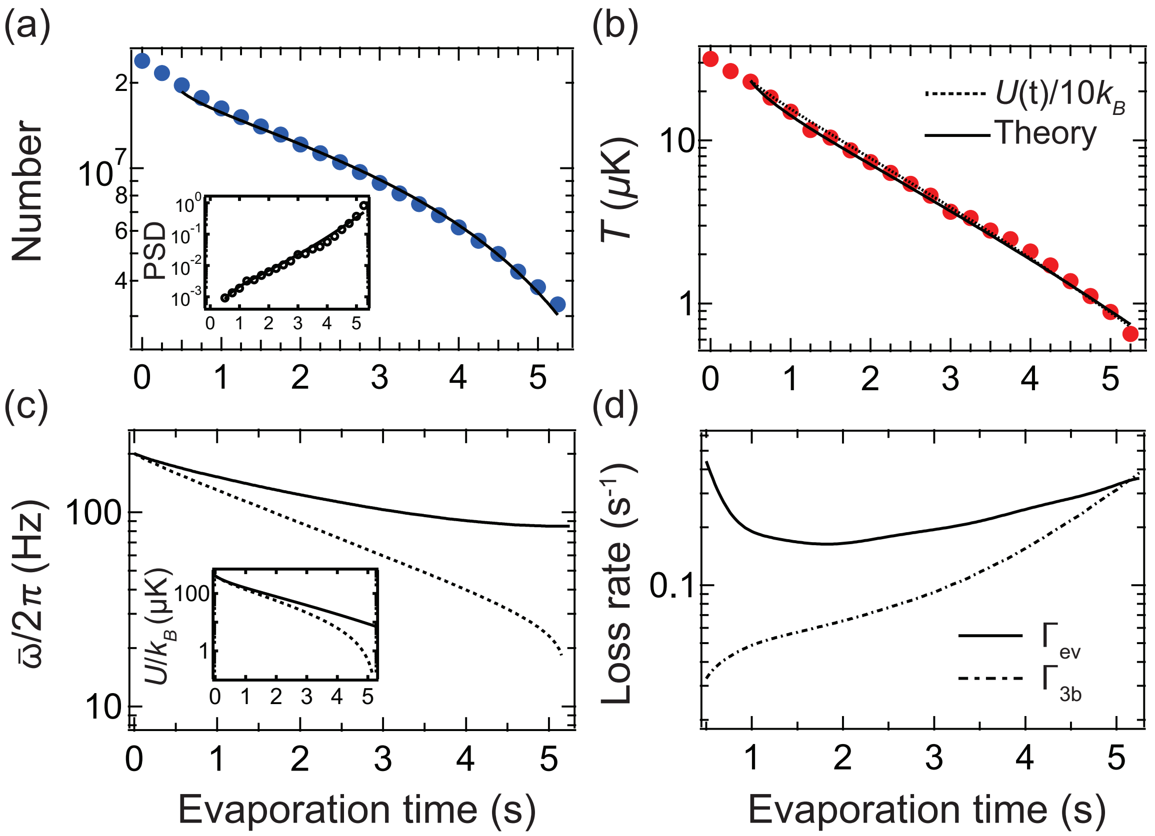

Figure 7.7: Experimentally optimized trajectory for evaportive cooling of ^{174}Yb in the dynamically shaped ODT. Measured number ((a), blue circles) and temperature ((b), red circles) evolution with least squares fit (solid black line) to the evaporation dynamics equations $\dot{N}$ and $\dot{T}$ from section 3.2.5 using the CPM trap model described in section 7.2.1. The temperature trajectory $T(t) = U(t)/(10k_B)$ is nearly equal to the fitted trajectory for the entirety of the cooling, demonstrating that the dynamically shaped ODT successfully maintains a large value of η. The inset shows the corresponding trajectory of phase space density (PSD), revealing that our theoretical model successfully captures the evaporation dynamics over 3 orders of magnitude in PSD. (c) Trap frequency and depth (inset) evolution for these measurements (solid lines) compared to the those with fixed CPM amplitude (dashed lines). (d) Per-particle loss rates for evaporation (solid line) and three-body inelastic loss (dot-dashed line) throughout the cooling sequence. From [94].

500 ms for atoms in the wings of the trap to escape. For the fits in figure 7.7(a) and (b) to the number and temperature evolution, the only free parameters are the initial number $N(0)$ and temperature $T(0)$ and the three-body inelastic rate coefficient K_3. The least squares fit to the data of the theoretical model, which includes the forced evaporative cooling dynamics described in section 3.2.5 and the CPM trap model described in 7.2.1, shows very good agreement with the observed dynamics over 3 orders of magnitude in phase space density (inset to figure 7.7(a)), and returns a value of $K_3 = (1.08 \pm 0.03) \times 10^{-28}$ cm^{6}s^{-1}.

From the experimental power and CPM amplitude profiles, we can plot the evolution of the trap frequency $\bar{\omega}(t)$ and depth $V_0(t)$ (see figure 7.7(c) and inset). Clearly, the dynamically shaped ODT successfully maintains a large value of $\bar{\omega}$ throughout evaporation, while still reducing the depth enough to reach quantum degeneracy. As is clear from the behavior of $\bar{\omega}(t)$ and $V_0(t)$ without CPM amplitude control (dashed lines in figure 7.7(c) and inset), the standard ODT would result in a drastically reduced elastic scattering rate, and therefore evaporative cooling rate, at the end of evaporation.

Finally, figure 7.7(d) demonstrates the ability of the dynamically shaped ODT to mitigate the problem of three-body inelastic loss, and maintain a dominance of evaporative loss over three-body loss. Furthermore, while maintaining a roughly constant value of $\eta(t) \approx 10$, the evaporative cooling rate begins increasing after an initial fast decay, due to the CPM trap's ability to maintain a high trap frequency. Clearly, with the dynamically shaped trap it is possible to achieve runaway evaporation where $d\Gamma_{\mathrm{el}}/dt > 0$. However, we do not find this to be an efficient cooling protocol due to the strong enhancement of three-body inelastic loss due to the large densities resulting from such trajectories.

7.3 Application to large and fast BEC production

In order to produce the largest condensates, we begin with an evaporation trajectory to the point $\rho = 1$ identical to that used for the measurements in figure 7.7, since this resulted in the largest efficiency γ and therefore largest final number $N(t_f)$. However, as can be seen in figure 7.7(d) towards the end of the sequence, the three-body inelastic loss rate grows

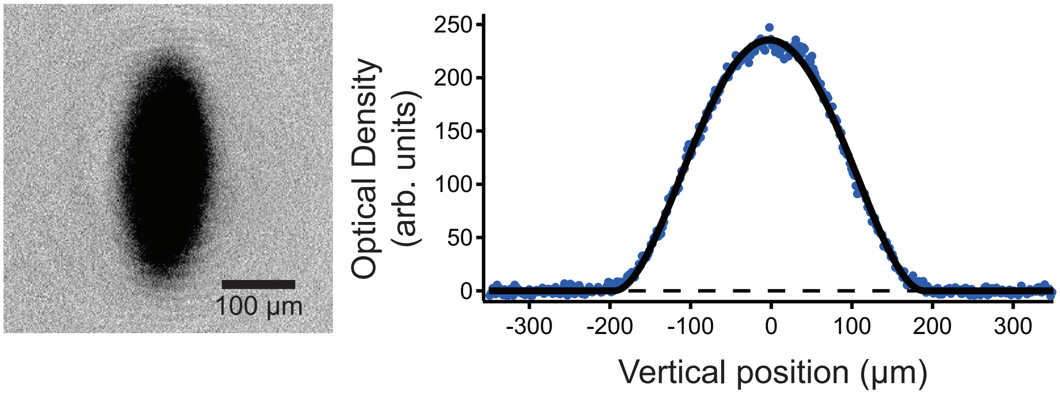

Figure 7.8: Achievement of the largest Yb BECs to date using the dynamically shaped optical trap. (left) Absorption image and (right) horizontally integrated optical density profile after 50 ms time-of-flight. The black solid line is a fit to a pure, Thomas-Fermi BEC distribution, giving an atom number of 1.2×10^6 atoms. From [94].

appreciably as the cloud approaches quantum degeneracy. Thus, in order to proceed towards the creation of a pure condensate, we stop the initial trajectory at the point $\rho \approx 1$ with $P = 1$ W and $h = 130$ μm, and subsequently fix the power and increase the CPM amplitude to 180 μm, resulting in the final trap frequencies $(\omega_x, \omega_y, \omega_z) = 2\pi \times (17, 110, 10)$ Hz. This further reduces the trap depth and decreases the density for the final stage of evaporation. Using this two-stage evaporation sequence, we can reliably create pure ^{174}Yb BECs consisting of 1.2×10^6 atoms (see figure 7.8), which is a factor of 4 improvement over the largest Yb BEC reported previously [41].

For the creation of BECs with fast cycle times, we cannot utilize the numerical simulations detailed in section 7.2.3 because the fast timescales violate the adiabaticity criterion, and the gas does not remain in a constant state of thermal equilibrium. Thus, we are left to optimize BEC production for speed by experimental means. After attempting many different schemes for reducing the laser power and painting amplitude, we find the 3 stage sequence shown in figure 7.9 to be best. In this evaporation sequence, the power is reduced in 3 segments with

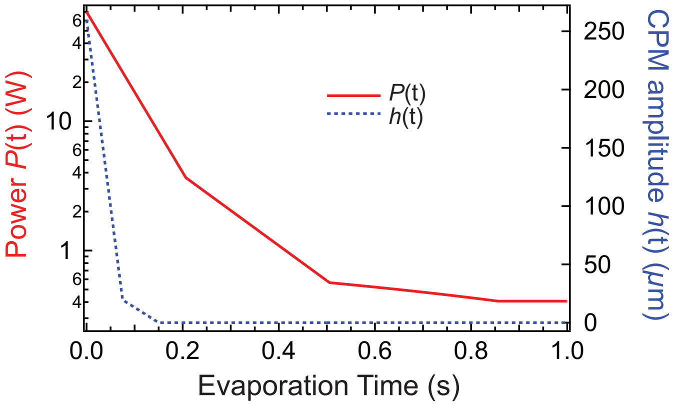

Figure 7.9: Experimentally optimized trajectory of power and CPM amplitude for fast BEC production. The sequence involves 3 stages of exponential power reduction, followed by a short hold at constant power for final evaporation to a nearly pure BEC to occur. The CPM amplitude is linearly reduced to zero during the first stage, resulting in a very high elastic scattering rate for the remainder of the sequence.

progressively increasing exponential timescale τ_P. The most notable difference between these profiles and those used for maximizing efficiency is the abrupt reduction of CPM amplitude at the beginning of evaporation to zero after 150 ms.

The resulting measurements of number and temperature during the first two stages of evaporation are shown in figure 7.10(a) and (b). To achieve the shortest cycle time possible, we decrease the MOT loading and compression time to a total of 0.8 s, and begin the forced evaporation sequence in figure 7.9 immediately after loading the atoms from the compressed MOT into the optical trap. The temperatures as measured in the horizontal and vertical directions initially decouple due to the non-adiabatic increase in the horizontal trap frequency associated with the rapid reduction the painting amplitude. Then, immediately following the painting reduction, the cloud rethermalizes. Figure 7.10(c) shows a progression for different final evaporation powers P_f towards a nearly pure BEC of $N = 1 \times 10^5$ atoms for a total cycle time of 1.8 s. By shortening the MOT loading and compression time to a total of 0.6 s, we can create nearly pure BECs of 0.5×10^5 atoms in 1.6 s. These cycle times are the fastest BEC production times to date in optical dipole traps, and make the dynamically shaped trap an attractive method to be applied in precision measurement experiments with BECs, where the usual long production times limits the rate of statistical sampling.

While it may seem from figure 7.9 that the CPM amplitude plays a small role in the achievement of fast BECs, the initial large volume afforded by the control over CPM is essential for this rapid cooling to quantum degeneracy. In fact, with the initial CPM amplitude of 259 μm, we are able to capture about 50% of the atoms from the compressed MOT into the optical trap, while without CPM, we typically capture $5 - 10\%$. The subsequent fast reduction of h quickly compresses the trapped cloud, increasing the density and therefore evaporation rate. Though this scheme will not result in a large value of γ, the large initial atom number gives the cloud significant cooling power that can be used to rapidly increase the phase space density to the point of quantum degeneracy, and indeed to create very fast BECs.

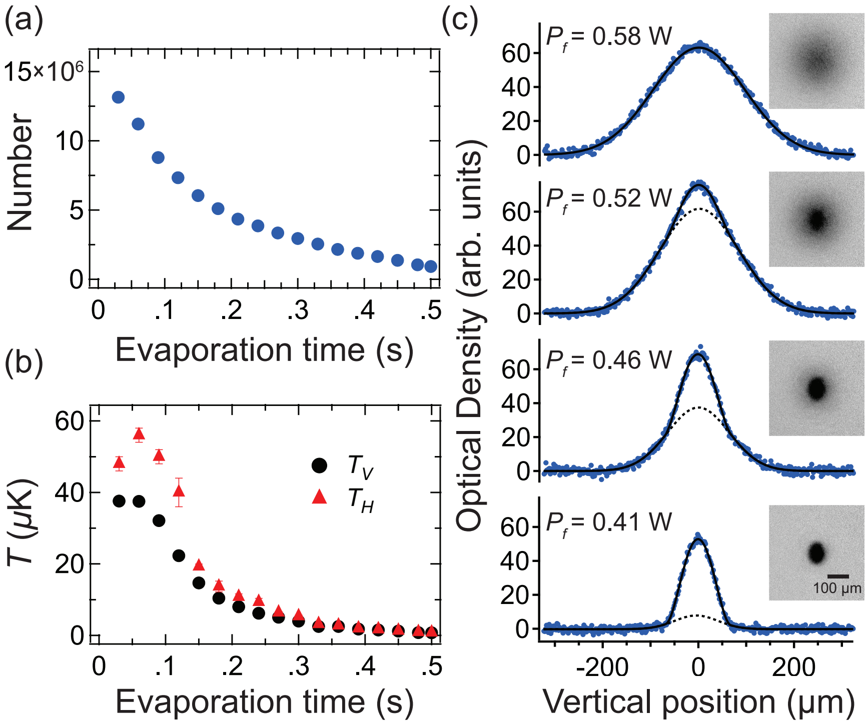

Figure 7.10: 1.8 second total cycle time for Yb BEC production. (a) and (b) Number and temperature evolution during the first two stages of the sequence depicted in figure 7.9. The horizontal and vertical temperatures initially decouple due to the non-adiabaticity of the painting reduction in the horizontal plane. (c) Bimodal fits to horizontally integrated OD density profiles with associated absorption images, taken after 25 ms time-of-flight. For $P_f = 0.41$ W, we detect a nearly pure BEC of 1×10^5 atoms. From [94].

Chapter 8

TWO-ELEMENT MIXTURE OF BOSE AND FERMI SUPERFLUIDS

In this chapter we will discuss our experimental realization of a two-element mixture of Bose and Fermi superfluids, namely a mixture of bosonic ^{174}Yb and fermionic ^{6}Li. We first establish the existence of simultaneous superfluidity through direct observation of condensation of the bosonic and fermionic components, and show the mixture to be long-lived. By selectively exciting dipole, or center-of-mass, oscillations in the bosonic component of the superfluid mixture, we directly observe elastic coupling between the two species, and determine the previously unknown sign of the interspecies s-wave scattering length to be positive, $a_{BF} = 13 \pm 3\, a_0$ [54]. In addition, we simultaneously detect the exchange of angular momentum between the superfluids from the observation of a scissors mode of oscillation in the bosonic component excited by interspecies interactions.

While the first realization of a Bose-Fermi superfluid mixture was reported just a couple of years ago (2014) in a mixture of ^{7}Li and ^{6}Li [31], ours is the first reported realization of such a mixture including two different elements from the periodic table [1]. As we shall see in this Chapter, utilizing elements from different rows and columns of the periodic table leads to a qualitatively different mixture than isotopic mixtures of a single element, or mixtures of elements from within the same group (e.g. alkalis).

Historically, the study of combined Bose-Fermi superfluid mixtures was motivated by the successful realization of superfluidity in liquid ^{3}He and ^{4}He, separately. The experimental prospect of preparing a homogeneous mixture of superfluid ^{3}He and ^{4}He led to numerous

---

[1] Concurrently with our realization of a ^{174}Yb-^{6}Li superfluid mixture, a group from the USTC in Hefei, China reported the detection of simultaneous Bose and Fermi superfluidity in a mixture of ^{41}K and ^{6}Li through the observation of a two-species vortex lattice [110].

theoretical proposals (see for example [3]). An important prediction from such studies of combined superfluidity is the appearance of a dissipationless drag between superfluids with relative velocity, and is often referred to as *entrainment*, or the *Andreev-Bashkin effect*. This drag, which exists for relative velocities below the Landau criterion, results from elastic forward scattering (i.e. scattering that does not change the momenta of the scattering particles) between the superfluids. Recently, theoretical interest in entrainment physics has been strongly renewed in the context of neutron stars due to possible implications of entrainment coupling between the neutron superfluid in the crust and an underlying lattice of nuclei [88].

In the case of ^{4}He-^{3}He mixtures, the propensity towards phase separation for dissolved ^{3}He concentrations above 6-7% (at 1 atm) results in an extremely low critical temperature (for bulk fluids) on the order of 10 to 100 μK [97]. While efforts are still underway to achieve such low temperatures in a bulk system, the technical challenges are considerable. Thus, cold atom systems offer a complementary approach where interspecies interactions do not greatly restrict the accessible phase space for combined Bose-Fermi superfluidity.

8.1 Preparation and detection of the Bose-Fermi superfluid mixture

This section describes the experimental procedure used to create the Bose-Fermi superfluid mixture in our Yb-Li apparatus, as well as the methods used to detect and characterize the superfluidity of each component. The achievement of Fermi superfluidity was a longstanding goal in the lab, however early attempts were thwarted due to low Li atom number (and thus low signal-to-noise absorption images) at temperatures low enough for condensation. The improvements to the apparatus detailed in chapter 7 as well as the implementation of D_1 cooling for Li proved essential to our ability to efficiently create large atom number quantum degenerate gases of ^{174}Yb and ^{6}Li. To begin, we will discuss properties of the Yb-Li combination that make it attractive for studies of combined Bose-Fermi superfluidity.

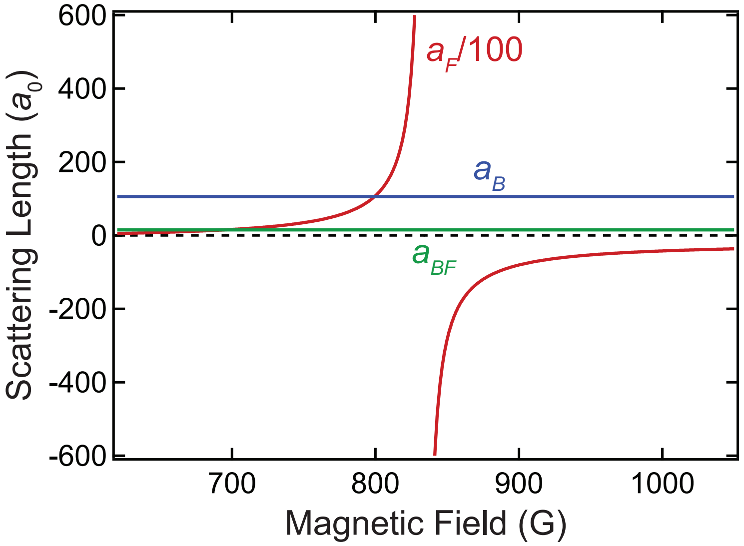

Figure 8.1: Relevant scattering lengths for the ^{174}Yb-^{6}Li mixture in the vicinity of the 832 G Feshbach resonance in ^{6}Li. The magnetic field independent scattering lengths are $a_B = 106\, a_0$ for Yb-Yb (blue) and $a_{BF} = 13\, a_0$ for Yb-Li (green). Note that the Li-Li scattering $a_F(B)$ is scaled down by a factor of 100 in the plot.

8.1.1 Relevant properties of the ^{174}Yb-^{6}Li system

Utilizing the combination of Yb (spin-singlet) and Li (spin-doublet) to form a Bose-Fermi superfluid mixture offers many advantageous and intriguing properties. As highlighted in the beginning of this chapter, interspecies interactions play a crucial role in the viability of achieving combined superfluidity in a Bose-Fermi mixture. As we will see, the relatively weak interspecies interactions and magnetic insensitivity of the Yb-Yb (a_B) and Yb-Li (a_{BF}) scattering lengths ensure miscibility of the mixture across the Feshbach resonance between states $|1\rangle$ and $|2\rangle$ in Li centered at 832 G (see figure 8.1). In addition, the large mismatch in mass between the two species is expected to result in interesting modifications of scattering properties, and suggests the use of Yb as an impurity thermometer for the strongly interacting Li Fermi gas [111].

To investigate the miscibility of a mixture of Bose and Fermi gases at zero temperature, we begin by defining the energy functional

$$E = \int d^3\vec{r}\,\mathcal{E}(n_B(\vec{r}), n_F(\vec{r})), \tag{8.1}$$

where $\mathcal{E}(n_B, n_F) = \frac{1}{2}g_{BB}n_B^2 + g_{BF}n_Bn_F + \mathcal{E}_F(n_F)$ is the energy density (units of energy/length^3) for the Bose-Fermi mixture in the mean-field approximation. In this expression, $g_{BB} = 4\pi\hbar^2 a_B/m_B$ is the boson-boson coupling constant, where a_B is the s-wave scattering length associated with boson-boson collisions, $g_{BF} = 2\pi\hbar^2 a_{BF}/\mu_{BF}$ is the boson-fermion coupling constant, with associated s-wave scattering length a_{BF} and reduced mass $\mu_{BF} = m_Bm_F/(m_B + m_F)$, and $\mathcal{E}_F(n_F)$ is the internal energy of the fermionic component, determined by the equation of state.

For simplicity, we will consider the case of uniform Bose and Fermi gases, which serves to elucidate the general characteristics of phase separation in the mixture [105]. To find the condition for dynamical stability of the homogeneous mixture, we minimize the functional $E - \mu_F N_F - \mu_B N_B$ with respect to $n_B(\vec{r})$ and $n_F(\vec{r})$. Here μ_B and μ_F are the chemical potentials of the Bose and Fermi gases. Setting $\partial(\mathcal{E} - \mu_F n_F - \mu_B n_B)/\partial n_\alpha = 0$ for $\alpha = F$ and B, we get the usual expression for the chemical potential, $\mu_\alpha = \frac{\partial\mathcal{E}}{\partial n_\alpha}$. Now, in order for this extremum to be a local minimum (and not maximum), we must have a positive definite Hessian matrix,

$$H = \begin{pmatrix} \frac{\partial^2\mathcal{E}}{\partial n_B^2} & \frac{\partial^2\mathcal{E}}{\partial n_F\partial n_B} \\ \frac{\partial^2\mathcal{E}}{\partial n_B\partial n_F} & \frac{\partial^2\mathcal{E}}{\partial n_F^2} \end{pmatrix}. \tag{8.2}$$

Using $\frac{\partial\mathcal{E}}{\partial n_\alpha} = \mu_\alpha$, the condition for dynamical stability then becomes

$$\frac{\partial\mu_B}{\partial n_B}\frac{\partial\mu_F}{\partial n_F} - \frac{\partial\mu_B}{\partial n_F}\frac{\partial\mu_F}{\partial n_B} > 0. \tag{8.3}$$

Then, using the expression for $\mathcal{E}(n_B, n_F)$ above, the inequality (8.3) becomes

$$\frac{\partial\mu_F}{\partial n_F} > \frac{g_{BF}^2}{g_B} = \frac{\pi\hbar^2 a_{BF}^2}{a_B}\frac{(m_B + m_F)^2}{m_F^2 m_B}. \tag{8.4}$$

We immediately see that the phase of the combined gas does not depend on the density of the bosonic component. It is interesting to note that this is only true for weakly interacting Bose gases, or more precisely, for systems where $n_B a_B^3 \ll 1$. When $n_B a_B^3$ is not small, the famous Lee-Huang-Yang (LHY) correction introduces a term proportional to $n^{5/2}$, thus bringing bosonic density dependence into the stability criterion. Using $\mu_F = \eta E_F = \eta \frac{\hbar^2}{2m_F}(3\pi^2 n_F)^{2/3}$, where $\eta = 1(\xi)$ for a non-interacting(unitary) two-component Fermi gas, and $\xi = 0.38$ is the Bertsch parameter, we find

$$n_F^{1/3} < \frac{(3\pi^2)^{2/3}}{3\pi} \frac{a_B}{a_{BF}^2} \frac{\eta m_F m_B}{(m_F + m_B)^2}. \tag{8.5}$$

For the scattering lengths in the Yb-Li Bose-Fermi system (see figure 8.1), this yields the constraint $n_F < 5.9 \times 10^{18}\,\mathrm{cm}^{-3}$ for a non-interacting Fermi gas, and $n_F < 3.2 \times 10^{17}\,\mathrm{cm}^{-3}$ for a unitary Fermi gas. Considering typical fermion densities of order $10^{13} - 10^{14}\,\mathrm{cm}^{-3}$, we are clearly quite far from phase separation at unitarity.

On the far BEC side of the Feshbach resonance, we can use the mean-field expression $\mu_d = g_{dd} n_d$ for the chemical potential of the molecular condensate, where $g_{dd} = 2\pi\hbar^2 a_d/m_F$, $a_d = 0.6 a_F$ [92], and $n_d = n_F/2$. Lastly, using $\mu_d = 2\mu_F$ we find that inequality (8.4) reduces to the condition $a_F > \frac{10}{3}\frac{(m_B+m_F)^2}{m_B m_F}\frac{a_{BF}^2}{a_B} \approx 170\, a_0$. From this we can conclude that the dual superfluid mixture should be dynamically stable[2] for magnetic fields above 570 G.

Other relevant properties of the ^{174}Yb-^{6}Li superfluid combination include the respective electronic structures and large mismatch in mass. The combination of a spin-half alkali atom (Li, $^2S_{1/2}$) and spin-zero alkaline-earth-like atom (Yb, $^1S_0$) results in interspecies collisions that are independent of magnetic field (a_{BF}), and allows for the use of magnetic fields as a species-specific tool. In the case of the ^{7}Li-^{6}Li system, the magnetic field dependence of both a_{BF} and a_B restricts the range of magnetic fields accessible near the 832 G Feshbach resonance in ^{6}Li. Furthermore, the large Yb-Li mass ratio of $m_B/m_F = 29$ ensures a significant difference in the harmonic trapping frequencies of the two species ($\omega_F/\omega_B \approx 8$ at 1064 nm),

---

[2] In fact, for magnetic fields well below the resonance position ($B \lesssim 700\,\mathrm{G}$), two-body atom-dimer inelastic collisions become the limiting effect for stability [60].

allowing for species-selective excitations by carefully choosing the timescale of trap parameter variation. In addition to being a useful tool, the large mass mismatch is predicted to result in interesting interaction phenomena in the superfluid mixture, including a change in the character of excitations leading to the Landau critical velocity criterion [18] and a strong modification of the Bose-Fermi interaction energy in the BEC regime [111].

Lastly, one can imagine using Yb as a precise thermometer of a deeply degenerate, strongly interacting Li Fermi gas. Because of the large ratio of trap frequencies, the degeneracy temperatures for the two species scale as $\frac{T_C}{T_F} = 0.06 \left(\frac{N_B}{N_F}\right)^{1/3}$, where T_C is the Yb BEC transition temperature. Hence, for a mixture with $N_F/N_B = 30$, a measured Yb condensate temperature of $T/T_C = 0.5$ implies a Fermi temperature of $T/T_F = 0.01$, assuming thermalization. Demonstrating such a technique for precise thermometry of Fermi gases near $T = 0$ would be a nontrivial advance for the field, as many experiments in quantum simulation using ultracold fermions offer no direct method for measuring temperature [45]. In recent experiments in a mixture of 6Li and ^{41}K, the impurity thermometry technique was used at a magnetic field of 1180 G (BCS side of resonance) to measure temperatures of a deeply degenerate mixture of Li states $|1\rangle$ and $|2\rangle$ as low as $T = 0.063(5)T_F$ [71].

8.1.2 Inelastic losses in the BEC-BCS crossover in ^{6}Li

An important consideration when attempting to create superfluid Fermi gases is the unavoidable inelastic losses associated with coupling to deeply bound molecular states near Feshbach resonances. While two-component Fermi gases are remarkably stable in the vicinity of such scattering resonances owing to Pauli suppression of three-body collisions, the presence of a distinguishable third scattering partner, in our case bosonic Yb, introduces a new three-body inelastic scattering process. This process results in the loss of one Li $|1\rangle$ atom, one Li $|2\rangle$ atom, and one Yb atom, with rate coefficient $K_3' \approx 10^{-27}\,\mathrm{cm}^6\mathrm{s}^{-1}$ at 810 G [60]. Hence, for typical peak densities in our crossed ODT of $n_F(0) \approx 10^{13}\,\mathrm{cm}^{-3}$ and $n_B(0) \approx 10^{14}\,\mathrm{cm}^{-3}$, we expect lifetimes of order 1 s near unitarity. Moreover, for lower magnetic fields corresponding to the molecular, or $a_F > 0$, side of the Feshbach resonance, both Yb-Li$_2$ and Li-Li$_2$

two-body collisions become severely lossy, with rate coefficients in excess of $10^{-13}\,\mathrm{cm}^3\mathrm{s}^{-1}$.

When one considers the order 10 s timescale for evaporative cooling of Yb and simultaneous sympathetic cooling of Li to quantum degeneracy[3], it is clear that such a long procedure cannot be performed with a two-component Li gas near the 832 G Feshbach resonance. Therefore, there are two clear alternative options from which to choose: (1) complete all or most of the evaporative plus sympathetic cooling at a benign field with both states $|1\rangle$ and $|2\rangle$ of Li, and subsequently ramp the field very quickly to the strongly interacting regime, or (2) work with only a single spin state of Li during the sympathetic cooling stage, and create a spin mixture of $|1\rangle$ and $|2\rangle$ at 832 G using an RF pulse once the cloud is deeply degenerate.

In our experiment, we find option (1) above to be an infeasible route towards Fermi superfluidity due to limitations on our magnetic field ramp speed. In fact, even our minimum ramp time from low field (530 G) to unitarity (832 G) of about 1 ms is too slow to prevent large atom losses and heating while crossing the notably lossy regime between 600 and 700 G. It is natural to consider ramping down to 832 G from far above resonance (i.e. far BCS side), but for the maximum magnetic field (≈ 1200 G) accessible with the Helmholtz coils in our system, the three-body losses incurred during the long sympathetic cooling step are too great. For these reasons we plan our dual superfluid preparation procedure around option (2).

Since option (2) requires preparing a spin mixture beginning from a near zero-temperature Fermi gas, it is important to consider how much further cooling is necessary to reach the Fermi superfluid transition. Here, we will use a greatly simplified model to gain a rough sense of the cooling necessary. To start, let us consider a single spin Fermi gas with N atoms in a harmonic trap with geometric mean frequency $\bar{\omega}$. We will then calculate the final reduced temperature $(T/T_F)_f$ after preparing a 50:50 spin mixture from a spin-polarized Fermi gas

---

[3] While we were able to achieve very fast cycle times (≈ 2 s) for Yb quantum degenerate gas production using the dynamically shaped trap, the addition of Li introduces the challenges of the interspecies thermalization timescale and the need for a large atom number Yb cloud (i.e. total heat capacity) in order to mitigate the heat load presented by Li.

with initial temperature $(T/T_F)_i$. To begin, we compute the (mean) total energy,

$$E_{\text{tot}} = \int_0^\infty \epsilon g(\epsilon) n(\epsilon) d\epsilon, \tag{8.6}$$

where $g(\epsilon) = \frac{g_s \epsilon^2}{2(\hbar\bar{\omega})^3}$ is the density of states, g_s is the number of spin states involved, and $n(\epsilon)$ is the Fermi-Dirac distribution. Using the Sommerfeld expansion for integrals involving the Fermi-Dirac distribution function [4], we find

$$\begin{aligned} E_{\text{tot}} = \frac{g_s}{2(\hbar\bar{\omega})^3} \int_0^\infty \epsilon^3 n(\epsilon) d\epsilon &\approx \frac{g_s}{2(\hbar\bar{\omega})^3} \left[\int_0^{\mu(T)} \epsilon^3 d\epsilon + \frac{\pi^2}{6} (k_B T)^2 \frac{d}{d\epsilon} (\epsilon^3) \bigg|_{\epsilon=\mu(T)} \right] \\ &= \frac{g_s \mu^4}{8(\hbar\bar{\omega})^3} \left[1 + 2\pi^2 \left(\frac{k_B T}{\mu} \right)^2 \right]. \end{aligned} \tag{8.7}$$

Thus, we need to know the temperature dependence of the chemical potential $\mu(T)$, which is determined by fixing the total particle number $N = \int_0^\infty g(\epsilon) n(\epsilon) d\epsilon$. The result is (again using the Sommerfeld expansion)

$$\mu(T) = E_F \left[1 - \frac{\pi^2}{3} \left(\frac{k_B T}{E_F} \right)^2 + \mathcal{O}(T^4) \right], \tag{8.8}$$

where the Fermi energy here is defined as $E_F = \hbar\bar{\omega} \left(\frac{6N}{g_s} \right)^{1/3}$. Combining equations (8.7) and (8.8) we get

$$E_{\text{tot}} \approx \frac{3}{4} N E_F \left[1 + \frac{2\pi^2}{3} \left(\frac{T}{T_F} \right)^2 \right]. \tag{8.9}$$

Finally, assuming the Fermi cloud fully rethermalizes after the 50:50 spin mixture is prepared, we can solve for the final temperature $(T/T_F)_f$ by equating the total energy of the initial and final clouds, yielding

$$\left(\frac{T}{T_F} \right)_f = \left[\frac{3}{2\pi^2} \left(2^{1/3} \left(1 + \frac{2\pi^2}{3} \left(\frac{T}{T_F} \right)_i^2 \right) - 1 \right) \right]^{1/2}. \tag{8.10}$$

Therefore, if we begin in a spin-polarized Fermi gas with temperature $(T/T_F)_i = 0.2$, the resulting two-component Fermi gas should thermalize to a temperature $(T/T_F)_f = 0.3$. In fact, even if we begin with a zero-temperature spin-polarized Fermi gas, the spin mixture will acquire a temperature of $(T/T_F)_f = 0.2$.

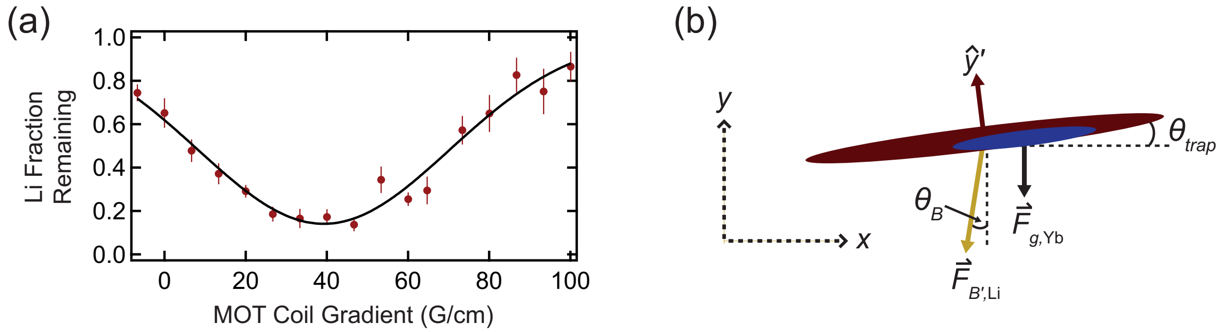

Figure 8.2: Calibration of the magnetic field gradient needed for optimum spatial overlap of the Yb-Li superfluid mixture. (a) We plot the fraction of Li atoms remaining after a 500 ms hold with Yb at 740 G, where Li loss is dominated by inelastic atom-dimer collisions between Yb and Li_2 molecules. (b) Qualitative schematic of the relevant directions in our trap. Slight misalignments of the magnetic field axis and nearly vertical principal axis of the optical trap with respect to gravity lead to an offset of the Li and Yb horizontal cloud centers. As shown in the figure, $\theta_B < 0$ and $\theta_{\mathrm{trap}} > 0$.

8.1.3 Tuning interspecies overlap with B'

While inelastic effects near the 832 G Feshbach resonance present an obstacle to Fermi superfluid formation, they can be used as a tool to probe the spatial overlap of the Yb and Li clouds. To investigate the gradient-tunable interspecies overlap, we measure the inelastic coupling between the Yb and Li clouds at 740 G as a function of B'. At this magnetic field, Yb-dimer collisions dominate over Li-dimer collisions [60]. Due to the density dependence of the atom-dimer loss rate, then, we expect to see a strong dependence of Li loss as a function of applied gradient, with the peak loss location corresponding to maximum interspecies overlap. The measurements are shown in figure 8.2(a), where we plot the fraction of Li atoms remaining after a 500 ms hold at 740 G in the presence of Yb. We identify a range of gradients from $20 - 65\,\mathrm{G/cm}$ for which the system exhibits strong interspecies spatial overlap, with the peak loss occurring at $B' = 39\,\mathrm{G/cm}$.

It is interesting to note that the peak loss does not occur at the "theoretical" overlap gradient of 68 G/cm. In our system this is due to slight differences in the directions defined by the bias magnetic field, gravity, and the nearly vertical principal axis of the ODT. Figure 8.2(b) provides a simplified 2D schematic of the directions involved, and the resulting displacement between the Yb and Li clouds for $B' = 68$ G/cm. Due to the angles θ_B and θ_{trap} of the magnetic field and nearly vertical trap principal axis with respect to gravity, Li and Yb will experience different horizontal displacements when their vertical centers are overlapped. For the "theoretical" overlap gradient, we have[4] $\mu_B B'/m_F\omega_{y,F}^2 = g/\omega_{y,B}^2$, which gives a relative displacement of the horizontal cloud centers of

$$\frac{x_B - x_F}{x_B} = 1 - \frac{\sin(\theta_{\text{trap}} - \theta_B)}{\sin\theta_{\text{trap}}} \approx \frac{\theta_B}{\theta_{\text{trap}}}. \tag{8.11}$$

Hence, for the situation depicted in figure 8.2(b), where we have $\theta_B < 0$ and $\theta_{\text{trap}} > 0$, we see that Li will be pushed further from the center of the optical trap than Yb. Of course, in reality these three independent directions (gravity, the magnetic field, and the vertical trap axis) are not likely to lie in a plane, but this analysis gives a good estimate of the displacements involved.

8.1.4 Improved Yb-Li quantum degenerate mixture

As mentioned in the beginning of this section, the upgrades made to the optical trapping setup detailed in chapter 7, along with the implementation of D_1 cooling of Li were necessary to push our two-species quantum degenerate gas production to the point where simultaneous superfluidity was possible. Thus, the first step towards creating an Yb-Li superfluid mixture was to realize high signal-to-noise (i.e. large atom number) degenerate Fermi clouds of Li in our apparatus with $T/T_F \leq T_{C,F}/T_F = 0.19$ [67, 31], where $T_{C,F}$ is the critical temperature for superfluidity in a spin-balanced, two-component, harmonically-trapped Fermi gas at unitarity ($1/k_F a_F = 0$). In this section we will detail the techniques used to improve our

---

[4] Note here that we neglect the force of gravity on Li, as the force from the applied magnetic field gradient is roughly 60 times greater. Furthermore, we neglect the effects of the angles θ_B and θ_{trap} in calculating the vertical displacement, as these come in at second order.

degenerate Fermi gas production and subsequently create the Yb-Li Bose-Fermi superfluid mixture.

A major difference in our redesigned crossed ODT is the much larger maximum trap volume achievable relative to our earlier configuration. This, in combination with the significantly reduced Li CMOT temperature after D_1 molasses of $60-70$ μK, allows us to perform a Li-first ODT loading scheme, opposite our previous Yb-Li experiments. We find this to be an important improvement to our cooling scheme, as we can evaporatively cool Li in a mixture of states $|1\rangle$ and $|2\rangle$ at 330 G before loading Yb, thus significantly decreasing the heat load presented by Li on Yb. In fact, since the trap depth ratio for the two-species is $U_F/U_B = 2.2$, once Yb is loaded into the ODT, only Yb atoms will escape during forced evaporative cooling, as Li will be continuously sympathetically cooled and will maintain a large value of $\eta = U_F/k_BT$. Therefore, we have to be careful not to have too many Li atoms in the trap upon loading of Yb, as it can hinder the final achievable phase space density at low trap depths. We solve this problem by simply evaporating further with Li at 330 G prior to Yb load, allowing us to begin sympathetic cooling with a larger initial phase space density for Li.

In a typical sequence, we load the Li MOT for 2 s and apply a moderate compression step before applying the D_1 molasses for 300 μs, resulting in $2-3\times10^8$ atoms at $60-70$ μK. After capturing up to 10^7 atoms in a 50:50 mixture of states $|1\rangle$ and $|2\rangle$ in the crossed ODT with initial power $P = 55$ W and CPM (or "painting") amplitude $h = 390$ μm, we hold for 100 ms at 330 G to allow for transient evaporation and thermalization, resulting in $N_F = 5\times10^6$ atoms at $T = 60$ μK. We then perform forced evaporative cooling of Li by reducing the laser power a factor of 10 in about 1 s, after which $N_F = 6\times10^5$ atoms remain. Next, we remove the 330 G bias field before loading the Yb MOT, making the Li cloud collisionless as the $|1\rangle$-$|2\rangle$ scattering length vanishes at $B = 0$.

During the Yb MOT loading time of 5 s, we observe no adverse effects on the trapped Li cloud[5] as the MOT is vertically displaced from the ODT location during load. In the 300 ms

---

[5] For this 5 s duration it is very important that the ODT laser power is low, as we observe significant

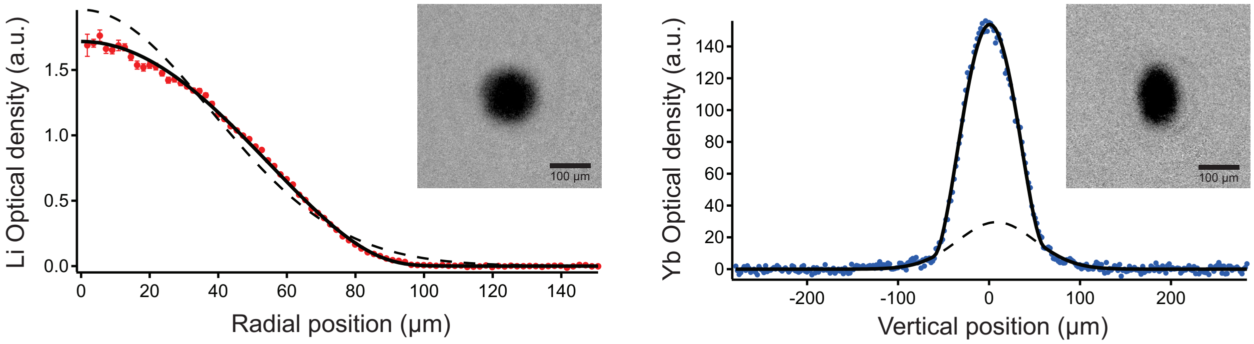

Figure 8.3: Simultaneous quantum degeneracy of Yb and Li. (Left) Optical density image and associated azimuthally averaged density profile of a single spin state ($|2\rangle$) Li Fermi gas of $N_F = 3 \times 10^5$ atoms imaged at 1 ms ToF. The solid line is a fit to a Fermi-Dirac distribution yielding a temperature of $T/T_F = 0.07(1)$, while the dashed line is an attempted fit to a Gaussian distribution. (Right) Optical density image and 2d horizontally integrated density profile of a nearly pure Yb BEC of 2×10^5 atoms imaged at 25 ms ToF. Solid line is a fit to a bimodal distribution consisting of a Gaussian thermal component (dashed line) and Thomas-Fermi condensed component.

preceding compression of the Yb MOT, we adiabatically increase the trapping laser power to the maximum 55 W, and maintain the CPM amplitude of 390 μm. Following 200 ms of Yb MOT compression, we capture $N_B = 20 - 30 \times 10^6$ atoms at $30 - 40$ μK in the ODT. We then immediately blast away all Li state $|1\rangle$ atoms by ramping the magnetic field to 530 G and applying a light pulse resonant with the $^2S_{1/2} \rightarrow {}^2P_{3/2}$ transition.

With $N_F = 3 \times 10^5$ Li atoms in state $|2\rangle$ remaining in the trap to be sympathetically cooled, we begin forced evaporative cooling of Yb in our dynamically shaped ODT utilizing the same concepts discussed in chapter 7. While we were able to push the cycle time of

---

heating of the Li cloud at high laser power due to stimulated two-photon transitions from the two beams of the crossed ODT. To minimize this heating, we tune the half-wave plate for the second pass of the ODT to maximize the Li lifetime. Nevertheless, there are some residual components of the electric fields from both ODT beams that have parallel polarization, allowing for these two-photon transitions.

our Yb only quantum degenerate gas production to below 2 seconds, the situation with Li is fundamentally limited by the thermalization rate between the two species, which is further limited by the large mass ratio [54]. Furthermore, large atom number Yb clouds are necessary for absorbing the heat load presented by the Li cloud. Thus, we find forced evaporation timescales on the order of 10 s to be necessary. We use exponential and linear ramp profiles for the power and CPM amplitude, respectively, until the point where Yb reaches quantum degeneracy.

We finish evaporative cooling to a pure Yb BEC by increasing the painting amplitude considerably from 80 μm to 450 μm and slightly increasing the laser power from 1 to 1.5 W, resulting in final trap frequencies for Yb of $(\omega_x, \omega_y, \omega_z)_B = 2\pi \times (23, 150, 10)$ Hz. This decreases the depth while greatly increasing the volume (and lowering the density), limiting the negative effects of three-body inelastic loss in the condensate. During this last evaporation step, the Li and Yb clouds thermally decouple, as the cloud centers are separated by 11 μm for a vertical Yb trap frequency of $2\pi \times 150$ Hz.

At this point, we achieve degenerate Li Fermi gases of 3×10^5 atoms in state $|2\rangle$ with $T/T_F \approx 0.2$, and pure Yb BECs of up to 3×10^5 atoms. For smaller values of the final CPM amplitude ($h \lesssim 100$ μm) we can prepare degenerate Li Fermi gases with temperatures as low as $T/T_F = 0.07$, but with slightly smaller Yb BECs (see figure 8.3). The lower Fermi gas temperature is presumably due to the larger horizontal trap frequencies associated with smaller CPM amplitude, which help maintain interspecies thermalization at the lowest trap depths. As we will see in section 8.1.5, the large gravitational sag of Yb and resulting complete spatial decoupling is advantageous for our Fermi superfluid preparation.

8.1.5 Fermi superfluid production

We are now poised to create a 50:50 mixture of states $|1\rangle$ and $|2\rangle$ in Li and proceed towards crossing the Fermi superfluid transition by performing forced evaporative cooling with a unitary Li gas. Figure 8.4 shows the characterization of our $|1\rangle - |2\rangle$ spin mixture preparation, beginning from a spin-polarized Li $|2\rangle$ cloud. After ramping the magnetic field to 832 G, we create the spin superposition state $\frac{1}{\sqrt{2}}(|1\rangle + |2\rangle)$ by applying a 10 ms Landau-Zener RF (linear) frequency sweep from 76.261 MHz to 76.281 MHz using 1 Watt of RF power.

To measure the decoherence time of this superposition state, we monitor the aspect ratio of the Li cloud at 1.1 ms ToF as a function of time after the Landau-Zener pulse (see figure 8.4(a)). As the cloud decoheres and becomes a 50:50 mixture of $|1\rangle$ and $|2\rangle$, it immediately becomes collisionally hydrodynamic, resulting in an inversion of the aspect ratio at long ToF with respect to that of a non-interacting gas. An exponential fit to the measurements in figure 8.4(a) yields a $1/e$ time of $\tau = 36(2)$ ms. Hence, 94% of the atoms have decohered after 100 ms.

In parts (b) and (c) of figure 8.4, we show two typical optical density (OD) images with elliptically averaged one-dimensional profiles for hold times of 10 ms and 1 s, respectively. Immediately, we can see in the image itself the aspect ratio inversion, signifying the transition from a spin-polarized, non-interacting gas to a collisionally hydrodynamic one. For the 1D profile in 8.4(b), we can easily extract the reduced temperature $T/T_F = 0.18(1)$ using a Fermi-Dirac distribution.

For the strongly interacting cloud in 8.4(c), the task is a little more difficult as the ToF expansion is not ballistic, but hydrodynamic. However, one can get a rough estimate of the temperature at unitarity by noting that the shape of the cloud in ToF is related to the in-trap shape by hydrodynamic scalings, and assuming that the functional form of the unitary Fermi gas differs little from that of a non-interacting Fermi gas[6]. Pragmatically, one performs a Fermi-Dirac fit to the elliptically averaged density profile, yielding an "empirical temperature" $\tilde{T}$. Using the EOS for a trapped, unitary Fermi gas, $\mu(T=0) = \sqrt{\xi}E_F$, one can argue that $\tilde{T} \approx T/(T_F\sqrt{\xi})$ [62]. For the profile in figure 8.4(c), the value determined by the fit of $\tilde{T} = 0.48(4)$ thus corresponds to a reduced temperature of $T/T_F = 0.30(3)$. This is not far off from the value predicted by equation (8.10) of $(T/T_F)_f = 0.28$ for an

---

[6] This assumption is inspired by the identical dependence of the equations of state of the non-interacting and unitary Fermi gases at $T = 0$ on density ($E \propto n^{5/3}$). In fact, this method was used in the group of John Thomas to obtain one of the early experimental estimates for the superfluid transition temperature of a unitary Fermi gas [62]

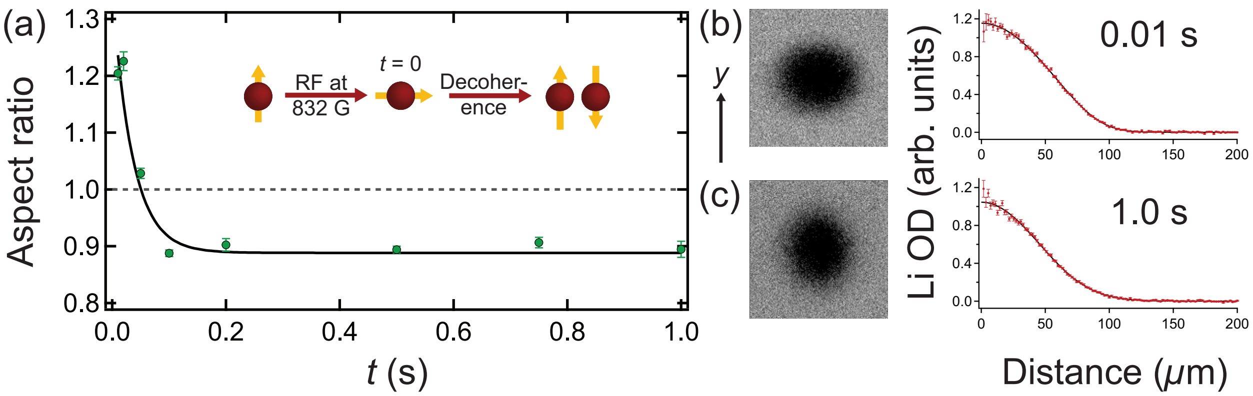

Figure 8.4: Decoherence of a spin-polarized, degenerate Li Fermi gas in the state $(|1\rangle + |2\rangle)/\sqrt{2}$ at 832 G. (a) Evolution of the aspect ratio of Li at 1.1 ms ToF vs. time t after application of the Landau-Zener RF pulse. As Li becomes strongly interacting with $1/k_F a_F = 0$ upon decohering, the aspect ratio at long ToF inverts due to the cloud being collisionally hydrodynamic. For these measurements, the in-trap aspect ratio is $\omega_y/\sqrt{\omega_x \omega_z} \approx 7$, where y points in the vertical direction. The solid line is a fit to an exponential decay, yielding a $1/e$ time of $\tau = 36(2)$ ms. (b)-(c) OD images of Li at 1.1 ms ToF with associated elliptically averaged 1D profiles for hold times of 10 ms and 1 s after the Landau-Zener pulse. The quoted distance corresponds to the major axis of the elliptical equipotential contours. The black solid lines are fits to Fermi-Dirac profiles, from which we determine temperatures of $T/T_F = 0.18(1)$ and 0.30(3) for the 10 ms and 1 s data, respectively, which agrees well with the prediction of equation (8.10). See discussion in section 8.1.5 for details on determining T/T_F for a unitary Fermi gas.

initially spin-polarized Fermi gas with temperature $(T/T_F)_i = 0.18$. It is important to note here that estimated final temperature in equation (8.10) assumes that the equation of state (EoS) before and after the spin-composition change are identical, which is not the case at unitarity. Nevertheless, the reduced temperature estimated using the empirical temperature method gives a rough sense of the further cooling needed to achieve Fermi superfluidity.

At this point, the Yb BEC is unaffected by increased temperature of Li, as the two are still thermally decoupled due to the gravitational sag of Yb. With a 50:50 mixture of states $|1\rangle$ and $|2\rangle$ at $T/T_F \approx 0.3$, we proceed towards crossing the superfluid transition at 832 G by applying a magnetic field gradient, thus lowering the trap depth for Li. Typically, we increase the gradient from zero to its final value in 500 ms, and then hold for 200 ms. Because of the unitary-limited collision cross section for Li at 832 G, evaporative cooling is extremely efficient. As we increase the gradient for Li-only evaporation, we control the interspecies separation such that by the time the two species acquire appreciable overlap, Li is cold enough to not cause heating of Yb.

8.1.6 Li thermometry: molecular BEC entropy determination

While performing evaporative cooling of a unitary Fermi gas is a relatively simple matter, performing precise thermometry and detecting superfluidity is a notoriously difficult task in this regime. The empirical temperature method discussed earlier in this section gives a rough idea of the reduced temperature T/T_F, but is certainly not quantitatively accurate. Methods developed over the years for directly detecting superfluidity include the rapid ramp technique [93], *in situ* detection of phase separation between a paired superfluid core and a shell of spin-polarized normal fermions in spin-imbalanced clouds [87, 25], measuring the equation of state (EoS) and observing a peak in the compressibility as a function of pressure [67], and exciting vortices and observing their subsequent crystallization into a lattice [114]. While these are wonderful techniques for verifying the presence of a Fermi superfluid, our apparatus was lacking certain technical capabilities at the time to easily adopt any of these. Instead, we opted for an indirect thermometry measurement in which we ramp the magnetic field to the weakly-interacting molecular BEC regime on the timescale of a few ms[7], measure the entropy of the resulting molecular BEC, and compare that entropy with the EoS of a unitary Fermi gas [67, 47].

Specifically, we ramp the magnetic field from 832 G to 690 G in 5 ms, and image the resulting molecular cloud in ToF. Since the binding energy of the Li_2 molecules is less than the natural linewidth, the imaging beam first dissociates molecules and then images the resulting atom cloud in the standard way. However, the Franck-Condon factor between the Li_2 Feshbach molecule and $\mathrm{Li}^* + \mathrm{Li}$ scattering state reduces the efficiency of molecule dissociation [7]. By comparing absorption images taken at 832 G and 690 G, we find the reduction in our detection efficiency to be 30%. Figure 8.5(a) displays images of molecular clouds for various final B' values, where we clearly see the appearance of a bimodal density distribution for $B' > 25$ G/cm. For a final evaporation gradient of $B' = 41$ G/cm, we detect pure molecular condensates consisting of 0.4×10^5 molecules, coexisting with a pure Yb superfluid of 1.1×10^5 atoms (figure 8.5(b)). The applied gradient of 41 G/cm ensures complete interspecies spatial overlap. For these measurements $1/k_F a_F = 2.9$ at 690 G, where $k_F = \sqrt{2 m_F \bar{\omega}_F (3N_F)^{1/3}/\hbar}$ is the Fermi wave vector for a harmonically-trapped, non-interacting, two-component gas with N_F atoms, and $\bar{\omega}_F$ is the geometric mean trap frequency.

To perform thermometry of Li using the observed bimodal distributions at 690 G, we utilize the fact that the entropy of the molecular BEC after the field ramp provides an upper bound on that of the initial unitary Fermi gas. Indeed, since the radius of a trapped Fermi gas changes drastically between unitarity and the deep BEC regime, one can excite collective modes by ramping the magnetic much faster than the inverse trap frequency, thus heating the cloud (i.e. the ramp is at best adiabatic). A potential issue is the possibility of cooling by evaporation or by collisions with Yb during the ramp to 690 G. To determine if this affects our measurement, we first verify that removing the gradient B' before ramping the field does not affect the detected condensate fraction. Since removal of this gradient increases the Li

---

[7] In practice, this timescale was set by the inductance of our magnetic field coils. We simply wanted to ramp as quickly as possible to avoid Yb-Li and Li-Li inelastic effects.

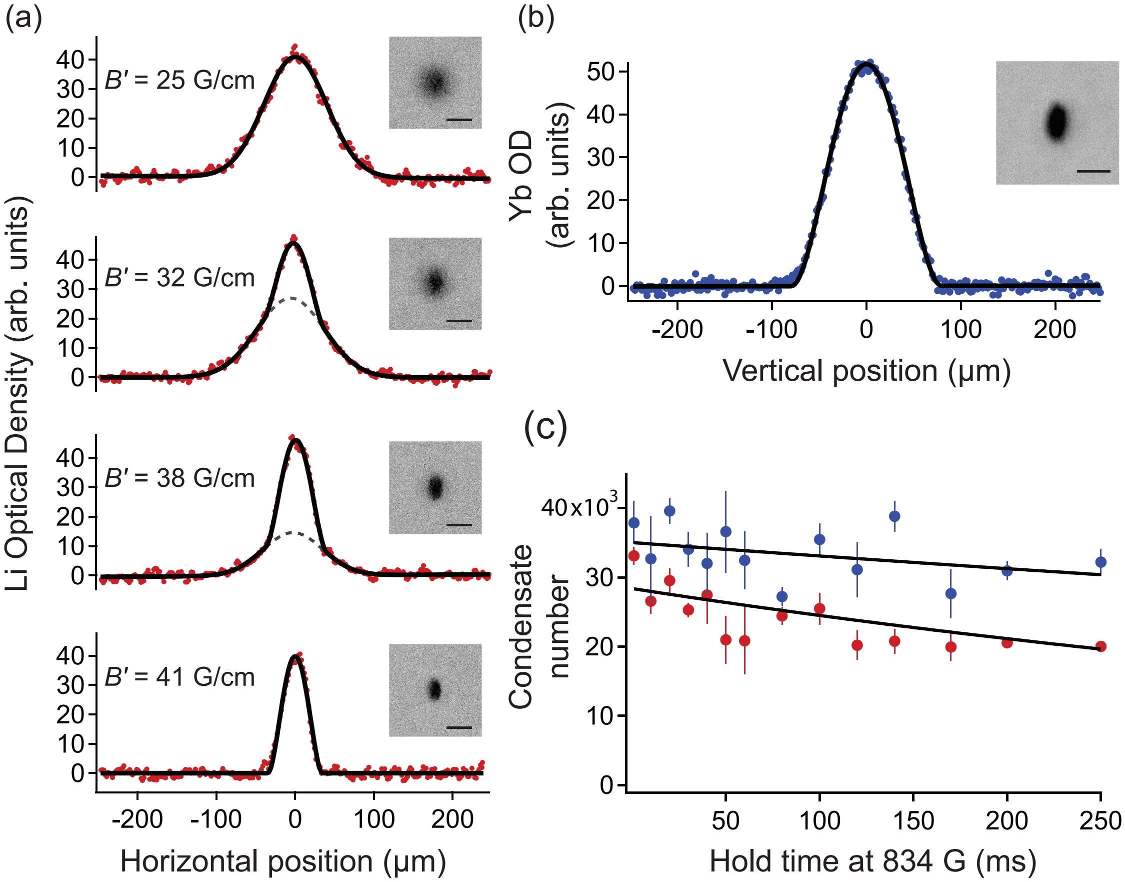

Figure 8.5: Evidence for simultaneous superfluidity of ^{174}Yb and a unitary Fermi gas of ^{6}Li. (a) OD images and vertically integrated 1D Li density profiles imaged at 690 G following a 5 ms field ramp from 832 G for various final evaporation gradient values. For $B' > 25$ G/cm we detect a bimodal density distribution signifying the presence of a molecular BEC, with a pure BEC of 0.4×10^5 molecules for $B' = 41$ G/cm. For these images, the ToF is 2 ms, and the scale bar indicates 100 μm. The condensate fractions from top to bottom are 0, 0.2, 0.5, and 1. See discussion in section 8.1.5 for connection between condensation at 690 G and superfluidity at 832 G. (b) OD image and horizontally integrated 1D density profile of a pure Yb BEC of 1.1×10^5 atoms coexisting with the Li superfluid at $B' = 41$ G/cm. The ToF is 30 ms. (c) Measurement of decay of Yb and Li condensate fractions as a function of hold time together at 832 G, where we ramp the magnetic field to 690 G in 5 ms after the variable hold. Exponential fits to the data return $1/e$ times of 1.8 s and 0.7 s for Yb and Li, respectively. Adapted from [95].

trap depth by a factor of 6 and consequently prohibits evaporation, we conclude that no evaporative cooling occurs in the case with B' present. Furthermore, the 5 ms timescale for the field ramp is 2 orders of magnitude smaller than the evaporation timescale at 832 G, where the collision rate is highest. Second, we perform the same ramp to 690 G after removing the Yb cloud from the trap with a resonant laser pulse, and find that the condensate fraction is again unchanged. Thus we can safely utilize the detected molecular BEC entropy to infer the Li temperature at unitarity.

For our typical condensate sizes ($\approx 0.4 \times 10^5$ molecules) at 690 G, we find that $n_m(0)a_m^3 = 0.001$, allowing us to treat the molecular BEC in the Thomas-Fermi regime. Here $n_m(0) = 1.3 \times 10^{13}$ cm^{-3} is the peak condensate density and $a_m = 0.6a_F = 0.6 \times 1420\,a_0$ is the molecule-molecule scattering length [92]. However, even though the interaction parameter $n_m(0)a_m^3$ is small, we cannot neglect interactions in the determination of the entropy, since it is the ratio of μ_m to k_BT that determines whether the gas is mostly in the free-particle regime, the phonon regime, or in between. Using the results of [17], we find that the entropy of the molecular BEC including the leading-order mean-field correction is

$$S = N_m k_B (1 - f_c) \left(\frac{4\zeta(4)}{\zeta(3)} + \frac{3\mu_m}{k_B T} \right), \tag{8.12}$$

where $N_m = N_F/2$ is the total number of molecules, f_c is the condensate fraction, and μ_m is the chemical potential of the molecular BEC. This result is accurate to 10% for $\mu_m/k_BT < 10$. For the pure condensate with 0.4×10^5 molecules, we use $\bar{\omega}_F = 2\pi \times 260$ Hz and find $\mu_m/k_B = 290$ nK.

To estimate the entropy of the purest condensate in Fig. 1(a), we use the thermal fraction corresponding to the detection limit of our system, $1 - f_c \leq 0.15$. The temperature consistent with this fraction is $T = (1-f_c)^{1/3} T_{c,m} = 230$ nK, where $T_{c,m} = 0.94\hbar\bar{\omega}_F (N_m)^{1/3}/k_B$ is the critical temperature for Bose-Einstein condensation of the molecules. Thus, we arrive at the upper bound for the entropy per *fermionic* particle of $S/(N_F k_B) \leq 0.55$, where we divide by the total number of fermions N_F in anticipation of connecting this quantity with the per-particle entropy of the unitary Fermi gas.

8.1.7 Li thermometry: connection with unitary Fermi gas equation of state

In order to compare our measured upper bound on the molecular BEC entropy with the homogeneous unitary Fermi gas (UFG) equation of state (EoS) measurements from [67], we must transform the homogeneous quantities to trap-averaged ones. In principle, this can be done for the entropy by computing

$$S = \int d^3\vec{r}\; n_F(\vec{r}) s^h(\vec{r}), \tag{8.13}$$

where $s^h(\vec{r})$ is the per-particle entropy of the homogeneous UFG evaluated at the point $\vec{r}$ using the local-density approximation. Unfortunately, computing $s^h(\vec{r})$ requires knowing the cloud temperature T and the local density $n(\vec{r})$ *a priori* (or equivalently knowing the "local" $T/T_F^h(\vec{r})$, where $k_B T_F^h(\vec{r}) = E_F^h(\vec{r}) = \hbar^2(3\pi^2 n_F(\vec{r}))^{2/3}/(2m_F)$ is the Fermi energy of a homogeneous two-component Fermi gas with density $n_F(\vec{r})$), which is exactly what we are trying to find.

An alternative method [66] to compute the trap-averaged entropy involves starting with the form of the UFG EoS that involves the density n_F, the chemical potential μ_F, and the temperature T. Due to the scale invariance of the unitary Fermi gas, one can show that this EoS must take the universal form

$$n_F \lambda^3 = f_n(\beta\mu_F), \tag{8.14}$$

where $\lambda = \sqrt{\frac{2\pi\hbar^2}{m_F k_B T}}$ is the thermal de Broglie wavelength, $\beta = 1/k_B T$, and $f_n(\beta\mu_F)$ is a universal function[8] of the dimensionless quantity $\beta\mu_F$ (see [50] for a derivation of the universal relations). Our goal is to find expressions for the trap-averaged thermodynamic quantities[9] that are necessary for computing the total entropy in the trap, S, in terms of the

---

[8] In the case of the ideal Fermi gas (also a scale invariant system), we know the phase-space density takes the form $n_F\lambda^3 = -2\,\mathrm{Li}_{3/2}(-\exp(\beta\mu_F))$, giving $f_n(\beta\mu_F) = -2\,\mathrm{Li}_{3/2}(-\exp(\beta\mu_F))$, where $\mathrm{Li}_m(x)$ is the m^{th}-order polylogarithm of x. The series expansion form of $\mathrm{Li}_{3/2}(-\exp(\beta\mu_F))$ automatically gives the virial coefficients in this case.

[9] Unless noted otherwise, all thermodynamic variables correspond to those averaged over the trap, *not* the homogeneous quantities (for which we use a superscript "h"). The "F" subscripts are used wherever necessary in order to be consistent with the definitions of fermionic versus bosonic variables throughout this chapter.

homogeneous EoS equation (8.14), which has been measured [67].

We start with the definition of the (homogeneous) grand potential,

$$\begin{aligned}\Omega^h &= E^h - TS^h - \mu_F N_F^h \\ d\Omega^h &= -S^h dT - P^h d\mathcal{V} - N_F^h d\mu_F \end{aligned} \tag{8.15}$$

where E^h is the total energy, P^h is the pressure, and $\mathcal{V}$ is the volume. For the homogeneous gas, the relation

$$\Omega^h = -P^h \mathcal{V} \tag{8.16}$$

follows from the extensive nature of $\Omega^h(T, \mathcal{V}, \mu_F)$. From equations (8.15) and (8.16) we arrive at the Gibbs-Duhem relation

$$dP^h = \frac{S^h}{\mathcal{V}} dT + n_F d\mu_F. \tag{8.17}$$

Thus in the trap, we can now speak of the "local" quantities

$$n_F(\vec{r}) = \left(\frac{\partial}{\partial \mu_F} P^h(\mu_F(\vec{r}), T)\right)_T, \text{ and } \Omega^h(\vec{r}) = -P^h(\mu_F(\vec{r}), T)\delta\mathcal{V}(\vec{r}), \tag{8.18}$$

where $\delta\mathcal{V}(\vec{r})$ is a volume element at the point $\vec{r}$, and we invoke the local-density approximation, writing $\mu_F(\vec{r}) = \mu_F^0 - V_{T,F}(\vec{r}) = \mu_F^0 - \frac{m_F}{2}(\omega_{x,F}^2 x^2 + \omega_{y,F}^2 y^2 + \omega_{z,F}^2 z^2)$, where μ_F^0 is the chemical potential at the center of the trap. Integrating the second equation in (8.18) to get the total grand potential in the trap $\Omega = \int d^3\vec{r}\, \Omega^h(\vec{r})$ and taking a derivative with respect to μ_F, we find

$$\left(\frac{\partial \Omega}{\partial \mu_F}\right)_{T,\mathcal{V}} = -\int d^3\vec{r} \frac{\partial}{\partial \mu_F} P^h(\mu_F(\vec{r}), T)) = -N_F. \tag{8.19}$$

Thus given the function $N_F(\mu_F, T)$, which we can easily get by integrating equation (8.14), we have a prescription for calculating Ω.

In the trap, the total grand potential is defined in analogy with equation (8.15), namely $\Omega = E - TS - \mu_F^0 N_F$, from which we find

$$S = \frac{1}{T}(E - \Omega - \mu_F^0 N_F). \tag{8.20}$$

From the relation $\Omega = -E/3$, valid at unitarity[10] (see for example [51]), we find $S = (-4\Omega - \mu_F^0 N_F)/T$. Integrating equation (8.14) over space to get the total number, we have

$$N_F(\mu_F^0, T) = \left(\frac{k_B T}{\hbar\bar{\omega}_F}\right)^3 \mathcal{F}(\beta\mu_F^0). \tag{8.21}$$

where

$$\mathcal{F}(\beta\mu_F^0) = \frac{2}{\sqrt{\pi}} \int_{-\infty}^{\beta\mu_F^0} dx\,(\beta\mu_F^0 - x)^{1/2} f_n(x). \tag{8.22}$$

From this result we can also parametrize the reduced temperature, T/T_F, in terms of $\beta\mu_F^0$, where $T_F = \hbar\bar{\omega}(3N_F)^{1/3}/k_B$ is the Fermi temperature in the trap,

$$\left.\frac{T}{T_F}\right|_{\beta\mu_F^0} = (3\mathcal{F}(\beta\mu_F^0))^{-1/3}. \tag{8.23}$$

To get the total grand potential, we integrate equation (8.19),

$$\begin{aligned}\Omega(\mu_F^0, T) &= -\int_{-\infty}^{\mu_F^0} d\mu'\, N_F(\mu', T) \\ &= -k_B T \left(\frac{k_B T}{\hbar\bar{\omega}}\right)^3 \frac{2}{\sqrt{\pi}} \int_{-\infty}^{\beta\mu_F^0} dy \int_{-\infty}^{y} dx (y - x)^{1/2} f_n(x), \end{aligned}\tag{8.24}$$

where $y \equiv \beta\mu'$. Next, we integrate by parts on the variable x, and use the fact that $\lim_{x\to-\infty} f_n(x) = 2e^x$, which follows from the leading order term in the virial expansion (i.e. the Boltzmann limit). This gives

$$\begin{aligned}\Omega(\mu_F^0, T) &= -k_B T \left(\frac{k_B T}{\hbar\bar{\omega}}\right)^3 \frac{4}{3\sqrt{\pi}} \int_{-\infty}^{\beta\mu_F^0} dy \int_{-\infty}^{y} dx (y - x)^{3/2} \frac{d}{dx} f_n(x) \\ &= -k_B T \left(\frac{k_B T}{\hbar\bar{\omega}}\right)^3 \frac{4}{3\sqrt{\pi}} \int_{-\infty}^{0} d\tilde{x}\,(-\tilde{x})^{3/2} \frac{d}{d\tilde{x}} \int_{-\infty}^{\tilde{x}} d\tilde{y}\, f_n(\tilde{y} + \beta\mu_F^0) \\ &= -k_B T \left(\frac{k_B T}{\hbar\bar{\omega}}\right)^3 \mathcal{G}(\beta\mu_F^0), \end{aligned}\tag{8.25}$$

where

$$\mathcal{G}(\beta\mu_F^0) = \frac{4}{3\sqrt{\pi}} \int_{-\infty}^{\beta\mu_F^0} dx\,(\beta\mu_F^0 - x)^{3/2} f_n(x), \tag{8.26}$$

---

[10] For the homogeneous (untrapped) gas, this relation is $E = -\frac{3}{2}\Omega$, where the factor of 2 difference comes from the quadratic nature of the trapping potential.

and we have performed two sequential changes of variables: first $\tilde{x} = x - y$, then $\tilde{y} = y - \beta\mu_F^0 + \tilde{x}$. Using equations (8.21) and (8.25), we can rewrite equation (8.20) as

$$\frac{S}{N_F k_B} = \frac{4\mathcal{G}(\beta\mu_F^0)}{\mathcal{F}(\beta\mu_F^0)} - \beta\mu_F^0. \tag{8.27}$$

To evaluate $\mathcal{F}(\beta\mu_F^0)$ and $\mathcal{G}(\beta\mu_F^0)$, we use an interpolating function for $f_n(\beta\mu)$ between the data points from [67], which exist for $-1.56 \leq \beta\mu_F^0 \leq 3.97$, and join this in a piecewise fashion with the known fourth-order virial expansion for $\beta\mu_F^0 < -1.56$ [70, 79, 67].

The results of this analysis are shown in figure 8.6. In figure 8.6(a) we plot the initial EoS $f_n(\beta\mu_F)$ from equation (8.14) normalized by that of the non-interacting Fermi gas $f_{n,0}(\beta\mu_F) = -2\,\mathrm{Li}_{3/2}(-\exp(\beta\mu_F))$, where the red open circles are the measurements from [67]. In figure 8.6(b), we show the trap-averaged reduced temperature T/T_F as a function of $\beta\mu_F^0$ for both the unitary Fermi gas and the non-interacting Fermi gas. In the case of the non-interacting Fermi gas, equation (8.22) can be calculated analytically, giving $\mathcal{F}(\beta\mu_F^0) = -2\,\mathrm{Li}_3(-\exp(\beta\mu_F^0))$. We then show the total trap energy EoS $E(T/T_F)$ in figure 8.6(c). Lastly, we plot the trap-averaged entropy per particle $S/(N_F k_B)$ vs. T/T_F in figure 8.6(c). Because the measurements in [67] only exist for trap-averaged reduced temperatures of $T/T_F \geq 0.15$, we additionally plot the theoretical prediction from [47], which agrees quite well with the MIT group's data where available. By comparing our observed upper bound on the per-particle entropy, $S/(N_F k_B) \leq 0.55$ (open black triangle in figure 8.6(d)), with the values from [47], we extract an upper bound on the UFG temperature of $T \leq 0.12 T_F = 0.55 T_{c,F}$. Thus the Li cloud prepared with an evaporation gradient of $B' = 41$ G/cm is deep in the superfluid regime, and we have established the existence and stability of the Yb-Li Bose-Fermi superfluid mixture.

8.2 *Observation of elastic coupling*

In general, observing the effects of interspecies mean-field interactions is a subtly difficult thing to do[11]. While elastic collisions are ubiquitously used in ultracold atomic physics (e.g.

---

[11] The most precise way to determine the value of the interspecies mean-field is to perform molecular spectroscopy of the ground state scattering potential, as the scattering length can be calculated exactly

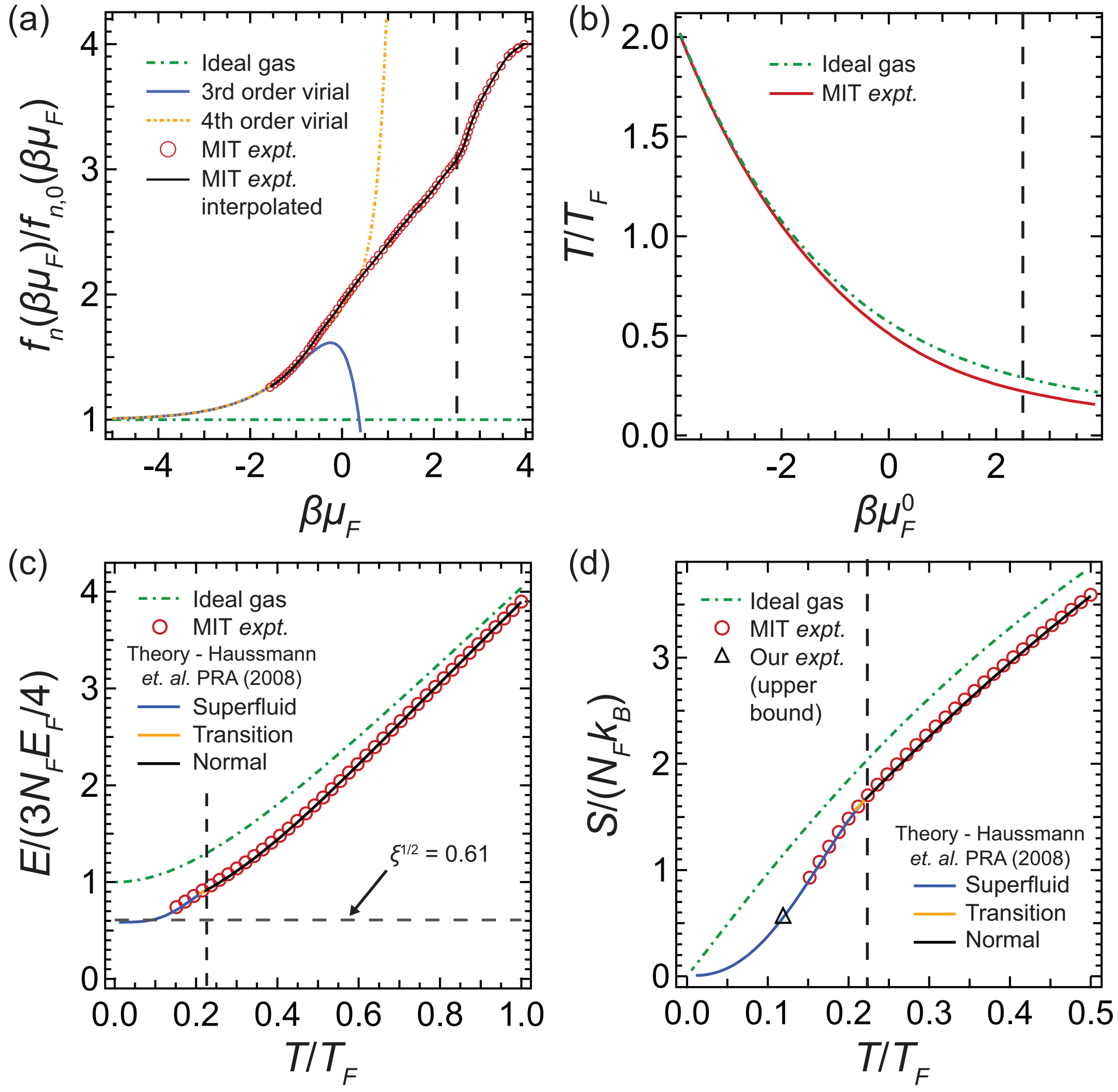

Figure 8.6: Transformation of the homogeneous EoS for the UFG from the MIT experiment [67] to trap-averaged quantities. For all plots, the superfluid transition is marked by a vertical dashed line. (a) Homogeneous EoS for the phase-space density (PSD), $n_F\lambda^3 = f_n(\beta\mu)$, in units of the ideal Fermi gas (IFG) PSD $f_{n,0}(\beta\mu)$, with 3rd and 4th order virial expansions shown for comparison. Error bars from [67] not shown. (b) Trap-averaged reduced temperature as a function of $\beta\mu_F^0$ for the IFG and UFG. (c) Total energy in the trap as a function of T/T_F. For the UFG at $T = 0$, $E = \sqrt{\xi}3N_FE_F/4$, where $\xi = 0.37$ is the Bertsch parameter [67, 112]. (d) Trap-averaged entropy EoS (per particle) versus T/T_F. For (c)-(d), we also show the theoretical EoS from [47], which enables us to use the upper bound on the entropy per particle $S/(N_Fk_B) \leq 0.55$ in our system to find $T \leq 0.12T_F = 0.55T_{c,F}$.

evaporative cooling, sympathetic cooling, etc.), they are in fact distinct from the effects of mean-field interactions. Specifically, elastic collisions correspond to collisions in which the directions of the particle momenta change as a result of the collision, while mean-field interactions arise because of a phase shift acquired from undergoing forward scattering. As an illustration of the difficulty in directly observing the mean-field interaction, we note that our lab was able to determine the Li-Yb s-wave collision cross section $\sigma_{\text{Li-Yb}} \propto |a_{BF}|^2$ a little over 5 years ago using interspecies thermalization studies [54], but the sign of a_{BF} remained unknown until completing the measurements described in this section.

8.2.1 Selective excitation of bosonic dipole modes

To probe elastic interactions in the Bose-Fermi superfluid mixture, we selectively excite vertical dipole oscillations in the bosonic component. Because of the large ratio of trap frequencies $\omega_F/\omega_B = 8$ for the two components, we can achieve this species-selective excitation by changing the vertical trap center position on a timescale that is diabatic for Yb and adiabatic for Li. As the Yb cloud subsequently undergoes dipole oscillations, we expect the mean-field interactions with Li will decrease(increase) the apparent oscillation frequency for repulsive(attractive) interactions, thus giving us a method for determining the sign of a_{BF}.

In the experiment, we begin with the superfluid mixture in the crossed ODT with frequencies $(\omega_x, \omega_y, \omega_z)_B = 2\pi \times (23, 150, 10)$ Hz and an applied magnetic field gradient of $B' = 41$ G/cm. Anticipating that we will increase the gradient to 68 G/cm in order to perfectly overlap the vertical cloud centers, we first slowly increase the ODT power from 1.5 to 4.1 W, as Li would otherwise spill out of the trap. Then we simultaneously increase the power from 4.1 to 4.8 W and increase the gradient to 68 G/cm over 1 ms in a linear fashion. This results in the diabatic excitation of a vertical dipole oscillation Yb, while Li adiabatically follows the changing vertical trap center position as $\omega_{y,F} = 2\pi \times 3.1$ kHz. We do not observe

---

from this potential. An alternative method is to measure interaction shifts on clock transitions, but this method suffers from the fact that one only determines the difference in mean-field energy between the two internal states involved.

the excitation of any modes in Li as a result of the ODT power ramp.

The trap frequencies after the excitation are $(\omega_x, \omega_y, \omega_z)_B = 2\pi \times (59, 388, 26)$ Hz, with typical atom numbers of $N_B = 10^5$ and $N_F = 1.3 \times 10^5$ atoms, resulting in peak densities[12] of $n_B(0) = 4 \times 10^{14}$ cm^{-3} and $n_F(0) = 3 \times 10^{13}$ cm^{-3}, a ratio of cloud radii of $R_B/R_F = \sqrt{\frac{\alpha_F}{\alpha_B}\frac{\mu_B}{\mu_F}} = 0.35$, and relative interspecies mean-field interaction energy of $V_{BF(FB)}(0)/\mu_{F(B)} = 0.10(0.13)$. Here $\alpha_{F(B)}$ is the polarizability of Li(Yb) and $V_{BF(FB)}$ is the mean-field interaction energy of Yb on Li (Li on Yb). Thus we can treat the interspecies mean-field as a small perturbation on each species.

The dipole oscillation measurements are shown in figure 8.7, where we ramp the magnetic field to 780 G during the species-selective excitation to increase the magnitude of the interspecies interaction effect on the Yb oscillation frequency. Clearly the presence of Li has an effect on the Yb oscillation, as the two data sets are roughly $\pi/2$ out of phase at 50 ms. When we perform the same measurement without a magnetic field present, we observe no effect on the Yb dipole oscillations, thus verifying the necessity of the species-selective tool for establishing interspecies coupling. In order to ensure that both species remain superfluid throughout the measurement, we perform a similar lifetime measurement to that shown in figure 8.5(c) and find that the data in figure 8.7 is within a single $1/e$ time.

While the presence of Li has a clear effect on the Yb dipole oscillations, we do not observe back action onto Li as a result of the oscillating Yb cloud. This can be understood by considering the trap frequency ratio. As Yb executes dipole oscillations, the Li cloud feels a time-dependent potential and adiabatically deforms as the mean-field interaction term oscillates at $\omega_{y,B} \ll \omega_{y,F}$.

By fitting the data to damped sinusoidal functions, we find oscillation frequencies with and without Li of $\omega_{y,B} = 2\pi \times 387.7(3)$ Hz and $\omega'_{y,B} = 2\pi \times 381.3(4)$ Hz, respectively. Thus, the presence of the Li superfluid results in a reduction of the Yb dipole oscillation frequency of 1.7(2)%. This provides the first measurement of the sign of the interspecies

---

[12] For the estimates in this paragraph we use the density profile of a $T = 0$ unitary Fermi gas.

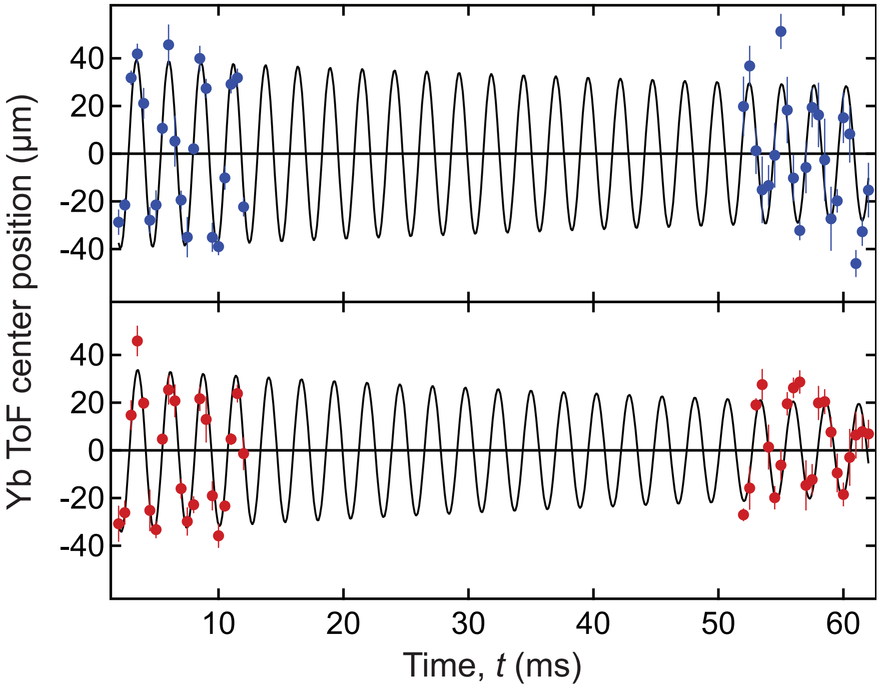

Figure 8.7: Vertical dipole oscillations of an Yb BEC in the absence (blue circles) and presence (red circles) of a Li superfluid at 780 G ($1/k_F a_F = 0.39$). The vertical position of the Yb center-of-mass at 30 ms ToF is plotted for different hold times after the species-selective excitation. The solid lines are fits to damped sinusoids. The oscillation with Li is of lower frequency than that without, indicating a repulsive interspecies interaction (i.e. $a_{BF} > 0$).

s-wave scattering length, and determines it to be positive (i.e. repulsive interactions). As we will see in the next section, this shift is in agreement with a theoretical calculation based on a mean-field model.

The extracted exponential decay constants with and without Li of $\tau' = 0.11(3)$ s and $\tau = 0.17(7)$ s are within error of each other. The finite damping in the measurements with only Yb reveals that our trapping potential has a finite quality factor (i.e. is slightly anharmonic). Still, a natural question is whether the presence of Li dampens the oscillatory motion of Yb. Now, for a unitary Fermi gas at zero temperature, the critical velocity for the creation of an excitation is[13] $v_{c,F} = \xi^{1/4} v_F/\sqrt{3} \approx 0.45 v_F$ [48], where $v_F = \sqrt{2E_F/m_F}$ and $E_F = \hbar\bar{\omega}_F(3N_F)^{1/3}$. For the measurements in figure 8.7, we have $E_F/k_B = 2.4\ \mu$K, yielding $v_F = 82$ mm/s and $v_{c,F} = 37$ mm/s. We then want to compare this to maximum velocity attained by Yb during the dipole oscillation, $v_{B,\max}$. We can easily compute this value from the initial amplitude A of the oscillations in figure 8.7, and using the known ToF time t_{ToF}, giving $v_{B,\max} = A/t_{\mathrm{ToF}} = (40\,\mu\mathrm{m})/(30\,\mathrm{ms}) = 1.3$ mm/s. Hence, we are roughly a factor of 30 below the critical velocity for the Fermi gas[14]. It is thus unfeasible for our experiment to probe critical velocity phenomena in this mixture using dipole oscillations of the bosonic component. While the damping times with and without Li are within error bars, we cannot rule out the possibility of increased damping due to a finite thermal component of the Fermi gas.

---

[13] It is important to note the 1/4 power of ξ in this expression, in contrast to $\sqrt{\xi}$ dependence that appears in many theoretical treatments (see for instance [48]). The discrepancy is due to whether one is considering a harmonically-trapped Fermi gas or a homogeneous one. As we saw in section 3.4.3, the Fermi wave vectors for the two cases are related by $k_F^{\mathrm{hom}} = k_F/\xi^{1/4}$. Hence, the Fermi velocities are related by the same factor, giving $v_{c,F} = v_F^{\mathrm{hom}}\sqrt{\xi/3} = v_F \xi^{1/4}/\sqrt{3}$.

[14] The nature of the critical velocity in a Bose-Fermi superfluid mixture is in fact still an open question. There is theoretical and experimental work to support the claim that $v_c = v_{c,B} + v_{c,F}$ [31, 18], where $v_{c,B}$ is the critical velocity in the BEC (i.e. the sound velocity), but the measurements are also consistent with $v_c = v_{c,F}$.

8.2.2 Mean-field model for dipole frequency shift

To model the effect of the fermionic component on the boson dipole oscillations, we use a mean-field model and calculate the local curvature of the full potential seen by the bosonic component [31]. Namely, we begin with $V_B(\vec{r}-\vec{d}) = V_{T,B}(\vec{r}-\vec{d}) + g_{BF} n_F(\vec{r})$, where we center the coordinate system on the Fermi cloud center and allow for arbitrary offsets of the cloud centers, indicated by $\vec{d}$. Here, $V_{T,B}(\vec{r}) = \frac{m_B}{2}(\omega_{x,B}^2 x^2 + \omega_{y,B}^2 y^2 + \omega_{z,B}^2 z^2)$ is the optical trapping potential seen by bosonic component. To compute the effective trap frequency for Yb at the point $\vec{d}$, then, we have

$$m_B \omega_{y,B}'^2 = m_B \omega_{y,B}^2 + g_{BF} \left. \frac{\partial^2 n_F}{\partial y^2} \right|_{\vec{r}=\vec{d}} . \tag{8.28}$$

In the local-density approximation, $n_F(\vec{r}) = n_F[\mu_F(\vec{r})]$, and we can use the zero-temperature equation of state $n_F(\mu_F, a_F)$ [80] to evaluate the fermionic density at the local chemical potential $\mu_F(\vec{r}) = \mu_F^0 - V_{T,F}(\vec{r})$. Since the interspecies mean-field interactions are small compared with the respective chemical potentials, we neglect the distortion of the Fermi density distribution due to the presence of Yb. Then, we rewrite the second term as

$$g_{BF} \frac{\partial^2 n_F}{\partial y^2} = g_{BF} \left(\frac{\partial n_F}{\partial \mu_F} \frac{\partial^2 \mu_F}{\partial y^2} + \frac{\partial^2 n_F}{\partial \mu_F^2} \left(\frac{\partial \mu_F}{\partial y} \right)^2 \right) . \tag{8.29}$$

As in section 3.4.3 we seek to write all relevant quantities in terms of $\delta = \hbar/(a\sqrt{2m_F\mu_F})$ and $h(\delta)$, where $h(\delta) = P(\mu_F, a_F)/(2P_0(\mu_F))$ relates the pressure P at $T = 0$ of the two-component, interacting gas to the single-component, non-interacting one P_0. Within the local density approximation, we have

$$\delta(\vec{r}) = \frac{\hbar}{a\sqrt{2m_F\mu_F(\vec{r})}} = \frac{\delta_0}{\sqrt{1 - (\delta_0 k_F a_F)^2 \left(\frac{x^2}{R_{0,x}^2} + \frac{y^2}{R_{0,y}^2} + \frac{z^2}{R_{0,z}^2} \right)}}, \tag{8.30}$$

where $\delta_0 = \hbar/(a_F\sqrt{2m_F\mu_F^0})$ and $R_{0,i} = \hbar k_F/(m_F\omega_{i,F})$ is the trapped, non-interacting Fermi gas radius. One can then use the Gibbs-Duhem relation $n_F = \partial P/\partial \mu_F$ to evaluate the terms in equation (8.29) and rewrite (8.28) as

$$\frac{\delta\omega_{y,B}}{\omega_{y,B}}\frac{1}{k_F a_{BF}} = -\frac{\alpha_F}{\alpha_B}\frac{m_F+m_B}{\pi m_B}(\delta k_F a_F)^{-1}\Bigg[h(\delta) - \frac{7\delta}{15}h'(\delta) + \frac{\delta^2}{15}h''(\delta) \\ - \left(\frac{d_y}{R_{0,y}}\right)^2 (\delta k_F a_F)^2 \left(h(\delta) - \delta h'(\delta) + \frac{2\delta^2}{5}h''(\delta) - \frac{\delta^3}{15}h'''(\delta)\right)\Bigg], \tag{8.31}$$

where $\delta\omega_{y,B} = \omega'_{y,B} - \omega_{y,B}$, α_F and α_B are the polarizabilities of the fermionic and bosonic components, and all instances of δ are evaluated at the point $\vec{d} = (d_x, d_y, d_z)$. For the unitary Fermi gas with $\vec{d} = 0$, we use that $h(0) = \xi^{-3/2}$ and $\lim_{\delta\to 0}\delta k_F a_F = \xi^{-1/4}$ to reproduce the result from [31],

$$\frac{\delta\omega_{y,B}}{\omega_{y,B}}\frac{1}{k_F a_{BF}} = -\frac{\alpha_F}{\alpha_B}\frac{m_F+m_B}{\pi m_B \xi^{5/4}}. \tag{8.32}$$

Amazingly, if the clouds are perfectly overlapped (i.e. $\vec{d} = 0$), the frequency shift only depends on the value of $1/k_F a_F$ (recall from section 3.4.3 that we parametrize the function δ in terms of $1/k_F a_F$). The predicted frequency shift as a function of $1/k_F a_F$ for perfectly overlapped Bose-Fermi clouds is shown as the solid green line in figure 8.8. The shaded region is the uncertainty in the prediction, coming entirely from the uncertainty in the measured value[15] of $|a_{BF}| = 15(2)\,a_0$ [54, 44]. For these calculations, we use the value from our experiment of $k_F a_{BF} = 0.006$. The red points in figure 8.8 are the values measured in our system at 780 G ($1/k_F a_F = 0.39$) and 720 G ($1/k_F a_F = 1.2$). While the 780 G measurement is in agreement with the mean-field model, that at 720 G is far from it. As we will see in the next section, this discrepancy results from a large offset of the Yb-Li cloud centers in the horizontal plane.

Indeed, for finite $\vec{d}$, there is a non-trivial dependence on the various trap frequencies through the radii $R_{0,i}$. In figure 8.9, we show the dependence of the mean-field frequency shift on horizontal displacement as predicted by equation (8.31). Without loss of generality, we assume the displacement to be along the x direction. For arbitrary displacements, the

---

[15] For this prediction, we use a weighted mean of the measured values of $|a_{BF}|$ from our group [54] and the Kyoto group [44].

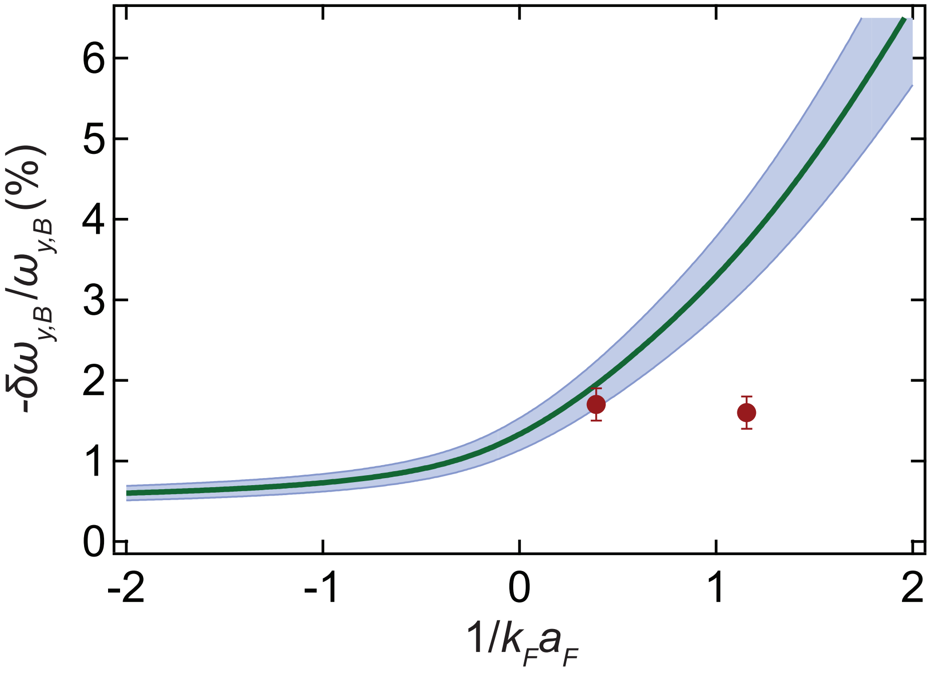

Figure 8.8: Mean-field shift of Yb dipole oscillation frequency in the presence of a perfectly-overlapped Li superfluid as a function of $1/k_F a_F$, where $k_F a_{BF} = 0.006$. (Solid green line) Value predicted by equation (8.31), shading represents uncertainty due to measured uncertainty in $|a_{BF}| = 15(2)\, a_0$. Red points are measurements at 780 G ($1/k_F a_F = 0.39$) and 720 G ($1/k_F a_F = 1.2$).

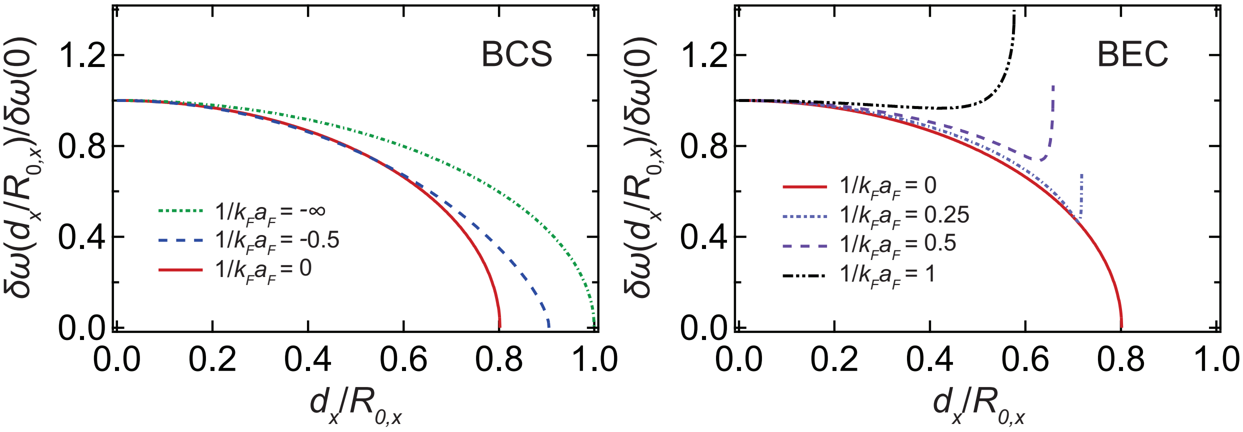

Figure 8.9: Relative frequency shift for vertically overlapped clouds (i.e. $d_y = 0$) with horizontal offset d_x. (Left) BCS side of resonance. Progression from the ideal to the unitary Fermi gas. (Right) BEC side of resonance. All curves are normalized to the frequency shift value for perfectly-overlapped clouds. The point at which each curve terminates corresponds to the Fermi radius for that value of $1/k_F a_F$.

frequency shift contours lie on ellipses defined by $((d_x/R_{0,x})^2 + (d_z/R_{0,z})^2)^{1/2}$. The left panel in figure 8.9 shows the behavior on the BCS side of resonance, while the right panel shows that on the BEC side. As expected, the curves for the ideal and unitary Fermi gases are scaled versions of each other. For the BEC curves, the qualitative behavior of the shift versus displacement quickly changes and becomes non-monotonic. Likely, the behavior near the edge of the cloud cannot be fully captured by this model since the local-density approximation is often violated here. In the far-BEC limit, we know the density profile acquires the shape $n_F \propto \mu_F^0 - V_{T,F}(\vec{r})$, and thus have constant curvature versus displacement (not shown in figure 8.9).

From the behavior on the BEC side of resonance, we see how the horizontal cloud offset can lead to a systematic error in the frequency measurement as observed at 720 G. In this case, the most important effect is the shortening of the radius of the molecular BEC. As we will see in the next section, our observation of angular momentum transfer between the two clouds reveals that there is a sizable horizontal offset in our system. Our model predicts a large value of about 60% of $R_{0,x}$. For the measurements with $1/k_F a_F = 1.2$, this places most of the Yb cloud outside of the Li cloud, and thus causes the "average" frequency shift seen by the Yb cloud to be much less than the $\vec{d} = 0$ value.

8.3 An unexpected twist: Scissors mode observation

In addition to observing elastic coupling between the superfluids via the mean-field shift of the Yb dipole oscillation frequency, we observe a modulation of the Yb BEC tilt angle due to interactions with the Li superfluid. By fitting the observed modulation with a sinusoid, we extract a frequency which is consistent with the dipole oscillation frequency. We interpret this modulation as the excitation of a scissors mode in Yb, driven by a combination of the sinusoidal motion of the Yb center-of-mass and the interspecies mean-field interaction with a horizontally-offset Li cloud. We develop an analytical model based on superfluid hydrodynamics that captures the essential features of this excitation.

8.3.1 Scissors modes: What are they?

The scissors mode in ultracold atomic systems is a small amplitude angular excitation of a superfluid (or any collsionally hydrodynamic fluid) about a symmetry axis of the ellipsoidal trap. In early experiments with BECs in trapped gases, the scissors mode was used to demonstrate and study superfluidity. By analyzing the different responses of a superfluid and a thermal gas to a small diabatic rotation of the trap eigenaxes, it was first theorized [38], and then shown experimentally [74], that the superfluid responds by performing an angular oscillation at a single frequency, called the scissors frequency ω_s, while the thermal cloud exhibits a two-frequency oscillation. In the superfluid regime, the internal flow resulting from the excitation obeys the constraint of irrotationality, $\nabla \times \vec{v} = 0$, but has an associated oscillating angular momentum with a mean of zero. For rotations of the trap axes about the z axis, the resulting frequencies are $\omega_s = (\omega_x^2 + \omega_y^2)^{1/2}$ for the BEC, and $\omega_{\text{th}} = |\omega_x \pm \omega_y|$

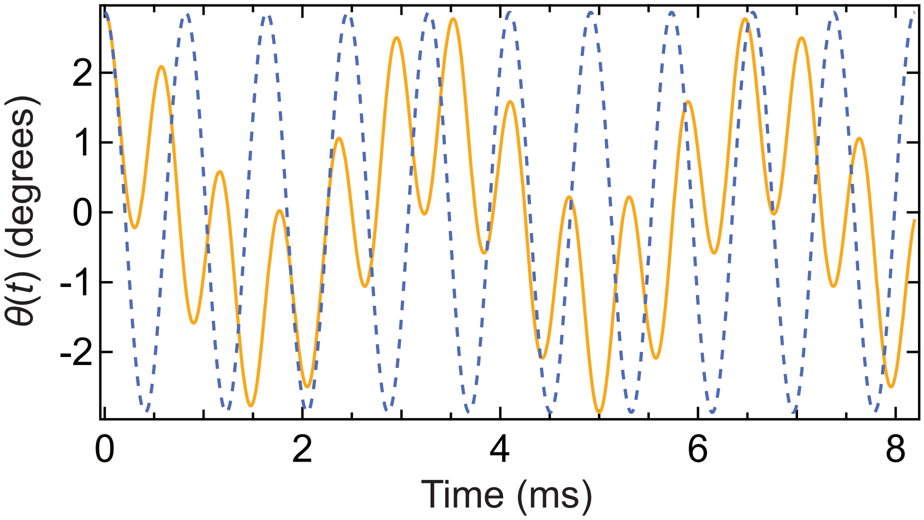

Figure 8.10: Characteristic angular oscillations of a pure superfluid (dashed blue line) and purely thermal gas (solid orange line) following a sudden rotation of the trap eigenaxes. For these curves, the trap axis rotation occurs about the z axis, and the relevant trap frequencies are $\omega_x = 2\pi \times 700$ Hz and $\omega_y = 2\pi \times 1000$ Hz, resulting in angular oscillation frequencies of $\omega_s = 2\pi \times 1221$ Hz and $\omega_{\mathrm{th}} = 2\pi \times 300$ Hz and $2\pi \times 1700$ Hz.

for the (collisionless) thermal cloud. Such characteristic oscillations are depicted in figure 8.10, where the beating of the two thermal cloud frequencies is clearly apparent. This clear qualitative difference between the superfluid and thermal angular oscillation modes allowed for one of the first measurements of superfluidity in trapped BECs [74].

8.3.2 Observation in ^{174}Yb BEC caused by presence of ^{6}Li superfluid

In order to detect modulation of the Yb BEC *in-trap* tilt angle, θ_B, we must infer such an effect from the absorption images obtained at 30 ms ToF (i.e. the same data set used in figure 8.7). In analogy with how the center-of-mass momentum maps linearly to position for long ToF, we expect the time-derivative of the in-trap angle $\dot{\theta}_B(t)$ to map onto the tilt angle in long ToF, $\theta_{B,\mathrm{ToF}}(t)$. In fact, the expansion dynamics of a rotating BEC are rather complicated [77], and display non-intuitive features due to the irrotational nature of the flow field. However, in the long-ToF regime, the observed angular oscillation amplitude will always be a factor of ≈ 2 greater than that in-trap, regardless of the aspect ratio, with some non-trivial phase shift with respect to the in-trap oscillation [77]. This is schematically shown in figure 8.11(a), where the principal axis about which the BEC performs an angular oscillation rotates by $\pi/2$ between the in-trap and long-ToF situations.

While one can numerically compute the tilt of a principal axis in an image by computing various central moments of the two-dimensional array, we find that simply fitting a two-dimensional Gaussian function to the absorption image accurately extracts the BEC tilt angle. To perform this fit, we use the following form for the density,

$$n_B(x,y) = n_B(0,0)\exp\left(\frac{-1}{2(1-\rho^2)}\left(\left(\frac{x-x_0}{\sigma_x}\right)^2 + \left(\frac{y-y_0}{\sigma_y}\right)^2 - \frac{2\rho(x-x_0)(y-y_0)}{\sigma_x\sigma_y}\right)\right), \tag{8.33}$$

where ρ is the correlation between the x and y directions. To find the principal axes of the density distribution, then, we simply rotate by the angle

$$\theta_{B,\mathrm{ToF}} = \frac{1}{2}\tan^{-1}\left(\frac{2\rho\sigma_x\sigma_y}{\sigma_x^2-\sigma_y^2}\right). \tag{8.34}$$

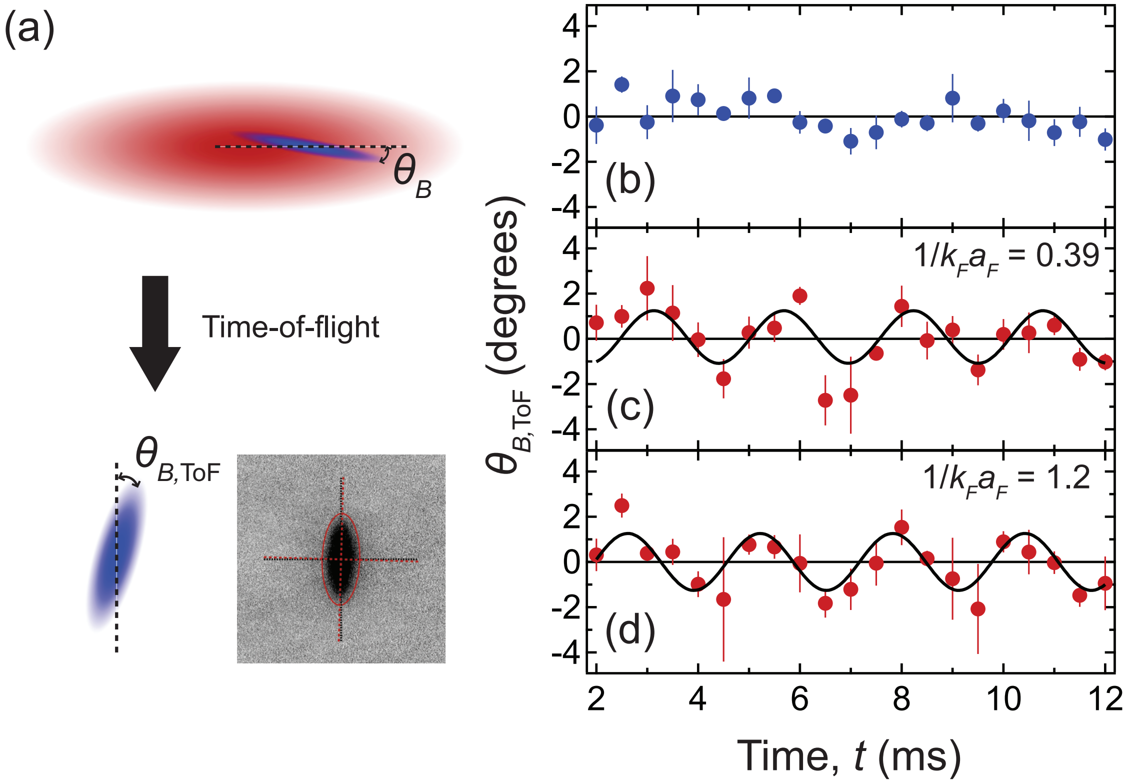

Figure 8.11: Observation of scissors mode excitation in Yb due to interactions with the Li superfluid. (a) Schematic of offset Yb-Li clouds leading to the scissors mode excitation during Yb dipole oscillations. In long ToF, the in-trap angular oscillation maps proportionally onto an angular oscillation (with some phase shift) about the perpendicular axis due to superfluid expansion dynamics. The red crosshairs are aligned to the imaged BEC principal axes, and are 1.3 degrees rotated with respect to the unperturbed BEC orientation. (b) Yb tilt angle dynamics in the absence of Li. A sinusoidal fit to the data is consistent with zero modulation amplitude. (c)-(d) Observed scissors mode at 780 G ($1/k_F a_F = 0.39$) and 720 G ($1/k_F a_F = 1.2$) due to interaction with Li. The frequency is consistent with the Yb dipole frequency at that field.

An absorption image (30 ms ToF) of a rotated Yb BEC is shown in figure 8.11(a), where the red ellipse is a contour of constant density determined by fitting the image with equation (8.33). The red crosshairs correspond to the principal axes of the imaged BEC, which are rotated by 1.3 degrees with respect to the unperturbed BEC orientation (black crosshairs).

The observations of the bosonic scissors mode are shown in figure 8.11(b)-(d), where we plot the tilt angle as a function of time for the first 12 ms of the Yb dipole oscillation. For the data in the absence of the Li superfluid (figure 8.11(b)), a sinusoidal fit returns an amplitude that is consistent with zero, whether or not we fix the frequency to be that of the dipole oscillation, $\omega_{y,B}$. In contrast, for the measurements with Li at 780 G ($1/k_F a_F = 0.39$, figure 8.11(c)), a sinusoidal fit to the data returns a modulation frequency that is in good agreement with the dipole oscillation frequency, $\omega_\theta/\omega'_{y,B} = 1.02(3)$, and an amplitude of 1.3(3) degrees. Additionally, we observe the excitation of the Yb scissors mode at 720 G ($1/k_F a_F = 1.2$, figure 8.11(d)), with $\omega_\theta/\omega'_{y,B} = 1.01(3)$ and an amplitude of 1.3(3) degrees. For each field, we present the frequency measurement as a ratio with respect to the mean-field shifted frequency $\omega'_{y,B}$ at that field. Because the ω_θ measurement precision is comparable with the frequency shift $\delta\omega_{y,B}$, the result is consistent with both $\omega_{y,B}$ and $\omega'_{y,B}$.

As with the Yb vertical dipole oscillations, we do not observe back action onto the Li cloud as a result of the angular motion of Yb, again due to the large mismatch in trap frequencies between the two species. As a result, the angular momentum transferred from Yb to Li during the scissors mode oscillation is adiabatically absorbed by the trap itself.

Associated with the tilt angle modulation $\theta_B(t)$ is an acquired angular momentum in the condensate proportional to $\dot{\theta}_B(t)$. Thus, from the observations in figure 8.11, we can immediately conclude that the Yb and Li cloud center positions must be offset in the horizontal plane, since we must have a term in the Hamiltonian that breaks the reflection symmetry about the vertical axis of the BEC. In the next section, we will explicitly calculate the time-dependence of the angular momentum in terms of the interspecies interactions within the framework of superfluid hydrodynamics for Yb.

8.4 Analytical model for driven scissors mode

In order to model the observed scissors mode excitation driven by interspecies interactions, we adopt the analysis from [38] based on superfluid hydrodynamics in the linear-response regime for the Yb BEC, and extend it to include the interaction with the Li superfluid. In our model, we assume that the Li density profile presents a static, mean-field potential for Yb, and neglect back action onto the Li cloud. This is justified by our observation that Li exhibits no angular oscillations during the Yb dipole oscillations, and by considering the large detuning of the two scissors oscillators (factor of 8). This analytical model captures the essential features of the observed scissors mode oscillation, and allows us to estimate the magnitude of the horizontal offset between the Yb-Li cloud centers.

8.4.1 Reducing the equations of superfluid hydrodynamics

Starting from the time-dependent Gross-Pitaevskii equation for the condensate wave function $\Phi(\vec{r},t) = \sqrt{n(\vec{r},t)}\exp(iS(\vec{r},t))$, one can show for a zero-temperature Bose gas in the Thomas-Fermi regime that [23]

$$\frac{\partial n}{\partial t} + \nabla \cdot (n\vec{v}) = 0 \tag{8.35}$$

$$m\frac{\partial \vec{v}}{\partial t} + \nabla\left(V_{\text{eff}}(\vec{r}) + gn(\vec{r}) + \frac{m\vec{v}^2}{2}\right) = 0, \tag{8.36}$$

where $n(\vec{r})$ is the Bose density distribution, $\vec{v} = (\hbar/m)\nabla S$ is the Bose superfluid velocity, $g = 4\pi\hbar^2 a/m$ is the Bose-Bose coupling constant, m is the Bose particle mass, and $V_{\text{eff}}(\vec{r})$ is the effective potential felt by the boson, consisting of both the effects of the trap and the interspecies mean-field due to the presence of the fermion. Note that for simplicity of notation we forgo the B subscripts for the bosonic parameters (e.g. $n(\vec{r})$ instead of $n_B(\vec{r})$), while we will retain all F subscripts for fermionic parameters. We write the effective potential as $V_{\text{eff}}(\vec{r}) = V_T(\vec{r}+y_0(t)\hat{y})+g_{BF}n_F(\vec{r}+\vec{d}(t))$, where we allow a vertical offset between the centers of the BEC and the trap, and allow for vertical *and* horizontal offsets between the centers of the BEC and the Fermi gas, with $\vec{d}(t) = (x_0, y_0(t), 0)$. Eventually, we will substitute in the vertical motion corresponding to the dipole oscillation, $y_0(t) = y_0 \cos(\omega'_{y,B} t)$. The trapping potential is given by

$$V_T(x, y + y_0(t), z) = \frac{m}{2}\left(\omega_x^2 x^2 + \omega_y^2 (y + y_0(t))^2 + \omega_z^2 z^2\right), \tag{8.37}$$

and the spatial dependence of the mean-field term $g_{BF} n_F(\vec{r} + \vec{d}(t))$ is determined by the zero-temperature equation of state $n_F(\mu_F, a_F)$ in the local-density approximation (see section 3.4.3).

The scissors mode is a small amplitude excitation of one of the odd-parity quadrupole modes (i.e. xy, yz, and zx). The excitation causes the superfluid to perform an angular oscillation about a principal axis, but does not deform the density distribution. Anticipating the excitation of such a mode rotating about the z axis, we reduce equations (8.35) and (8.36) to extract the linear-response dynamics of $\langle xy \rangle$, where

$$\langle f(\vec{r}) \rangle = \frac{1}{N} \int d^3\vec{r}\, f(\vec{r}) n(\vec{r}). \tag{8.38}$$

For equation (8.35), we accomplish this by multiplying by xy and integrating over space, giving

$$\begin{aligned} N \frac{d\langle xy \rangle}{dt} &= -\int d^3\vec{r}\, (\nabla \cdot (n\vec{v}))xy \\ &= -\int d^3\vec{r} \left(\frac{\partial}{\partial x}(n v_x) + \frac{\partial}{\partial y}(n v_y) + \frac{\partial}{\partial z}(n v_z) \right) xy \end{aligned} \tag{8.39}$$

For the first term in the integrand on the RHS, we integrate by parts as follows,

$$\int_{-\infty}^{\infty} dx\, xy \frac{\partial}{\partial x}(n v_x) = xy n v_x \Big|_{-\infty}^{\infty} - \int_{-\infty}^{\infty} dx\, y v_x n, \tag{8.40}$$

where the boundary term will vanish since $n \to 0$ as $x \to \infty$[16]. Evaluating the remaining

---

[16] In the Thomas-Fermi limit, we have $n(\vec{r}) = \mathrm{Max}(\mu - V_T(\vec{r}), 0)/g$, for which the boundary term would trivially vanish. However, the Thomas-Fermi approximation must break down near the Thomas-Fermi radius, since at this point $\mu \approx V_T(\vec{r})$. Nevertheless, in the limit $x \to \infty$, the interaction term in the Gross-Pitaevskii equation becomes negligible and we are left with the Schrödinger equation for a harmonic oscillator, and thus n falls off as $\exp(-m\omega_x x^2/\hbar)$.

terms in the same way, we find

$$\frac{d\langle xy\rangle}{dt} = \langle xv_y + yv_x\rangle. \tag{8.41}$$

For equation (8.36), the procedure is slightly more involved. To being with, we multiply the whole equation by n, take the divergence, multiply by xy, and then integrate over all of space. For the first term on the RHS of equation (8.36) this gives

$$\begin{aligned} m\int d^3\vec{r}\, xy\, \nabla\cdot\left(n\frac{\partial\vec{v}}{\partial t}\right) &= m\frac{d}{dt}\int d^3\vec{r}\, xy\,\nabla\cdot(n\vec{v}) - m\int d^3\vec{r}\, xy\,\nabla\cdot\left(\vec{v}\frac{\partial n}{\partial t}\right) \\ &= mN\frac{d}{dt}\langle xv_y + yv_x\rangle - m\int d^3\vec{r}\, xy\,\nabla\cdot\left(\vec{v}\frac{\partial n}{\partial t}\right), \end{aligned} \tag{8.42}$$

where we use equation (8.40) to simplify the first term on the RHS. Integrating by parts for the second term and dropping the boundary term, we have

$$\begin{aligned} \int d^3\vec{r}\, xy\,\nabla\cdot\left(\vec{v}\frac{\partial n}{\partial t}\right) &= -\int d^3\vec{r}\,\frac{\partial n}{\partial t}(xv_y + yv_x) \\ &= +\int d^3\vec{r}\,\left(\nabla\cdot(n\vec{v})\right)(xv_y + yv_x) \\ &= -\int d^3\vec{r}\, 2v_xv_yn. \end{aligned} \tag{8.43}$$

To get the above result we first use the continuity equation (8.35), then integrate by parts once again and drop the boundary term. Since equation (8.43) is second order in the velocity, we neglect it in linear response.

Lastly, manipulating the second term on the LHS of equation (8.36) in the same way as the first, one can show that (dropping the term proportional to $\vec{v}^2$) the full equation reduces to

$$\frac{d\langle xv_y + yv_x\rangle}{dt} = -\frac{1}{m}\left\langle x\frac{\partial V_{\text{eff}}}{\partial y} + y\frac{\partial V_{\text{eff}}}{\partial x}\right\rangle. \tag{8.44}$$

Thus we see that the variables xy and $xv_y + yv_x$ have an analogous relationship to position and momentum in this coupled first-order system of equations, (8.41) and (8.44). Reducing the system to a single second-order differential equation, we finally get

$$\frac{d^2\langle xy\rangle}{dt^2} = -(\omega_x^2+\omega_y^2)\langle xy\rangle - \omega_y^2 y_0(t)\langle x\rangle - \frac{g_{BF}}{m}\left\langle x\frac{\partial n_F(\vec{r}+\vec{d}(t))}{\partial y} + y\frac{\partial n_F(\vec{r}+\vec{d}(t))}{\partial x}\right\rangle . \tag{8.45}$$

8.4.2 Solving for the driven-scissors dynamics

In order to solve equation (8.45), we take the following ansatz for the BEC density distribution,

$$n(\vec{r},t) = \frac{1}{g}\mathrm{Max}\left(\mu - \frac{m}{2}\left(\omega_x^2 x^2 + \omega_y^2 y^2 + \omega_z^2 z^2 + (\omega_x^2+\omega_y^2)\alpha(t)xy\right), 0\right), \tag{8.46}$$

where we expect $\alpha(t)$ to be small due to the perturbative nature of the excitation. One can show that if we define new coordinates $(x',y',z') = (x\cos\theta - y\sin\theta, x\sin\theta + y\cos\theta, z)$, or in matrix notation $\vec{r}\,' = R(\theta)\vec{r}$, where

$$\tan(2\theta(t)) = \frac{(\omega_x^2+\omega_y^2)\alpha(t)}{\omega_y^2-\omega_x^2}, \tag{8.47}$$

the BEC density distribution can be written as

$$n(R^{-1}\vec{r}\,',t) = \frac{1}{g}\mathrm{Max}\left(\mu - \frac{m}{2}\left(\omega_{x'}(t)^2 x'^2 + \omega_{y'}(t)^2 y'^2 + \omega_z^2 z'^2\right), 0\right), \tag{8.48}$$

for some new frequencies $\omega_{x'}(t)$ and $\omega_{y'}(t)$. The angle defined by equation (8.47) is the tilt angle associated with the scissors mode oscillation. One can then show that for $|\alpha(t)| \ll \epsilon = \left|\frac{\omega_x^2-\omega_y^2}{\omega_x^2+\omega_y^2}\right|$, $\omega_{x'}(t)^2 = \omega_x^2 + \mathcal{O}((\alpha/\epsilon)^2)$ and $\omega_{y'}(t)^2 = \omega_y^2 + \mathcal{O}((\alpha/\epsilon)^2)$. As noted in the previous section, the scissors mode requires a small enough excitation such that the BEC shape is unaffected by the oscillation. Thus, our linear-response treatment is valid so long as $|\alpha(t)| \ll \epsilon$, or equivalently $|\theta(t)| \ll 1$, since the density distribution is unchanged in shape to lowest order.

For the first term on the RHS of equation (8.45), we find

$$\begin{aligned}
\langle xy\rangle &= \frac{1}{N}\int d^3\vec{r}\, xy\, n(\vec{r},t)\\
&= \frac{1}{N}\int d^3\vec{r}\,'\,(x'\cos\theta + y'\sin\theta)(-x'\sin\theta + y'\cos\theta)n(R^{-1}\vec{r}\,',t)\\
&= \frac{\cos\theta\sin\theta}{N}\int d^3\vec{r}\,'\,(y'^2 - x'^2)n(R^{-1}\vec{r}\,',t) + \frac{\cos^2\theta - \sin^2\theta}{N}\int d^3\vec{r}\,'\,x'y'n(R^{-1}\vec{r}\,',t).
\end{aligned} \tag{8.49}$$

Since $n(R^{-1}\vec{r}\,',t)$ is an even function of x' and y', the second term will vanish. Therefore, using $\omega_{x'}(t) \approx \omega_x$ and $\omega_{y'}(t) \approx \omega_y$, we get

$$\begin{aligned}
\langle xy\rangle &= \frac{\sin(2\theta)}{m}\left(\frac{1}{\omega_y^2}\left\langle \frac{m}{2}\omega_y^2 y'^2\right\rangle - \frac{1}{\omega_x^2}\left\langle \frac{m}{2}\omega_x^2 x'^2\right\rangle\right)\\
&= -\frac{(\omega_x^2+\omega_y^2)\alpha(t)}{3m\omega_x^2\omega_y^2}\langle V_T(\vec{r})\rangle_0\\
&= -\frac{2(\omega_y^2-\omega_x^2)\theta(t)}{3m\omega_x^2\omega_y^2}\langle V_T(\vec{r})\rangle_0
\end{aligned} \tag{8.50}$$

where we've used that $\left\langle \frac{m}{2}\omega_x^2 x'^2\right\rangle = \left\langle \frac{m}{2}\omega_y^2 y'^2\right\rangle = \left\langle \frac{m}{2}\omega_z^2 z'^2\right\rangle = \langle V_T(\vec{r})\rangle_0/3$, and $\sin(2\theta) \approx \tan(2\theta) \approx 2\theta$. Here, $\langle V_T(\vec{r})\rangle_0 = 3\mu/7$ is the trap-averaged potential energy of a BEC in the ground state in the Thomas-Fermi regime. For the second term on the RHS of equation (8.45), we recognize that the expectation value can be written $\langle x\rangle = (1/N)\int d^3\vec{r}\,'\,(x'\cos\theta + y'\sin\theta)n(R^{-1}\vec{r}\,',t)$, which again vanishes due to the even nature of the function $n(R^{-1}\vec{r}\,',t)$.

In order to compute the interspecies-interaction term in equation (8.45), we begin by expanding the BEC density $n(\vec{r},t) \equiv n(\vec{r},\theta(t))$ in the small angle $\theta(t)$,

$$n(\vec{r},\theta(t)) = n(\vec{r},0) + \theta(t)\left.\frac{\partial n}{\partial\theta}\right|_{\theta=0} + \mathcal{O}(\theta^2), \tag{8.51}$$

where

$$\left.\frac{\partial n}{\partial\theta}\right|_{\theta=0} = \frac{m}{g}(\omega_x^2-\omega_y^2)xy\,\Theta\Big(\mu - \frac{m}{2}\left(\omega_x^2x^2+\omega_y^2y^2+\omega_z^2z^2\right)\Big), \tag{8.52}$$

and Θ is the Heaviside function. Therefore, the third term on the RHS of equation (8.45) becomes

$$\begin{aligned}\frac{g_{BF}}{m}\langle\cdots\rangle = {}& \frac{g_{BF} n_0 \bar{R}^3}{mN}\int d^3\tilde{\vec{r}}\,\mathrm{Max}(1-\tilde{x}^2-\tilde{y}^2-\tilde{z}^2,0)\left(\beta\tilde{x}\frac{\partial}{\partial\tilde{y}}+\frac{\tilde{y}}{\beta}\frac{\partial}{\partial\tilde{x}}\right)n_F(\vec{r}+\vec{d}(t))\\ &+\theta(t)\frac{g_{BF} n_0 \bar{R}^3}{mN}\frac{2(\omega_x^2-\omega_y^2)}{\omega_x\omega_y}\int d^3\tilde{\vec{r}}\,\tilde{x}\tilde{y}\Theta(1-\tilde{x}^2-\tilde{y}^2-\tilde{z}^2)\left(\beta\tilde{x}\frac{\partial}{\partial\tilde{y}}+\frac{\tilde{y}}{\beta}\frac{\partial}{\partial\tilde{x}}\right)n_F(\vec{r}+\vec{d}(t)),\end{aligned} \tag{8.53}$$

where $n_0 = \mu/g = 15N/(8\pi\bar{R}^3)$, $\bar{R}^3 = R_x R_y R_z$, $R_i = (2\mu/m\omega_i^2)^{1/2}$, $\beta = R_x/R_y = \omega_y/\omega_x$, and we have nondimensionalized the integral by changing to the scaled variables $\tilde{x}_i = x_i/R_i$. Finally, using the local-density approximation, the Gibbs-Duhem relation, and the $T = 0$ EoS to evaluate the derivatives of the Fermi density distribution (as in section 8.2.2), we get

$$\begin{aligned}\frac{g_{BF}}{m}\langle\cdots\rangle = {}& \frac{45\eta^2}{8\pi m} g_{BF} n_{0,F}(0)\int d^3\tilde{\vec{r}}\left(\beta\tilde{x}(\tilde{y}+\tilde{y}_0(t))+\frac{\tilde{y}}{\beta}(\tilde{x}+\tilde{x}_0)\right)\mathcal{H}(\delta(\tilde{\vec{r}}+\tilde{\vec{d}}(t)))\\ &\times\left[\mathrm{Max}(1-\tilde{x}^2-\tilde{y}^2-\tilde{z}^2,0)+\frac{2\theta(t)(\omega_x^2-\omega_y^2)}{\omega_x\omega_y}\tilde{x}\tilde{y}\Theta(1-\tilde{x}^2-\tilde{y}^2-\tilde{z}^2)\right].\end{aligned} \tag{8.54}$$

Here $\eta = \bar{R}/\bar{R}_{0,F}$, $R_{0,i} = (2E_F/m_F\omega_{F,i}^2)^{1/2}$ is the Fermi radius for a two-component, ideal Fermi gas, $n_{0,F}(0) = 8N_F/(\pi^2\bar{R}_{0,F}^3)$ is the peak density for the ideal Fermi gas, and

$$\mathcal{H}(\delta(\tilde{\vec{r}}+\tilde{\vec{d}}(t))) = (\tilde{\delta}k_F a_F)^{-1}\left[-h(\tilde{\delta})+\frac{7\tilde{\delta}}{15}h'(\tilde{\delta})-\frac{\tilde{\delta}^2}{15}h''(\tilde{\delta})\right], \tag{8.55}$$

where $\tilde{\delta} \equiv \delta(\tilde{\vec{r}}+\tilde{\vec{d}}(t)) = \delta_0[1-\eta^2(\delta_0 k_F a_F)^2(\tilde{x}^2+\tilde{y}^2+\tilde{z}^2)]^{-1/2}$ and $\delta_0 = \hbar/(a_F\sqrt{2m_F\mu_F^0})$ (see sections 3.4.3 and 8.2.2).

For compactness, we rewrite equation (8.54) as

$$\frac{g_{BF}}{m}\langle\cdots\rangle = \frac{45\eta^2}{8\pi m} g_{BF} n_{0,F}(0)\left[I_1(\tilde{x}_0,\tilde{y}_0(t))+\theta(t)\frac{2(\omega_x^2-\omega_y^2)}{\omega_x\omega_y}I_2(\tilde{x}_0,\tilde{y}_0(t))\right], \tag{8.56}$$

and expand the two integrals in the small dipole oscillation amplitude $\tilde{y}_0(t) = (y_0/R_y)\cos(\omega_y' t)$, giving

$$I_1(\tilde{x}_0,\tilde{y}_0(t)) = I_1(\tilde{x},0)+\frac{y_0}{R_y}\left.\frac{\partial I_1}{\partial\tilde{y}_0}\right|_{\tilde{y}_0=0}\cos(\omega_y' t)+\mathcal{O}(\tilde{y}_0^2), \tag{8.57}$$

and similarly for I_2. Figure 8.12 shows a surface plot of the integral $I_1(\tilde{x}_0,\tilde{y}_0)$ for the Yb BEC in the presence of a unitary Fermi gas ($\delta_0 = 0$). Because of the symmetries of the

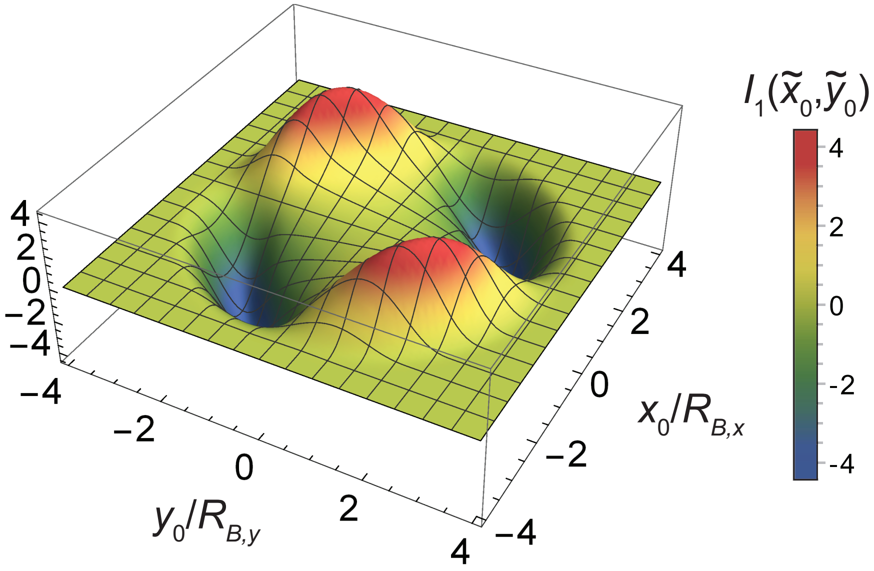

Figure 8.12: Surface plot of the integral $I_1(\tilde{x}_0, \tilde{y}_0)$ as a function of the horizontal ($\tilde{x}_0 = x_0/R_{B,x}$) and vertical ($\tilde{y}_0 = y_0/R_{B,y}$) Yb-Li cloud-center displacements in units of the BEC cloud radii. Because of the symmetry of the integrand, $I_1(x_0, 0) = I_1(0, y_0) = 0$ always.

integrands in I_1 and I_2, $I_1(\tilde{x}_0, 0) = \partial I_2(\tilde{x}_0, 0)/\partial \tilde{y}_0 = 0$. It is important to note that this is the only place in the scissors analysis where the vertical dipole oscillation frequency enters. Finally, we can rewrite equation (8.45) in terms of the tilt angle, $\theta(t)$, giving

$$\frac{d^2\theta}{dt^2} = -(\omega_y^2 + f(x_0)\omega_x^2)\theta + g(x_0, y_0)\omega_x^2 \cos(\omega_y' t), \tag{8.58}$$

where

$$f(x_0) = 1 + \frac{315\eta^2}{8\pi}\frac{\omega_y}{\omega_x}\frac{g_{BF} n_{0,F}(0)}{\mu} I_2(\tilde{x}_0, 0) \tag{8.59}$$

and

$$g(x_0, y_0) = \frac{315\eta^2}{16\pi}\frac{\omega_y^2}{\omega_y^2 - \omega_x^2}\frac{g_{BF} n_{0,F}(0)}{\mu}\frac{y_0}{R_y}\left.\frac{\partial I_1}{\partial \tilde{y}_0}\right|_{\tilde{y}_0 = 0}. \tag{8.60}$$

Thus, the dynamics of the scissors mode in the presence of the Li superfluid are identical to those of a forced harmonic oscillator. From equation (8.58), we identify the natural frequency of the scissors mode in this interacting Bose-Fermi system as $\omega_s = (\omega_y^2 + f(x_0)\omega_x^2)^{1/2}$. As we will see, the magnitude of the function $f(x_0)$ is always of order 1, and consequently $\omega_s \approx \omega_y$. Therefore, the forcing term in equation (8.58) presents a near-resonant drive of the scissors oscillator, thanks to the large trap aspect ratio and therefore near degeneracy of the scissors and dipole frequencies.

Figures 8.13(a)-(b) show the functions f and g for our experimentally relevant situation at 780 G ($1/k_F a_F = 0.39$). For these, $R_{B,y} = 1.14$ μm and $R_{0,y} = 4.2$ μm, giving $\eta = 0.27$, $n_{0,F}(0) = 1.5 \times 10^{13}$ cm^{-3} and $\mu/k_B = 81$ nK, giving $g_{BF} n_{0,F}(0)/\mu = 0.08$, $y_0 = 0.5$ μm, $\omega_y = 2\pi \times 388$ Hz, $\omega_y' = 2\pi \times 381$ Hz, and $\omega_x = 2\pi \times 59$ Hz. Part (c) of the same figure shows the integration of equation (8.58) for three different horizontal cloud displacement values: $0.3R_{0,x}$, $0.45R_{0,x}$, and $0.6R_{0,x}$.

8.4.3 Angular momentum in the scissors mode

In order to investigate the role of angular momentum in the scissors mode oscillation, we evaluate the expectation value of the operator $L_z = m(xv_y - yv_x)$. As we showed in section

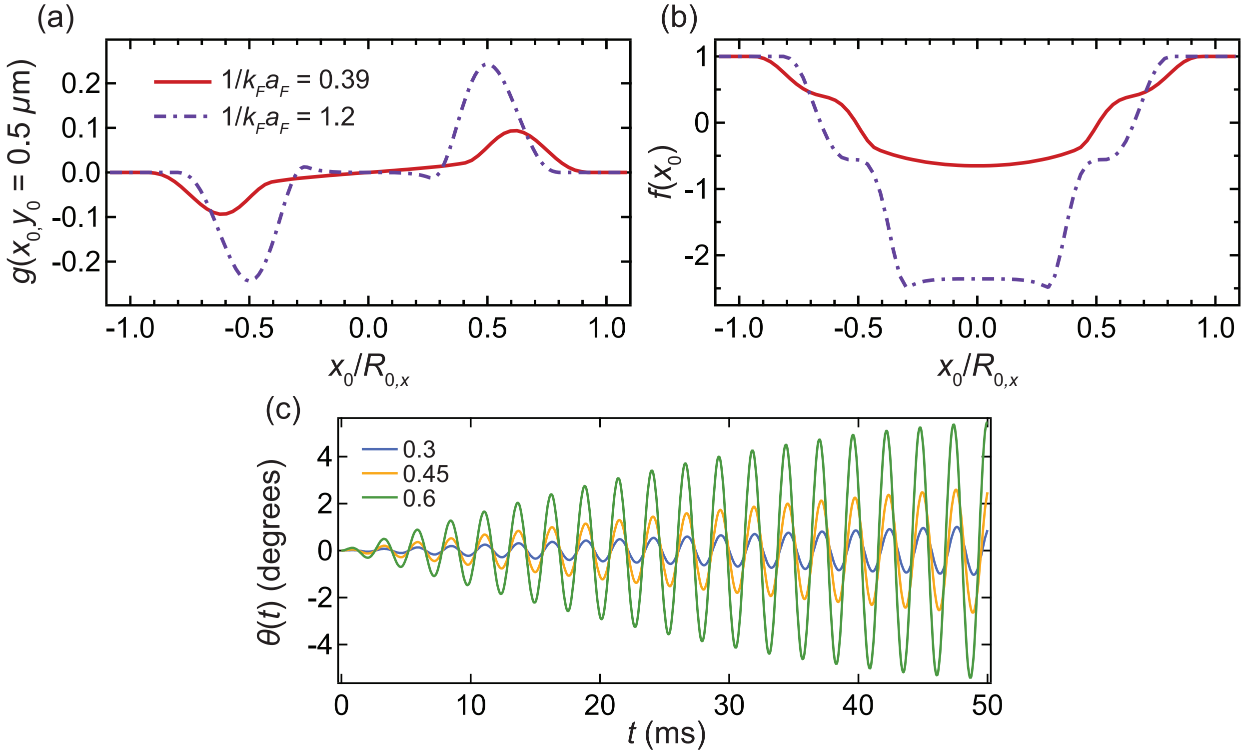

Figure 8.13: (a)-(b) Relevant functions $g(x_0, y_0)$ and $f(x_0)$ for the analytical model of the driven scissors mode during Yb dipole oscillations. Specific parameters used correspond to those in the dipole oscillation experiments (see text). Note that the horizontal displacement is expressed in units of the ideal Fermi gas radius. (c) Solutions to the tilt angle dynamics (equation (8.58)) for three different displacements $x_0/R_{0,x} = 0.3$ (blue), 0.45 (orange), and 0.6 (green), as a function of time after the diabatic excitation of the Yb vertical dipole oscillation.

8.4.2, the density profile does not change in shape as a result of the scissors excitation. Another way of saying this is that the material derivative of the density is zero, $(\partial/\partial t + \vec{v} \cdot \nabla)n = 0$. Using the continuity equation (8.35), we then find that $\nabla \cdot \vec{v} = 0$ (incompressible flow). In combination with the irrotationality constraint $\nabla \times \vec{v} = 0$, this implies that $\vec{v} = \gamma(t)\nabla(xy)$, for some $\gamma(t)$ [73]. Using equations (8.35), (8.46), and (8.51), one can show that $\gamma(t) = \dot{\theta}(t)(\omega_y^2 - \omega_x^2)/(\omega_y^2 + \omega_x^2)$, and therefore

$$\begin{aligned} \langle L_z \rangle (t) &= \frac{m}{N}\dot{\theta}(t)\frac{\omega_y^2 - \omega_x^2}{\omega_y^2 + \omega_x^2}\int d^3\vec{r}(x^2 - y^2)n(\vec{r}, t) \\ &= \frac{2}{3}\frac{(\omega_y^2 - \omega_x^2)^2}{\omega_y^2\omega_x^2(\omega_y^2 + \omega_x^2)}\langle V_T(\vec{r})\rangle_0\,\dot{\theta}(t) \end{aligned} \tag{8.61}$$

Thus, we see directly that a time-dependent in-trap angle necessitates the existence of angular momentum in the condensate. Furthermore, this derivation only used the continuity equation (8.35) and the fact that the superfluid flow is incompressible, and therefore applies to both the interspecies-interaction-driven scissors mode in our experiment, as well as the "standard" scissors excitation achieved by a diabatic rotation of the trap eigenaxes.

8.4.4 Comparison with observed scissors mode

Our theoretical model (equation (8.58)) captures the essential feature of this interspecies-interaction-driven scissors oscillation; the modulation of the Yb vertical position during dipole oscillations coupled with mean-field interactions with a horizontally-offset Li cloud results in a near-resonant drive of the Yb scissors mode. However, our model qualitatively differs from the observed tilt angle dynamics in figure 8.11(c)-(d) in that the observed amplitude of oscillation does not grow linearly with time. We take this to be indicative of a sizable damping effect in the scissors mode. Thus, in order to quantitatively compare our model to the measurements, we add a heuristic damping term to equation (8.58), giving

$$\frac{d^2\theta}{dt^2} = -\omega_s^2\theta - \frac{\omega_s}{Q_s}\frac{d\theta}{dt} + g(x_0, y_0)\omega_x^2\cos(\omega_y' t). \tag{8.62}$$

Here Q_s is the quality factor association with the scissors mode. The steady-state solution to equation (8.62) is then $\theta(t) = A\cos(\omega'_y t + \phi_s)$, where

$$A = \frac{g(x_0, y_0)\omega_x^2}{\sqrt{(\omega_s^2 - \omega_y'^2)^2 + \left(\frac{\omega_s \omega'_y}{Q_s}\right)^2}}, \tag{8.63}$$

and ϕ_s is the phase of the response relative to the drive. Using $\omega'_y \approx \omega_y \approx \omega_s$, we get

$$A \approx Q_s g(x_0, y_0) \left(\frac{\omega_x}{\omega_y}\right)^2. \tag{8.64}$$

Note that in the limit of low damping, the amplitude A responds very strongly to frequency near resonance, and the approximation in equation (8.64) is not necessarily valid. However, since we are expecting considerable damping in this mode, we need not worry about this. Indeed, using equation (8.64) we find that our observed scissors mode amplitude with $1/k_F a_F = 0.39$ of 1.3(3) degrees is consistent with the model (8.62) for a displacement of $x_0 = 0.6R_{0,x}$ and quality factor of $Q_s = 4$. For this estimate, we use the fact that the measurements in figure 8.11(c) are in the long ToF regime, which results in a factor of 2 difference between the in-trap oscillations $\theta(t)$ and those following the superfluid expansion $\theta_{\mathrm{ToF}}(t)$ [77].

An important question raised here is the origin of damping in the bosonic scissors mode. One potential cause could be collisions between the BEC and some finite thermal component of the Yb cloud. Another possible cause is severe anharmonicity in the horizontal trapping directions, since we know from the dipole oscillation measurements that the quality factor in the vertical direction is quite large ($\omega'_y \tau \approx 250$). Further systematic investigation in the Yb-Li dual superfluid system in conjunction with full numerical simulations of the coupled-superfluid dynamics should shed light on the nature of damping in this driven-scissors mode, as well as provide reliable quantification of the relative phase ϕ_s observed at long ToF.

BIBLIOGRAPHY

[1] A. Altmeyer, S. Riedl, C. Kohstall, M. J. Wright, R. Geursen, M. Bartenstein, C. Chin, J. H. Denschlag, and R. Grimm. Precision measurements of collective oscillations in the BEC-BCS crossover. *Phys. Rev. Lett.*, 98:040401, 2007.

[2] M. H. Anderson, J. R. Ensher, M. R. Matthews, C. E. Wieman, and E. A. Cornell. Observation of Bose-Einstein condensation in a dilute atomic vapor. *Science*, 269:198, 1995.

[3] A.F. Andreev and E.P. Bashkin. Three-velocity hydrodynamics of superfluid solutions. *Zh. Eksp. Teor. Fiz.*, 69:319, 1975.

[4] N. W. Ashcroft and N. D. Mermin. *Solid State Physics*. Brooks/Cole, 1976.

[5] S. Baier, M. J. Mark, D. Petter, K. Aikawa, L. Chomaz, Z. Cai, M. Baranov, P. Zoller, and F. Ferlaino. Extended Bose-Hubbard models with ultracold magnetic atoms. *Science*, 352(6282):201–205, 2016.

[6] G. A. Baker. Neutron matter model. *Phys. Rev. C*, 60:054311, 1999.

[7] M. Bartenstein, A. Altmeyer, S. Riedl, S. Jochim, C. Chin, J. Hecker Denschlag, and R. Grimm. Crossover from a molecular Bose-Einstein condensate to a degenerate Fermi gas. *Phys. Rev. Lett.*, 92:120401, 2004.

[8] H. A. Bethe. Theory of the effective range in nuclear scattering. *Phys. Rev.*, 76:38–50, Jul 1949.

[9] I. Bloch, J. Dalibard, and S. Nascimbne. Quantum simulations with ultracold quantum gases. *Nature Physics*, 8:267, 2012.

[10] I. Bloch, J. Dalibard, and W. Zwerger. Many-body physics with ultracold gases. *Rev Mod Phys*, 80:885, 2008.

[11] J. L. Bohn and P. S. Julienne. Prospects for influencing scattering lengths with far-off-resonant light. *Phys. Rev. A*, 56:1486–1491, 1997.

[12] J. L. Bohn and P. S. Julienne. Semianalytic theory of laser-assisted resonant cold collisions. *Phys. Rev. A*, 60:414–425, Jul 1999.

[13] D. Boiron, A. Michaud, P. Lemonde, Y. Castin, C. Salomon, S. Weyers, K. Szymaniec, L. Cognet, and A. Clairon. Laser cooling of cesium atoms in gray optical molasses down to $1.1\,\mu$K. *Phys Rev A*, 53:R3734, 1996.

[14] D. Boiron, C. Triché, D. R. Meacher, P. Verkerk, and G. Grynberg. Three-dimensional cooling of cesium atoms in four-beam gray optical molasses. *Phys. Rev. A*, 52:R3425–R3428, 1995.

[15] D.A. Brue and J.M. Hutson. Magnetically tunable Feshbach resonances in ultracold Li-Yb mixtures. *Phys. Rev. Lett.*, 108:043201, 2012.

[16] A. Burchianti, G. Valtolina, J. A. Seman, E. Pace, M. De Pas, M. Inguscio, M. Zaccanti, and G. Roati. Efficient all-optical production of large ^{6}Li quantum gases using D_1 gray-molasses cooling. *Phys. Rev. A*, 90:043408, Oct 2014.

[17] L. D. Carr, G. V. Shlyapnikov, and Y. Castin. Achieving a BCS transition in an atomic Fermi gas. *Phys. Rev. Lett.*, 92:150404, 2004.

[18] Y. Castin, I. Ferrier-Barbut, and C. Salomon. The Landau critical velocity for a particle in a Fermi superfluid. *Comptes Rendus Physique*, 16:241, 2015.

[19] Miguel A Cazalilla and Ana Maria Rey. Ultracold Fermi gases with emergent SU(N) symmetry. *Reports on Progress in Physics*, 77(12):124401, 2014.

[20] L. Cheuk, M. Nichols, K. Lawrence, M. Okan, H. Zhang, E. Khatami, N. Trivedi, T. Paiva, M. Rigol, and M. Zwierlein. Observation of spatial charge and spin correlations in the 2D Fermi-Hubbard model. *Science*, 353(6305):1260–1264, 2016.

[21] C. Chin, R. Grimm, P. S. Julienne, and E. Tiesinga. Feshbach resonances in ultracold gases. *Rev. Mod. Phys.*, 82:1225, 2010.

[22] C. Cohen-Tannoudji, J. Dupont-Roc, and G. Grynberg. *Atom-Photon Interactions: Basic Processes and Applications.* John Wiley, New York, NY, 1992.

[23] Franco Dalfovo, Stefano Giorgini, Lev P. Pitaevskii, and Sandro Stringari. Theory of Bose-Einstein condensation in trapped gases. *Rev. Mod. Phys.*, 71:463–512, 1999.

[24] K.B. Davis, M.-O. Mewes, M. R. Andrews, N. J. van Druten, D. S. Durfee, D. M. Kurn, and W. Ketterle. Bose-Einstein condensation in a gas of sodium atoms. *Phys. Rev. Lett.*, 75:3969, 1995.

[25] T. N. De Silva and E. J. Mueller. Profiles of near-resonant population-imbalanced trapped Fermi gases. *Phys. Rev. A*, 73:051602, 2006.

[26] J. P. D'Incao and B. D. Esry. Scattering length scaling laws for ultracold three-body collisions. *Phys. Rev. Lett.*, 94:213201, 2005.

[27] W.H. Dowd, R.J. Roy, R.K. Shrestha, A. Petrov, C. Makrides, S. Kotochigova, and S. Gupta. Magnetic field dependent interactions in an ultracold Li-Yb($^3P_2$) mixture. *New J. Phys.*, 17:055007, 2015.

[28] B. D. Esry, Chris H. Greene, and H. Suno. Threshold laws for three-body recombination. *Phys. Rev. A*, 65:010705, 2001.

[29] T. Esslinger, H. Ritsch, M. Weidemüller, F. Sander, A. Hemmerich, and T. W. Hänsch. Purely optical dark lattice. *Opt. Lett.*, 21(13):991–993, 1996.

[30] D. Rio Fernandes, F. Sievers, N. Kretzschmar, S. Wu, C. Salomon, and F. Chevy. Sub-Doppler laser cooling of fermionic ^{40}K atoms in three-dimensional gray optical molasses. *Europhysics Letters*, 100(6):63001, 2012.

[31] I. Ferrier-Barbut, M. Delehaye, S. Laurent, A.T. Grier, M. Pierce, B.S. Rem, F. Chevy, and C. Salomon. A mixture of Bose and Fermi superfluids. *Science*, 345:1035, 2014.

[32] A. L. Fetter and J. D. Walecka. *Quantum Theory of Many-Particle Systems.* Dover Publications, 2003.

[33] C. J. Foot. *Atomic Physics.* Oxford University Press, Oxford, UK, 2005.

[34] Nir Friedman, Ariel Kaplan, Dina Carasso, and Nir Davidson. Observation of chaotic and regular dynamics in atom-optics billiards. *Phys. Rev. Lett.*, 86:1518–1521, 2001.

[35] Maykel L. González-Martínez and Jeremy M. Hutson. Magnetically tunable Feshbach resonances in Li + Yb(^3P_J). *Phys. Rev. A*, 88:020701, 2013.

[36] A. Grier, I. Ferrier-Barbut, B. Rem, M. Delehaye, L. Khaykovich, F. Chevy, and C. Salomon. Λ-enhanced sub-Doppler cooling of lithium atoms in D_1 gray molasses. *Phys. Rev. A*, 87:063411, 2013.

[37] M. Grimm, R. Weidemüller and Y. Ovchinnikov. Optical dipole traps for neutral atoms. *Advances in Atomic, Molecular, and Optical Physics*, 42:95, 2000.

[38] D. Guery-Odelin and S. Stringari. Scissor mode and superfluidity of a trapped Bose-Einstein condensed gas. *Phys. Rev. Lett.*, 83:4452, 1999.

[39] M. Guo, B. Zhu, B. Lu, X. Ye, F. Wang, R. Vexiau, N. Bouloufa-Maafa, G. Quéméner, O. Dulieu, and D. Wang. Creation of an ultracold gas of ground-state dipolar ^{23}Na^{87}Rb molecules. *Phys. Rev. Lett.*, 116:205303, May 2016.

[40] Subhadeep Gupta. *Experiments with Degenerate Bose and Fermi Gases.* PhD thesis, Massachusetts Institute of Technology, 2003.

[41] A. H. Hansen, A. Khramov, W. H. Dowd, A. O. Jamison, B. Plotkin-Swing, R. J. Roy, and S. Gupta. Production of quantum degenerate mixtures of ytterbium and lithium with controllable interspecies overlap. *Phys. Rev. A.*, 87:013615, 2013.

[42] Anders Hansen. *Interacting Quantum Gases of Lithium and Ytterbium.* PhD thesis, University of Washington, 2013.

[43] H. Hara, H. Konishi, S. Nakajima, Y. Takasu, and Y. Takahashi. A three-dimensional optical lattice of ytterbium and lithium atomic gas mixture. *Journal of the Physical Society of Japan*, 83(1):014003, 2014.

[44] H. Hara, Y. Takasu, Y. Yamaoka, J.M. Doyle, and Takahashi Y. Quantum degenerate mixtures of alkali and alkaline-earth-like atoms. *Phys. Rev. Lett.*, 106:205304, 2011.

[45] R. A. Hart, P. M. Duarte, T.-L. Yang, X. Liu, T. Paiva, E. Khatami, R. T. Scalettar, N. Trivedi, D. A. Huse, and R. G. Hulet. Observation of antiferromagnetic correlations in the Hubbard model with ultracold atoms. *Nature*, 519:211–214, 2015.

[46] R. Haussmann, W. Rantner, S. Cerrito, and W. Zwerger. Thermodynamics of the BCS-BEC crossover. *Phys. Rev. A*, 75:023610, Feb 2007.

[47] R. Haussmann and W. Zwerger. Thermodynamics of a trapped unitary Fermi gas. *Phys. Rev. A*, 78:063602, 2008.

[48] H. Heiselberg. Sound modes at the BCS-BEC crossover. *Phys. Rev. A*, 73:013607, 2006.

[49] K. Henderson, C. Ryu, C. MacCormick, and M.G. Boshier. Experimental demonstration of painting arbitrary and dynamic potentials for Bose-Einstein condensates. *New Journal of Physics*, 11:043030, 2009.

[50] T.-L. Ho. Universal thermodynamics of degenerate quantum gases in the unitarity limit. *Phys. Rev. Lett.*, 92:090402, 2004.

[51] Hui Hu, Xia-Ji Liu, and Peter D Drummond. Universal thermodynamics of a strongly interacting Fermi gas: theory versus experiment. *New Journal of Physics*, 12(6):063038, 2010.

[52] Jeremy M Hutson. Feshbach resonances in ultracold atomic and molecular collisions: threshold behaviour and suppression of poles in scattering lengths. *New Journal of Physics*, 9(5):152, 2007.

[53] Zbigniew Idziaszek and Paul S. Julienne. Universal rate constants for reactive collisions of ultracold molecules. *Phys. Rev. Lett.*, 104:113202, Mar 2010.

[54] V. V. Ivanov, A. Khramov, A. H. Hansen, W. H. Dowd, F. Münchow, A. O. Jamison, and S. Gupta. Sympathetic cooling in an optically trapped mixture of alkali and spin-singlet atoms. *Phys. Rev. Lett.*, 106:153201, 2011.

[55] Kevin M. Jones, Eite Tiesinga, Paul D. Lett, and Paul S. Julienne. Ultracold photoassociation spectroscopy: Long-range molecules and atomic scattering. *Rev. Mod. Phys.*, 78:483–535, May 2006.

[56] H. Kadau, M. Schmitt, M. Wenzel, C. Wink, T. Maier, I. Ferrier-Barbut, and T. Pfau. Observing the Rosensweig instability of a quantum ferrofluid. *Nature*, 530:194–197, 2016.

[57] W. Ketterle and N. J. van Druten. Evaporative cooling of trapped atoms. *Advances in Atomic, Molecular, and Optical Physics*, 37:181 – 236, 1996.

[58] W. Ketterle and M. W. Zwierlein. Making, probing and understanding ultracold Fermi gases. In M. Inguscio, W. Ketterle, and C. Salomon, editors, *Proceedings of the International School of Physics Enrico Fermi, Course CLXIV: Ultracold Fermi Gases, Varenna.* IOS Press, Amsterdam, 2008.

[59] A. Khramov, A. H. Hansen, W. H. Dowd, R. J. Roy, C. Makrides, A. Petrov, S. Kotochigova, and S. Gupta. Ultracold heteronuclear mixture of ground and excited state atoms. *Phys. Rev. Lett.*, 112:033201, 2014.

[60] A. Y. Khramov, A. H. Hansen, A. O. Jamison, W. H. Dowd, and S. Gupta. Dynamics of Feshbach molecules in an ultracold three-component mixture. *Phys. Rev. A*, 86:032705, 2012.

[61] Alex Khramov. *Experiments in the Ultracold Lithium - Ytterbium System*. PhD thesis, University of Washington, 2013.

[62] J. Kinast, A. Turlapov, J. E. Thomas, Q. Chen, J. Stajic, and K. Levin. Heat capacity of a strongly interacting Fermi gas. *Science*, 307:1296, 2005.

[63] T. Kinoshita, T. Wenger, and D. S. Weiss. All-optical Bose-Einstein condensation using a compressible crossed dipole trap. *Phys. Rev. A*, 71:011602(R), 2005.

[64] Thorsten Köhler, Krzysztof Góral, and Paul S. Julienne. Production of cold molecules via magnetically tunable Feshbach resonances. *Rev. Mod. Phys.*, 78:1311–1361, Dec 2006.

[65] Svetlana Kotochigova. Controlling interactions between highly magnetic atoms with Feshbach resonances. *Reports on Progress in Physics*, 77(9):093901, 2014.

[66] M. Ku. *PhD. thesis, Massachusetts Institute of Technology*, 2015.

[67] M. J. H. Ku, A. T. Sommer, L. W. Cheuk, and M. Zwierlein. Revealing the superfluid lambda transition in the universal thermodynamics of a unitary Fermi gas. *Science*, 335:563, 2012.

[68] T. Lahaye, C. Menotti, L. Santos, M. Lewenstein, and T. Pfau. The physics of dipolar bosonic quantum gases. *Reports on Progress in Physics*, 72(12):126401, 2009.

[69] N. D. Lemke, A. D. Ludlow, Z. W. Barber, T. M. Fortier, S. A. Diddams, Y. Jiang, S. R. Jefferts, T. P. Heavner, T. E. Parker, and C. W. Oates. Spin-1/2 optical lattice clock. *Phys. Rev. Lett.*, 103:063001, 2009.

[70] Xia-Ji Liu, Hui Hu, and Peter D. Drummond. Virial expansion for a strongly correlated Fermi gas. *Phys. Rev. Lett.*, 102:160401, 2009.

[71] R. S. Lous, I Fritsche, M. Jag, B. Huang, and R. Grimm. Thermometry of a deeply degenerate Fermi gas with a Bose-Einstein condensate. *arXiv:1702.02772*, 2017.

[72] O. J. Luiten, M. W. Reynolds, and J. T. M. Walraven. Kinetic theory of the evaporative cooling of a trapped gas. *Phys. Rev. A*, 53:381–389, 1996.

[73] O.M. Marago, G. Hechenblaikner, E. Hodby, S.A. Hopkins, and C.J. Foot. The moment of inertia and the scissors mode of a Bose-condensed gas. *Journal of Physics: Condensed Matter*, 14(3):343, 2002.

[74] O.M. Marago, J. Hopkins, S.A. ad Arlt, E¿ Hodby, G. Hechenblaikner, and C.J. Foot. Observation of the scissors mode and evidence for superfluiditiy of a trapped Bose-Einstein condensed gas. *Phys. Rev. Lett.*, 84:2056, 2000.

[75] H. J. Metcalf and P. van der Straten. *Laser Cooling and Trapping.* Springer, New York, NY, 1999.

[76] V. Milner, J. L. Hanssen, W. C. Campbell, and M. G. Raizen. Optical billiards for atoms. *Phys. Rev. Lett.*, 86:1514–1517, 2001.

[77] M. Modugno, G. Modugno, G. Roati, C. Fort, and M. Inguscio. Scissors mode of an expanding Bose-Einstein condensate. *Phys. Rev. A*, 67:023608, 2003.

[78] P. K. Molony, P. D. Gregory, Z. Ji, B. Lu, M. P. Köppinger, C. R. Le Sueur, C. L. Blackley, J. M. Hutson, and S. L. Cornish. Creation of ultracold ^{87}Rb^{133}Cs molecules in the rovibrational ground state. *Phys. Rev. Lett.*, 113:255301, 2014.

[79] S. Nascimbene, N. Navon, K.J. Jiang, F. Chevy, and C. Salomon. Exploring the thermodynamics of a universal Fermi gas. *Nature*, 463:1057, 2010.

[80] N. Navon, S. Nascimbène, F. Chevy, and C. Salomon. The equation of state of a low-temperature Fermi gas with tunable interactions. *Science*, 328(5979), 2010.

[81] K.-K. Ni, S. Ospelkaus, M. H. G. de Miranda, A. Peer, B. Neyenhuis, J. J. Zirbel, S. Kotochigova, P. S. Julienne, D. S. Jin, and J. Ye. A high phase-space-density gas of polar molecules. *Science*, 322:231, 2008.

[82] T. L. Nicholson, S. Blatt, B. J. Bloom, J. R. Williams, J. W. Thomsen, J. Ye, and Paul S. Julienne. Optical Feshbach resonances: Field-dressed theory and comparison with experiments. *Phys. Rev. A*, 92:022709, 2015.

[83] K. M. O'Hara, M. E. Gehm, S. R. Granade, and J. E. Thomas. Scaling laws for evaporative cooling in time-dependent optical traps. *Phys. Rev. A.*, 64:051403(R), 2001.

[84] A. J. Olson, R. J. Niffenegger, and Y. P. Chen. Optimizing the efficiency of evaporative cooling in optical dipole traps. *Phys Rev A*, 87:053613, 2013.

[85] J.W. Park, S.A. Will, and M.W. Zwierlein. Ultracold dipolar gas of fermionic ^{23}Na^{40}K molecules in their absolute ground state. *Phys. Rev. Lett.*, 114:205302, 2015.

[86] M. F. Parsons, A. Mazurenko, C. S. Chiu, G. Ji, D. Greif, and M. Greiner. Site-resolved measurement of the spin-correlation function in the Fermi-Hubbard model. *Science*, 353(6305):1253–1256, 2016.

[87] G. B. Partridge, W. Li, R. I. Kamar, Y. Liao, and R. G. Hulet. Pairing and phase separation in a polarized Fermi gas. *Science*, 311(5760):503–505, 2006.

[88] C. J. Pethick, N. Chamel, and S. Reddy. Superfluid dynamics in neutron star crusts. *Progress of Theoretical Physics Supplement*, 186:9–16, 2010.

[89] C. J. Pethick and H. Smith. *Bose-Einstein Condensation in Dilute Gases.* Cambridge University Press, Cambridge, UK, 2008.

[90] A. Petrov, E. Tiesinga, and S. Kotochigova. Anisotropy-induced Feshbach resonances in a quantum dipolar gas of highly magnetic atoms. *Phys. Rev. Lett.*, 109:103002, 2012.

[91] A. Petrov, C. Makrides, and S. Kotochigova. Magnetic control of ultra-cold ^{6}Li and ^{174}Yb($^3P_2$) atom mixtures with Feshbach resonances. *New Journal of Physics*, 17(4):045010, 2015.

[92] D. S. Petrov, C. Salomon, and G. V. Shlyapnikov. Weakly bound dimers of fermionic atoms. *Phys. Rev. Lett.*, 93:090404, 2004.

[93] C. A. Regal, M. Greiner, and D. S. Jin. Observation of resonance condensation of fermionic atom pairs. *Phys. Rev. Lett.*, 92:040403, 2004.

[94] Richard Roy, Alaina Green, Ryan Bowler, and Subhadeep Gupta. Rapid cooling to quantum degeneracy in dynamically shaped atom traps. *Phys. Rev. A.*, 93:043403, 2016.

[95] Richard Roy, Alaina Green, Ryan Bowler, and Subhadeep Gupta. Two-element mixture of Bose and Fermi superfluids. *Phys. Rev. Lett.*, 118:055301, Feb 2017.

[96] Richard Roy, Rajendra Shrestha, Alaina Green, Subhadeep Gupta, Ming Li, Svetlana Kotochigova, Alexander Petrov, and Chi Hong Yuen. Photoassociative production of ultracold heteronuclear YbLi* molecules. *Phys. Rev. A*, 94:033413, 2016.

[97] J. Rysti, J. Tuoriniemi, and A. Salmela. Effective ^{3}He interactions in dilute ^{3}He-^{4}He mixtures. *Phys. Rev. B*, 85:134529, 2012.

[98] C. Ryu, P. W. Blackburn, A. A. Blinova, and M. G. Boshier. Experimental realization of Josephson junctions for an atom SQUID. *Phys. Rev. Lett.*, 111:205301, 2013.

[99] H. R. Sadeghpour, J. L. Bohn, M. J. Cavagnero, B. D. Esry, I. I. Fabrikant, J. H. Macek, and A. R. P. Rau. Collisions near threshold in atomic and molecular physics. *Journal of Physics B: Atomic, Molecular and Optical Physics*, 33(5):R93, 2000.

[100] J. J. Sakurai. *Modern Quantum Mechanics.* Addison Wesley, 1994.

[101] F. Sievers, N. Kretzschmar, D. Rio Fernandes, D. Suchet, M. Rabinovic, S. Wu, C. V. Parker, L. Khaykovich, C. Salomon, and F. Chevy. Simultaneous sub-Doppler laser cooling of fermionic ^{6}Li and ^{40}K on the D_1 line: Theory and experiment. *Phys. Rev. A*, 91:023426, Feb 2015.

[102] S. Stellmer, B. Pasquiou, R. Grimm, and F. Schreck. Creation of ultracold Sr_2 molecules in the electronic ground state. *Phys. Rev. Lett.*, 109:115302, 2012.

[103] T. Takekoshi, L. Reichsöllner, A. Schindewolf, J. M. Hutson, C. R. Le Sueur, O. Dulieu, F. Ferlaino, R. Grimm, and H.-C. Nägerl. Ultracold dense samples of dipolar RbCs molecules in the rovibrational and hyperfine ground state. *Phys. Rev. Lett.*, 113:205301, 2014.

[104] S. Tan. Energetics of a strongly correlated Fermi gas. *Annals of Physics*, 323(12):2952 – 2970, 2008.

[105] L. Viverit, C. J. Pethick, and H. Smith. Zero-temperature phase diagram of binary boson-fermion mixtures. *Phys. Rev. A*, 61:053605, 2000.

[106] T. Weber, J. Herbig, M. Mark, H-C. Nagerl, and R. Grimm. Three-body recombination at large scattering lengths in an ultracold atomic gas. *Phys. Rev. Lett.*, 91:123201, 2003.

[107] M. Weissbluth. *Atoms and Molecules.* Academic Press, New York, NY, 1978.

[108] B. Yan, S. A. Moses, B. Gadway, J. P. Covey, K. R. A. Hazzard, A. Maria Rey, D. S. Jin, and J. Ye. Observation of dipolar spin-exchange interactions with lattice-confined polar molecules. *Nature*, 501:521–525, 2013.

[109] M. Yan, R. Chakraborty, A. Mazurenko, P. G. Mickelson, Y. N. Martinez de Escobar, B. J. DeSalvo, and T. C. Killian. Numerical modeling of collisional dynamics of Sr in an optical dipole trap. *Phys Rev A*, 83:032705, 2011.

[110] X-C Yao, H. Chen, Y. Wu, X. Liu, X. Wang, X. Jiang, Y. Deng, Y. Chen, and J. Pan. Observation of Coupled Vortex Lattices in a Mass-Imbalance Bose and Fermi Superfluid Mixture. *Phys. Rev. Lett.*, 117:145301, 2016.

[111] R. Zhang, W. Zhang, H. Zhai, and P. Zhang. Calibration of the interaction energy between Bose and Fermi superfluids. *Phys Rev A*, 90:063614, 2014.

[112] G. Zürn, T. Lompe, A. N. Wenz, S. Jochim, P. S. Julienne, and J. M. Hutson. Precise characterization of ^{6}Li Feshbach resonances using trap-sideband-resolved rf spectroscopy of weakly bound molecules. *Phys. Rev. Lett.*, 110:135301, 2013.

[113] W. Zwerger. Ed., *The BCS-BEC Crossover and the Unitary Fermi Gas*, vol 836 of *Lecture Notes in Physics.* Springer, Berlin, 2012.

[114] M. W. Zwierlein, J. R. Abo-Shaeer, A. Schirotzek, C. H. Schunck, and W. Ketterle. Vortices and superfluidity in a strongly interacting Fermi gas. *Nature*, 435(7045):1047–1051, 2005.